LRP 638/99 June 1999

The extension of the FIR interferometer of TCV to a polarimeter and measurements of the Faraday rotation caused by the poloidal magnetic field

S. Barry

ISSN 0458-5895

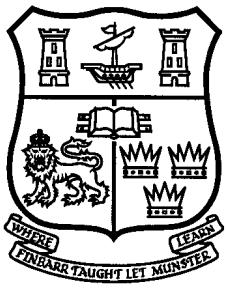

The Extension of the FIR Interferometer of TCV to a Polarimeter and Measurements of the Faraday Rotation caused by the Poloidal Magnetic Field

Siobhán M. Barry B.E., M.Eng.Sc.

A Thesis Presented to the National University of Ireland, Cork
for the Degree of

Ph.D.

March 1999

Internal Supervisor : Dr. Seán Prunty, Department of Electrical Engineering and Microelectronics.

External Supervisor : Dr. Christoph Nieswand, Ecole Polytechnique Fédérale de Lausanne, Switzerland.

Abstract

Interferometry is a well known technique for measuring the line-integrated electron density of magnetically confined plasmas. It is based on the phase change that an electromagnetic wave experiences on passing through a plasma with respect to that of a vacuum. In addition, the plane of polarisation of the wave is, in general, rotated due to the birefringence of the plasma. The total rotation angle, which can be measured by polarimetric techniques, is known as the Faraday rotation and is proportional to the line-integrated value of the product of electron density and the magnetic field component parallel to the probing beam. In order to maximise its information gathering capability the TCV (Tokamak à Configuration Variable) tokamak's multi-channel interferometer system has been modified to include a polarimeter.

The reconstruction of the density profile is difficult for non-circular highly shaped plasmas, as is the case on TCV and requires the line-integrated measurements over a large number of chords. Consequently, a 14 channel instrument with two possible polarimeter methods was installed. Both methods are based on an optically pumped far-infrared (FIR) laser with a rotating polarisation where both the interferometer and polarimeter information are determined from phase measurements with only one detector required per probing chord. The feasibility of the methods were verified during bench tests prior to the installation of the instrument on TCV. These tests also provided an opportunity to test and modify some of the essential components.

The instrument was used to measure the Faraday rotation of various TCV plasmas. This thesis concentrates, however, on the highly elongated plasmas where the measured rotation angles are relatively large and where the inclusion of the Faraday rotation information was predicted to improve the accuracy of the equilibrium reconstruction. The polarimetric precision of 2% required for the reconstruction has not yet been achieved. However, an independent determination of the central safety factor q_0 calculated from the slope of the Faraday rotation profile, the electron density and some geometric parameters resulted in values of q_0 which were in disagreement with the reconstructed values. This led to a re-definition of the base functions used during the reconstruction calculations and the attainment of values of the reconstructed q_0 which were in closer agreement with measurements from other diagnostics.

Contents

1 Introduction **1**

1.1 Thermonuclear Fusion 1

1.2 The Tokamak Concept 4

1.2.1 Tokamak à Configuration Variable 6

1.2.2 Relevant Diagnostics 8

Magnetic Diagnostics 8

Soft X-ray Tomography 10

Thomson Scattering 11

1.3 Tokamak Equilibrium 11

1.4 Poloidal Field Measurements 13

1.4.1 Spectroscopic Measurements 13

Zeeman Splitting 13

Motional Stark Effect 13

1.4.2 Faraday Rotation 14

1.5 Outline of the Thesis 15

2 The Theory of Refractive Index Measurements **16**

2.1 The State of Polarisation of an Electromagnetic Wave 16

2.1.1 Stokes Parameters and Poincaré Sphere 18

2.1.2 Jones Matrices 19

2.2 The Propagation of an Electromagnetic Wave through a Magnetised Plasma 21

2.2.1 Characteristic plasma frequencies 21

2.2.2 Evolution of the State of Polarisation 23

Jones Matrix Analysis 26

3 Wavelength Selection **29**

3.1 Fringe count 31
3.2 Refraction 33
3.3 Vibrations 35
3.4 Faraday Rotation 35
3.5 Equilibrium Reconstruction 36
3.6 Conclusions 40

4 Method Description **41**

4.1 Basic Principles 41
4.1.1 Interferometry 41
4.1.2 Polarimetry 43
4.2 Polarisation Modulation 45
Crystalline Quartz Optics 45
4.3 Method 1 47
4.3.1 Polarimeter 51
4.3.2 Interferometer 51
4.4 Method 2 54
4.4.1 Polarimeter 56
4.4.2 Interferometer 56
4.4.3 Non-idealities 57
Non-zero phase difference between the **A** and **B** beams 57
Polarisation Sensitive Beamsplitters 60
4.5 Polarimetric Measurement Accuracy 63
4.5.1 Demodulation 63
4.5.2 Noise Analysis 64
4.6 Conclusions 69

5 Bench Tests **70**

5.1 Interferometer Bench Test 70
5.2 Polarimeter Bench Test 74
5.3 Conclusions 80

6 Instrument Description **81**

6.1 The Laser System 81

6.2 Probe and LO Beam Production 83

6.2.1 ABCD 84

6.2.2 Beamsplitters 87

Metallic Meshes 87

50:50 Beamsplitter 89

A, B Beamsplitter 90

Polarisation insensitive 50:50 beamsplitter 91

High Transmittance Mesh 92

6.2.3 Rotating Grating 92

6.2.4 Rotating Spindle 94

Quartz Plates 96

6.2.5 Waveguides 96

6.3 The Mach-Zehnder Interferometer Optics 99

6.3.1 Support Structure 99

6.3.2 Beam Expansion Optics 99

6.3.3 Reference Signal 104

6.3.4 Windows 104

6.3.5 The Main Beamcombiner 105

6.3.6 Polariser 105

6.3.7 Waveguide Array 105

6.4 Detectors 106

Cryogenics 107

6.5 Electronics 108

6.5.1 Interferometer 108

6.5.2 Polarimeter 109

6.6 Calibration 110

U100 Controller 112

7 Experimental Results **113**

7.1 Interferometer 114

7.1.1 Vibrations 117
7.1.2 Density Profile Reconstruction 119
Equilibrium Reconstruction Code 120
7.2 Polarimeter 121
7.2.1 Method 1 126
7.2.2 Method 2 127
7.2.3 Direct Determination of the Central Safety Factor 130
7.3 LIUQE Reconstructions 135
7.3.1 Faraday Rotation 137
7.3.2 Thomson Scattering 143
7.3.3 Standard 147
7.4 Modifications/Improvements 150
7.5 Conclusion 150

Chapter 1

Introduction

This chapter begins with a brief introduction to the basic principles of fusion and magnetic confinement. The tokamak concept is then introduced with reference to the importance of the measurement of the poloidal magnetic field. The TCV (Tokamak à Configuration Variable) tokamak, on which the experimental work has been performed, is presented along with the diagnostics relevant to this work. The existing techniques for the measurement of the poloidal magnetic field are then briefly reviewed.

1.1 Thermonuclear Fusion

The worlds present annual energy consumption is approximately 3×10^{11} GJ with the electrical energy consumption at about 3×10^{10} GJ per annum[?]. These figures are expected to increase dramatically as third world countries develop. The remaining fossil fuel reserves have been estimated at only 300 years at the present rate of consumption (see Table 1.1). Other sources of energy will, therefore, be required to meet the future demand. Nuclear fission technology, including advanced schemes such as breeder reactors, has the potential of providing 10^{16} GJ or some 30,000 years of energy. The exploitation of this technology is hampered, however, by the generation of radioactive waste with long half-lives and the possibility, however small, of a nuclear meltdown.

Thermonuclear fusion is widely regarded as one of the principal potential long-term energy sources. It is a relatively clean energy source with a virtually endless supply of fuel. Present research is directed towards the fusion reaction in which the nuclei of deuterium and tritium fuse to produce an alpha particle with the release of a neutron, that is,

$$\begin{array}{lccc} {}_1\mathrm{D}^2 + {}_1\mathrm{T}^3 \rightarrow & {}_2\mathrm{He}^4 & + & {}_0\mathrm{n}^1 \\ & | & & | \\ & 3.5\,\mathrm{MeV} & + & 14.1\,\mathrm{MeV} \quad = 17.6\,\mathrm{MeV} \end{array} \tag{1.1}$$

Resource		Energy [GJ]	Estimated reserves [Years]
Coal		10^{14}	300
Oil		1.2×10^{13}	40
Natural Gas		1.4×10^{13}	50
Uranium 235 (fission reactors)		10^{13}	30
Uranium 238 and Thorium 232 (breeder reactors)		10^{16}	30,000
Lithium (D-T fusion reactors)	Land	10^{16}	30,000
	Ocean	10^{19}	30×10^{6}

Table 1.1: Estimated world energy reserves[1].

where the energies given are the kinetic energies of the reaction products. This reaction is preferred over others due to its high reaction rate coefficient $< \delta v > \approx 10^{-22}\mathrm{m}^3\mathrm{s}^{-1}$, at the relatively low temperature of 10 keV.

Deuterium is a plentiful resource, its natural abundance being 0.015Mol% of hydrogen. The mass of the water in the worlds oceans is 1.4×10^{21} kg and consequently 4×10^{16} kg of deuterium. In a D-T reactor with a thermal efficiency of 1/3 this would allow for the production of 10^{22} GJ (electrical) or 3×10^{11} times the present annual consumption. On the other hand tritium has a half-life of only 12.3 years and is virtually non-existent in nature. It can, however, be bred from lithium using the neutron induced fission reactions,

$$\begin{aligned} \mathrm{Li}^6 \; + \; \mathrm{n} &\rightarrow \mathrm{T} + \mathrm{He}^4 + 4.8\,\mathrm{MeV} \\ \mathrm{Li}^7 \; + \; \mathrm{n} &\rightarrow \mathrm{T} + \mathrm{He}^4 + \mathrm{n} - 2.5\,\mathrm{MeV}. \end{aligned} \tag{1.2}$$

The relative abundance of the two lithium isotopes Li^6 and Li^7 are 7.4% and 92.6% respectively. The resources of lithium on land are large enough to provide energy for several thousand years not to mention the potential of millions of years worth of lithium in the worlds oceans (see Table 1.1). The design of potential fusion reactors includes a blanket surrounding the reactor vessel which absorbs the 14MeV neutrons and transforms their energy into heat which is then carried away by a suitable coolant to provide most of the reactor output power. A blanket composed of a compound of lithium can also allow the necessary breeding of the tritium to fuel the reactor.

In order to induce the fusion of nuclei of deuterium and tritium it is necessary to overcome their large mutual repulsion due to their positive charges. The most promising method of supplying the energy is to heat the deuterium-tritium fuel to a sufficiently high temperature so that the thermal velocities of the nuclei are high enough to overcome the Coulomb barrier. Fusion brought about in this way is called thermonuclear. The necessary

temperature is around 10 keV or 100 million degrees centigrade. At such temperatures the fuel is completely ionised and the resulting collection of ions and electrons constitutes a quasi-neutral plasma. Since such high temperatures preclude confinement by a material wall another method of confinement is required.

In a reactor it would be necessary to confine the energy of a sufficiently dense plasma for a time which allows an adequate fraction of the fuel to react. The product of ion temperature T, ion density n, and energy confinement time τ_E, known as the triple product, is commonly used to indicate the performance of a fusion experiment. The required $n\tau_E$ as a function of temperature has a minimum close to 30 keV and the requirement for ignition at this temperature is,

$$nT\tau_E \geq 4.5 \times 10^{21}\ \mathrm{m}^{-3}\mathrm{keVs}. \tag{1.3}$$

Present research aimed at satisfying this requirement is concentrated on two principle methods namely,

1. *Inertial Confinement*: This approach is characterised by very high particle densities ($n \approx 10^{30}\ \mathrm{m}^{-3}$) and very short confinement times ($\tau_\mathrm{E} \approx 0.1$ns). A small D-T pellet is isotropically compressed and ignited by very short high energy laser pulses or particle beams, producing small thermonuclear explosions. Heat from the explosions is deposited in the chamber walls and extracted by coolants to be used to generate electricity.

2. *Magnetic Confinement*: This method is characterised by relatively low densities ($n \approx 10^{20}\mathrm{m}^{-3}$) and long confinement times (τ_Es of around 1 s have been achieved on the large experiments[2]). Charged particles in a uniform magnetic field have helical orbits which are composed of a circular orbital motion perpendicular to the magnetic field and a uniform velocity along the field. This gyro-motion reduces heat and particle transfer perpendicular to the direction of the magnetic field. Confinement along the field lines is obtained by either squeezing the magnetic field at the edges of the device to produce high magnetic fields from which the particles are bounced, (in the so-called mirror machines) or by using a toroidal geometry to close the field lines back on themselves. Different methods have been employed to produce this toroidal magnetic confinement including stellarators, reversed field pinches (RFP) and tokamaks. Of these the tokamak concept is currently favoured as the basis of the first working fusion reactor.

1.2 The Tokamak Concept

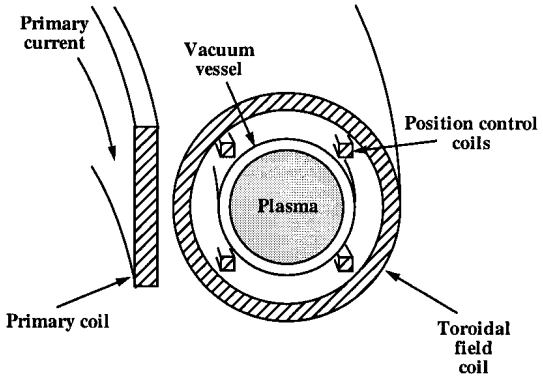

Figure 1.1: Basic tokamak coils.

The word 'tokamak' is derived from the Russian words for 'toroidal magnetic chamber', **to**roidalnaya **ka**mera **ma**gnitnaya **k**atuschka and was invented in the Soviet Union in the early 1950s. It consists of a toroidal vacuum vessel with a major radius R_0, which is defined as the distance between the centre of the torus and that of the vacuum vessel. The half width of the poloidal cross-section is known as the minor radius a. The aspect ratio is defined as R_0/a and the elongation of the plasma as the ratio b/a of its half-height and half-width. The principle confining magnetic field is the toroidal field B_ϕ, created by a number of toroidal field coils, one of which is shown schematically in Fig. 1.1, and is typically of the order of $1 - 10$ T. The toroidal curvature of the field lines, coupled with the radial decrease in $B_\phi \approx B_{\phi_0} R_0/R$ (where R denotes the radial position and B_{ϕ_0} the field at the mid-plane with $R = R_0$), leads to particle drifts which displace electrons and ions in opposite vertical directions. The resulting space charge generates an electric field perpendicular to the toroidal magnetic field and the resulting $\mathbf{E} \times \mathbf{B}$ force drives the plasma particles outwards in major radius[1]. To avoid this a second weaker field B_p ($0.1 - 1.0$ T), is applied poloidally producing magnetic field lines which have a helical trajectory around the torus. The magnetic field lines lie in nested toroidal surfaces of equal poloidal flux known as the "magnetic surfaces". A unique feature of the tokamak is that the poloidal field is produced by currents flowing in the plasma itself. A transformer coil running through the centre of the torus induces a toroidal electrical field which drives the plasma current. Additional coils are required to generate the vertical and radial fields necessary for plasma control. For increased stability and improved confinement plasmas are often made elliptically elongated or even triangular which necessitates the employment of additional shaping coils. A complete system of toroidal and poloidal coils is illustrated schematically in Fig. 1.1.

The safety factor q, specifies the number of complete toroidal circuits a field line must make before completing a single poloidal circuit. For a large aspect ratio tokamak of circular cross-section it is approximated by,

$$q = \frac{aB_\phi}{R_0 B_p}. \tag{1.4}$$

If $q = m/n$, where m and n are integers, the magnetic field line joins up on itself after m toroidal and n poloidal rotations around the torus. These rational values of q play an important role in plasma stability. A $q = 2$ line is illustrated in Fig. 1.2 along with the toroidal B_ϕ,and poloidal B_p magnetic fields and the plasma current I_p.

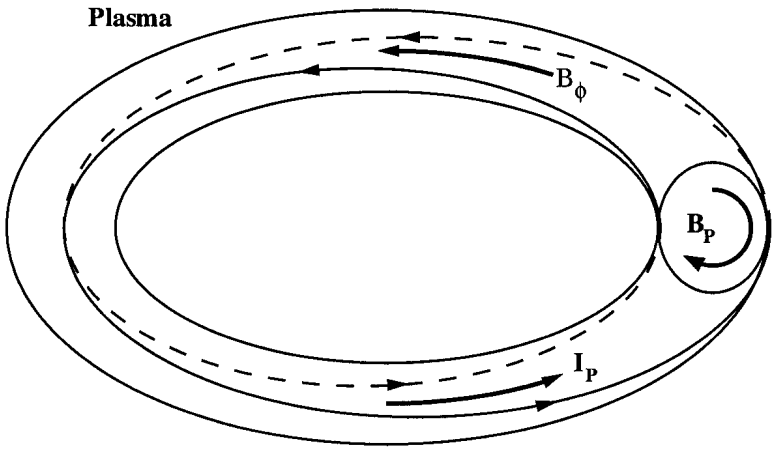

Figure 1.2: A schematic of the toroidal B_ϕ, and poloidal B_p magnetic fields, the plasma current I_p and a field line on the $q = 2$ surface.

The profile of q or equivalently B_p or J the current density, has been shown to be a key parameter in transport models as well as the in magnetohydrodynamic (MHD) stability theory of tearing modes, sawteeth and disruptions. Knowledge of the poloidal field profile is, therefore, essential to an advanced understanding of the complex phenomena which govern the behaviour of tokamak plasmas. This knowledge is even more important in tokamaks where non-inductive current drive techniques are used to modify the J profile to control the MHD instabilities and improve plasma confinement.

Since the plasma is resistive the toroidal plasma current provides ohmic heating. The plasma resistivity is mainly proportional to $T_e^{-3/2}$, where T_e is the electron temperature. Hence the efficiency of the ohmic heating decreases with increasing temperature and additional heating will be necessary to obtain ignition. This heating can be performed by either injecting highly energetic neutral particle beams into the plasma (NBI) or by launching electromagnetic waves into the plasma which can be absorbed either by the ions or the electrons, for example ion or electron cyclotron resonance heating (ICRH,ECRH).

Two techniques are currently employed to separate the plasma from the vacuum vessel. The first is to define an outer boundary of the plasma using a material limiter as shown in Fig. 1.3(a) while the second keeps the particles away from the vacuum vessel by means of a modification of the magnetic field to produce a magnetic divertor as shown in Fig. 1.3(b). The limiter is designed to withstand high power deposition and is usually at one poloidal position. It can also simply be a part of the material wall, as in the case of TCV where plasmas are generally limited on the central column (see Fig. 1.5). Outside the last closed flux surface (LCFS) the plasma still exists in a layer known as the scrape-off (SOL). Field lines in this region are interrupted by the limiter and consequently do not carry any current. In the divertor configuration plasma particles outside the LCFS are diverted towards target plates which are designed to handle high energy fluxes.

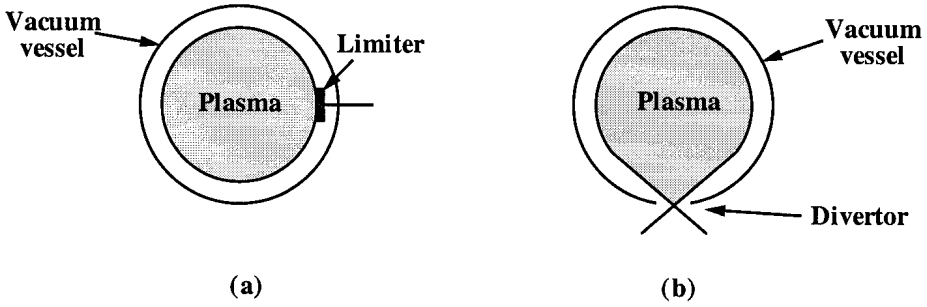

Figure 1.3: Separation of the plasma from the vacuum vessel by (a) a limiter and (b) a divertor.

1.2.1 Tokamak à Configuration Variable

The Tokamak à Configuration Variable (TCV) at the Centre de Recherches en Physique des Plasmas (CRPP) is a compact medium sized highly elongated tokamak capable of producing limited and diverted plasmas with currents up to 1 MA[3]. The machine has been designed to study the effect of plasma shape on confinement and stability and can produce diverse plasma shapes without requiring hardware modifications. This flexibility is due in part to the provision of 16 independently driven poloidal shaping coils mounted in two vertical stacks on both sides of the vacuum vessel. The basic design parameters of the machine are listed in Table 1.2 and a schematic of the tokamak is shown in Fig. 1.4.

Since the beginning of operation in November 1992, TCV has produced a wide range of limited discharges with the LCFS defined by the central column tiles. A host of diverted configurations including upper and lower single null (SNU,SNL) and double null (DND) equilibria have also been produced. To date limited ohmic L-modes (Low energy

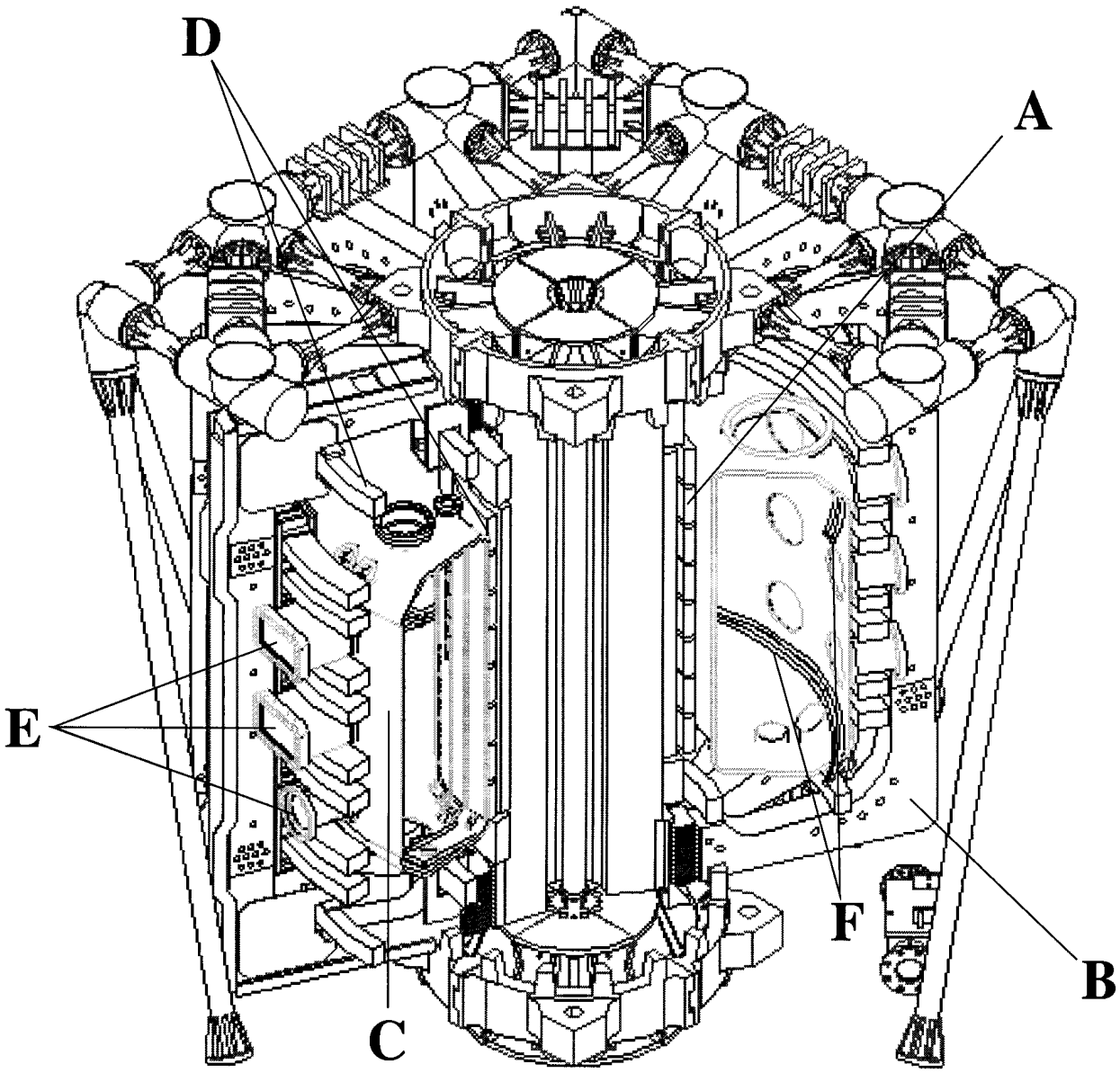

Figure 1.4: Schematic view of TCV showing in particular, (A) the OH transformer coils, (B) the toroidal field coils, (C) the vacuum vessel, (D) the shaping coils, (E) observation ports and (F) the internal shaping coils.

Parameter	Symbol	Value
Major radius	R_0	0.875 m
Plasma width	$2a$	0.48 m (max)
Plasma height	$2b$	1.44 m (max)
Nominal aspect ratio	R_0/a	3.66
Plasma elongation	κ	3 (max), 2.58 (achieved)
Plasma triangularity	δ	-0.77 – 0.86 (achieved)
Plasma current	I_p	1.2 MA(max), 1 MA (achieved)
Toroidal field on magnetic axis	B_t	1.43 Tesla (max)
Loop voltage	V_{loop}	1 V (typical)
Additional heating (ECRH)	P_{aux} (P_{ohmic})	4.5 MW (max), 1.5 MW (installed) (0.15 – 1.5 M (typical))
Plasma duration	-	2 s (max)
Central electron density	n_{e0}	$0.2 - 20 \times 10^{19}$ m^{-3}

Table 1.2: Main TCV parameters.

confinement mode) and H-modes (High energy confinement) together with diverted ELMy (Edge Localised Mode) and ELM-free H-modes have been achieved. A selection of the plasma configurations produced is shown in Fig. 1.5.

1.2.2 Relevant Diagnostics

Table 1.3 summarises the main diagnostics currently available on TCV. The following sections present the diagnostics of particular importance to this work in more detail.

Magnetic Diagnostics

Magnetic pick-up probes (Mirnov coils) and flux loops are required for plasma control and equilibrium reconstruction. Arrays of 38 probes have been placed in poloidal bands at four toroidal locations behind the graphite protection tiles inside the vacuum vessel. These probes measure the component of the poloidal field tangential to the vessel wall. Further identical probes have been positioned to form three sets of toroidal belts of 8 and 16 equidistant probes on the high and low field sides respectively which are used to determine the toroidal mode numbers of observed MHD-activity. A set of 38 full or partial poloidal flux loops and 24 saddle coils are wound on the outside of the vacuum vessel. The magnetic measurements are used in the equilibrium reconstruction code, LIUQE (see Section 3.5). The magnetic probes are also used to measure magnetic activity such as Mirnov oscillations, plasma turbulence and ELMs using a limited number of fast acquisition modules.

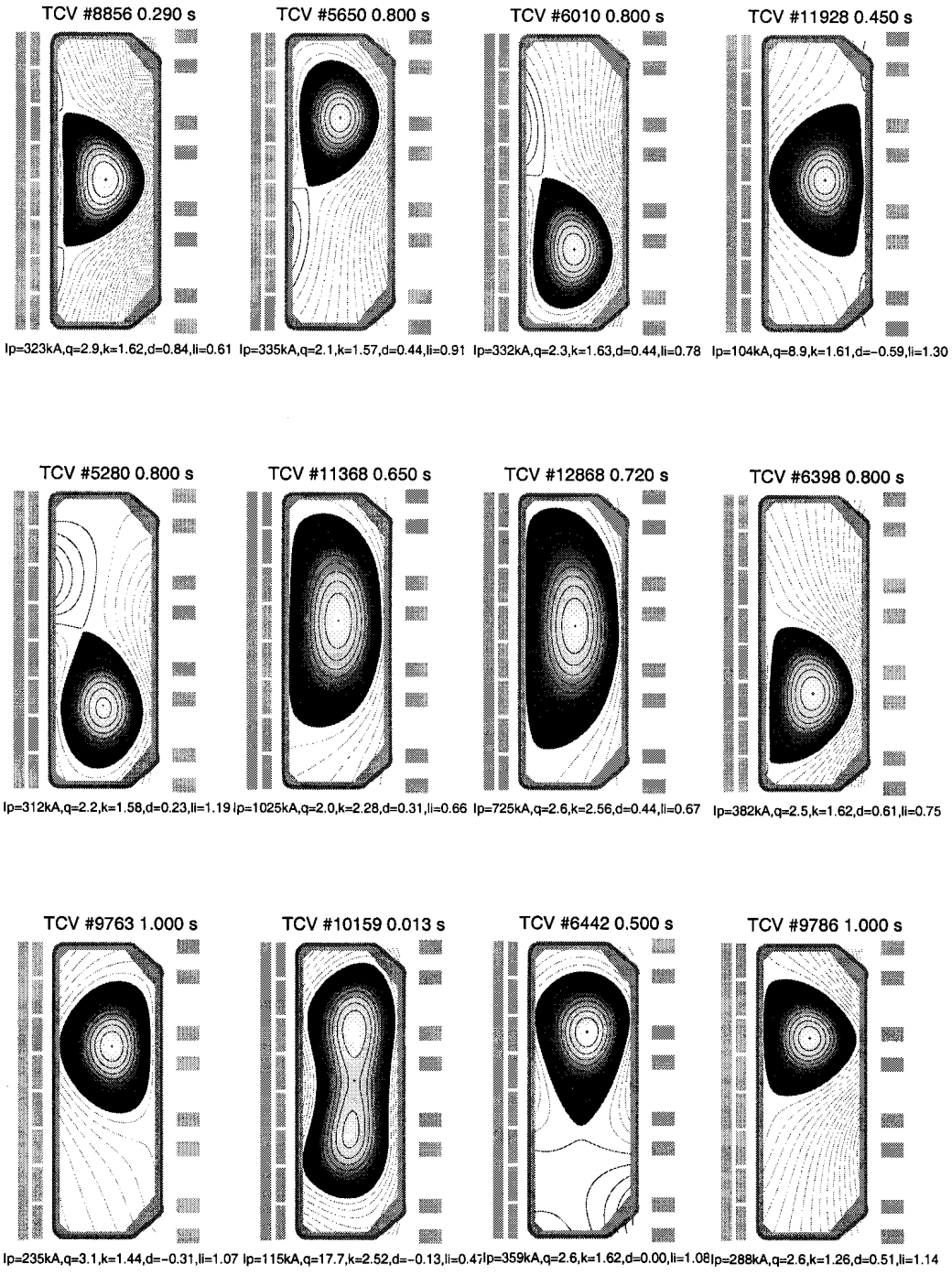

Figure 1.5: Various discharge configurations produced in the TCV tokamak.

Diagnostic	Measured Parameter
Magnetics: Pick-up coils, flux loops and diamagnetic loop	Plasma equilibrium and shape control, equilibrium reconstruction, plasma stored energy.
Far infrared (FIR) Interferometer	Line integrated electron density.
Soft X-ray tomography	Plasma x-ray emissivity.
Ultrasoft X-ray spectroscopy	Helium and Hydrogen-like light impurities.
X-ray monitor diodes	Central electron temperature, toroidal mode numbers.
Bolometry	Plasma radiated power distribution.
Neutral Particle Analyser (NPA)	Central ion temperature.
Visible spectroscopy	Impurity lines, Bremsstrahlung, edge ion temperature, plasma rotation.
Visible light monitors	D_α and impurity lines.
Pulse height analyser (PHA)	Metallic impurities, suprathermal electrons.
Langmuir probe array	Electron density and temperature in the SOL.
Hard X-ray monitor	Suprathermal electrons.
Visible camera (tangential)	Plasma position and boundary shape.

Table 1.3: The main diagnostics on TCV.

Soft X-ray Tomography

This diagnostic measures the line-integrated plasma X-ray emissivity in the energy range $1-10\,\mathrm{keV}$. The impurity line emission from the plasma edge in the visible and VUV range is filtered by $47\,\mu\mathrm{m}$ thick Beryllium absorption foils and therefore the X-ray signal consists essentially of the bremsstrahlung and recombination radiation. The system consists of 10 linear detector arrays each consisting of a strip of 20 Silicon pin diodes. The arrays are distributed over 9 ports in a single poloidal sector to give full poloidal coverage. The resulting 200 lines-of-sight are used to perform a tomographic reconstruction[4] of the local X-ray emissivity for all plasma configurations in TCV with a typical spatial resolution of $30-40$ mm.

Since the local X-ray emissivity is a strong function of the electron temperature T_e and the electron density n_e, the measured signals are sensitive, for example, to the presence of MHD instabilities. In the particular case of sawtooth oscillations, analysis of the emissivities using a SVD (single value decomposition)[5] yields the geometric location of the sawtooth inversion radius.

Thomson Scattering

Thomson scattering experiments measure the plasma electron temperature and density profiles. A vertical visible light laser pulse, at the radial position $R = 900$ mm on TCV, is scattered by the electrons in the plasma and the scattered light is detected. The spectral broadening of the light due to the Doppler effect yields the electron temperature at the scattering position and its intensity the electron density. The Thomson scattering detection system on TCV consists of 25 spatial channels distributed over three horizontal ports covering almost the entire poloidal cross-section.

1.3 Tokamak Equilibrium

The basic condition for tokamak equilibrium is that the force on the plasma be zero at all points. The plasma pressure exerts an outward force across the minor radius and the poloidal magnetic field exerts an inward force. The imbalance between these two forces is taken up by the magnetic pressure of the toroidal magnetic field which can be either inward or outward in direction. Using the magnetohydrodynamic (MHD) approach where the plasma is described as a single fluid and the separate identities of the ions and electrons do not appear, the governing equation can be written as,

$$\mathbf{j} \times \mathbf{B} = \nabla p \tag{1.5}$$

where $\mathbf{j}$ is the current density, $\mathbf{B}$ the magnetic field and p the plasma pressure. It is clear from Eqn. 1.5 that $\mathbf{B}\cdot\nabla p = 0$. Thus, there is no pressure gradient along the magnetic field lines and the magnetic surfaces are surfaces of constant pressure. Furthermore, Eqn. 1.5 gives $\mathbf{j}\cdot\nabla p = 0$, and consequently the current lines also lie in the magnetic surfaces.

It is convenient to introduce the poloidal magnetic flux function ψ, which is determined by the poloidal flux lying within each magnetic surface and is, therefore, constant on that

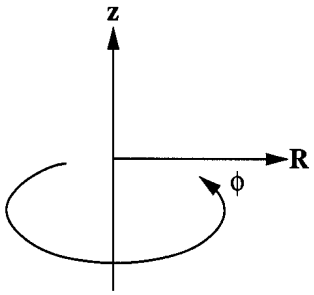

Figure 1.6: Cylindrical coordinate system. $R = 0$ is the major axis of the torus.

surface. Introducing a cylindrical coordinate system based on the major axis of the torus as shown in Fig. 1.6 and defining ψ to be the poloidal flux per radian of ϕ, the relationship between the poloidal magnetic field and ψ is,

$$B_R = -\frac{1}{R}\frac{\delta\psi}{\delta z} \qquad B_z = \frac{1}{R}\frac{\delta\psi}{\delta R}. \tag{1.6}$$

From the symmetry of $\mathbf{j}$ and $\mathbf{B}$ it is clear that there is also a current flux function f which is a function of ψ and is related to the poloidal current density by,

$$j_R = -\frac{1}{R}\frac{\delta f(\psi)}{\delta z} \qquad j_z = \frac{1}{R}\frac{\delta f(\psi)}{\delta R}. \tag{1.7}$$

Comparing Eqn. 1.7 with Ampères equation gives the relationship between f and the toroidal magnetic field,

$$f = \frac{RB_\phi}{\mu_0}. \tag{1.8}$$

After some manipulation Eqn. 1.5 can be re-written as,

$$R\frac{\partial}{\partial R}\frac{1}{R}\frac{\partial\psi}{\partial R} + \frac{\partial^2\psi}{\partial z^2} = -\mu_0 R^2 p'(\psi) - \mu_0^2 f(\psi) f'(\psi) \tag{1.9}$$

which is usually called the Grad-Shafranov equation and must, in general, be solved numerically. The flux surfaces and profiles of j_ϕ, p and B_ϕ obtained by a numerical solution of the equation for a typical case are shown in Fig. 1.7. The boundary conditions are usually defined by the magnetic measurements.

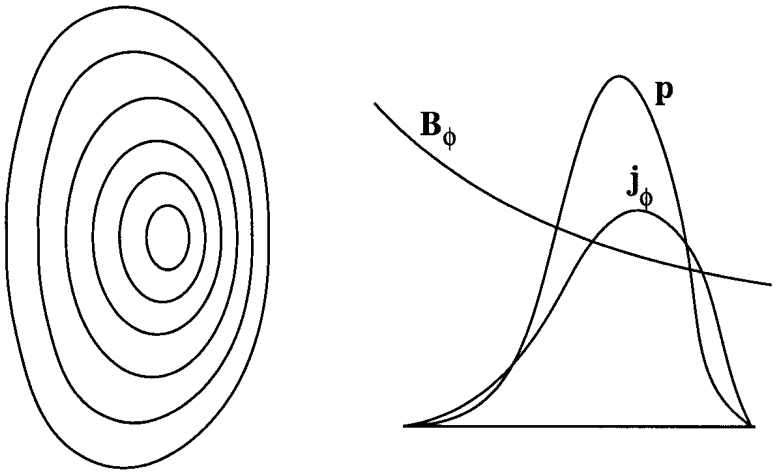

Figure 1.7: (a) Typical equilibrium flux surfaces and (b) the corresponding toroidal current j_ϕ, plasma pressure p, and toroidal magnetic field B_ϕ, across the mid-plane.

Typically $f(\psi)$ and $p(\psi)$ are specified initially and then Eqn. 1.9 is solved for ψ. The two functions are then recalculated and these steps repeated iteratively until a suitable convergence criterion between the measured and calculated values is reached. As the poloidal magnetic field is one of the fundamental quantities governing tokamak equilibrium, knowledge of its behaviour should help the convergence of the solution of Eqn. 1.9.

1.4 Poloidal Field Measurements

Measurement of the poloidal field shape at the plasma edge is relatively straightforward and is performed on virtually every tokamak by means of a set of magnetic coils (see Section 1.2.2). The measurement of the poloidal magnetic field distribution in the plasma interior is, however, much more complicated. The different techniques used to measure this quantity can be grouped into two categories, namely a local measurement of the poloidal field at a point in the plasma and a line-integrated measurement along a chord passing through the plasma. Of the local measurements two spectroscopic techniques are currently the most promising while the Faraday rotation method is, to date, the only line-integrated technique.

1.4.1 Spectroscopic Measurements

Zeeman Splitting

The first spectroscopic method proposed was the measurement of the Zeeman [6] splitting and polarisation of the magnetic dipole radiation from heavy impurity ions in the plasma. The fractional circular polarisation of the emitted spectral lines is proportional to the component of the magnetic field in the direction of observation and the geometry of the experiment is usually chosen in such a way that the poloidal component of the magnetic field is measured directly. Such a simple approach is rather useless, however, for high-temperature tokamak plasmas where the Zeeman splitting is completely obscured by the thermal (Doppler) broadening of the spectral lines. One way to eliminate this broadening is to study the radiation from high-energy monoenergetic atomic beams or pellets[7].

Motional Stark Effect

Recently a second spectroscopic technique, based on the measurement of the motional Stark effect (MSE) in hydrogenic emissions from high-energy neutral beams, has been demonstrated as a promising alternative to Zeeman splitting[8]. A strong Lorentz field $\mathbf{E} = \mathbf{v} \times \mathbf{B}$, where $\mathbf{v}$ is the velocity of the beam particles and $\mathbf{B}$ the tokamak magnetic field,

observed in the reference frame of the beam particle produces splitting and polarisation of the line emissions via the Stark effect. The local magnetic field direction can be determined from measurements of the polarisation of the Stark components. Equipment to perform such measurements have been installed on many devices already equipped with neutral beam injection for plasma fuelling purposes. A high powered beam is required due to the strong interaction of the beam with the plasma. Even then the penetration of the beam in many large devices is insufficient for measurements at the plasma centre.

The spectroscopic methods have the advantage of directly measuring the local field pitch angle but they suffer from limitations in time response, radial resolution and the range of plasma parameters over which they can operate. These techniques are only suited to tokamaks which are equipped with high-energy beams.

1.4.2 Faraday Rotation

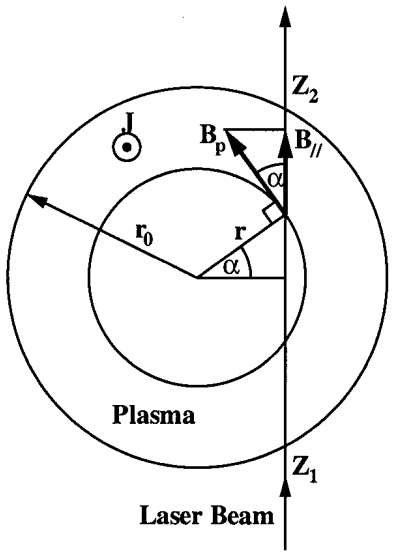

Figure 1.8: Schematic of the geometry of a typical Faraday rotation polarimeter.

A plasma immersed in a magnetic field is a birefringent medium which has two orthogonal polarisation eigenstates with slightly different refractive indices. This birefringence causes a rotation of the direction of polarisation of a linearly polarised probing wave, as will be described in Chapter 2. This effect was first observed in glass under the influence of a strong magnetic field by Michael Faraday in 1845 and has consequently been called Faraday rotation.

The Faraday rotation is caused by the presence of a magnetic field component parallel to the direction of propagation of the probing beam. Setting this direction to one of

the components of the poloidal magnetic field provides information on that quantity and hence the current density distribution in the plasma.

A Faraday rotation diagnostic was first proposed by DeMarco and Segre[9] who derived the following equation for the rotation of the polarisation of a linearly polarised far-infrared (FIR) beam passing vertically though the plasma poloidal cross section as shown in Fig. 1.8,

$$\Psi = 2.62 \times 10^{-13} \lambda^2 \int_{Z_1}^{Z_2} n_e B_{//} dz \tag{1.10}$$

where $B_{//}$ is the component of the poloidal field parallel to the FIR beam, $Z_1 - Z_2$ the beam path and n_e the electron density. If several parallel chords are passed though the plasma (or equivalently a continuous beam imaged onto an array of detectors) the Faraday rotation profile can be determined thus providing information on the current density profile. As the required geometry and probing wavelength are similar to those of standard interferometers most Faraday rotation polarimeters have been based on upgrades of interferometric diagnostics. The theory behind the Faraday rotation measurement is discussed in Chapter 2 and various experimental methods including the system installed on TCV are described in Chapter 4.

1.5 Outline of the Thesis

In this thesis the extension of the FIR interferometer on TCV to include a polarimeter is presented. A brief introduction to nuclear fusion and the tokamak concept has been given in this chapter. The TCV tokamak on which the work was performed was introduced and the importance of poloidal magnetic field measurements was outlined. The following chapter describes the theory behind refractive index measurements in magnetised plasmas. Chapter 3 discusses the choice of probing wavelength in order to provide reasonable measurements over the entire range of TCV plasmas. Chapter 4 begins with a introduction to interferometry and polarimetry in general and a brief description of some of the interferometer/polarimeter methods installed on other machines. A detailed description of the two methods chosen for TCV is then presented. Chapter 5 describes the bench tests which were performed prior to the installation of the system on TCV in order to confirm its feasibility. A description of the instrument from the laser system to the detection electronics is presented in Chapter 6. Finally, Chapter 7 presents the experimental results obtained and discusses possible future improvements to the system.

Chapter 2

The Theory of Refractive Index Measurements

This chapter details the theory behind refractive index measurements. Two formulations which can be used to describe the polarisation of an electromagnetic wave are presented and the evolution of the polarisation through a magnetised plasma is described.

2.1 The State of Polarisation of an Electromagnetic Wave

Consider a right-handed rectangular coordinate system x, y and z with a plane electromagnetic wave propagating in the z direction. Consider the wave to be time harmonic, i.e. each component of the electric vector $\mathbf{E}$ is of the form[10],

$$a\cos(\tau+\delta) = \Re\left(ae^{-i(\tau+\delta)}\right) \qquad (E>0) \tag{2.1}$$

where $\tau = \omega t - kz$, ω being the angular frequency of the wave and $k = 2\pi/\lambda$ the wave number. The electrical vector components can then be expressed as,

$$\left.\begin{array}{ll} E_x(z,t) & = E_{0x}\cos(\tau+\delta_x), \\ E_y(z,t) & = E_{0y}\cos(\tau+\delta_y), \\ E_z(z,t) & = 0 \end{array}\right\} \tag{2.2}$$

where $E_{0x,0y}$ are the maximum amplitudes and $\delta_{x,y}$ the phases. Defining $\delta = \delta_y - \delta_x$ and combining these two equations we obtain,

$$\frac{E_x^2}{E_{0x}^2} + \frac{E_y^2}{E_{0y}^2} - 2\frac{E_x}{E_{0x}}\frac{E_y}{E_{0y}}\cos\delta = \sin^2\delta \tag{2.3}$$

which represents a rotated ellipse shown schematically in Fig. 2.1.

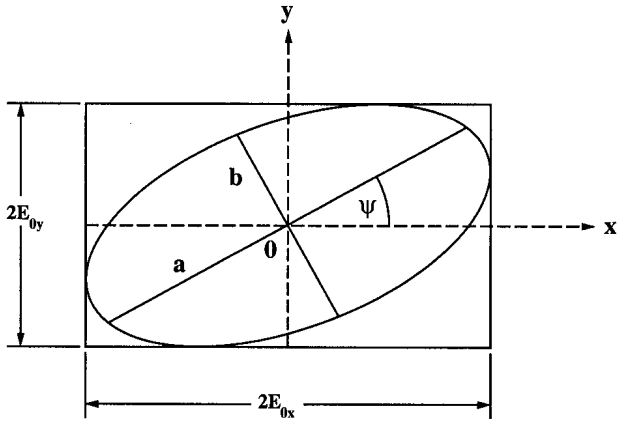

Figure 2.1: Vibrational ellipse for the electric field vector.

It can be shown that with $\delta = n\pi$ $(n = 0, \pm1, \pm2, \cdots)$, Eqn. 2.3 reduces to,

$$E_y = (-1)^n \left(\frac{E_{0y}}{E_{0x}}\right) E_x \tag{2.4}$$

which is easily recognised as representing a straight line with slope $\pm E_{0y}/E_{0x}$ and we say that **E** is linearly polarised. If $\delta = n\pi/2$ $(n = \pm1, \pm3, \pm5 \cdots)$ and $E_{0x} = E_{0y} = E$, the polarisation ellipse reduces to,

$$\frac{E_x^2}{E^2} + \frac{E_y^2}{E^2} = 1 \tag{2.5}$$

which is the equation of circle. The light is then said to be right-hand ($\sin\delta > 0$) or left-hand ($\sin\delta < 0$) circularly polarised.

By introducing an auxiliary angle α, such that,

$$\tan\alpha = \frac{E_{0y}}{E_{0x}} \qquad (0 \leq \alpha \leq \frac{\pi}{2}) \tag{2.6}$$

the principle semi-axes a and b of the ellipse shown in Fig. 2.1 and the orientation angle ψ, which the major axis makes with the x-axis can be specified by the formulae[10],

$$a^2 + b^2 = E_{0x}^2 + E_{0y}^2 \tag{2.7}$$

$$\tan 2\psi = \tan 2\alpha \cos\delta \qquad (0 \leq \psi < \pi) \tag{2.8}$$

$$\sin 2\chi = \sin 2\alpha \sin\delta \tag{2.9}$$

where χ is an auxiliary angle which specifies the ellipticity,

$$\tan\chi = \pm\frac{b}{a} \qquad (-\frac{\pi}{4} \leq \chi \leq \frac{\pi}{4}) \tag{2.10}$$

with $-\pi/4 \leq \chi < 0$ representing left-hand and $0 < \chi \leq \pi/4$ right-hand polarisation. It can also be shown that[10],

$$\epsilon = \frac{b}{a} = \frac{|E_{0x}|^2 + |E_{0y}|^2}{2|E_{0x}||E_{0y}|\sin\delta} - \left\{\left(\frac{|E_{0x}|^2 + |E_{0y}|^2}{2|E_{0x}||E_{0y}|\sin\delta}\right)^2 - 1\right\}^{1/2} \tag{2.11}$$

and,

$$\psi = \frac{1}{2}\tan^{-1}\left(\frac{2|E_{0x}||E_{0y}|}{|E_{0x}|^2 - |E_{0y}|^2}\cos\delta\right) \tag{2.12}$$

where ϵ is the ellipticity of the polarisation. The state of polarisation can, therefore, be completely described by either α and δ or the orientation angle ψ and the ellipticity angle χ. Two states of polarisation (ψ_1, χ_1) and (ψ_2, χ_2) are said to be orthogonal if $\psi_2 = \psi_1 + \pi/2$ and $\chi_2 = -\chi_1$.

2.1.1 Stokes Parameters and Poincaré Sphere

The Stokes polarisation parameters for a plane wave are given by,

$$\begin{array}{lll} S_1 & = S_0\cos 2\chi\cos 2\psi & = E_{0x}^2 - E_{0y}^2 \\ S_2 & = S_0\cos 2\chi\sin 2\psi & = 2E_{0x}E_{0y}\cos\delta \\ S_3 & = S_0\sin 2\chi & = 2E_{0x}E_{0y}\sin\delta \end{array} \tag{2.13}$$

where S_0 is the total intensity of the light,

$$S_0 = \sqrt{S_1^2 + S_2^2 + S_3^2} = E_{0x}^2 + E_{0y}^2. \tag{2.14}$$

The polarisation vector $\mathbf{S}$ is defined as $\mathbf{S} \equiv (S_0\ S_1\ S_2\ S_3)$. The parameter S_1 describes the amount of linear horizontal or vertical polarisation, S_2 the amount of linear $+45^o$ or -45^o polarisation and S_3 the amount of right or left circular polarisation contained within the beam. The Stokes parameters are usually given in their normalised form with $S_0 = 1$.

Each state of polarisation can also be uniquely represented by a point P on the surface of a sphere Σ of unit radius called the Poincaré sphere, shown in Fig. 2.2. The Cartesian coordinates s_1, s_2, s_3 of P are the normalised Stokes parameters,

$$\begin{array}{ll} s_1 & = \cos 2\chi\cos 2\psi \\ s_2 & = \cos 2\chi\sin 2\psi \\ s_3 & = \sin 2\chi. \end{array} \tag{2.15}$$

To every possible state of polarisation of a plane monochromatic wave of a given intensity there corresponds one point on Σ and vice versa. Right-hand polarisation is represented by points on Σ which lie above the equatorial (xy) plane and left-hand polarisation by points below this plane. All linear polarisations are represented by points in the equatorial plane and circular polarisation by the two poles with $s_3 = \pm 1$.

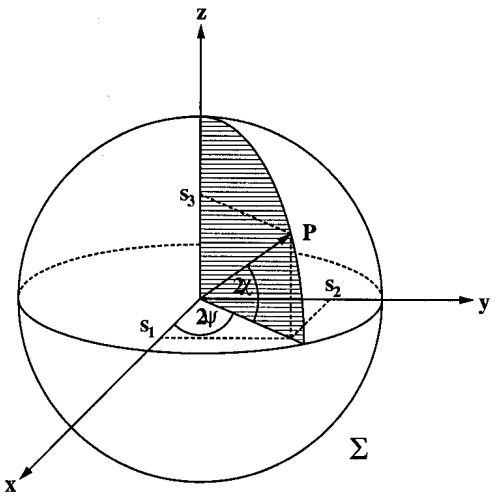

Figure 2.2: Representation of the state of polarisation of a monochromatic wave (Poincaré Sphere).

2.1.2 Jones Matrices

Jones[11] showed that it was possible to represent the effect of any optical element on light as a linear operator acting upon the electric vector of the light wave. The operator is expressed in the form of a two-by-two matrix whose matrix elements are in general complex. It follows that a complete optical system can also be represented by a two-by-two complex matrix.

Consider the elements of the optical system to be arranged along the z axis. At any fixed point along this axis the components of the electric field can be written as,

$$\begin{aligned} E_x &= E_{0x}e^{i(\tau+\delta_x)} \\ E_y &= E_{0y}e^{i(\tau+\delta_y)} \end{aligned} \tag{2.16}$$

with $\tau = \omega t - kz$ where $E_{0x,0y}$ the amplitudes and $\delta_{x,y}$ the phases are real. Eqn. 2.16 can be arranged into a 2×1 column matrix $\mathbf{E}$,

$$\mathbf{E} = \begin{bmatrix} E_x \\ E_y \end{bmatrix} = \begin{bmatrix} E_{0x}e^{i(\tau+\delta_x)} \\ E_{0y}e^{i(\tau+\delta_y)} \end{bmatrix} \tag{2.17}$$

called the Jones column matrix or Jones vector. The total intensity I, of the optical field is given by,

$$\begin{aligned} I &= E_xE_x^* + E_yE_y^* \\ &= \begin{bmatrix} E_x^* & E_y^* \end{bmatrix} \cdot \begin{bmatrix} E_x \\ E_y \end{bmatrix} \\ &= \mathbf{E}^\dagger \cdot \mathbf{E}. \end{aligned} \tag{2.18}$$

Carrying out the matrix multiplication in Eqn. 2.18 yields,

$$E_{ox}^2 + E_{0y}^2 = I = E_0^2. \tag{2.19}$$

It is customary to set $E_0^2 = 1$ whereupon the Jones vector is said to be normalised.

The Jones vector can only be used to describe completely polarised light. In the case of linear horizontally polarised (LHP) light $E_y = 0$ and the Jones vector becomes,

$$\mathbf{E} = \begin{bmatrix} E_{0x}e^{i(\tau+\delta_x)} \\ 0 \end{bmatrix}. \tag{2.20}$$

Changes which occur within the very short optical periods cannot be observed and consequently we can average over the optical period by setting $e^{i\tau} = 1$. By setting $\delta_x = 0$ the normalised Jones vector for linearly horizontally polarised light can be written as,

$$\mathbf{E}_{LHP} = \begin{bmatrix} 1 \\ 0 \end{bmatrix}. \tag{2.21}$$

For right-hand circularly polarised (RCP) light $E_{0x} = E_{0y}$ and $\delta = 90^o$. Then $2E_{0x}^2 = 1$ and we have,

$$\mathbf{E}_{RCP} = \frac{1}{\sqrt{2}} \begin{bmatrix} 1 \\ +i \end{bmatrix}. \tag{2.22}$$

Similarly, left-hand circularly polarised (LCP) light is represented as,

$$\mathbf{E}_{LCP} = \frac{1}{\sqrt{2}} \begin{bmatrix} 1 \\ -i \end{bmatrix}. \tag{2.23}$$

Two vectors $\mathbf{A}$ and $\mathbf{B}$ are said to be orthogonal if $\mathbf{A}^\dagger \cdot \mathbf{B} = 0$.

Jones matrix calculus can be used to superpose coherent amplitudes, that is Jones vectors. For example the superposition of left and right circularly polarised light of equal amplitudes results in,

$$\begin{aligned} \mathbf{E} &= \frac{1}{\sqrt{2}} \begin{bmatrix} 1 \\ +i \end{bmatrix} + \frac{1}{\sqrt{2}} \begin{bmatrix} 1 \\ +i \end{bmatrix} \\ &= \frac{2}{\sqrt{2}} \begin{bmatrix} 1 \\ 0 \end{bmatrix}. \end{aligned} \tag{2.24}$$

which, aside from the normalising factor, is the Jones vector for LHP light.

The effect of an optical component on a beam of light can be written as,

$$\begin{bmatrix} E'_x \\ E'_y \end{bmatrix} = \begin{bmatrix} m_{xx} & m_{xy} \\ m_{yx} & m_{yy} \end{bmatrix} \begin{bmatrix} E_x \\ E_y \end{bmatrix} \tag{2.25}$$

where E_x,E_y represent the incident beam and E'_x,E'_y the beam emerging from the optical component represented by the 2×2 matrix. This matrix is called the Jones matrix of the component and its elements, m_{xx}, m_{xy}, m_{yx}, m_{yy} are complex numbers.

It is useful to know the Jones matrix for a rotator, the defining equations of which are,

$$\begin{aligned} E'_x &= \cos\theta E_x + \sin\theta E_y \\ E'_y &= -\sin\theta E_x + \cos\theta E_y \end{aligned} \tag{2.26}$$

where θ is the anti-clockwise angle of rotation. The corresponding Jones matrix is therefore given by,

$$\begin{bmatrix} E'_x \\ E'_y \end{bmatrix} = \begin{bmatrix} \cos\theta & \sin\theta \\ -\sin\theta & \cos\theta \end{bmatrix} \begin{bmatrix} E_x \\ E_y \end{bmatrix} = \begin{bmatrix} E_x\cos\theta + E_y\sin\theta \\ -E_x\sin\theta + E_y\cos\theta \end{bmatrix}. \tag{2.27}$$

Jones matrices are used extensively in this thesis to determine the change in polarisation of an electromagnetic wave traversing a plasma (see Section 2.2.2) and for the analysis of the two polarimeter/interferometer methods (see Chapter 4).

2.2 The Propagation of an Electromagnetic Wave through a Magnetised Plasma

2.2.1 Characteristic plasma frequencies

A plasma has a characteristic frequency which can be understood by considering a displaced sheet of electrons and the resulting electric field as shown in Fig. 2.3. It is assumed that because of their larger mass the ions are stationary and have uniform density. The electrons are accelerated by the electric field and move to cancel out the positive charge. At the time of cancellation the electron momentum is at a maximum and this allows the electrons to recreate the charge separation in the opposite direction. The process is repeated and the resulting motion of the electrons constitutes plasma oscillations with the characteristic plasma frequency ω_p, given by,

$$\omega_p = \sqrt{\frac{n_e e^2}{\epsilon_0 m_e}} \tag{2.28}$$

where n_e is the electron density, m_e the electron mass, e the elementary charge and ϵ_0 the dielectric constant of a vacuum. The electron density in TCV ranges between $1 \times 10^{19}\,\mathrm{m}^{-3}$ and $5 \times 10^{20}\,\mathrm{m}^{-3}$ which corresponds to plasma frequencies between 30 and 200 GHz.

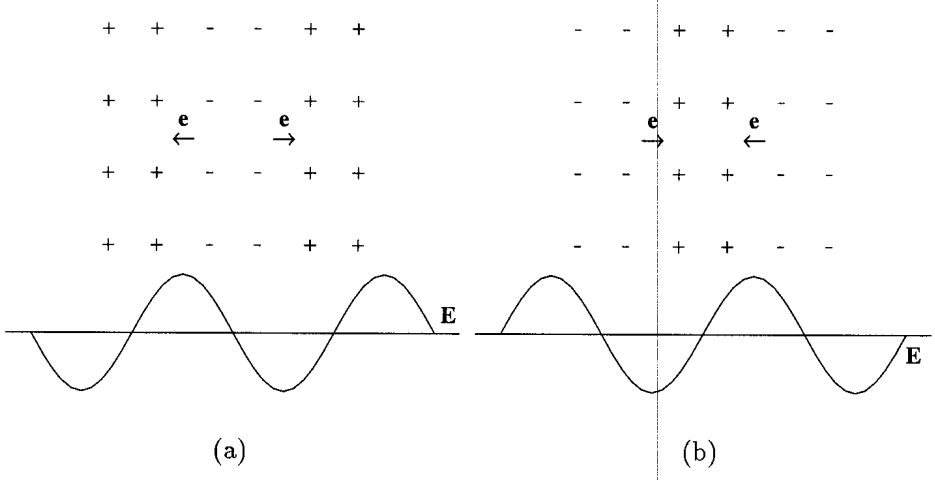

Figure 2.3: Description of the origins of the plasma frequency, (a) displaced electrons give rise to a restoring force and acceleration, (b) after half a cycle the charges are interchanged.

For a fixed probing frequency ω, the critical density n_c, is defined as the density at which the probing frequency equals the plasma frequency and is given by,

$$n_c = \frac{\epsilon_0 m_e \omega^2}{e^2}. \tag{2.29}$$

For densities below this critical value the medium acts as a nearly transparent dielectric for the probing beam but for higher densities it is opaque and highly reflecting. For a probing frequency of 1400 GHz ($\lambda = 214.6$ μm, see Chapter 3) the critical density is 2.4×10^{22} m^{-3} which is two orders of magnitude greater than the maximum densities in TCV.

The angular frequency with which an electron gyrates in a magnetic field is known as the electron cyclotron frequency and is given by,

$$\omega_{ce} = \frac{|q| \cdot B}{m} \tag{2.30}$$

where q and m are the charge and mass respectively of the particle and B the magnetic field strength. The nominal magnetic field B_{tor} on the magnetic axis of TCV is 1.4 T and the corresponding electron cyclotron frequency at the center of the plasma is 39 GHz. If an electromagnetic wave of this frequency, or certain harmonics, is injected into the plasma most of its power will be resonantly absorbed by the plasma.

2.2.2 Evolution of the State of Polarisation

For each direction of propagation in a uniform medium it can be shown that there exist two characteristic waves, with different phase velocities and orthogonal polarisations, whose states of polarisation remain constant during propagation[12]. It has also been shown that any polarised wave is a unique linear combination of two waves with orthogonal polarisations. Therefore, the state of polarisation during the propagation, for an arbitrary initial polarisation, can be obtained by first resolving the wave into the two characteristic waves which propagate independently with their respective characteristic phase velocities and then superposing the two resulting components to obtain the resultant wave at any desired point.

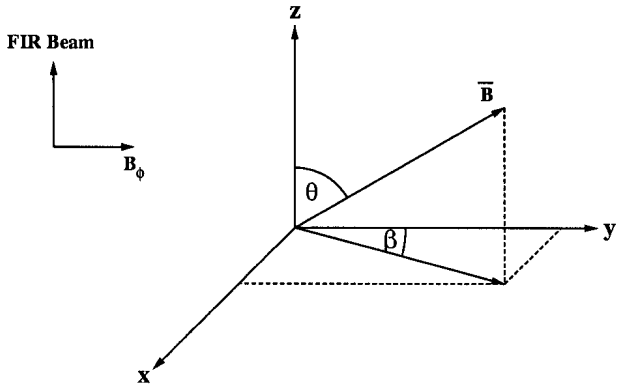

Figure 2.4: Magnetic field vector diagram.

Consider the propagation of a wave through a magnetised plasma using the coordinate system as shown in Fig. 2.4. Under this system **y** represents the toroidal direction, **x** the radial direction and **z** the vertical direction parallel to the probing FIR beam. The angle between the magnetic field **B** and the direction of propagation is represented by θ while β represents the angle between $\mathbf{z} \times (\mathbf{B} \times \mathbf{z})$ and **y** as shown. Considering a cold plasma and neglecting collisions and ion motion the refractive indices for the slow and fast waves are given by the Appleton-Hartree formula[13],

$$\mu_{\pm}^2 = 1 - \frac{\omega_p^2}{\omega^2}\left\{1 - \frac{\omega_{ce}^2}{\omega^2}\frac{\sin^2\theta}{2(1-\omega_p^2/\omega^2)} \pm \frac{\omega_{ce}^2}{\omega^2}\frac{\sin^2\theta}{2(1-\omega_p^2/\omega^2)}[1+F^2]^{1/2}\right\}^{-1} \tag{2.31}$$

where

$$F = \frac{2\omega}{\omega_{ce}}\left(1 - \frac{\omega_p^2}{\omega^2}\right)\frac{\cos\theta}{\sin^2\theta}. \tag{2.32}$$

In general the angle θ varies depending on the position in the plasma. Here we consider the two particular cases of $\mathbf{k} \perp \mathbf{B}$ and $\mathbf{k} \parallel \mathbf{B}$. For $\mathbf{k} \perp \mathbf{B}$ ($\theta = \pi/2$) the characteristic

waves are known as the ordinary ($\mathbf{E} \parallel \mathbf{B}$) and the extraordinary ($\mathbf{E} \perp \mathbf{B}$) waves the refractive indices of which are given by,

$$\mu_{ord} = \left[1 - \frac{\omega_p^2}{\omega^2}\right]^{1/2} \tag{2.33}$$

$$\mu_{ex} = \left[1 - \frac{\omega_p^2(\omega^2 - \omega_p^2)}{\omega^2(\omega^2 - \omega_p^2 - \omega_{ce}^2)}\right]^{1/2}. \tag{2.34}$$

The ordinary wave is linearly polarised and the extraordinary elliptically polarised. Since ω is typically at least one order of magnitude greater than both ω_p and ω_{ce} we can expand the square root giving,

$$\mu_{ord} = \mu_{ex} \approx 1 - \frac{1}{2}\left(\frac{\omega_p}{\omega}\right)^2. \tag{2.35}$$

Using this expression the phase shift between a beam probing the plasma and a reference beam in vacuum becomes,

$$\Phi = \frac{2\pi}{\lambda}\int[\mu_v - \mu_{ord}]dz = \frac{2\pi}{\lambda}\int\frac{1}{2}\left(\frac{\omega_p}{\omega}\right)^2 dz. \tag{2.36}$$

where the integral over dz refers to the line integral along the path of the probing beam and μ_v is the refractive index of a vacuum. Substituting for ω_p gives,

$$\Phi = \frac{\lambda e^2}{4\pi c^2 \epsilon_0 m_e}\int n_e(z)dz \tag{2.37}$$

or in mks units,

$$\Phi = 2.82 \times 10^{-15}\lambda\int n_e(z)dz \tag{2.38}$$

which is standard expression for the interferometry phase shift.

For $\mathbf{k} \parallel \mathbf{B}$, ($\theta = 0$) the characteristic waves are left and right hand circularly polarised waves (LCP and RCP) with refractive indices,

$$\mu_{L,R} = \left[1 - \frac{\omega_p^2/\omega^2}{1 \pm \omega_{ce}/\omega}\right]^{1/2}. \tag{2.39}$$

Expanding the square root with $\omega \gg \omega_p, \omega_{ce}$ gives,

$$\mu_{L,R} = 1 - \frac{1}{2}\left(\frac{\omega_p^2}{\omega^2}\right)\left(1 \mp \frac{\omega_{ce}}{\omega}\right). \tag{2.40}$$

The average refractive index is given by,

$$\frac{\mu_L + \mu_R}{2} \approx 1 - \frac{1}{2}\left(\frac{\omega_p}{\omega}\right)^2 \tag{2.41}$$

which also gives the standard interferometry equation (Eqn. 2.38). The difference in phase between the characteristic waves is,

$$\begin{aligned}\psi &= \frac{2\pi}{\lambda}\int(\mu_L-\mu_R)dz = \frac{2\pi}{\lambda}\int\left(\frac{\omega_p^2\omega_{ce}}{\omega^3}\right)dz \\ &= \frac{\lambda^2 e^3}{4\pi^2 c^3\epsilon_0 m_e^2}\int n_e B dz. \end{aligned} \tag{2.42}$$

The significance of this phase shift can be seen by considering a incident beam which is linearly polarised in the x direction. The polarisation can then easily be expressed as the sum of the two characteristic waves $\mathbf{E}_R$ and $\mathbf{E}_L$ (see Eqn. 2.24),

$$\mathbf{E} = \mathbf{E}_R + \mathbf{E}_L \tag{2.43}$$

$$\begin{bmatrix}1\\0\end{bmatrix}E_0 e^{i\tau} = \begin{bmatrix}1\\i\end{bmatrix}\frac{1}{2}E_0 e^{i\tau} + \begin{bmatrix}1\\-i\end{bmatrix}\frac{1}{2}E_0 e^{i\tau}. \tag{2.44}$$

After propagation through the plasma there is a phase shift ψ between $\mathbf{E}'_R$ and $\mathbf{E}'_L$,

$$\begin{aligned}\mathbf{E}' &= \mathbf{E}'_R + \mathbf{E}'_L \\ &= \begin{bmatrix}1\\i\end{bmatrix}\frac{1}{2}E_0 e^{i\tau} + \begin{bmatrix}1\\-i\end{bmatrix}\frac{1}{2}E_0 e^{i(\tau+\psi)}. \end{aligned} \tag{2.45}$$

Recombining these two components gives,

$$\mathbf{E}' = \begin{bmatrix}E'_x\\E'_y\end{bmatrix} = \begin{bmatrix}1+e^{i\psi}\\i(1-e^{i\psi})\end{bmatrix}\frac{1}{2}E_0 e^{i\tau} = \begin{bmatrix}\cos(\psi/2)\\\sin(\psi/2)\end{bmatrix}E_0 e^{i(\tau+\psi/2)} \tag{2.46}$$

which represents a linearly polarised beam rotated through an angle $\psi/2$. Defining the Faraday angle as $\Psi = \tan^{-1}(E'_y/E'_x)$ we have,

$$\begin{aligned}\Psi &= \psi/2 \\ &= \frac{\lambda^2 e^3}{8\pi^2 c^3\epsilon_0 m_e^2}\int n_e B_{//} dz \end{aligned} \tag{2.47}$$

where $B_{//}$ is the component of the magnetic field parallel to the probing beam. Evaluating the constants gives the standard expression for the Faraday rotation angle,

$$\Psi = 2.62\times 10^{-13}\lambda^2\int n_e B_{//} dz. \tag{2.48}$$

In a typical interferometer/polarimeter setup neither of these limiting cases will be completely valid as most probing beams will experience a sizeable poloidal field component parallel to $\mathbf{k}$. Therefore $\mathbf{k}$ will, in general, be neither parallel nor perpendicular to $\mathbf{B}$. The characteristic waves will be elliptically polarised with the ellipticity going to unity

(circular polarisation) when the wave propagates along the magnetic field and to zero (linear polarisation) when it propagates perpendicular to the field. For a more complete treatment we will follow the formalism introduced by Soltwisch[14] which describes the change in polarisation of an electromagnetic wave traversing a non-uniform magnetised plasma in terms of a 2×2 Jones matrix. This method is used in Section 3.4 to determine the range of expected Faraday rotation angles in TCV plasmas with various probing wavelengths.

Jones Matrix Analysis

Consider a plane electromagnetic wave traversing a layer of uniform plasma. Using the coordinate system shown in Fig. 2.4 and the characteristic refractive indices given by the Appleton-Hartree formula (Eqn. 2.31), the wave polarisation coefficient $R_{\pm}$, which is related to the ellipticity of the eigenstate, can be given by[13],

$$R_{\pm} = \frac{E_x}{E_y} = \frac{i}{\cos\theta}\left\{\frac{(\omega_c/\omega)\sin^2\theta}{2(1-\omega_p^2/\omega^2)} \mp \sqrt{\cos^2\theta + \left(\frac{(\omega_c/\omega)\sin^2\theta}{2(1-\omega_p^2/\omega^2)}\right)^2}\right\} \tag{2.49}$$

where $R_+R_- = 1$. In particular, $R = \mp i$ for left and right-hand circular polarisation, respectively. Defining,

$$\alpha = \frac{R_+}{i} = -i\frac{E_x^+}{E_y^+} \tag{2.50}$$

the characteristic modes can be expressed as,

$$\begin{aligned} \mathbf{E}^+(z,t) &= \begin{bmatrix} E_x^+ \\ E_y^+ \end{bmatrix} e^{i(\omega t - k_+ z)} = \begin{bmatrix} 1 \\ -i/\alpha \end{bmatrix} e^{i(\omega t - k_+ z)} \\ \mathbf{E}^-(z,t) &= \begin{bmatrix} E_x^- \\ E_y^- \end{bmatrix} e^{i(\omega t - k_- z)} = \begin{bmatrix} 1 \\ i\alpha \end{bmatrix} e^{i(\omega t - k_- z)} \end{aligned} \tag{2.51}$$

where $k_{\pm} = \mu_{\pm}(\omega/c)$ are the propagation constants.

Thus an incident wave of arbitrary polarisation at $z = 0$ may be written as,

$$\mathbf{E}(0,t) = A_+\mathbf{E}^+(0,t) + A_-\mathbf{E}^-(0,t) \tag{2.52}$$

where the components are

$$\begin{aligned} E_x(0) &= A_+ + A_- \\ E_y(0) &= (-i/\alpha)A_+ + (i\alpha)A_-. \end{aligned} \tag{2.53}$$

Solving these equations for the amplitudes of the characteristic modes, we obtain,

$$\begin{aligned} A_+ &= \frac{\alpha^2}{1+\alpha^2}E_x(0) + i\frac{\alpha}{1+\alpha^2}E_y(0) \\ A_- &= \frac{1}{1+\alpha^2}E_x(0) - i\frac{\alpha}{1+\alpha^2}E_y(0). \end{aligned} \tag{2.54}$$

After having traversed the plasma layer of thickness z_0, the modes exhibit a relative phase shift,

$$d\psi = \frac{\omega}{c}(\mu_+ - \mu_-)z_0 \tag{2.55}$$

and their superposition yields the emergent wave,

$$\mathbf{E}(z_0,t) = A_+\mathbf{E}(z_0,t)^+ A_-\mathbf{E}^-(z_0,t) \tag{2.56}$$

$$= \left[A_+ \begin{pmatrix} 1 \\ -i/\alpha \end{pmatrix} e^{-i\frac{d\psi}{2}} + A_- \begin{pmatrix} 1 \\ i\alpha \end{pmatrix} e^{i\frac{d\psi}{2}} \right] e^{i(\omega t - d\phi)} \tag{2.57}$$

with a total phase shift of $d\phi = (\omega/2c)(\mu_+ + \mu_-)z_0$. By substituting the amplitudes A_+ and A_- into this equation we find the following relationship between the electric field at the input and output of a homogeneous plasma slab,

$$\mathbf{E}(z_0,t) = \mathbf{S}\mathbf{E}(0,t)e^{-id\phi} \tag{2.58}$$

where the 2 x 2 matrix,

$$\mathbf{S} = \begin{bmatrix} \cos\frac{d\psi}{2} + i\frac{1-\alpha^2}{1+\alpha^2}\sin\frac{d\psi}{2} & \frac{2\alpha}{1+\alpha^2}\sin\frac{d\psi}{2} \\ -\frac{2\alpha}{1+\alpha^2}\sin\frac{d\psi}{2} & \cos\frac{d\psi}{2} - i\frac{1-\alpha^2}{1+\alpha^2}\sin\frac{d\psi}{2} \end{bmatrix} \tag{2.59}$$

takes into account the transmission properties.

For parallel propagation we have $\theta = 0$ and correspondingly $\alpha = -1$ and the plasma matrix simplifies to,

$$\mathbf{S}_{\alpha=1} = \begin{bmatrix} \cos(d\psi/2) & -\sin(d\psi/2) \\ \sin(d\psi/2) & \cos(d\psi/2) \end{bmatrix} \tag{2.60}$$

which is a matrix describing a clockwise rotation of the polarisation of the incident wave by $d\psi/2$. If $\alpha = 1$ the corresponding matrix is,

$$\mathbf{S}_{\alpha=1} = \begin{bmatrix} \cos(d\psi/2) & \sin(d\psi/2) \\ -\sin(d\psi/2) & \cos(d\psi/2) \end{bmatrix} \tag{2.61}$$

which describes an anti-clockwise rotation of the polarisation by $d\psi/2$. In the case of perpendicular propagation $\alpha = 0$ and the plasma matrix reduces to,

$$\mathbf{S}_{\alpha=0} = \begin{bmatrix} e^{id\psi/2} & 0 \\ 0 & e^{-id\psi/2} \end{bmatrix} \tag{2.62}$$

which introduces opposed phase shifts and converts an initial linear polarisation into an elliptical one. This is known as the Cotton-Mouton effect.

The general case of oblique propagation results in a mixture of both effects. For the Faraday rotation to be dominant it is necessary that the polarisation coefficient α of the characteristic modes is close to unity which is generally satisfied for,

$$\omega \gg \frac{eB_{\perp}^2}{2m_e B_{//}} \tag{2.63}$$

where $B_{//} = (m_e/e)\omega_c \cos\theta$ and $B_{\perp} = (m_e/e)\omega_c \sin\theta$, assuming $\omega_p^2 \ll \omega^2$.

For an linearly polarised incident wave with non-circular polarisation eigenstates it is well established that for small angles $d\psi/2$ the Faraday angle is given by[15],

$$d\alpha_F = \frac{2\alpha}{1+\alpha^2}\frac{d\psi}{2} = \frac{1}{2}\frac{\omega_p^2}{\omega^2}\frac{\omega_{ce}}{\omega}\cos\theta\frac{\omega}{c}dz. \tag{2.64}$$

A derivation of the propagation of elliptically polarised waves was performed by Rommers[16]. It was shown that the phase shift of an elliptically polarised input wave with its major axis tilted by the angle ξ to the laboratory x-axis and with ellipticity $\epsilon = 1 - \Delta\epsilon$, can be given by,

$$d\Phi = \frac{\alpha^2 - 1 \pm 2\alpha[1 + \Delta\epsilon\cos 2\xi]}{1+\alpha^2}\frac{d\psi}{2} - d\phi. \tag{2.65}$$

It was also shown that the phase difference between two orthogonally polarised waves with ellipticities $(1 - \Delta\epsilon_1)$ and $(1 - \Delta\epsilon_2)$ can be given by,

$$\Delta(d\Phi) = \frac{2\alpha}{1+\alpha^2}[2 + \Delta\epsilon_1\cos 2\xi_1 + \Delta\epsilon_2\cos 2\xi_2]\frac{d\psi}{2} \tag{2.66}$$

which is proportional to the Faraday rotation angle $d\psi/2$. When the probing waves are not exactly circular the fractional error term is less than or equal to half the sum of the two deviations, depending on the exact orientations of the polarisation ellipse.

This matrix analysis is readily extended to an inhomogeneous plasma if its properties vary sufficiently slowly over distances comparable with the probing wavelength. In that case the beam path can be divided into a series of nearly uniform sections with locally defined refractive indices and characteristic modes which can be regarded as individual homogeneous slabs. The transmission behaviour of the non-uniform plasma is then obtained by multiplying the matrices of the individual slabs. The underlying assumptions are generally well satisfied for typical plasmas probed with submillimetre waves.

Chapter 3

Wavelength Selection

Due to the diverse range of plasma shapes and sizes in TCV optimal interferometer/polarimeter measurements for all possible configurations cannot be fulfilled by one wavelength. The basic requirement for the instrument is the provision of interferometric measurements over the entire density range and polarimetric measurements in as many cases as possible. In order to obtain sufficiently accurate information it is advantageous to use a wavelength whose corresponding refractive index varies strongly with the parameters to be measured, namely the electron and current densities. However, large changes in refractive index lead to significant refractive index gradients. The existence of such a gradient perpendicular to the direction of propagation will give rise to refraction of the probing beam and the amount of refraction which can be tolerated will effectively set the upper wavelength limit. The lower wavelength limit is usually set by either the tolerance of the system to mechanical vibrations or the detection accuracy.

This chapter outlines the main issues involved in the wavelength selection and the reasons behind the choice of 214.6μm as the operating wavelength. The results of simulations of both the interferometric and polarimetric measurements on actual TCV plasmas for a selection of possible probing wavelengths are presented. The simulations were performed on four of the possible TCV plasma configurations (see Section 1.2.1) which cover the entire density range. The flux contours of the these plasma configurations are shown in Fig. 3.1 and their relevant parameters listed in Table 3. The chosen configurations are a high current, highly elongated plasma (Fig. 3.1(a)), a high density diverted H-mode (Fig. 3.1(b)), a low-density ECRH target plasma (Fig. 3.1(c)) and a high elongation plasma (Fig. 3.1(d)).

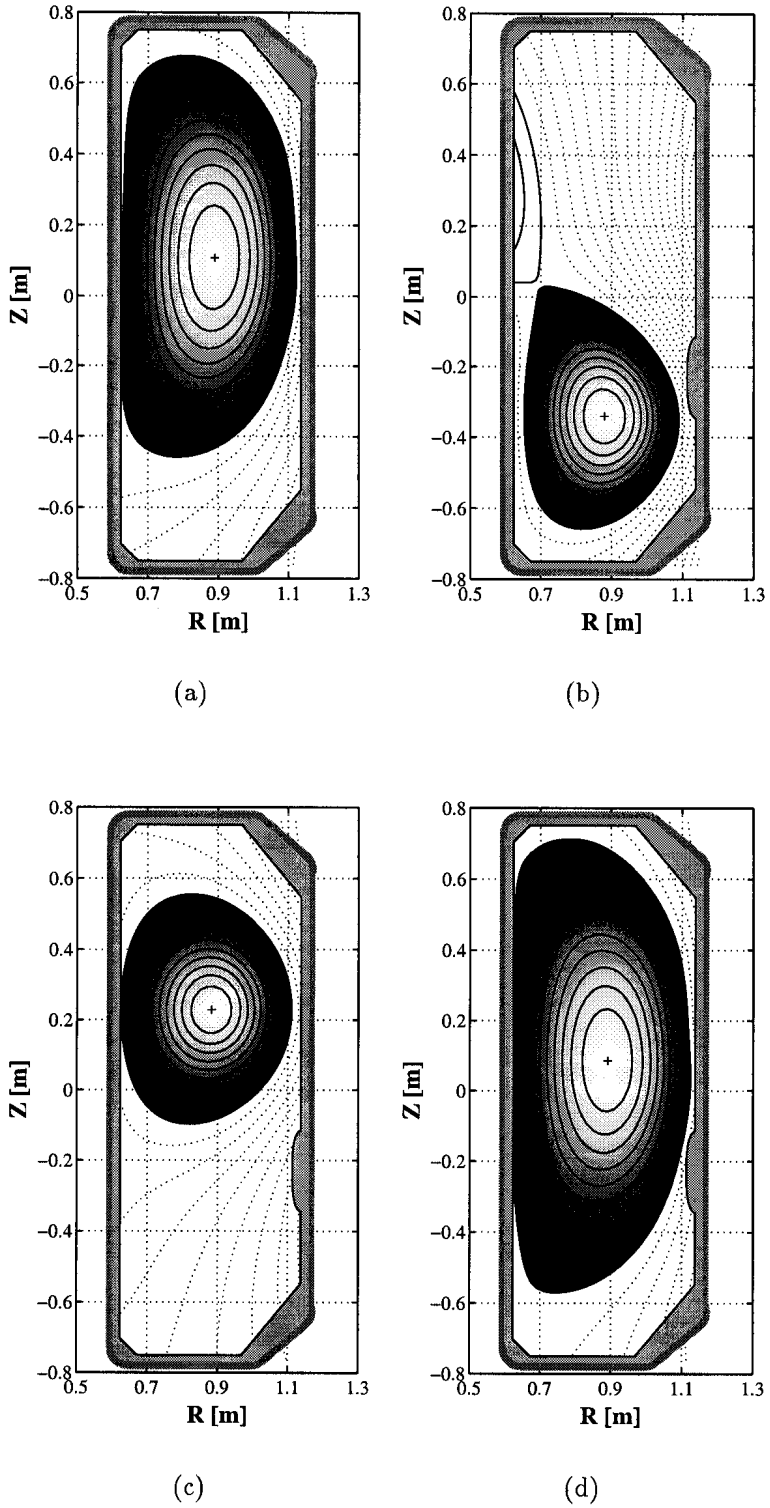

Figure 3.1: The flux contours of the shots used in the simulations (a) the high current highly elongated plasma (#11368) (b) the high density diverted H-mode plasma (#11404) (c) the low density ECRH target plasma (#12814) and (d) the highly elongated plasma (#12868).

Shot no.	11368	11404	12814	12868
Shot type	High current	Diverted	ECRH target	High elongation
Time [s]	0.65	1.0	1.0	0.72
Current [kA]	1025	324	179	725
Central density [10^{19} m^{-3}]	8.8	10.2	1.72	6.8
Profile parameter (α)	0.144	0.222	0.755	0.25
Elongation (κ)	2.3	1.6	1.3	2.55

Table 3.1: Parameters of the plasmas used in the simulations.

3.1 Fringe count

The number of fringes in a Mach-Zehnder interferometer scales linearly with the wavelength and the line-integrated density (Eqn. 2.38),

$$F = \frac{\Phi}{2\pi} = 4.49 \times 10^{-16} \lambda \int_{z_1}^{z_2} n_e(z) dz. \tag{3.1}$$

The simulated fringe count for the high current and ECRH target plasmas which represent

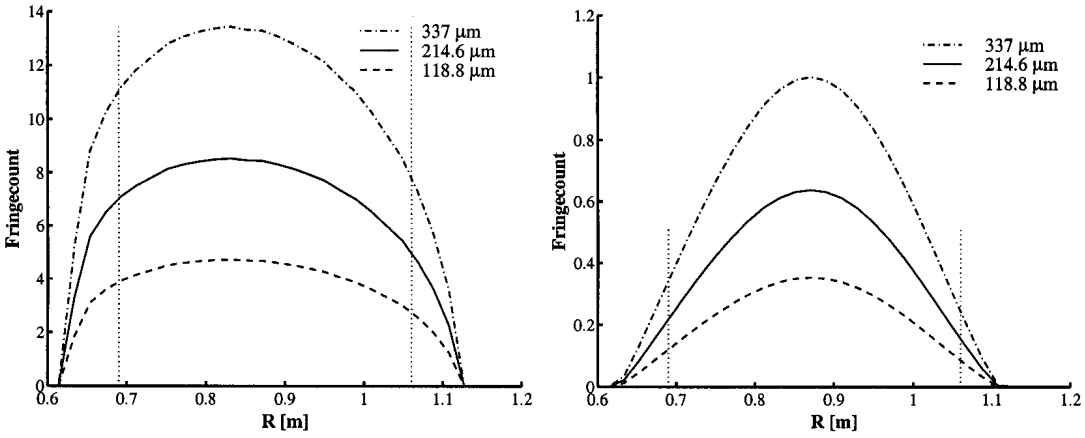

(a) (b)

Figure 3.2: The simulated fringe count for (a) the high current highly elongated plasma (#11368) and (b) the ECRH target plasma (#12814) for probing wavelengths of 118.8 μm, 214.6 μm and 337 μm. The dotted lines show the accessible part of the plasma which is limited by the vacuum windows.

either end of the density range are shown in Fig. 3.2 for three probing wavelengths of 118.8 μm, 214.6 μm and 337 μm. These particular wavelengths were chosen as they correspond to actual laser lines. The dotted lines show the accessible part of the plasma

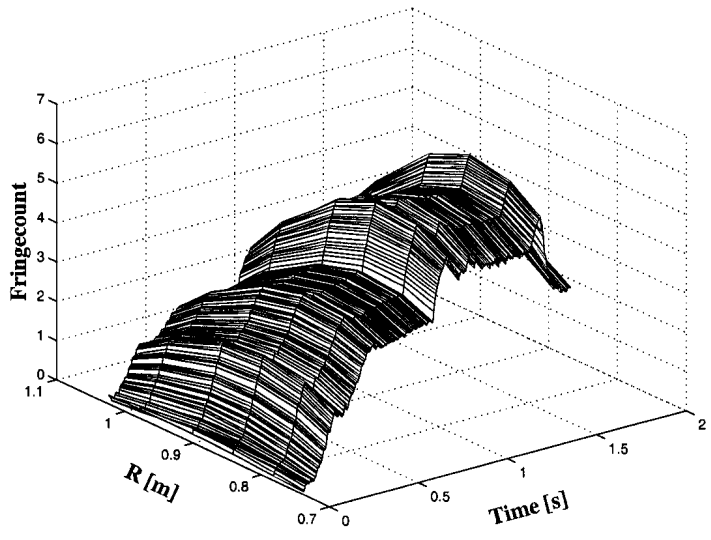

Figure 3.3: Actual evolution of the line-integrated density of the H-mode plasma (#11404) for a probing wavelength of 214.6 μm.

cross-section which is limited by the vacuum windows (see Section 6.3.4). The density profile is assumed to be parabolic with,

$$n_e = n_{e0}\psi_{norm}^{\alpha} \tag{3.2}$$

where n_e is the line-integrated density, n_{e0} the central electron density, α the parabolic fit parameter given in Table 3 and ψ_{norm} the normalised flux calculated from the equilibrium reconstruction code (see Sections 1.3 and 3.5).

Assuming a reasonable resolution of the phase measurement of 0.05 fringes (or 20°), the predicted maximum of 0.4 fringes for a wavelength of 118.8 μm probing the ECRH target plasma would be at the limit of useful operation. A wavelength of 214.6 μm probing the same plasma has a maximum predicted value of about 0.7 fringes which is more acceptable.

The actual evolution of the line-integrated density of the H-mode plasma (#11404) is shown in Fig. 3.3 for a probing wavelength of 214.6 μm and shows quite steep density variations. As the fringe count scales linearly with wavelength the possibility of losing fringes with a real time fringe counter would increase with increasing wavelength. The 2 mm interferometer on TCV for example, which uses an identical fringe counter, was seen to lose fringes during sawteeth crashes.

3.2 Refraction

Plasma density gradients which have components perpendicular to the probing beam produce refractive effects and the beam does not propagate in a straight line. The refraction angle for a single pass scales approximately with λ^2 and linearly with the central density (assuming a parabolic density profile)[17]. The amount of refraction varies with the position of the beam. Since the windows though which the probing beam enters and exits the vacuum vessel are limited in size (see Section 6.3.4) and since the chord positions are well defined by an array of waveguides (see Section 6.3.7) these refractive effects must be kept as small as possible.

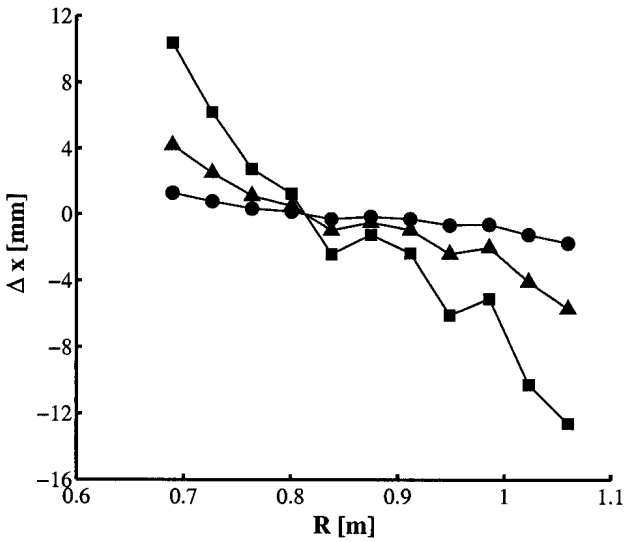

(a)

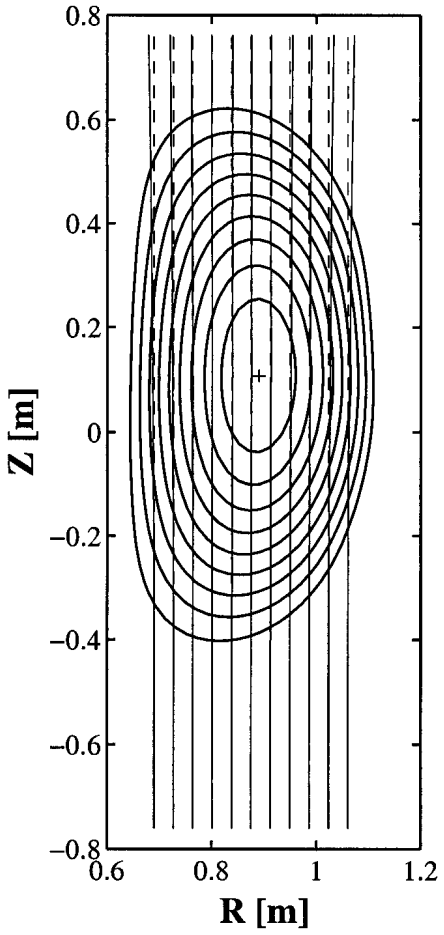

(b)

Figure 3.4: The calculated refraction in millimeters of a fan of rays of wavelengths λ = 118.8 μm (circles), λ = 214.6 μm (triangles) and λ = 337 μm (squares) by the high current, highly elongated plasma (#11368) and (b) the calculated beam trajectory for the case with λ = 337 μm. The dashed lines show the straight-through beam propagation.

The refraction of the probing beam for some TCV plasmas was calculated using a ray tracing code with assumed parabolic density profiles (see Section 3.1). The result of two such simulations are shown in Fig. 3.4 and Fig. 3.5 for the high current and the high

density H-mode plasmas, respectively, with probing wavelengths of 118.8 μm, 214.6 μm and 337 μm. The refraction is represented in the first plot of each figure as the horizontal distance between the actual beam as it exits the tokamak vessel and an ideal non-refracted beam propagating straight through the plasma. The second plot shows the calculated trajectory of a $\lambda = 337$ μm beam through the plasma. Similar simulations of the ECRH target plasma predicted negligible refraction for all three probing wavelengths. It can be seen in Fig. 3.4 that there is some refraction at the edges of the high current plasma which is only significant for the probing wavelength of 337 μm. The simulations of the H-mode plasma, however, show considerable refraction already at 214.6 μm which corresponds to observed decreases in the actual detected signals of the edge channels during high density H-mode plasmas. The calculated refraction of the 337 μm beam for this plasma would result in the loss of at least some of the edge channels.

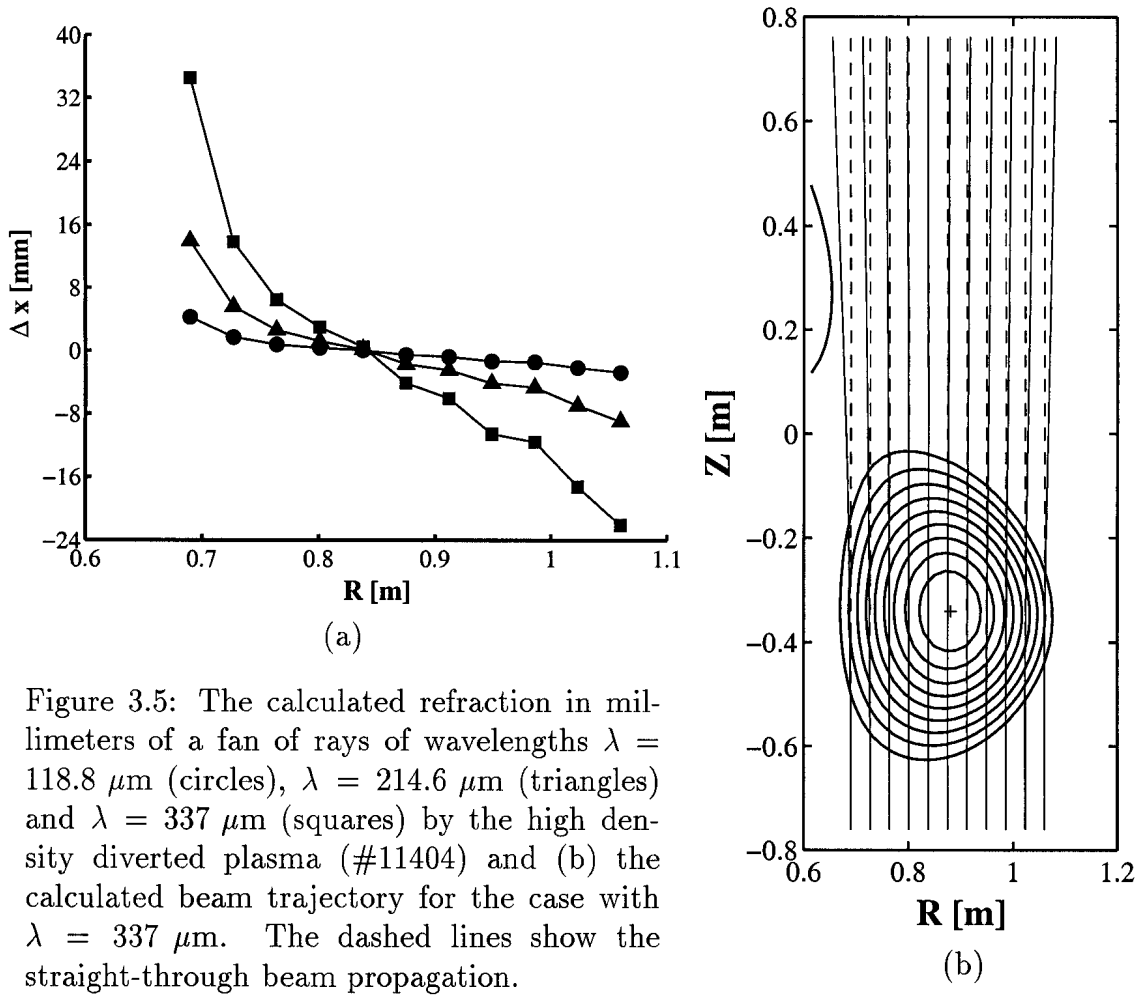

Figure 3.5: The calculated refraction in millimeters of a fan of rays of wavelengths $\lambda = 118.8$ μm (circles), $\lambda = 214.6$ μm (triangles) and $\lambda = 337$ μm (squares) by the high density diverted plasma (#11404) and (b) the calculated beam trajectory for the case with $\lambda = 337$ μm. The dashed lines show the straight-through beam propagation.

The divertor leg which contains a large number of cold electrons, is not sufficiently

diagnosed and is difficult to model. Therefore, the effect of possible density gradients in this region on the refraction of the beam have not been included in these calculations.

3.3 Vibrations

Any interferometer, particularly one in the usually noisy environment of a tokamak, is subject to spurious changes in path length due to vibrations of its optical components. A total vibrational path disturbance l, is equivalent to a change in the interferometer phase of,

$$\Delta\Phi = \frac{2\pi l}{\lambda} \tag{3.3}$$

where λ is the probing wavelength. As the phase shift introduced by the plasma is proportional to the probing wavelength the ratio of spurious vibrational phase error to phase change is proportional to λ^{-2}. Again assuming a reasonable resolution of the phase measurement of 0.05 fringes (see Section 3.1) and that the typical change in the optical path induced by vibrations is of the order of 10 μm, a minimum wavelength of at least 200 μm is required.

The effect of the vibrations can be compensating for by measuring the phase shift simultaneously at two very different wavelengths. The shorter wavelength (usually in the visible) is sensitive mainly to the vibrations while the longer wavelength measures the refractive index changes. The effects of vibrations can be removed by subtracting an appropriate proportion of the phase of the short wavelength interferometer from that of the long. Such a device using a HeNe laser was previously installed on the central channel of the old TCV interferometer. To prove a useful tool the compensating interferometer should operate on the all the chords of the density interferometer. If the compensation of vibrations is deemed necessary such a system can be installed on the TCV interferometer/polarimeter.

3.4 Faraday Rotation

The instrument should be capable of measuring the Faraday rotation with sufficient sensitivity for at least some of the range of TCV plasma configurations. The rotation angle is proportional to the plasma density, the plasma current and the wavelength squared (Eqn. 2.48). The lower wavelength limit is set by the precision which can be realised by the instrument, seen during the bench tests to be of the order of $0.1 - 0.2^{o}$ (see Chapter 5). For large rotation angles the birefringence of the plasma due to the toroidal magnetic field

adds some ellipticity to the polarisation of the probe beam which can make the interpretation of the results more difficult. This is known as the Cotton-Mouton effect and is discussed briefly in Section 2.2.2. The effect scales with λ^3, B_ϕ^2 and the central electron density n_{e0} and hence sets the upper wavelength limit.

The design of elaborate detection electronics including fringe counters can be avoided by limiting the maximum phase shift to 180^o. As one of the proposed methods measures twice the rotation angle (see Section 4.3) and as there will be offset in order to distinguish between positive and negative rotation this would limit the detectable rotation angles to $\pm 45^o$.

As the main reason for the inclusion of a polarimeter diagnostic on TCV was to improve the equilibrium reconstruction of highly elongated plasmas (see Section 3.5) the choice of a suitable wavelength for polarimetry will concentrate on this type of plasma. The Jones matrix formalism discussed in Section 2.2.2 was used to predict the rotation angles and added ellipticity of various TCV plasma configurations with different probing wavelengths. The results of such a simulation for the high current plasma in shown in Fig. 3.6 and for the highly elongated plasma in Fig. 3.7. Both figures also show the polarisation parameter α and the difference in refractive indices both calculated for a probing wavelength of 214.6 μm.

The simulation results of the high current shot (Fig. 3.6) show that the use of the 337 μm wavelength, with a maximum predicted rotation angle of 70^o, would require the installation of a phase detection system which includes a fringe counter. The additional ellipticity of 0.085(max), obtained by the beam as it traverses the plasma is also quite significant. The 214.6μm wavelength produces a reasonable maximum angle of rotation of 28^o and almost negligible ellipticity. The maximum angle produced by the 118.8μm probing wavelength is 8.6^o and its additional ellipticity is negligible. These values correspond to the maximum expected rotations and ellipticities on TCV.

The simulations shown in Fig. 3.7 for the highly elongated, but lower current plasma, show maximum angles of 4.2^o, 13.7^o and 33.8^o for the three wavelengths in ascending order and negligible ellipticity.

3.5 Equilibrium Reconstruction

The problem of reconstructing tokamak equilibria based on external measurements is becoming increasingly important in view of the recent evolution towards highly elongated and shaped plasmas. The problem consists of finding a solution to the Grad-Shafranov

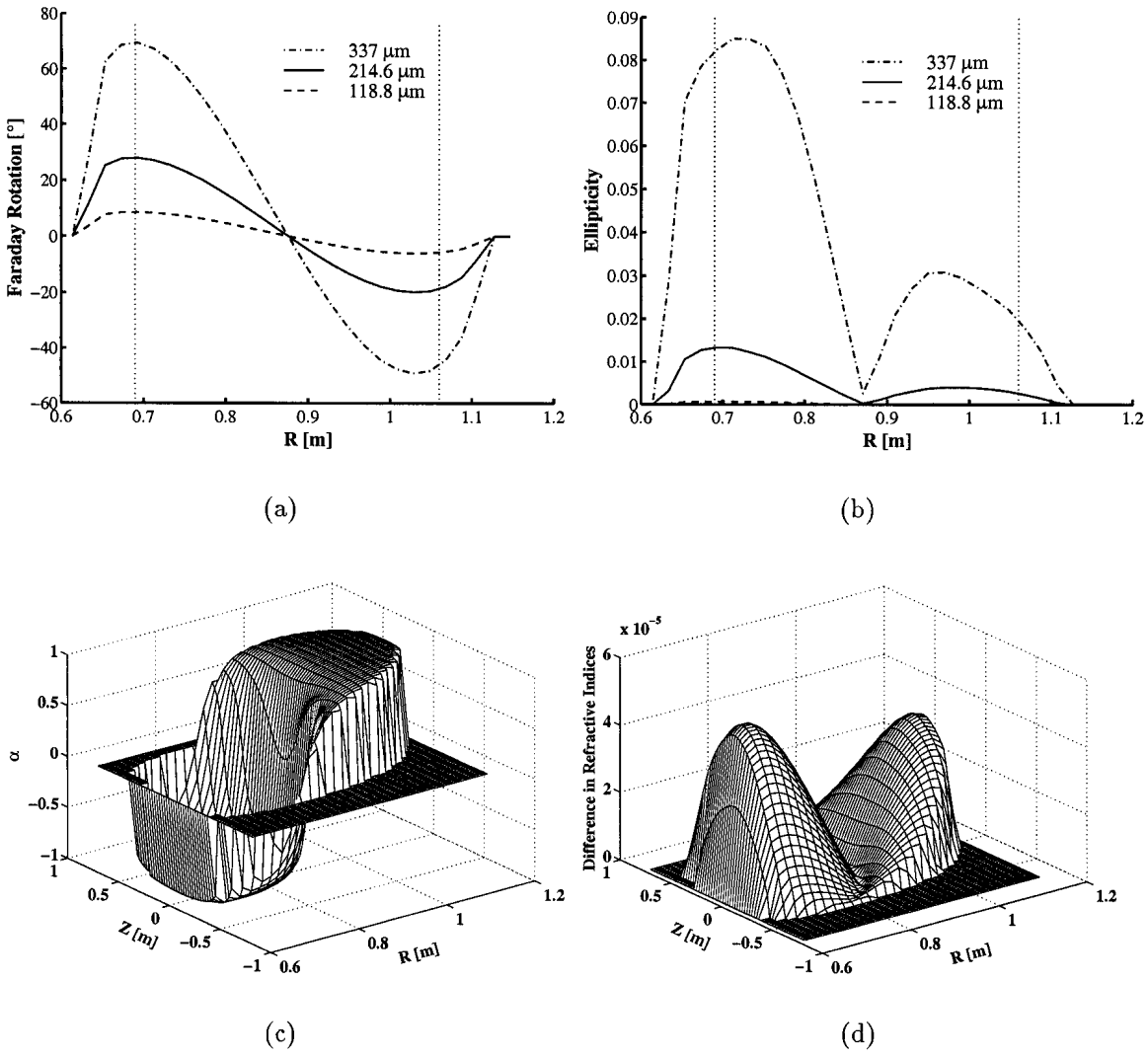

Figure 3.6: The simulated (a) Faraday rotation angle and (b) additional ellipticity for the high current plasma (#11368) for probing wavelengths of 118.8 μm, 214.6 μm and 337 μm and (c) the polarisation coefficient α and (d) the difference in refractive indices associated with the eigenmodes of the plasma calculated for a probing wavelength of 214.6 μm.

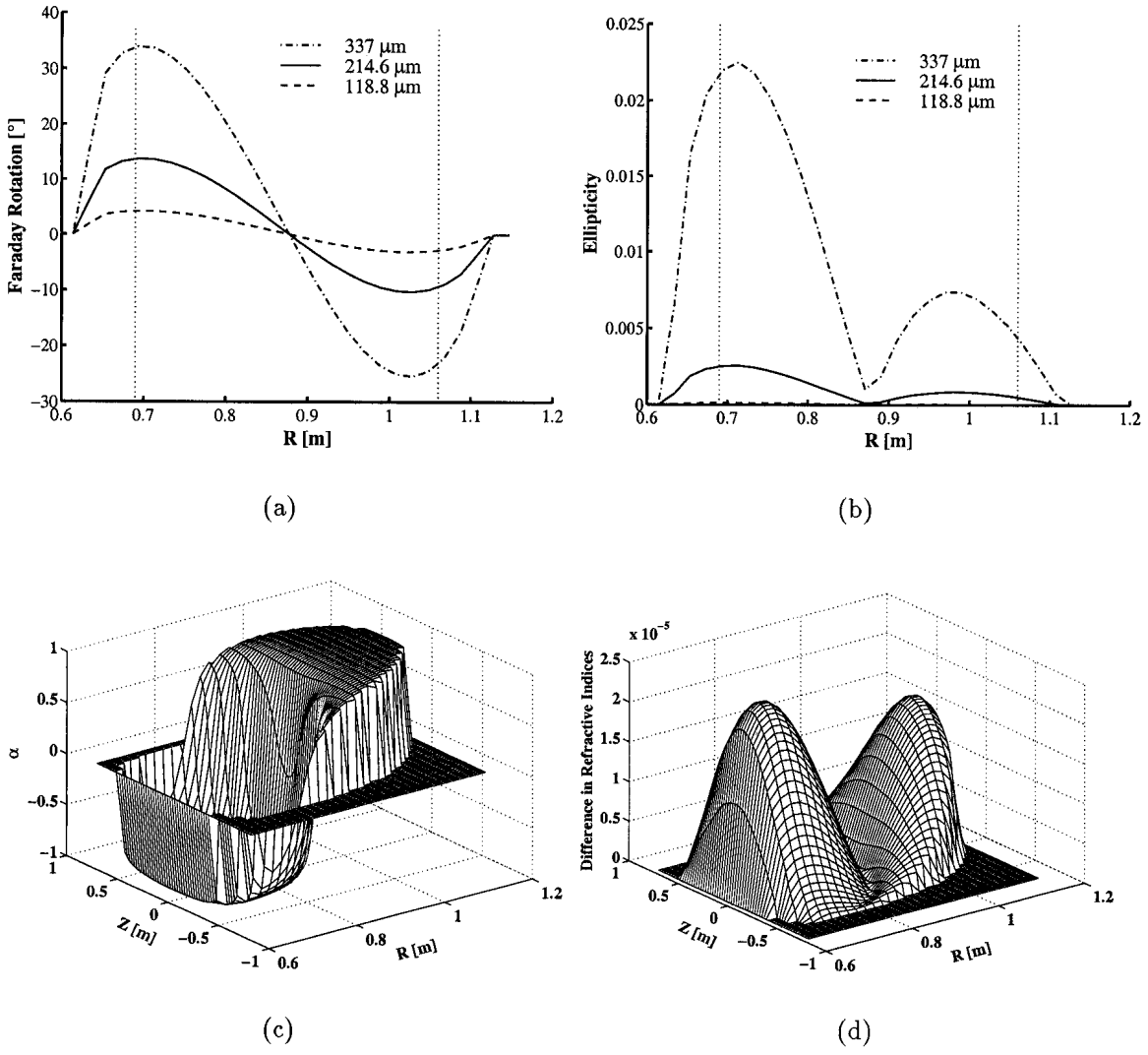

Figure 3.7: The simulated (a) Faraday rotation angle and (b) additional ellipticity for the high elongation plasma (#12868) for probing wavelengths of 118.8 μm, 214.6 μm and 337 μm and (c) the polarisation coefficient α and (d) the difference in refractive indices associated with the eigenmodes of the plasma calculated for a probing wavelength of 214.6 μm.

equation (see Section 1.3),

$$R\frac{\partial}{\partial R}\frac{1}{R}\frac{\partial \psi}{\partial R}+\frac{\partial^2 \psi}{\partial z^2}=-\mu_0 R^2 p'(\psi)-\mu_0^2 f(\psi)f'(\psi) \tag{3.4}$$

with arbitrary source functions, such that the measurements are reproduced as well as possible. The solution is complicated by the fact that it is mathematically ill-posed and that all measurements are subject to errors. Consequently, there is no rigorously accurate nor unique solution.

When trying to reconstruct tokamak equilibria with arbitrary source functions, using magnetic measurements, one soon encounters a fundamental problem. The toroidal plasma current density must be split into two parts one proportional to Rp' and the other to TT'/R where R is the major radius, p the plasma pressure, $T = RB_\phi$ and the prime denotes differentiation with respect to ψ. The relative importance of these terms can, in principle, be determined due to the difference in their R-dependence. For the outer flux surfaces the decomposition can be performed quite accurately but as one approaches the magnetic axis the accuracy decreases rapidly. On axis, where the radial extent of the flux surface shrinks to zero, it becomes impossible to compute p' and TT' separately. In fact, these values are generally obtained by extrapolating from the outer regions, the validity of the extrapolation depending essentially on the size of the measurement errors and the type of measurements used. One would therefore expect the accuracy of an equilibrium reconstruction to improve considerably with the inclusion of information on the internal poloidal magnetic field.

It has been shown that the inclusion of additional measurements such as line-integrated density and Faraday rotation into the TCV reconstruction code LIUQE together with the standard magnetic measurements would improve the accuracy of the equilibrium reconstructions[18]. For these simulations it was assumed that in the reconstructed equilibrium, the source functions and electron density can be expressed in terms of poloidal flux,

$$p' = \sum_{n=0}^{N_p} a_n U_n(\varphi) \tag{3.5}$$

$$TT' = \sum_{n=0}^{N_T} b_n V_n(\varphi) \tag{3.6}$$

$$n_e = \sum_{n=0}^{N_n} c_n W_n(\varphi) \tag{3.7}$$

where a_n, b_n, c_n are constants to be determined, $U_n(\varphi)$, $V_n(\varphi)$, $W_n(\varphi)$ are arbitrary base functions and $\varphi = (\psi - \psi_{lim})/(\psi_{ax} - \psi_{lim})$ with ψ_{lim} and ψ_{ax} the values of the poloidal flux

function at the limiter and magnetic axis, respectively. In general the error of the mean value decreases and the RMS error increases with increasing numbers of source functions. Optimum values of N_p and N_T are found by searching for the minimum total error.

The simulations described in [18] were performed on a D-shaped plasma with an elongation of $\kappa = 2$, similar in form to the high current and high elongation plasmas used in the simulations. It was seen that without Faraday rotation, measurement values of $N_p > 2$ and $N_T > 2$ must be avoided as they lead to a very large uncertainty in q_0 (the safety factor on the magnetic axis, Section 1.2). The addition of line-integrated density and Faraday rotation data on 10 chords was seen to allow the determination of up to six independent source function parameters and the error in q_0 was reduced by at least a factor of two compared with the cases without Faraday rotation data provided that the random errors on the measurements were below $\pm 2\%$ of the maximum signal. Assuming a measurement precision of 0.2^0, Faraday rotation profiles with a maximum angle of at least 10^o are, therefore, required.

3.6 Conclusions

It was seen from the simulations that there was some refraction on high density H-mode plasmas at wavelengths as low as 214.6 μm and that the refraction at wavelengths greater than this would lead to the loss of at least some of the edge channels. The effects of vibrations and the low fringe count for the ECRH target plasma coupled with the small Faraday rotation angles ruled out probing wavelengths below about 200 μm.

It was concluded, therefore, that a probing wavelength of 214.6 μm would fulfill the tight requirement between reasonable interferometer measurements over the entire density range while avoiding strong refractive effects. This wavelength would also provide useful Faraday rotation measurements for the high elongation plasmas where its inclusion in the equilibrium reconstruction code was seen to be valuable.

Chapter 4

Method Description

This chapter outlines the basic principles of far-infrared (FIR) interferometry and polarimetry and describes briefly the progression of polarimeter operation on interferometer/polarimeters from an amplitude measurement on a two detector per chord instrument through to a phase measurement with only one detector per chord. This development was made possible by the introduction of techniques to modulate the polarisation of the probing beam. The two interferometer/polarimeter methods which have been installed on TCV are then described in detail. The fundamental difference between the two methods is the type of polarisation modulation used.

4.1 Basic Principles

4.1.1 Interferometry

As described in Chapter 2 the phase of an electromagnetic wave traversing a plasma is shifted according to,

$$\Phi = 2.82 \times 10^{-15} \lambda \int n_e(z) dz \tag{4.1}$$

where λ is the wavelength of the probing beam and n_e the electron density as a function of the probing path z, all in mks units and with the constant in metres. The change in phase of the emerging beam is monitored as a function of time and is used to derive the electron density integrated along the beam path. This technique cannot, therefore, determine a local value of the electron density. In order to obtain a thorough knowledge of the density distribution it is necessary to probe the plasma along different chords. The determination of the density profile then requires the inversion of the line-integrated signals. In a purely cylindrical geometry the well-known Abel inversion technique can be used. There is also a technique available for extending the Abel inversion to include asymmetries normal to

the direction of observation[19]. However, for highly non-symmetric plasmas, as in the case of TCV, it is common practice to look for a best fit of measured values of Φ obtained along each chord with values calculated from given density profiles.

The essence of the measurement is the determination of the phase of the beam emerging from the plasma. This is usually performed by mixing the probing beam with one having a well defined phase behaviour, known as the local oscillator (LO). One of the simplest techniques, known as homodyne or single-frequency detection, is to split a laser beam into two branches one of which probes the plasma. The two beams are then recombined on a detector. The electric vectors of the two beams before recombination can be represented by $E_{lo} = E_1 e^{i(\omega t + \phi_{lo})}$ and $E_{probe} = E_2 e^{i(\omega t + \Phi(t) + \phi_{probe})}$ for the LO and probing branches, respectively, where $\Phi(t)$ is the time-varying phase shift due to the plasma electron density and ϕ_{lo} and ϕ_{probe} are constant over time. The resulting intensity on the detector can then be written as,

$$\begin{aligned} I_{plas} &= E_{probe}E^*_{probe} + E_{lo}E^*_{lo} \\ &= E_1^2 + E_2^2 + 2E_1E_2\cos\Big(\Phi(t) + \phi_{probe} - \phi_{lo}\Big). \end{aligned} \tag{4.2}$$

Filtering out the dc terms leaves a signal proportion to,

$$\begin{aligned} S_{plas} &= E_1E_2 cos\Big(\Phi(t) + \phi_{probe} - \phi_{lo}\Big) \\ &= E_1E_2\cos\Big(\Phi(t) + \phi_{plas}\Big) \end{aligned} \tag{4.3}$$

where ϕ_{plas} is constant over time. The detected signal is, therefore, related quite simply to the density induced phase shift. This technique has a few drawbacks. Firstly, variations in beam power can be interpreted as density changes and secondly, it is not possible to determine whether $\Phi(t)$ is increasing or decreasing.

Most interferometer experiments today, however, make use of heterodyne or double-frequency detection where the LO beam $E_{lo} = E_1 e^{i(\omega t + \Delta\omega t + \phi_{lo})}$, has a slight frequency offset $\Delta\omega$, from the probing beam. The resulting intensity on the detector is then,

$$\begin{aligned} I_{plas} &= E_{probe}E^*_{probe} + E_{lo}E^*_{lo} \\ &= E_1^2 + E_2^2 + 2E_1E_2\cos\Big(\Delta\omega t - \Phi(t) - \phi_{plas}\Big). \end{aligned} \tag{4.4}$$

The resulting signal after filtering out the dc terms is proportional to,

$$S_{plas} = E_1E_2\cos\Big(\Delta\omega t - \Phi(t) - \phi_{plas}\Big). \tag{4.5}$$

The phase shift $\Phi(t)$ due to the plasma can be determined by comparing the phase of the plasma signal to that of a reference signal proportional to,

$$S_{ref} = E_1E_2\cos\Big(\Delta\omega t - \phi_{ref}\Big). \tag{4.6}$$

The detected phase shift, namely $\Phi(t) + \phi_{plas} - \phi_{ref}$, is the plasma induced phase shift with a constant offset due to the different path lengths traveled by the various beams. As the offset $\phi_{plas} - \phi_{ref}$, remains constant over time it will, for simplicity, be neglected during the following discussions.

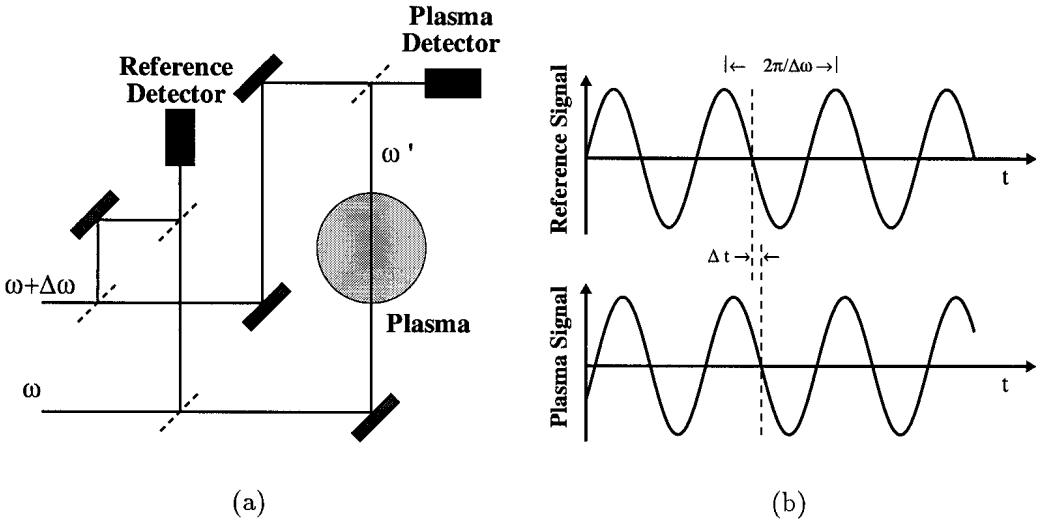

Figure 4.1: (a) Schematic of a single channel Mach-Zehnder heterodyne interferometer showing (b) the resulting reference and probing detector signals.

A schematic of a simple single channel Mach-Zehnder heterodyne interferometer is shown in Fig. 4.1 along with typical detector signals. The temporal resolution which can be obtained using heterodyne detection is directly related to the difference frequency (or intermediate frequency IF) between the probing and LO beams. In the visible spectrum the IF can be produced by various schemes including the acousto-optical effect. In the FIR regime, however, the IF is created either via the Doppler effect by the reflection of one of the beams off a rotating grating[17] or by using two separate lasers which are slightly detuned in frequency[20]. With the rotating grating IFs of up to several 100 kHz are attainable while double-laser systems can provide IFs two orders of magnitude greater[21].

4.1.2 Polarimetry

It was also shown in Chapter 2 that the plane of polarisation of an electromagnetic wave traversing a plasma is rotated by the angle Ψ, known as the Faraday rotation and given by,

$$\Psi = 2.62 \times 10^{-13} \lambda^2 \int n_e B_{//} dz \tag{4.7}$$

where $B_{//}$ is the component of the poloidal magnetic field parallel to the probing beam. All the parameters are in mks units with the constant in Tesla^{-1}. The profile of $B_{//}$ can be determined once the line-integrated density is known. It is, therefore, advantageous to combine the polarimeter and interferometer measurements on one instrument.

The first multichannel interferometer/polarimeter was installed by Soltwisch on the TEXTOR tokamak[22]. The system had nine probing channels with two detectors per channel. A polarising beamsplitter separated the probing beam after passage through the plasma into components with polarisations parallel and perpendicular to the initial polarisation. The perpendicular component, produced by the Faraday rotation, is mixed with a local oscillator to yield a beat signal with an amplitude proportional to the angle of rotation. The interferometer information is contained in the phase shift between the parallel component and a reference signal. This technique requires two detectors per chord and as the polarimeter measurement is an amplitude measurement it is sensitive to variations in beam power. This influence can, however, be eliminated during the signal processing.

Dodel and Kunz[23] developed an interferometer/polarimeter technique based on the modulation of the polarisation of the probing beam. Right and left-hand circularly polarised beams of angular frequencies ω and $\omega+\omega_m$, respectively, are superimposed to form a linearly polarised beam whose plane of polarisation rotates at a frequency of $\omega_m/2$. The ac component of the signal produced by this beam, sent through an analyser on a square law detector is, therefore, proportional to $S_{ref} = S_0 \cos \omega_m t$. A magnetised plasma in the probing beam causes an additional Faraday rotation $\Psi = (\Delta\phi_+ - \Delta\phi_-)/2$, of the plane of polarisation where $\Delta\phi_+$ and $\Delta\phi_-$, are the phase shifts of the left and right-hand circularly polarised beams, respectively. The detected signal is then proportional to $S_{plas} = S_0 \cos(\omega_m t + 2\Psi)$. The Faraday rotation is readily measured from the phase shift between the two signals. Interferometer operation can be included by installing extra components including an additional detector per probing chord.

On MTX an alternative modulation method which uses a beam with a continuously rotating elliptical polarisation to probe the plasma was employed[24]. Both the interferometer and Faraday rotation measurements are phase measurements and only one detector per probing chord is required. This is one of the methods installed on TCV (Method 1) and is discussed in detail in Section 4.3. A second method (Method 2) which is a modified version of Method 1 was also installed and is discussed in Section 4.4. The fundamental difference between these two methods is the type of polarisation modulation employed.

4.2 Polarisation Modulation

Various schemes exist to modulate the polarisation of FIR beams. The polarisation can be modulated either before or after the probing beam traverses the plasma. The former is more convenient for multi-channel devices as one single modulator can be used for many beams. The modulation schemes can be divided into two categories namely alternating and progressive modulation where a typical polarisation parameter ρ, varies according to[25],

$$\rho_{alt} = \delta_0 \cos \omega_m t \tag{4.8}$$

and

$$\rho_{prog} = \omega_m t \tag{4.9}$$

respectively. Alternating polarisation requires special optical components which introduce an alternating time behaviour in a particular polarisation parameter. An example of this is the intra-cavity polarisation modulation of an optically pumped FIR laser where the pump polarisation is modulated by a suitable Faraday device [26]. As the polarisation of the FIR laser generally follows or is perpendicular to the pump polarisation its polarisation will modulate correspondingly.

The rotating linearly polarised beam used by Dodel and Kunz[23] and described in Section 4.1.2 is a form of progressive polarisation modulation. The modulation was produced by combining two frequency shifted circularly polarised beams. A more straightforward method, however, of rotating the plane of polarisation of a beam is to direct it through a retarder plate rotating at a constant frequency. This technique forms the basis of the two modulation schemes used on the TCV interferometer/polarimeter.

Crystalline Quartz Optics

Crystals whose physical properties, such as refractive index, vary with direction are known as anisotropic. The simplest anisotropic crystal has a single axis of symmetry known as the optic axis. Consider a thin slab of anisotropic crystal cut so that its optic axis lies in the plane of its surface. Suppose that polarised light falls at normal incidence on the slab. We may resolve the electric vector into two components parallel and perpendicular to the optic axis. The parallel component, or extraordinary wave, propagates through somewhat faster than the perpendicular, or ordinary wave, therefore leading it on exiting the crystal. The superposition of the two components on exiting the crystal can result in a beam whose polarisation has changed with respect to that of the incident beam. We make use of this phenomenon, known as birefringence, to modify the polarisation of light.

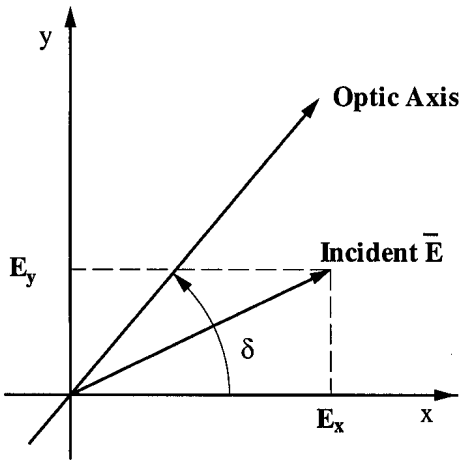

Figure 4.2: The coordinates of the crystal axis.

Crystalline quartz is a low-loss birefringent material in the far-infrared making it an obvious choice for waveplates. Consider an arbitrarily polarised beam with horizontal and vertical components $E_{x0} = A_x e^{i(\omega t+\phi_x)}$ and $E_{y0} = A_y e^{i(\omega t+\phi_y)}$, incident on a quartz plate as shown in Fig. 4.2. The angle between the crystal optic axis and the horizontal or x-axis is given by δ. The transformation of the polarisation state of a beam traversing the plate can be most conveniently expressed in terms of Jones matrices (see Section 2.1.2). The method used is to transform **E** into the coordinate system of the crystal, apply the phase shift due to birefringence and then transform back to the original coordinate system. The result of these transformations is,

$$\begin{bmatrix} E_x \\ E_y \end{bmatrix} = \begin{bmatrix} \cos\delta & -\sin\delta \\ \sin\delta & \cos\delta \end{bmatrix} \begin{bmatrix} 1 & 0 \\ 0 & e^{i\sigma} \end{bmatrix} \begin{bmatrix} \cos\delta & \sin\delta \\ -\sin\delta & \cos\delta \end{bmatrix} \begin{bmatrix} E_{x0} \\ E_{y0} \end{bmatrix} \tag{4.10}$$

where σ is the difference in phase between the two characteristic modes (ordinary and extraordinary) in the crystal. The above equation can be reduced to,

$$\begin{bmatrix} E_x \\ E_y \end{bmatrix} = \begin{bmatrix} \cos^2\delta + \sin^2\delta e^{i\sigma} & \sin\delta\cos\delta(1-e^{i\sigma}) \\ \sin\delta\cos\delta(1-e^{i\sigma}) & \sin^2\delta + \cos^2\delta e^{i\sigma} \end{bmatrix} \begin{bmatrix} E_{x0} \\ E_{y0} \end{bmatrix}. \tag{4.11}$$

Of particular interest are both the $\lambda/2$ and $\lambda/4$ plates. In the case of the $\lambda/2$ plate, $\sigma = \pi$ and, for the simple case of a linearly polarised incident beam, represented here for simplicity as being horizontally polarised, the transformation becomes,

$$\begin{aligned} \begin{bmatrix} E_x \\ E_y \end{bmatrix} &= \begin{bmatrix} \cos 2\delta & \sin 2\delta \\ \sin 2\delta & -\cos 2\delta \end{bmatrix} \begin{bmatrix} E_{x0} \\ 0 \end{bmatrix} \\ &= \begin{bmatrix} \cos 2\delta E_{x0} \\ \sin 2\delta E_{x0} \end{bmatrix}. \end{aligned} \tag{4.12}$$

Therefore the $\lambda/2$ plate rotates the incident polarisation by twice the angle between the optic axis and the x-axis. To examine the effect of a $\lambda/4$ wave plate we substitute $\sigma = \pi/2$ into Eqn. 4.11 and again with horizontal incident polarisation obtain,

$$\begin{aligned}\begin{bmatrix} E_x \\ E_y \end{bmatrix} &= \begin{bmatrix} \cos^2\delta + i\sin^2\delta & \sin\delta\cos\delta(1-i) \\ \sin\delta\cos\delta(1-i) & \sin^2\delta + i\cos^2\delta \end{bmatrix} \begin{bmatrix} E_{x0} \\ 0 \end{bmatrix} \\ &= \begin{bmatrix} E_{x0}(\cos^2\delta + i\sin^2\delta) \\ E_{x0}(\sin\delta\cos\delta(1-i)) \end{bmatrix}. \end{aligned} \tag{4.13}$$

In the extreme case of $\delta = \pi/4$ this reduces to,

$$\begin{bmatrix} E_x \\ E_y \end{bmatrix} = \begin{bmatrix} \frac{1}{2}E_{x0}e^{i\pi/4} \\ \frac{1}{2}E_{x0}e^{-i\pi/4} \end{bmatrix} \tag{4.14}$$

which represents a circularly polarised beam. For the case of $\delta = 0$ the incident beam remains unchanged. Setting the plate at angles between these two extremes results in elliptically polarised beams. Therefore, a $\lambda/4$ plate can change the ellipticity and plane of polarisation of an incident beam while a $\lambda/2$ plate can rotate the polarisation.

4.3 Method 1

This scheme is based on the polarimeter system installed on MTX[24] and requires a rotating elliptically polarised probing beam and a frequency shifted linearly polarised LO. The rotating polarisation ellipse is produced by passing a horizontally linearly polarised beam, represented by $E_{0x} = Ae^{i\omega t}$, through a $\lambda/4$ plate which introduces some ellipticity and then through a rapidly rotating $\lambda/2$ plate which rotates the incident polarisation ellipse at twice the angular frequency of the plate. The resultant beam is given by,

$$\begin{aligned}\begin{bmatrix} E_{ellipse_x} \\ E_{ellipse_y} \end{bmatrix} &= \begin{bmatrix} \cos 2\omega_r t & \sin 2\omega_r t \\ \sin 2\omega_r t & -\cos 2\omega_r t \end{bmatrix} \begin{bmatrix} \cos^2\delta + i\sin^2\delta & \cos\delta\sin\delta(1-i) \\ \cos\delta\ sin\delta(1-i) & \sin^2\delta + i\cos^2\delta \end{bmatrix} \begin{bmatrix} E_{0x} \\ 0 \end{bmatrix} \\ &= \begin{bmatrix} E_{0x}[\cos(2\omega_r t - \delta)\cos\delta - i\sin(2\omega_r t - \delta)\sin\delta] \\ E_{0x}[\sin(2\omega_r t - \delta)\cos\delta + i\cos(2\omega_r t - \delta)\sin\delta] \end{bmatrix} \end{aligned} \tag{4.15}$$

where δ is the angle between the optic axis of the $\lambda/4$ plate and the x or horizontal axis and $\omega_r t$ the angle of rotation of the $\lambda/2$ plate. Substituting for E_{0x} results in,

$$\begin{bmatrix} E_{ellipse_x} \\ E_{ellipse_y} \end{bmatrix} = \begin{bmatrix} \frac{A}{\sqrt{2}}[1 + \cos 2\delta\cos(4\omega_r t - 2\delta)]^{1/2} e^{i(\omega t + \chi_{refx})} \\ \frac{A}{\sqrt{2}}[1 - \cos 2\delta\cos(4\omega_r t - 2\delta)]^{1/2} e^{i(\omega t + \chi_{refy})} \end{bmatrix} \tag{4.16}$$

where,

$$\chi_{refx} = -\tan^{-1}(\tan\delta\tan(2\omega_r t - \delta)) \tag{4.17}$$

$$\chi_{refy} = \tan^{-1}(\tan\delta/\tan(2\omega_r t - \delta)). \tag{4.18}$$

Thus the amplitude of the beam is modulated by the rotating plate and the amount of modulation is determined by δ, the fixed angle of the $\lambda/4$ plate. There are also additional phase shifts χ_{refx} and χ_{refy} in the beam due to the combination of the plates. This rotating elliptically polarised probing beam is then split in two with one part going through the plasma and onto the plasma detector while the other is directed onto the reference detector. Both beams are superimposed with the frequency shifted linearly polarised LO,

$$\begin{bmatrix} E_{lo_x} \\ E_{lo_y} \end{bmatrix} = \begin{bmatrix} Ee^{i(\omega+\Delta\Omega)t} \\ 0 \end{bmatrix} \tag{4.19}$$

and passed through horizontal polarisers just before detection. The beam incident on the reference detector is then,

$$\begin{bmatrix} E_{ref_x} \\ E_{ref_y} \end{bmatrix} = \begin{bmatrix} \frac{A}{\sqrt{2}}[1+\cos 2\delta\cos(4\omega_r t - 2\delta)]^{1/2} e^{i(\omega t+\chi_{refx})} + Ee^{i(\omega+\Delta\Omega)t} \\ 0 \end{bmatrix}. \tag{4.20}$$

The resultant intensity on the reference detector is, therefore,

$$\begin{aligned} I_{ref} &= E_{ref_x}E^*_{ref_x} + E_{ref_y}E^*_{ref_y} \\ &= \frac{A^2}{2}(1+\cos 2\delta\cos(4\omega_r t - 2\delta)) + E^2 \\ &\quad +\sqrt{2}AE(1+\cos 2\delta\cos(4\omega_r t - 2\delta))^{1/2}\cos(\Delta\Omega t - \chi_{ref_x}). \end{aligned}$$

Bandpass filtering around the difference frequency $\Delta\Omega$, results in a signal proportional to,

$$S_{ref} = AE(1+\cos 2\delta\cos(4\omega_r t - 2\delta))^{1/2}\cos(\Delta\Omega t - \chi_{ref_x}). \tag{4.21}$$

An amplitude modulated or AM signal is one in which the amplitude of a carrier signal $\cos\omega_c t$, is modulated by a signal at a lower frequency. The simplest AM signal is one in which the modulation takes the form of a sinusoid and can be represented as follows,

$$S_{AM} = X(1 + m\cos\omega_m t)\cos\omega_c t \tag{4.22}$$

where ω_c, ω_m are the carrier and modulation frequencies respectively, X a constant and m the modulation index. AM signals with various values of m are plotted in Fig. 4.3. The modulation goes to zero for $m = 0$ and the signal is 100% modulated with $m = 1$. If

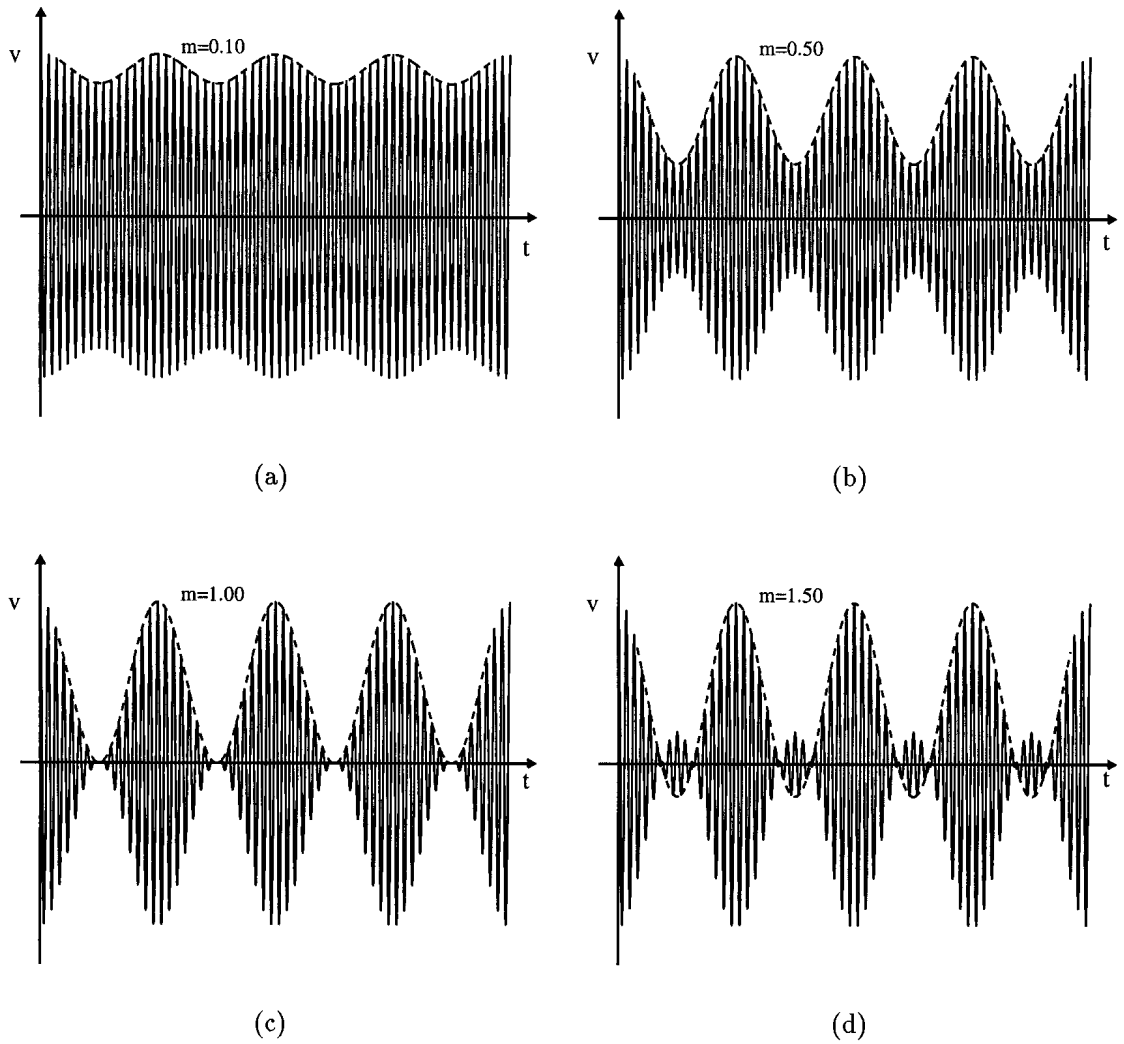

Figure 4.3: Simulated amplitude modulated (AM) signals with $\omega_c/\omega_m = 15$ for various values of modulation index showing (a) 10% modulation ($m = 0.1$), (b) 50% modulation ($m = 0.5$), (c) 100% modulation signal ($m = 1$) and (d) an over-modulated signal ($m = 1.5$). The modulation waveforms are also shown (dashed lines).

$m > 1$ the modulation waveform is negative for part of the cycle, as seen in Fig. 4.3(d) and the signal is said to be overmodulated. The recovery of the modulation waveform from an overmodulated signal would require complex detection circuitry.

The signal given in Eqn. 4.21 is equivalent to an AM signal since the frequency shift $\Delta\Omega$, of the LO is set to be at least an order of magnitude greater than the rotation frequency ω_r, of the $\lambda/2$ plate. The modulation in this case is not purely sinusoidal and is given by $(1 + \cos 2\delta \cos(4\omega_r t - 2\delta))^{1/2}$.

Now introducing the plasma effects, namely a phase shift Φ, due to the plasma density and an additional rotation Ψ, of the polarisation (Faraday rotation) into the probing beam we obtain,

$$\begin{aligned}\begin{bmatrix} E_{probe_x} \\ E_{probe_y} \end{bmatrix} &= \begin{bmatrix} \cos\Psi & -\sin\Psi \\ \sin\Psi & \cos\Psi \end{bmatrix} \begin{bmatrix} Ae^{i(\omega t+\Phi)}[\cos(2\omega_r t-\delta)\cos\delta - i\sin(2\omega_r t-\delta)\sin\delta] \\ Ae^{i(\omega t+\Phi)}[\sin(2\omega_r t-\delta)\cos\delta + i\cos(2\omega_r t-\delta)\sin\delta] \end{bmatrix} \\ &= \begin{bmatrix} Ae^{i(\omega t+\Phi)}[\cos(2\omega_r t-\delta+\Psi)\cos\delta - i\sin(2\omega_r t-\delta+\Psi)\sin\delta] \\ Ae^{i(\omega t+\Phi)}[\sin(2\omega_r t-\delta+\Psi)\cos\delta + i\cos(2\omega_r t-\delta+\Psi)\sin\delta] \end{bmatrix}. \end{aligned} \tag{4.23}$$

Any additional ellipticity due to plasma birefringence has been neglected. This beam can also be represented as,

$$\begin{bmatrix} E_{probe_x} \\ E_{probe_y} \end{bmatrix} = \begin{bmatrix} \frac{A}{\sqrt{2}}(1 + \cos 2\delta \cos(4\omega_r t - 2\delta + 2\Psi))^{1/2} e^{i(\omega t+\Phi+\chi_{plasx})} \\ \frac{A}{\sqrt{2}}(1 - \cos 2\delta \cos(4\omega_r t - 2\delta + 2\Psi))^{1/2} e^{i(\omega t+\Phi+\chi_{plasy})} \end{bmatrix} \tag{4.24}$$

where,

$$\chi_{plasx} = -\tan^{-1}(\tan\delta \tan(2\omega_r t - \delta + \Psi)) \tag{4.25}$$

$$\chi_{plasy} = \tan^{-1}(\tan\delta / \tan(2\omega_r t - \delta + \Psi)). \tag{4.26}$$

This beam is then combined with the LO and passed through a polariser. The resulting beam incident on the plasma detector is therefore,

$$\begin{bmatrix} E_{plas_x} \\ E_{plas_y} \end{bmatrix} = \begin{bmatrix} \frac{A}{\sqrt{2}}(1 + \cos 2\delta \cos(4\omega_r t - 2\delta + 2\Psi))^{1/2} e^{i(\omega t+\Phi+\chi_{plasx})} + Ee^{i(\omega+\Delta\Omega)t} \\ 0 \end{bmatrix}. \tag{4.27}$$

The detected signal, again after bandpass filtering around $\Delta\Omega$, is proportional to,

$$S_{plas} = AE(1 + \cos 2\delta \cos(4\omega_r t - 2\delta + 2\Psi))^{1/2} \cos(\Delta\Omega t - \Phi - \chi_{plasx}) \tag{4.28}$$

which is again equivalent to an AM signal where the carrier signal $\cos(\Delta\Omega t - \Phi - \chi_{plasx})$, is modulated by the lower frequency $(1 + \cos 2\delta \cos(4\omega_r t - 2\delta + 2\Psi))^{1/2}$ term.

4.3.1 Polarimeter

The polarimeter data can be extracted by demodulating the signals. This is performed by passing the signals through a basic demodulator, consisting of diode and an RC circuit (see Section 4.5.1), resulting in signals proportional to,

$$S_{ref_p} = (1 + \cos 2\delta \cos(4\omega_r t - 2\delta))^{1/2} \tag{4.29}$$

$$S_{plas_p} = (1 + \cos 2\delta \cos(4\omega_r t - 2\delta + 2\Psi))^{1/2}. \tag{4.30}$$

The $\lambda/4$ plate is set such that $\cos 2\delta < 1$ and the square root can be expanded giving,

$$\begin{aligned} S_{ref_p} &= 1 + \frac{\cos 2\delta}{2} \cos(4\omega_r t - 2\delta) - \frac{\cos^2 2\delta}{8} \cos^2(4\omega_r t - 2\delta) + \cdots \\ &= 1 + \frac{\cos 2\delta}{2} \cos(4\omega_r t - 2\delta) - \frac{\cos^2 2\delta}{16} \cos(8\omega_r t - 4\delta) + \cdots \end{aligned} \tag{4.31}$$

$$\begin{aligned} S_{plas_p} &= 1 + \frac{\cos 2\delta}{2} \cos(4\omega_r t - 2\delta + 2\Psi) - \frac{\cos^2 2\delta}{8} \cos^2(4\omega_r t - 2\delta + 2\Psi) + \cdots \\ &= 1 + \frac{\cos 2\delta}{2} \cos(4\omega_r t - 2\delta + 2\Psi) - \frac{\cos^2 2\delta}{16} \cos(8\omega_r t - 4\delta + 4\Psi) + \cdots \end{aligned} \tag{4.32}$$

These signals are then band-pass filtered around $4\omega_r$ resulting in signals proportional to,

$$S_{ref_p} = \frac{\cos 2\delta}{2} \cos(4\omega_r t - 2\delta) \tag{4.33}$$

$$S_{plas_p} = \frac{\cos 2\delta}{2} \cos(4\omega_r t - 2\delta + 2\Psi). \tag{4.34}$$

The phase difference 2Ψ, between the two signals can then be determined. A simulated time history of the polarimeter waveforms and the corresponding detected and demodulated waveforms are shown in Fig. 4.4.

4.3.2 Interferometer

The interferometer information is determined by measuring the phase shift between the carrier signals which are proportional to,

$$S_{ref_i} = \cos(\Delta\Omega t - \chi_{refx}) \tag{4.35}$$

$$S_{plas_i} = \cos(\Delta\Omega t - \Phi - \chi_{plasx}). \tag{4.36}$$

It can be seen that the density measurement is corrupted by an additional time-varying phase term which is superimposed on the required interferometer data Φ. This term can

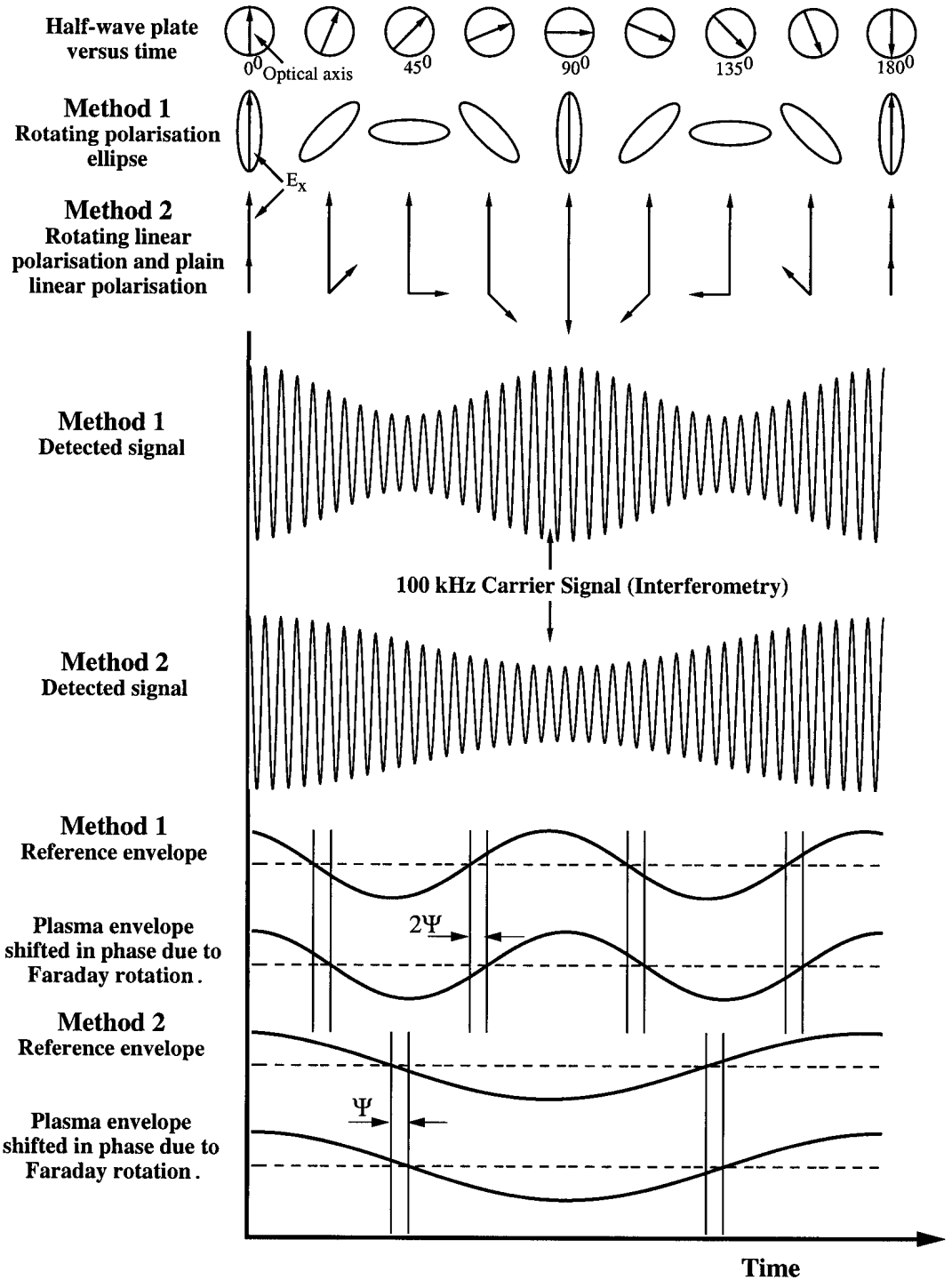

Figure 4.4: A graphical representation of the two methods showing simulated time histories of the polarimeter waveforms for a 180^0 rotation of the $\lambda/2$ plate. The polarisations are rotated by the plasma resulting in the phase shifts of the modulation envelopes.

be expressed as[27],

$$\begin{aligned}\Delta\Phi &= \chi_{plasx} - \chi_{refx} \\ &= -\arctan[\tan\delta\tan(2\omega_r t - \delta + \Psi)] + \arctan[\tan\delta\tan(2\omega_r t - \delta)] \end{aligned} \quad (4.37)$$

where $\tan\delta$ is a measure of the ellipticity of the FIR beam. This term becomes significant for large Faraday rotation angles and large ellipticities of the polarisation of the probing beam. It should be noted that this term does not represent a plasma effect but is an artefact of the rotating polarisation technique itself. The underlying physics behind this term has been discussed by Rommers et al.[28].

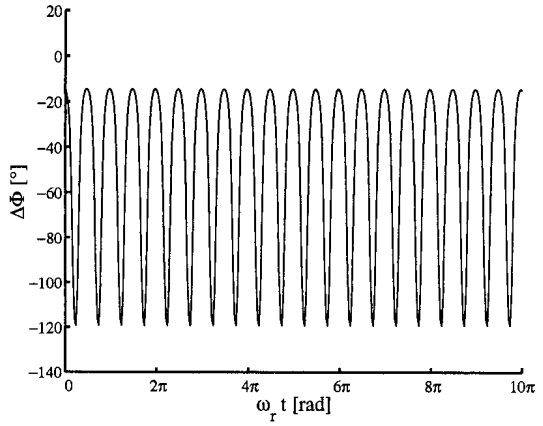

Figure 4.5: The calculated time dependence of $\Delta\Phi$ with $\Psi = 50^o$ and $\delta = 15^o$.

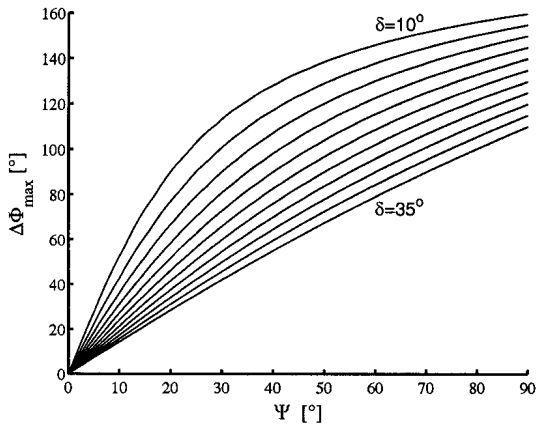

Figure 4.6: The maximum of $\Delta\Phi$ as a function of Ψ with $\delta = 10^o - 35^o$ in steps of 2.5^o.

A typical calculated time trace of this term is shown in Fig. 4.5 for a Faraday rotation of 50^0 and a modulation index of 0.58 ($\delta = 15^0$). From similar calculations a plot is provided in Fig. 4.6 of the maximum of this additional term as a function of Faraday rotation for various modulation depths.

This extra term can be effectively removed by low-pass filtering the interferometer data with the subsequent loss of time resolution. Systems with two separate lasers for the probe beam and LO can, in principle, provide a time resolution which is determined by the difference in frequency between the two lasers, usually in the order of MHz. This excellent time resolution is lost by the necessity to low-pass filter at a frequency close to that of the rotating polarisation ellipse, usually of the order of some kHz.

Rather complex computational methods can also be employed to reconstruct the correct interferometer data once the Faraday rotation angle and the ellipticity of polarisation

have been determined. It was therefore proposed to also install a modification of this method on TCV. The modified scheme (Method 2) incorporates the essential features of the original method but does not contain any additional time-dependent phase terms[29]. Accordingly the interferometer time resolution, which is set by the frequency shift of the LO, can be preserved.

4.4 Method 2

The polarisation modulation technique used in this method requires a rotating linearly polarised beam of amplitude A, produced by passing a linearly polarised beam $E_{0x} = Ae^{i\omega t}$ through a rapidly rotating $\lambda/2$ plate,

$$\begin{aligned}\begin{bmatrix} E_{A_x} \\ E_{A_y} \end{bmatrix} &= \begin{bmatrix} \cos 2\omega_r t & -\sin 2\omega_r t \\ \sin 2\omega_r t & \cos 2\omega_r t \end{bmatrix} \begin{bmatrix} Ae^{i\omega t} \\ 0 \end{bmatrix} \\ &= \begin{bmatrix} Ae^{i\omega t}\cos 2\omega_r t \\ Ae^{i\omega t}\sin 2\omega_r t \end{bmatrix} \end{aligned} \tag{4.38}$$

and a plain linearly polarised beam of amplitude B,

$$\begin{bmatrix} E_{B_x} \\ E_{B_y} \end{bmatrix} = \begin{bmatrix} Be^{i(\omega t+\phi_0)} \\ 0 \end{bmatrix} \tag{4.39}$$

where ϕ_0 is the phase difference between the rotating beam and the linearly polarised beam. These two beams combine to form the probing beam,

$$\begin{bmatrix} E_{probe_x} \\ E_{probe_y} \end{bmatrix} = \begin{bmatrix} E_{A_x} \\ E_{A_y} \end{bmatrix} + \begin{bmatrix} E_{B_x} \\ E_{B_y} \end{bmatrix} = \begin{bmatrix} Ae^{i\omega t}\cos 2\omega_r t + Be^{i(\omega t+\phi_0)} \\ Ae^{i\omega t}\sin 2\omega_r t \end{bmatrix}. \tag{4.40}$$

The LO is again a frequency shifted linearly polarised beam,

$$\begin{bmatrix} E_{LO_x} \\ E_{LO_y} \end{bmatrix} = \begin{bmatrix} Ee^{i(\omega+\Delta\Omega)t} \\ 0 \end{bmatrix}. \tag{4.41}$$

The beam incident on the reference detector is the combination of the probing beam and the LO which have been passed though a polariser in order to transmit only the radiation parallel to that of the LO,

$$\begin{bmatrix} E_{ref_x} \\ E_{ref_y} \end{bmatrix} = \begin{bmatrix} Ae^{i\omega t}\cos 2\omega_r t + Be^{i(\omega t+\phi_0)} + Ee^{i(\omega+\Delta\Omega)t} \\ 0 \end{bmatrix}. \tag{4.42}$$

The resultant intensity is given by,

$$\begin{aligned} I_{ref} &= E_{ref_x}E^*_{ref_x} + E_{ref_y}E^*_{ref_y} \\ &= \frac{A^2}{2} + B^2 + E^2 + 2AB\cos\phi_0\cos 2\omega_r t + \frac{A^2}{2}\cos 4\omega_r t \\ &\quad +2AE\cos 2\omega_r t\cos\Delta\Omega t + 2BE\cos(\Delta\Omega t - \phi_0). \end{aligned} \tag{4.43}$$

The detector signal is bandpass filtered around the difference frequency $\Delta\Omega$ resulting in a signal proportional to,

$$S_{ref} = AE\cos 2\omega_r t\cos\Delta\Omega t + BE\cos(\Delta\Omega t - \phi_0). \tag{4.44}$$

The presence of the ϕ_0 term introduces an extra phase term in the measured data. Dc blocking and appropriate filtering of the detector signal (Eqn. 4.43) can extract the low-frequency term which is proportional to,

$$S_{f_{low}} = AB\cos\phi_0\cos 2\omega_r t. \tag{4.45}$$

By adjusting the optical path length of the non-rotating beam to maximise this signal the ϕ_0 term will be set to a multiple of π. This fine adjustment is undertaken using a precision micrometer driven translator. Under this condition the filtered signal (Eqn. 4.44) can be represented as being proportional to,

$$S_{ref} = BE\cos\Delta\Omega t\left(1 + \frac{A}{B}\cos 2\omega_r t\right). \tag{4.46}$$

This is equivalent to the basic sinusoidally modulated AM signal given by Eqn. 4.22 with the modulation index given by $m = A/B$.

The plasma probing beam undergoes a plasma induced phase shift Φ, while the Faraday effect causes a rotation Ψ, of its polarisation resulting in,

$$\begin{aligned}\begin{bmatrix} E_{probe_x} \\ E_{probe_y} \end{bmatrix} &= \begin{bmatrix} \cos\Psi & -\sin\Psi \\ \sin\Psi & \cos\Psi \end{bmatrix}\begin{bmatrix} Ae^{i(\omega t+\Phi)}\cos 2\omega_r t + Be^{i(\omega t+\Phi+\phi_0)} \\ Ae^{i(\omega t+\Phi)}\sin 2\omega_r t \end{bmatrix} \\ &= \begin{bmatrix} Ae^{i(\omega t+\Phi)}\cos\Psi\cos 2\omega_r t - Ae^{i(\omega t+\Phi)}\sin\Psi\sin 2\omega_r t \\ +Be^{i(\omega t+\Phi+\phi_0)}\cos\Psi \\ Ae^{i(\omega t+\Phi)}\sin\Psi\cos 2\omega_r t + Ae^{i(\omega t+\Phi)}\cos\Psi\sin 2\omega_r t \\ +Be^{i(\omega t+\Phi+\phi_0)}\sin\Psi \end{bmatrix}.\end{aligned} \tag{4.47}$$

Therefore, the incident beam on the plasma detector, again having passed through a polariser is,

$$\begin{bmatrix} E_{plas_x} \\ E_{plas_y} \end{bmatrix} = \begin{bmatrix} Ae^{i(\omega t+\Phi)}\cos\Psi\cos 2\omega_r t - Ae^{i(\omega t+\Phi)}\sin\Psi\sin 2\omega_r t \\ +Be^{i(\omega t+\Phi+\phi_0)}\cos\Psi + Ee^{i(\omega+\Delta\Omega)t)} \\ 0 \end{bmatrix}. \tag{4.48}$$

The resulting intensity on the detector is,

$$\begin{aligned} I_{plas} &= \frac{A^2\cos^2\Psi}{2} + \frac{A^2\sin^2\Psi}{2} + B^2\cos^2\Psi + E^2 \\ &\quad +2AB\cos^2\Psi\cos\phi_0\cos 2\omega_r t - 2AB\cos\Psi\sin\Psi\cos\phi_0\sin 2\omega_r t \end{aligned}$$

$$+\frac{A^2\cos^2\Psi}{2}\cos 4\omega_r t - \frac{A^2\sin^2\Psi}{2}\cos 4\omega_r t$$
$$+2AE\cos\Psi\cos 2\omega_r t\cos(\Delta\Omega t-\Phi) - 2AE\sin\Psi\sin 2\omega_r t\cos(\Delta\Omega t-\Phi)$$
$$+2BE\cos\Psi\cos(\Delta\Omega t-\Phi-\phi_0) \quad (4.49)$$

after bandpass filtering a signal proportional to,

$$\begin{aligned} S_{plas} &= AE\cos\Psi\cos 2\omega_r t\cos(\Delta\Omega t-\Phi) - AE\sin\Psi\sin 2\omega_r t\cos(\Delta\Omega t-\Phi) \\ &\quad +BE\cos\Psi\cos(\Delta\Omega t-\Phi-\phi_0) \\ &= AE\cos(2\omega_r t+\Psi)\cos(\Delta\Omega t-\Phi)+BE\cos\Psi\cos(\Delta\Omega t-\Phi-\phi_0) \end{aligned} \quad (4.50)$$

is obtained. If ϕ_0 can be set to zero this reduces to,

$$S_{plas} = BE\cos\Psi\cos(\Delta\Omega t-\Phi)\left(1+\frac{A}{B\cos\Psi}\cos(2\omega_r t+\Psi)\right). \quad (4.51)$$

4.4.1 Polarimeter

As for Method 1 the detected signals are AM signals where the demodulated signals are proportional to,

$$S_{ref_p} = \frac{A}{B}\cos(2\omega_r t) \quad (4.52)$$

$$S_{plas_p} = \frac{A}{B\cos\Psi}\cos(2\omega_r t+\Psi). \quad (4.53)$$

The polarimeter data Ψ, can then be extracted from the phase shift of the demodulated plasma signal with respect to that of the reference signal. A simulated time history of the polarimeter waveform and the resulting detected and demodulated signals are shown in Fig. 4.4.

The modulation indices (see Eqn. 4.22) for the reference and plasma signals are given by A/B and $A/B\cos\Psi$ respectively. Ideally these ratios should be kept below unity. If the modulation indices exceed unity the signals are said to be overmodulated and additional polarimeter phase terms are introduced. To prevent this the ratio of B to A should be set to an appropriate value to avoid overmodulation for all expected values of Faraday rotation.

4.4.2 Interferometer

The carrier signals are proportional to,

$$S_{ref_i} = BE\cos\Delta\Omega t \quad (4.54)$$

$$S_{plas_i} = BE\cos\Psi\cos(\Delta\Omega t-\Phi) \quad (4.55)$$

and have no time-varying phase shifts other than the desired interferometer data Φ.

4.4.3 Non-idealities

Certain assumptions were made in the previous section to facilitate the derivation of the interferometer/polarimeter detected signals and the information which can be extracted from them. The main assumption was that the phase difference ϕ_0 between the **A** and **B** beams had been set to a multiple of π. This can be performed by adjusting the path length of the **B** beam to maximise the term given by Eqn. 4.45. However, it is worthwhile investigating the effect of this term to determine the precision required in the adjustment of this path length.

The second assumption made was that the beamsplitter used to combine the **A** and **B** beams was polarisation insensitive. As will be discussed in Section 6.2.2 the metallic mesh beamsplitters, used throughout the system, are polarisation insensitive at zero incidence but become increasingly polarisation sensitive with increasing angle of incidence. It is often not possible, geometrically, to use small angles of incidence so beamsplitters designed to be polarisation insensitive for specific wavelengths and angles of incidence must be used. On the TCV interferometer/polarimeter an asymmetric mesh designed for a wavelength of 195 μm and an angle of incidence of 45° was used. This mesh is not 100% polarisation insensitive at the operating wavelength of 214.6 μm, the difference between the measured power transmission of the two polarisations being about 6% (see Section 6.2.2). Therefore, some analysis of the effect of this mesh is required.

Non-zero phase difference between the A and B beams

Consider the equations for the signals on the reference and plasma detectors given by Eqn. 4.44 and 4.50 respectively, namely,

$$\begin{aligned} S_{ref} &= AE\cos 2\omega_r t\cos\Delta\Omega t + BE\cos(\Delta\Omega t - \phi_0) \\ S_{plas} &= AE\cos(2\omega_r t + \Psi)\cos(\Delta\Omega t - \Phi) + BE\cos\Psi\cos(\Delta\Omega t - \Phi - \phi_0). \end{aligned}$$

Using the relation,

$$a_1\cos(\omega t - \alpha_1) + a_2\cos(\omega t - \alpha_2) = X\cos(\omega t - \delta) \tag{4.56}$$

where,

$$X^2 = a_1^2 + a_2^2 + 2a_1a_2cos(\alpha_1 - \alpha_2) \quad 4.56(a)$$

$$\delta = \tan^{-1}\left(\frac{a_1\sin\alpha_1 + a_2\sin\alpha_2}{a_1\cos\alpha_1 + a_2\cos\alpha_2}\right) \quad 4.56(b)$$

these signals can be represented as,

$$S_{ref} = X_{ref}\cos(\Delta\Omega t - \delta_{ref_i}) \quad (4.57)$$

$$S_{plas} = X_{plas}\cos(\Delta\Omega t - \delta_{plas_i}) \quad (4.58)$$

where,

$$X_{ref} = E\left(A^2 cos^2 2\omega_r t + B^2 + 2AB cos 2\omega_r t \cos\phi_0\right)^{1/2} \quad 4.57(a)$$

$$\delta_{ref_i} = \tan^{-1}\left(\frac{B\sin\phi_0}{A\cos 2\omega_r t + B\cos\phi_0}\right) \quad 4.57(b)$$

and

$$X_{plas} = E(A^2\cos^2(2\omega_r t + \Psi) + B^2\cos^2\Psi + 2AB\cos\Psi\cos(2\omega_r t + \Psi)\cos\phi_0)^{1/2} \quad 4.58(a)$$

$$\delta_{plas_i} = \tan^{-1}\left(\frac{A\cos(2\omega_r t + \Psi)\sin\Phi + B\cos\Psi\sin(\Phi + \phi_0)}{A\cos(2\omega_r t + \Psi)\cos\Phi + B\cos\Psi\cos(\Phi + \phi_0)}\right). \quad 4.58(b)$$

The detected interferometer phase shift is given by,

$$\delta_{ref_i} - \delta_{plas_i} = \tan^{-1}\left(\frac{B\sin\phi_0}{A\cos 2\omega_r t + B\cos\phi_0}\right) - \tan^{-1}\left(\frac{A\cos(2\omega_r t + \Psi)\sin\Phi + B\cos\Psi\sin(\Phi + \phi_0)}{A\cos(2\omega_r t + \Psi)\cos\Phi + B\cos\Psi\cos(\Phi + \phi_0)}\right) \quad (4.59)$$

and as can been seen has a time dependency which varies with modulation index (determined by the ratio of A to B) and Faraday rotation.

Simulations of both methods have been employed in order to investigate the effect of various parameters on both the interferometer and polarimeter outputs. In each case the entire system was simulated starting with the matrices representing the initial beams. The plasma effects were then introduced into the probing beam and the detected signals determined. The appropriate demodulation and phase detection was then performed. The ideal case without the effect of the additional terms under investigation was also simulated in order to indicate the accuracy of the calculation.

Plots of the simulated interferometer operation for typical signals with a constant interferometer phase shift of 60^o, Faraday angle of 50^o and $\phi_0 = 10^o$ are shown in Fig. 4.7(a) and (b) for modulation indices of 0.4 and 0.5 respectively. The theoretical phase shifts, calculated from Eqn. 4.59, are also shown and correspond very well with the results of the simulations. The ideal case with $\phi_0 = 0^o$ is also shown. It can be concluded that for correct interferometer operation the ϕ_0 term should indeed be set to a multiple of π. The acceptable precision of ϕ_0 depends on modulation index. Assuming a reasonable

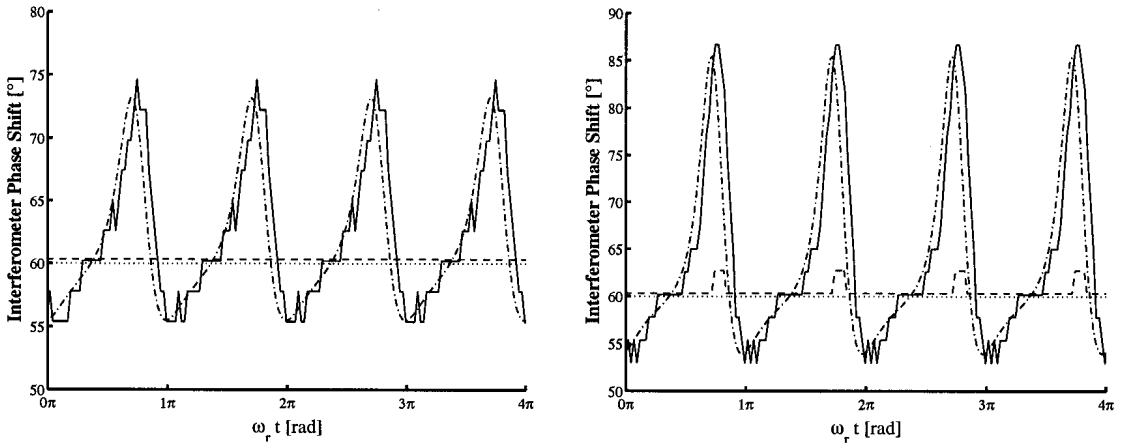

(a) (b)

Figure 4.7: The simulated detected interferometer phase shift for signals with $\Psi = 50^0$, for Φ constant (=60^0, dotted line) with $\phi_0 = 0^o$ (dashed line) and $\phi_0 = 10^o$ (full line) for modulation indices of (a) 0.4 and (b) 0.5. Also shown are the theoretical phase shifts, calculated from Eqn. 4.59 (dot-dashed line).

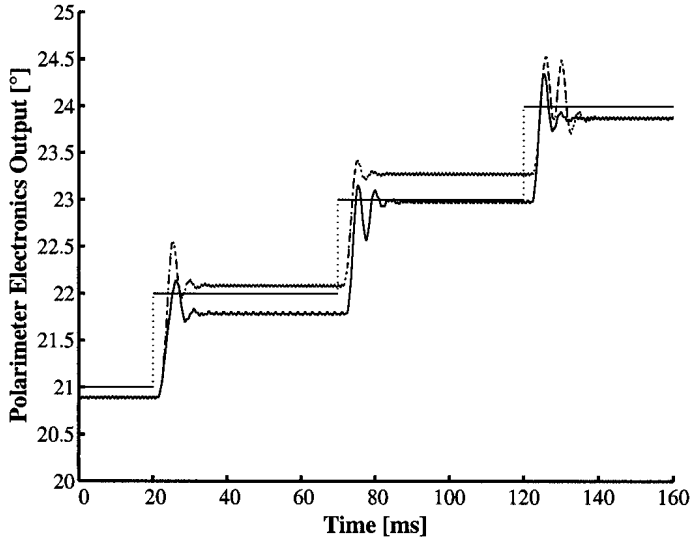

Figure 4.8: The simulated polarimeter electronics outputs for Method 2 with steps of 1^o Faraday rotation (dotted line) for signals with $m = 0.4$ and a constant interferometer phase $\Phi = 60^0$, for $\phi_0 = 0^o$ (dot-dashed line) and $\phi_0 = 20^o$ (full line).

interferometer resolution of 0.05 fringes or about 20° (see Section 3.1), a modulation index of 0.4, for example allows for a precision in ϕ_0 of up to 10° as shown in Fig. 4.7(a) while a modulation index of 0.5 requires a more accurate setting of ϕ_0 as seen in Fig. 4.7(b).

The polarimeter phase output is the phase shift between the signals represented by X_{ref} and X_{plas} (Eqns. 4.57(a) and 4.58(a), respectively). There is not a straightforward expression for this phase shift so simulations were again performed in order to investigate the effect of ϕ_0 on the polarimeter output. The results of a typical simulation are shown in Fig. 4.8 for $\phi_0 = 20°$ and as with previous calculations the results of the ideal case with $\phi_0 = 0°$ are also plotted. There is no obvious time dependent term and any nonlinearities in the response can be accounted for in the calibration of the instrument. The oscillations seen on the outputs after each step in Faraday rotation are simply filtering effects.

Polarisation Sensitive Beamsplitters

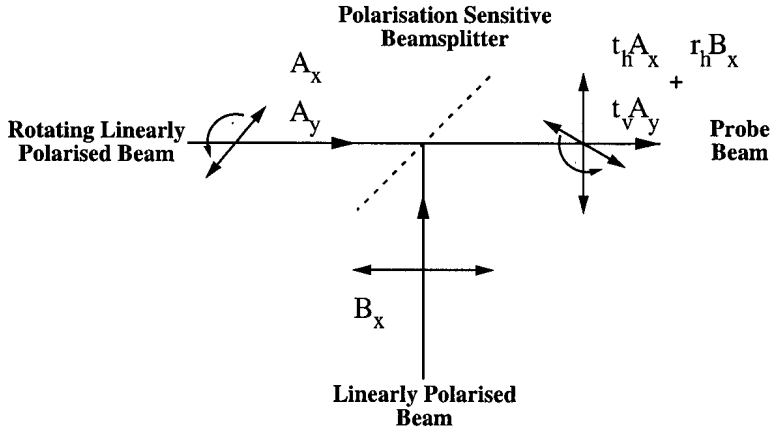

Figure 4.9: A schematic of the beamsplitter used to combine the **A** and **B** beams.

Consider the diagram in Fig. 4.9 showing a schematic of the beamsplitter used to combine the **A** and **B** beams to form the probing beam. The **A** beam is transmitted through the beamsplitter with horizontal and vertical amplitude transmission coefficients t_h and t_v, respectively, while the **B** beam is reflected with a reflection coefficient r_h. This process can be represented by the following Jones matrices,

$$\begin{aligned}\begin{bmatrix} E_{probe_x} \\ E_{probe_y} \end{bmatrix} &= \begin{bmatrix} t_h & 0 \\ 0 & t_v \end{bmatrix} \begin{bmatrix} E_{A_x} \\ E_{A_y} \end{bmatrix} + \begin{bmatrix} r_h & 0 \\ 0 & r_v \end{bmatrix} \begin{bmatrix} E_{B_x} \\ 0 \end{bmatrix} \\ &= \begin{bmatrix} t_h A e^{i\omega t} \cos 2\omega_r t + r_h B e^{i(\omega t + \phi_0)} \\ t_v A e^{i\omega t} \sin 2\omega_r t \end{bmatrix}. \end{aligned} \tag{4.60}$$

The beamsplitting is performed by a metallic mesh (see Section 6.2.2). The phase shifts of the transmitted and reflected waves are functions of the transmission and reflection

coefficients of the mesh and the difference between them is always equal to $\pi/2$[30]. The phase shifts have been omitted here as the transmitted phase forms part of the constant phase offset (see Section 4.1.1) and the reflected phase shift is contained within the ϕ_0 term discussed previously.

It follows that the signal on the reference detector after filtering and setting $\phi_0 = n\pi$ is proportional to,

$$S_{ref} = E\cos\Delta\Omega t\,(r_h B + t_h A\cos 2\omega_r t)\,. \tag{4.61}$$

The corresponding signal on the plasma detector is proportional to,

$$\begin{aligned} S_{plas} = E\cos\Psi\cos(\Delta\Omega t - \Phi)(r_h B\cos\Psi + t_h A\cos\Psi\cos 2\omega_r t \\ -t_v A\sin\Psi\sin 2\omega_r t). \end{aligned} \tag{4.62}$$

The interferometer information is contained within the carrier signals which are proportional to,

$$S_{ref_i} = BE\cos\Delta\Omega t \tag{4.63}$$

and

$$S_{plas_i} = BE\cos\Psi\cos(\Delta\Omega t - \Phi) \tag{4.64}$$

and is unaffected by the non-ideal beamsplitter.

The demodulated signals containing the polarimeter information are proportional to,

$$S_{ref_p} = t_h A\cos 2\omega_r t \tag{4.65}$$

and

$$S_{plas_p} = t_h A\cos\Psi\cos 2\omega_r t - t_v A\sin\Psi\sin 2\omega_r t. \tag{4.66}$$

Using the following expression,

$$a_1\cos(\omega t - \alpha_1) - a_2\sin(\omega t - \alpha_2) = X\cos(\omega t + \delta) \tag{4.67}$$

where,

$$X^2 = a_1^2 + a_2^2 - 2a_1 a_2 sin(\alpha_1 - \alpha_2) \quad 4.67(a)$$

$$\delta = -tan^{-1}\left(\frac{a_1\sin\alpha_1 - a_2\cos\alpha_2}{a_1\cos\alpha_1 + a_2\sin\alpha_2}\right) \quad 4.67(b)$$

Eqn. 4.66 can be expressed as,

$$S_{plas_p} = X_{plas_p}\cos(2\omega_r t - \delta_{plas_p}) \tag{4.68}$$

where,

$$X_{plas_p} = \sqrt{t_h^2 \cos^2 \Psi + t_v^2 \sin^2 \Psi} \quad 4.68(a)$$

$$\delta_{plas_p} = -\tan^{-1}\left(\frac{-t_v}{t_h} \tan \Psi\right). \quad 4.68(b)$$

The Faraday rotation angle can then be extracted from the detected phase using the following expression,

$$\Psi = \tan^{-1}\left(\frac{t_h}{t_v} \tan \delta_{plas_p}\right). \quad (4.69)$$

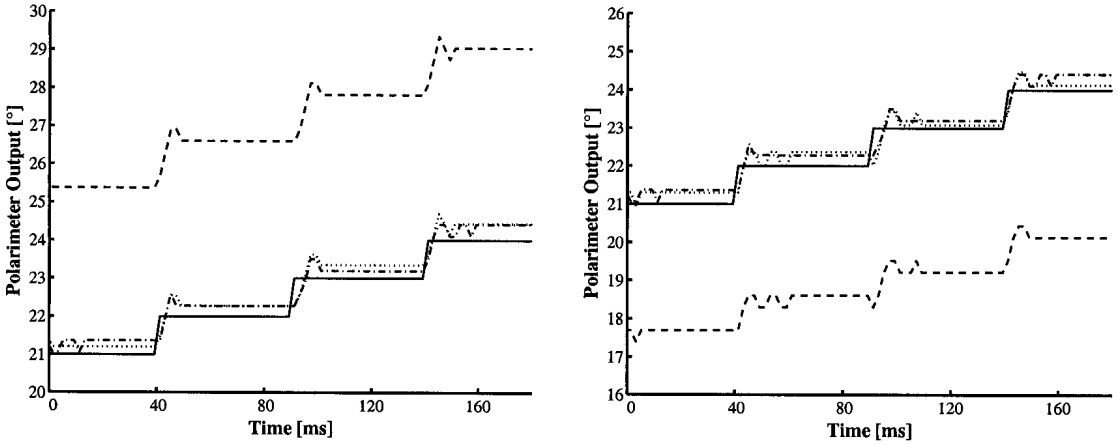

(a) (b)

Figure 4.10: Simulated polarimeter electronics output (dashed line) for steps of 1° Faraday rotation (full line) with (a) $t_h/t_v = 0.82$ and (b) $t_h/t_v = 1.2$. The output for $t_h/t_v = 1$ is also shown (dot-dashed line) along with the corrected output (dotted line).

Simulations were performed of the interferometer/polarimeter operation with polarisation sensitive beamsplitters and the results are presented in Fig. 4.10(a) and (b) for the cases with $t_h/t_v = 0.82$ and $t_h/t_v = 1.2$, respectively. A trace of the output, corrected for the polarisation sensitivity of the mesh using Eqn. 4.69, is also shown and agrees with the input within the precision of the simulation. The results of the ideal case with $t_h/t_v = 1$ are also shown.

Typical calibration curves for t_h/t_v varying from $0.5 \rightarrow 1.5$ are shown in Fig. 4.11(a) with the ideal case of $t_h/t_v = 1$ shown as a dashed line. As can be seen polarisation sensitive meshes produce nonlinear output responses which can be recorded during the calibration of the instrument. A plot is also shown in Fig. 4.11(b) of the relative error in

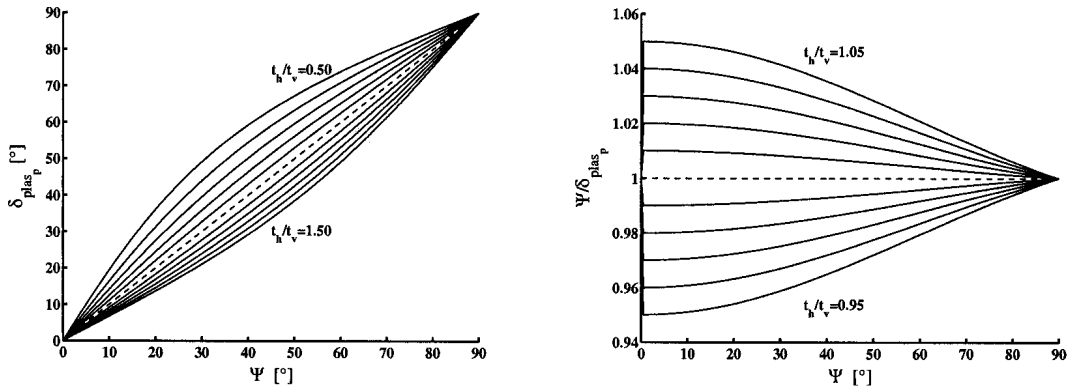

(a) (b)

Figure 4.11: (a) Simulated calibration curves of the polarimeter output for values of t_h/t_v ranging from 0.5 → 1.5 in steps of 0.1 and (b) the relative error in the measured phase δ_{plas_p} as a function of Ψ for t_h/t_v ranging from 0.95 → 1.05 in steps of 0.01. The ideal case with $t_h/t_v = 1$ is presented as a dashed line in both plots.

the measured phase δ_{plas_p}, as a function of Faraday rotation for values of t_h/t_v ranging from 0.95 → 1.05. This can be used to determine the measurement error when a linear response is assumed. The asymmetric mesh used in the TCV interferometer/polarimeter has a value of $t_h/t_v = .97$ (see Section 6.2.2) which results in an maximum error before correction of about 3%.

4.5 Polarimetric Measurement Accuracy

4.5.1 Demodulation

In order to recover the modulation waveform of an AM wave it is necessary to convert the amplitude variations of the wave at the carrier frequency into a signal at the modulation frequency. The most basic demodulator circuit is the peak detector shown in Fig. 4.12(a). During the increasing portion of the positive half cycle of the input v_{AM}, the diode conducts and enough current flows to charge the capacitor up to the value of v_{AM}. Once v_{AM} passes a peak, however, the diode becomes reverse-biased and the voltage on the capacitor discharges with a time constant given by $\tau = RC$, as shown in Fig. 4.12(b). Once the output voltage v_{Env}, drops below that of the input v_{AM}, the diode is once again forward biased and the capacitor is recharged. The result of these alternating periods of charging and discharging is that, with an RC time constant long compared to the carrier

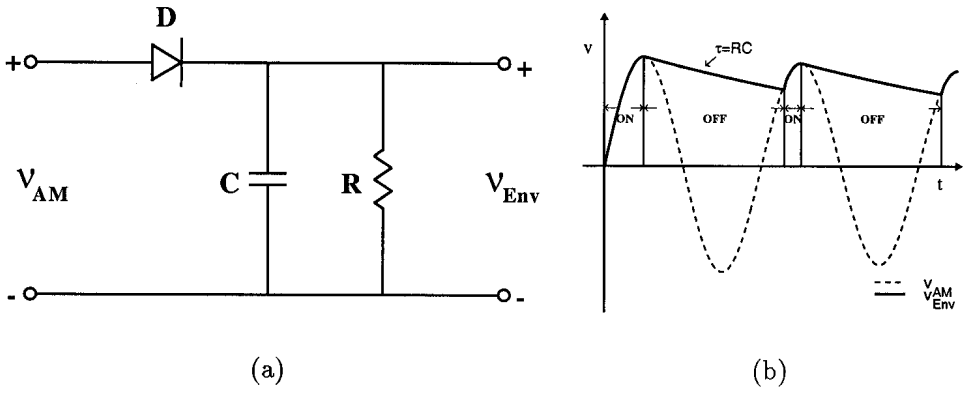

(a) (b)

Figure 4.12: (a) A schematic of the peak detector demodulation circuit and (b) the output waveform v_{Env} for a peak detector driven by an AM wave, v_{AM}.

period, the output voltage remains near the peak voltage of the carrier, hence the name peak detector.

For the case of a peak detector circuit excited by an AM wave the output voltage follows the peaks as they rise and fall with the amplitude modulation as can be seen in Fig. 4.13. The ability of the circuit to follow the peak amplitude depends on how rapidly the amplitude is changing. A typical demodulation scenario is shown in Fig. 4.13(a). The demodulated signal is then filtered to remove the peaks due to the charging of the capacitor. To accurately demodulate the AM wave the carrier frequency should be at least an order of magnitude greater than the modulation frequency. As can be seen in Fig. 4.13(b) when the ratio of carrier frequency to modulation frequency is too low, $f_c/f_m = 5$ in this case compared to $f_c/f_m = 10$ in case (a), the periods of capacitor charging and discharging become more accentuated obscuring the modulation. If the chosen time constant is too large, as in the case of Fig. 4.13(c), the capacitor voltage is above the peaks for a couple of cycles which leads to distortion. The demodulated waveform for a AM signal with a modulation index, $m = 0.2$, compared with $m = 0.4$ in case (a) is shown in Fig. 4.13(d).

4.5.2 Noise Analysis

To show that a high precision measurement of the Faraday rotation angle is possible with a carrier frequency of 100 kHz and a $\lambda/2$ plate rotation frequency of 2 kHz, which is above the maximum attainable spindle frequency (see Section 6.2.4), the two methods were simulated numerically. This rotation frequency produces modulation frequencies of 8 and 4 kHz for Methods 1 and 2 respectively. In each case the ideal plasma and reference

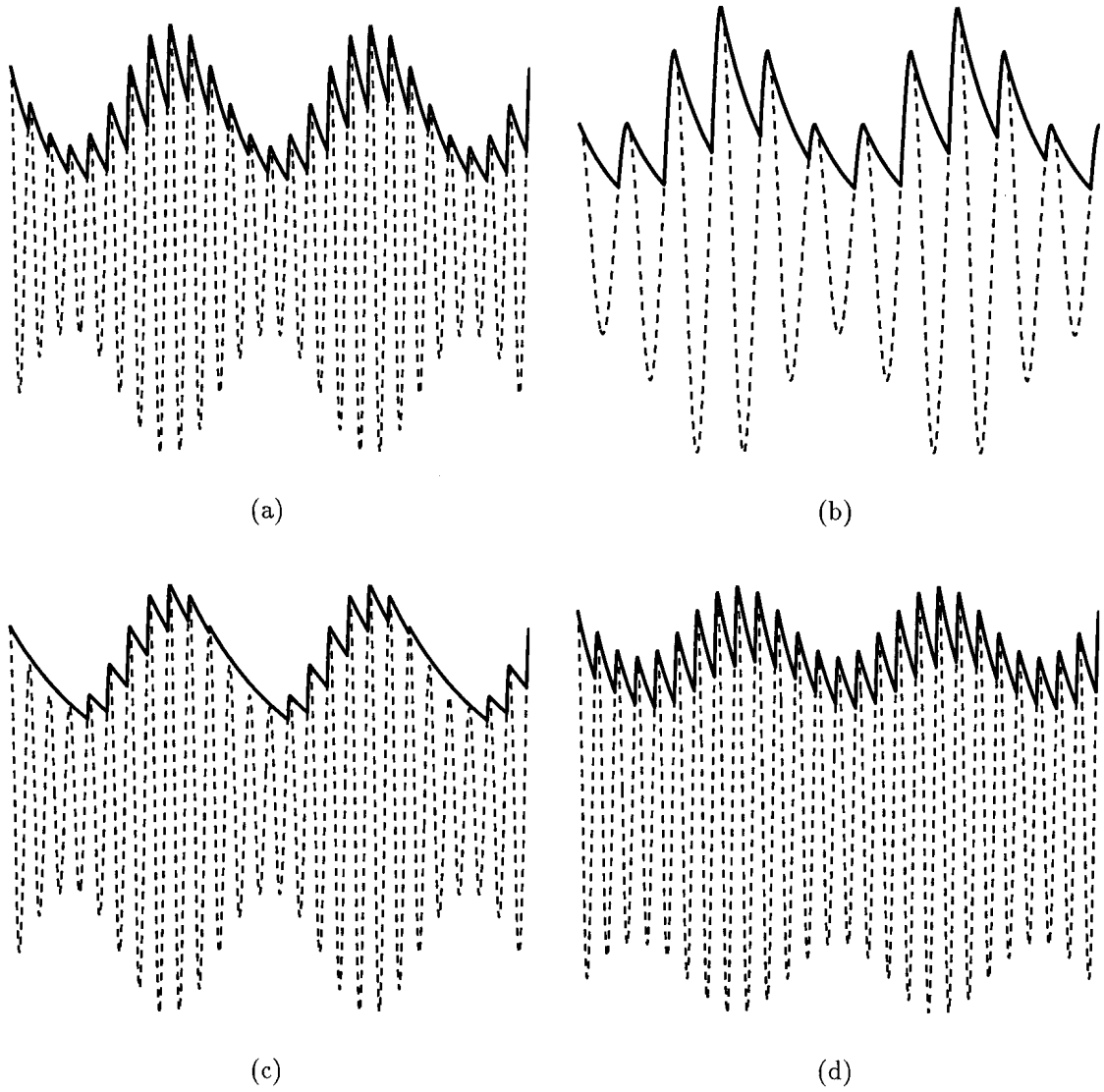

Figure 4.13: The simulated response of the peak detector circuit to (a) an AM waveform with a ratio of carrier to modulation frequency of $f_c/f_m = 10$ a modulation index of $m = 0.4$ and a time constant $\tau = 0.2/f_m$, (b) an AM waveform with $f_c/f_m = 5$, $m = 0.4$ and $\tau = 0.2/f_m$, (c) an AM waveform with $f_c/f_m = 10$, $m = 0.4$ and $\tau = 0.5/f_m$ and (d) an AM waveform with $f_c/f_m = 10$, $m = 0.2$ and $\tau = 0.2/f_m$.

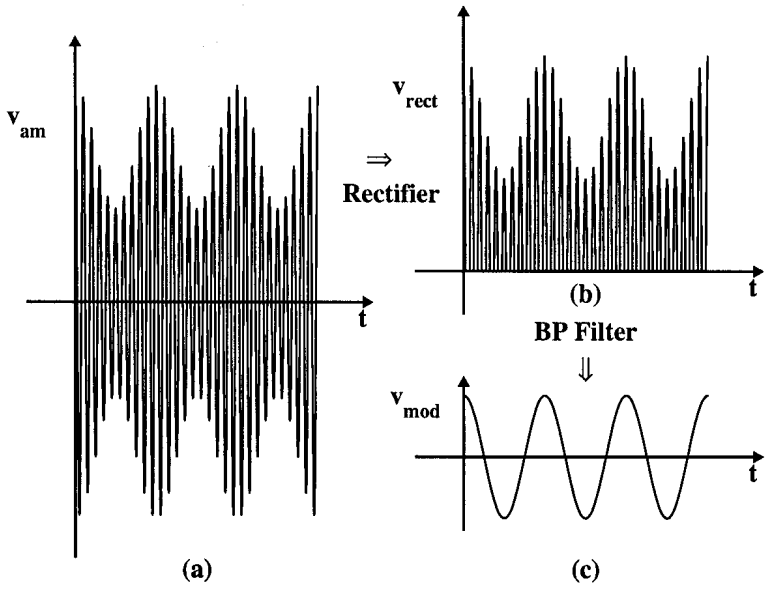

Figure 4.14: An overview of the demodulation process used during the noise analysis. The AM signal is (a) rectified and then (b) band-pass filtered producing the (c) modulation waveform.

signals given by Eqns. 4.21, 4.28 and Eqns. 4.46, 4.51 for Methods 1 and 2 respectively, were calculated and polluted with normally distributed uncorrelated noise. The amplitude of the noise was measured relative to the signal amplitude. The demodulation process as described in Section 4.5.1 can be performed numerically in a slightly different manner by rectifing the signals and then passing them through basic band-pass filters. This has the same effect as a peak detector circuit followed by a low-pass filter but has the advantage of being much easier to simulate. A schematic of this demodulation process is shown in Fig. 4.14. The Faraday rotation can then determined by measuring the phase difference between the zero crossings of the resulting signals.

The results of a series of simulations for Method 1 are shown in Fig. 4.15 and those for Method 2 in Fig. 4.16 where the measurement accuracy is plotted against the imposed noise level. The bandwidths of the band-pass filters in each case is equivalent to half the modulation frequency. The first plot in each figure shows the measurement precision for a range of modulation depths with the Faraday rotation held constant at $\Psi = 20°$. It can be seen that the accuracy of the measurement depends strongly on the modulation depth with the precision increasing with increasing modulation. With a judicious choice of modulation depth noise levels of up to 3% could, therefore, be acceptable for Method 1 and 2% for Method 2. For the latter method the measurement accuracy is, in general, inferior to that of Method 1 in spite of the fact that the modulation frequency is lower

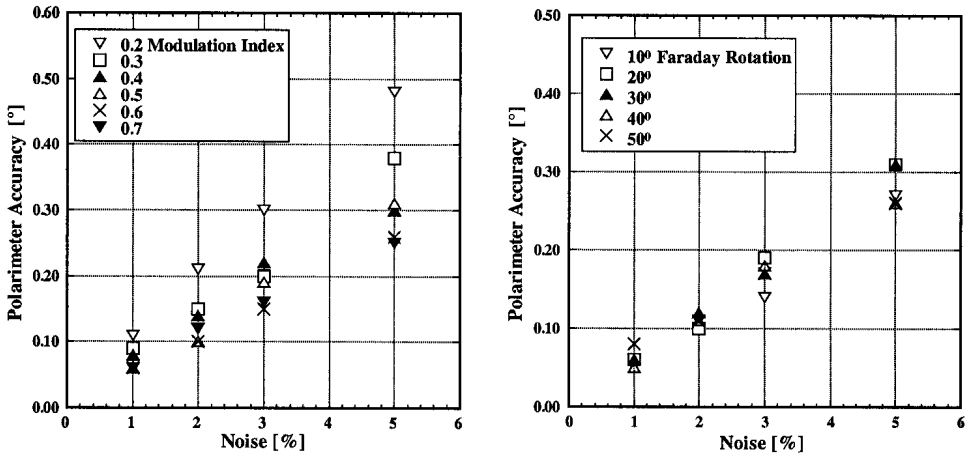

(a) (b)

Figure 4.15: Precision of the simulated Faraday rotation as a function of imposed noise levels for Method 1 with a carrier frequency of 100 kHz, rotation frequency of 2 kHz and a filter bandwidth of 4 kHz for (a) a constant Faraday rotation of 20^0 with varying modulation depths and (b) a constant modulation depth of 0.5 with varying Faraday rotation.

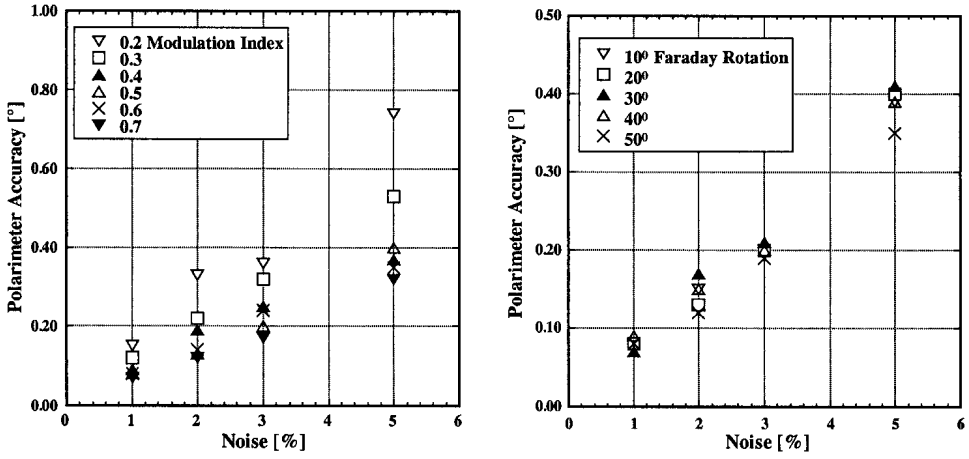

(a) (b)

Figure 4.16: Precision of the simulated Faraday rotation as a function of imposed noise levels for Method 2 with a carrier frequency of 100 kHz, rotation frequency of 2 kHz and a filter bandwidth of 2kHz for (a) a constant Faraday rotation of 20^o with varying modulation depths and (b) a constant modulation depth of 0.5 with varying Faraday rotation.

by a factor of two (see below). This is because Method 2 measures the actual Faraday rotation Ψ while the measurement in Method 1 is 2Ψ.

The second plot in each figure shows the measurement accuracy for a constant modulation depth of 0.5 as the Faraday angle is varied. No obvious trend is apparent for either method.

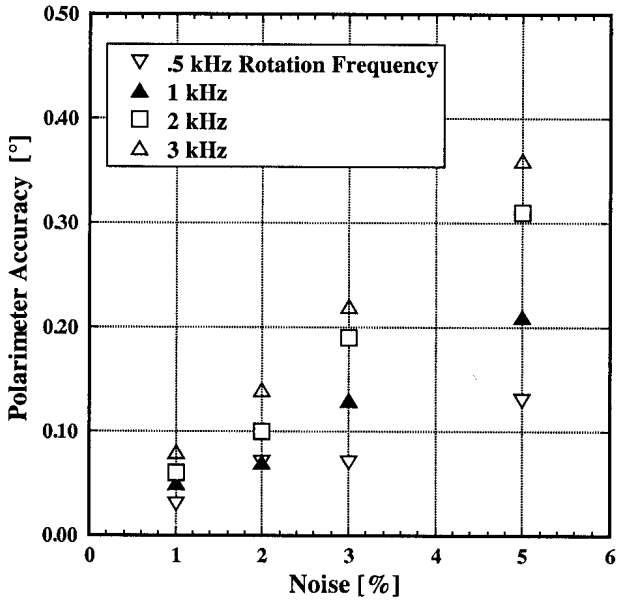

Figure 4.17: Precision of the simulated Faraday rotation as a function of imposed noise levels for Method 1 with a carrier frequency of 100 kHz, a modulation index of 0.5 and filter bandwidths of half the modulation frequency for a constant Faraday rotation of 20° with varying rotation frequencies.

The precision is, in general, slightly better for lower modulation frequencies as can be seen from the results of the simulations plotted in Fig. 4.17. In this case the Faraday rotation and modulation depths were held constant at 20° and 0.5, respectively and the rotation frequency of the spindle varied. The bandwidth of the demodulating filter in each case was set to half the modulation frequency. It can be seen that the measurement accuracy increases with decreasing rotation frequency. The maximum rotation frequency attainable with the rotating spindle was seen to be about 700 Hz (see Section 6.2.4) and consequently the measurement accuracy is expected to be better than that quoted above for a rotation frequency of 2 kHz.

4.6 Conclusions

The two polarimeter/interferometer methods installed on TCV have been described in detail. Method 2 which is a new method is very similar to Method 1 as can be seen graphically in Fig. 4.4. The main differences are as follows; (a) the modulation in Method 2 is a purely cosine variation without higher order harmonics, (b) its modulation frequency is lower by a factor of 2, (c) its measured polarimeter phase shift is the Faraday rotation Ψ, as opposed to 2Ψ and (d) its interferometer phase measurement is not corrupted by additional terms provided $\phi_0 = n\pi$.

Simulations of the measurement accuracy have shown that the required precision of 0.2^o is attainable using the chosen carrier and modulation frequencies with noise levels of up to 2%. This low noise level can be easily achieved with the liquid Helium cooled InSb detectors employed on the TCV interferometer/polarimeter.

The main motivation behind developing Method 2 as an alternative to Method 1 was to avoid the inherent limitation in its interferometer time resolution. This has been achieved with a more complicated optical layout and the loss of some polarimeter precision.

Chapter 5

Bench Tests

An interferometer/polarimeter based on Method 1 has been installed and tested on the MTX tokamak[24]. It has been shown during the theoretical derivation of the method, described in Chapter 4, that a neglected phase term first identified by Geck et al.[27], would significantly reduce the potential time resolution of the interferometer. It was for this reason that an alternative method, known as Method 2, was developed. To confirm the presence of the limiting term, given by Eqn. 4.37, bench tests of both methods were performed in the laboratory. As Method 2 was previously untried it was also deemed advantageous to prove its feasibility as a polarimeter. The bench tests were also used to test the optical components which would be employed on the actual instrument.

5.1 Interferometer Bench Test

The optical arrangement, shown in Fig. 5.1, was set up in UCC and was used initially to directly compare the interferometer operation of Methods 1 and 2. The Edinburgh Instruments laser system produces a 118.8 μm vertically polarised Gaussian beam. After some beam forming mirrors a small fraction of this beam is reflected by a Mylar beamsplitter (9:1 transmission to reflection ratio) towards the rotating half-wave plate which is fixed to the shaft of a turbine driven air-bearing spindle, supplied by Westwind Air Bearings Ltd., to form the **A** beam (see Section 6.2.4). The transmitted beam is further divided by a 2:1 Cu mesh into the **B** (for Method 2 only) and LO beams. This arrangement produces, for Method 2, a ratio between the **A** and **B** beams of 1:3. This ratio produces amplitude modulated (AM) waveforms on the detectors with basic modulation indices of 0.58 (see Eqn. 4.22). With this modulation index the AM signals will only become over-modulated for Faraday rotation angles of over 55^o (see Section 4.4.1). The beamsplitter which recombines the **A** and **B** beams to form the probing beam is the most critical of

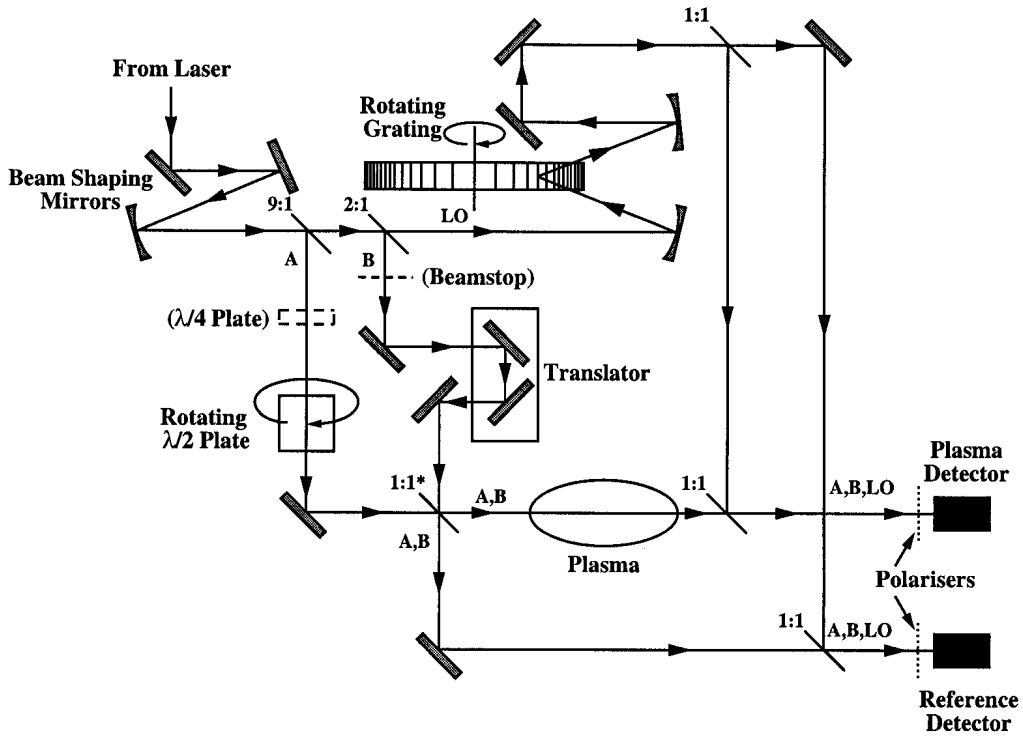

Figure 5.1: Illustration of the optical arrangement used in UCC during the interferometer bench tests.

the beamsplitters. Ideally it should have a 1:1 transmission to reflection ratio for both polarisations to ensure that the transmitted and reflected power of the **A** beam remains constant as its polarisation rotates (see Section 4.4.3). The beamsplitter used during these tests is an asymmetric mesh supplied by Prof. Volkov of the General Physics Institute of the Russian Academy of Sciences. It is polarisation insensitive for 118.8 μm at an angle of incidence of 45°. This mesh also serves to split the probing beam into its plasma and reference arms. The plasma phase shift and the Faraday rotation are simulated using a perspex plate and a precision rotatable half-wave plate, respectively. All the quartz plates were supplied and anti-reflection coated on both sides by Francis Lord Optics, Australia.

The LO beam is focused onto a rotating grating which Doppler shifts its frequency[17] (see Section 6.2.3). The size of the frequency shift, which corresponds to the carrier frequency of the detected signal, can be regulated by adjusting the rotation frequency of the grating. A 1:1 splitter then divides it into its reference and plasma components.

The recombination of the probing beams and the LO is also performed by beamsplitters with 1:1 splitting ratios at 45° for vertical polarisation. Vertical polarisers are also placed in front of each of the Schottky diode detectors to pass only radiation parallel to that of the LO.

The optical setup can be employed to simulate Method 1 by simply inserting a beam-stop in the **B** beam path, as shown, and by introducing a quarter-wave plate into the **A** beam path before the rotating half-wave plate. For the simulations a carrier frequency of 10 kHz, at which frequency the Schottky diode detector responsivity is still reasonably high, and a modulation frequency of 500 Hz corresponding to a mechanical rotation frequency of the spindle of 125 and 250 Hz for Methods 1 and 2, respectively, were adopted.

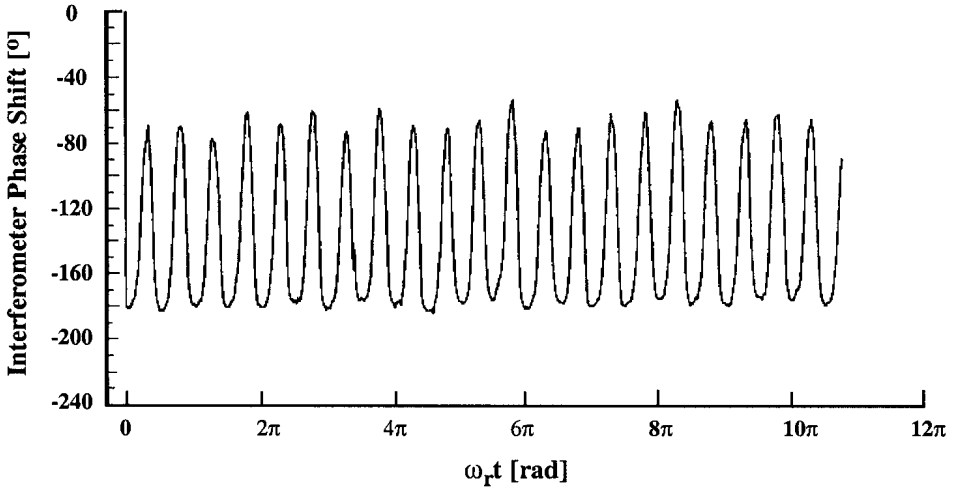

Figure 5.2: The measured interferometer phase shift Φ (set to -180^{o}) for Method 1 showing the inherent time-dependent phase error $\Delta\Phi$, for a Faraday rotation angle of 50^{o} and a modulation depth of 0.59 where ω_r is the rotational frequency of the half-wave plate.

The optical arrangement was initially set to simulate Method 1 and to confirm the presence of its inherent additional interferometer phase term (Eqn. 4.37). The precision half-wave plate was adjusted prior to the measurement to give a constant Faraday rotation of 50^{o} with the quarter-wave plate set to produce an average modulation index of 0.59. Some uncertainty in the modulation index arose from the slightly differing modulation depths of the reference and probe AM waveforms and additional modulation due to the non-uniformity of the rotating grating. In order to measure the interferometric phase shift the detector signals were squared up using high-gain limiting amplifiers to remove the modulation. The resulting signals were then fed into a lock-in amplifier set to produce an output proportional to their relative phase shift. An arbitrary interferometer phase shift of -180^{o} was introduced using the perspex plate. The resulting trace is plotted in Fig. 5.2 and shows the time-dependent phase term which is consistent with expectations (see

Fig. 4.5). From similarly recorded plots a comparison between theory and experiment of the maximum interferometer error in degrees as a function of Faraday rotation is provided in Fig. 5.3. The theoretical maximum was determined by calculating the maximum of Eqn. 4.37. The experimental uncertainty in the phase measurements is about $\pm 5^{\circ}$. It is clear from this plot that the results obtained are quite consistent with the theoretical predictions.

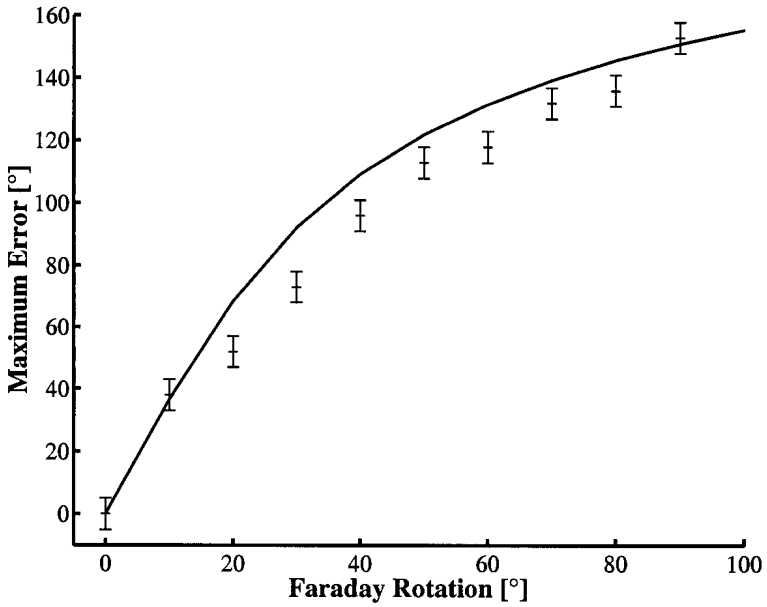

Figure 5.3: Maximum theoretical (full line) and experimental interferometer phase error in Method 1 as a function of Faraday rotation for a modulation depth of 0.59.

Method 2 was then simulated to confirm experimentally the absence of any unwanted interferometer phase terms. The low-frequency term described in Section 4.4 and given by Eqn. 4.45 was maximised by adjusting the translator shown in Fig. 5.1. The precision half-wave plate was then stepped from 0 through 25 mechanical degrees, corresponding to a Faraday rotation of $\Psi = 0^{\circ} \rightarrow 50^{\circ}$. The resulting interferometer phase shift with an arbitrary initial value of 180° is shown plotted in Fig. 5.4 . It can be seen that the phase is not affected by the rotation of the half-wave plate i.e. it is independent of Faraday rotation (see [28]). The noise on the signal again limits the measurement accuracy to $\pm 5^{\circ}$. The absence of additional phase terms in the measured interferometer data implies that a real-time measurement of line-integrated plasma density with a time resolution limited only by the carrier frequency is possible with this method.

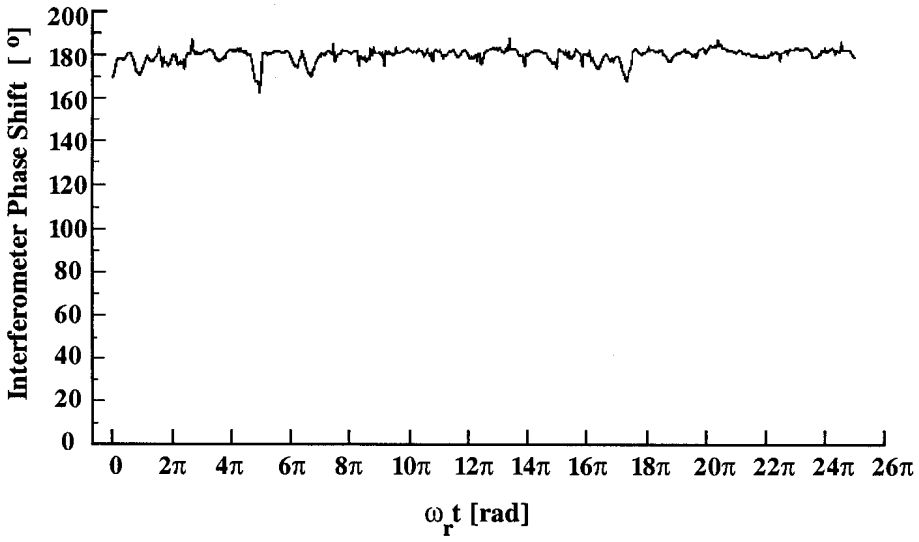

Figure 5.4: The time history of the measured interferometer phase shift Φ (set to 180°) for Method 2 as the Faraday rotation is stepped from $\Psi = 0° \rightarrow 50°$ in steps of 5° where ω_r is the rotational frequency of the half-wave plate.

5.2 Polarimeter Bench Test

In order to avail of the highly sensitive low-noise InSb detectors (see Section 6.4) it was decided to perform the polarimeter bench tests at the CRPP. The tests were also performed at the operating wavelength of 214.6 μm thereby incorporating the testing of some of the optical components which would be be used on the actual instrument. The optical set-up employed during these tests is shown in Fig. 5.5 and is essentially the same as that used during the interferometer tests. The 1:6.5 splitting ratio between the **A** and **B** beams, performed by a 428 lpi mesh, produces AM signals with a basic modulation index of 0.4 and consequently a maximum allowable Faraday rotation angle of 65° (see Section 4.4.1). The quartz plates were anti-reflection coated by QMC Instruments Ltd. and the 1:1 beamsplitters are the Buckbee Mears 300 lpi (MN-36) meshes discussed in Section 6.2.2. The beamsplitter which recombines the **A** and **B** beams to form the probing beam is again an asymmetric mesh supplied by Dr. Volkov which has a design wavelength of 195 μm for an angle of incidence of 45°. This mesh is slightly polarisation sensitive at 214.6μm as discussed in Section 6.2.2. However, the maximum error of 3% associated with the use of this mesh is quite acceptable for the purposes of these tests (see Section 4.4.3).

The carrier and modulation frequencies were set to 100 kHz and 500 Hz, respectively. This carrier frequency is the chosen operating frequency and consequently the center frequency of the filters on the detector pre-amplifiers. The high ratio of carrier to modulation

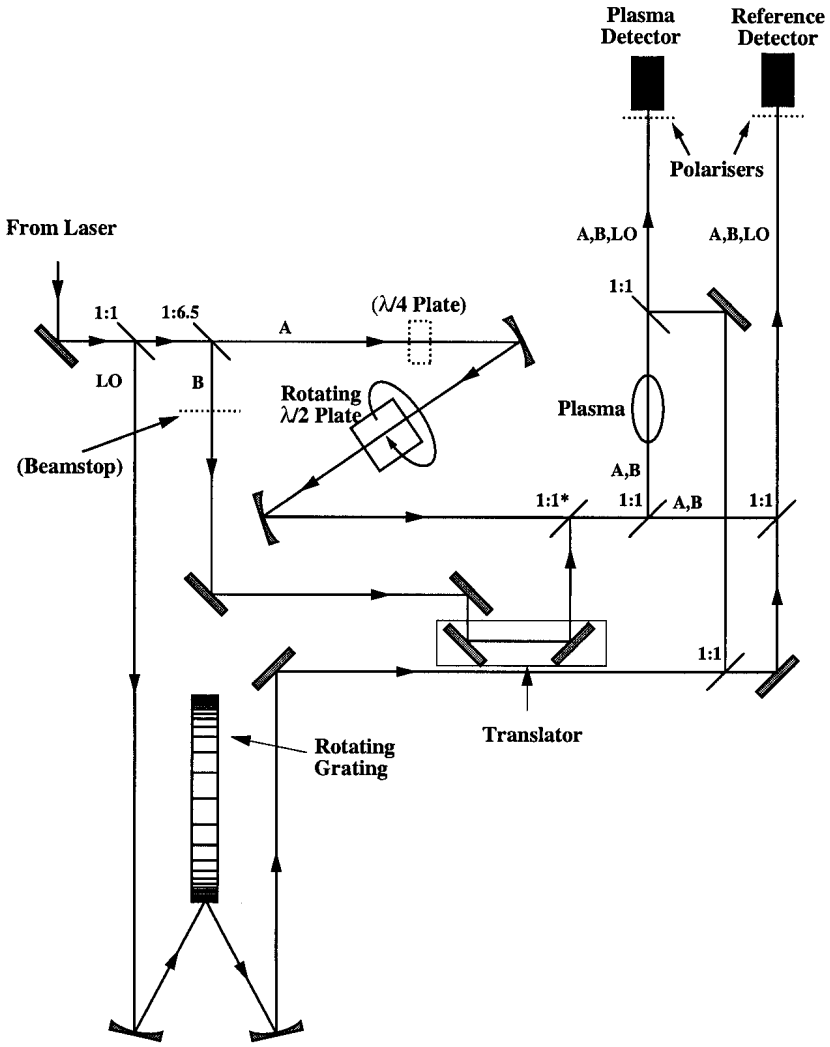

Figure 5.5: Illustration of the optical layout used during the polarimeter bench tests at the CRPP.

frequencies is required for the accurate demodulation of the signals (see Section 4.5). The demodulation was performed electronically using a standard diode-resistor-capacitor arrangement and the resulting signals bandpass filtered (500 Hz $\pm$ 100 Hz). The Faraday rotation Ψ, was then extracted using the phase comparator circuit shown schematically in Fig. 5.6. The circuit is very similar to the TCV polarimeter electronics described in more detail in Section 6.5.2. The filtered demodulated signals were first passed through high-gain amplifiers followed by comparators and then an XOR gate producing a train of pulses with widths proportional to Ψ. The pulse train was then low-pass filtered with a cutoff frequency of 100 Hz. The final output of the polarimeter circuitry is a dc voltage level proportional to Ψ. As the output signal is proportional to the absolute value of the phase difference between the signals an offset in Faraday rotation must be introduced in

order to differentiate between positive and negative phase shifts (see Section 6.5.2).

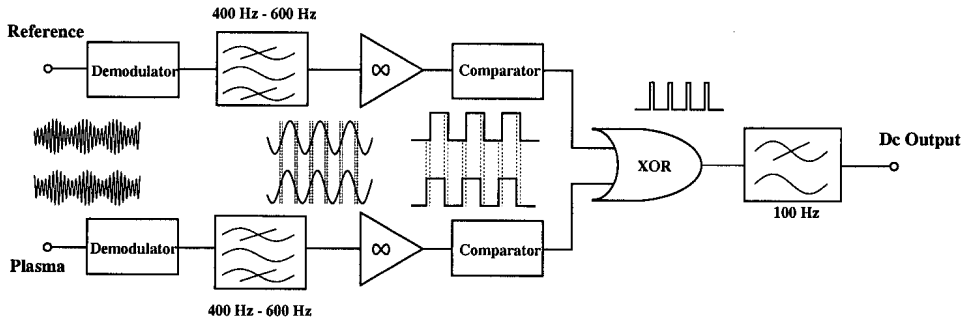

Figure 5.6: Schematic diagram of the polarimeter demodulation and phase comparison electronics.

The optical arrangement was initially configured to simulate Method 1. The achievement of the required polarimeter resolution of 0.2^o (see Section 3.5) was frustrated by the presence of strong fluctuations on the output which limited the resolution to approximately 1.0^o. A typical polarimeter electronics output signal is shown in Fig. 5.7 for Faraday rotation steps of 1.0^o. Spectral analysis of this signal showed the dominant fluctuation to be at the rotation frequency of the grating. A separate experiment was, therefore, performed to assess the grating quality by essentially measuring the localised reflectivity.

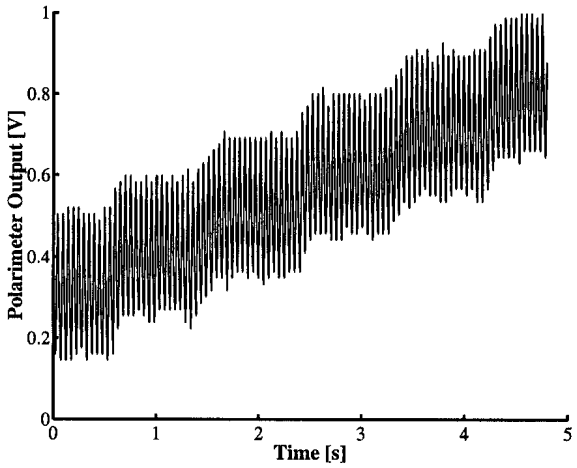

Figure 5.7: Polarimeter electronics output for Method 1 with steps of 1.0^o Faraday rotation using the original grating.

The reflected beam from the grating, rotating at about 0.4 Hz and chopped at 500 Hz, was focused onto a pyroelectric detector and the signal fed into a lock-in amplifier with a time constant of 10 ms. The resulting trace is shown in Fig. 5.8. Considerable variations

in the reflectivity around the circumference of the grating can easily be seen. These variations are a consequence of the manufacturing process where the grating grooves were cut sequentially with the result that possible tooling wear caused localised non-uniformities resulting in poor reflection/diffraction efficiency at these positions. This problem was discussed with Dr. G. Dodel and his colleagues in the Institut für Plasmaforschung at the University of Stuttgart who supplied us with a new grating. The grooves on the replacement grating were machined randomly so as to distribute possible tooling errors in a uniform manner over the entire circumference. The results of a test of this grating, conducted under conditions similar to the previous test, are plotted in Fig. 5.9 and show a substantial improvement over the original.

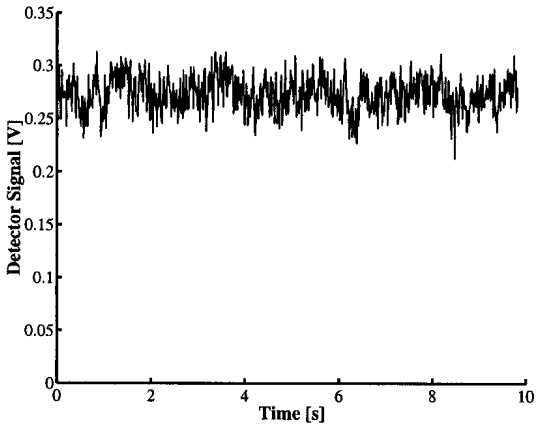

Figure 5.8: Time history of the beam amplitude reflected off the original grating rotating at 0.4 Hz.

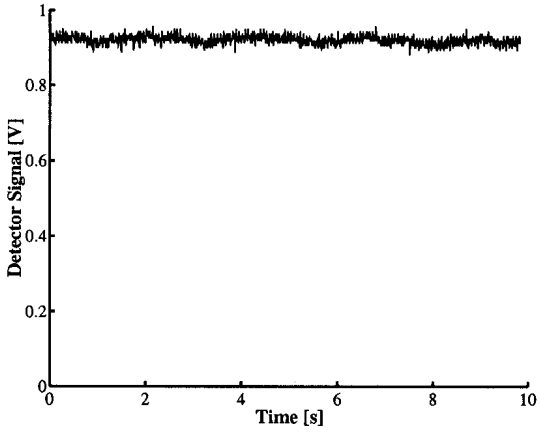

Figure 5.9: Time history of the beam amplitude reflected off the new grating rotating at 0.4 Hz.

Method 1 was again simulated with the new grating in place. A typical experimental output for this setup during which the precision half-wave plate was stepped through steps of 0.05 mechanical degrees, corresponding to a 0.1^o Faraday rotation step, is shown in Fig. 5.10. From this trace we can conclude that the Faraday angle can be measured with an accuracy of approximately 0.05^o or less. A power spectrum analysis showed that the residual noise on the polarimeter was attributed largely to the rotating grating with a smaller contribution from the spindle. To achieve this noise level, good optical alignment and beam overlap were found to be essential. The optimisation of the beam overlap was performed by the adjustment of the shape of the LO beam by tweaking its alignment onto and off the grating using the two spherical focusing mirrors. The grating is a highly asymmetric device and the shape of a beam reflected by it varies considerably with its angles of incidence.

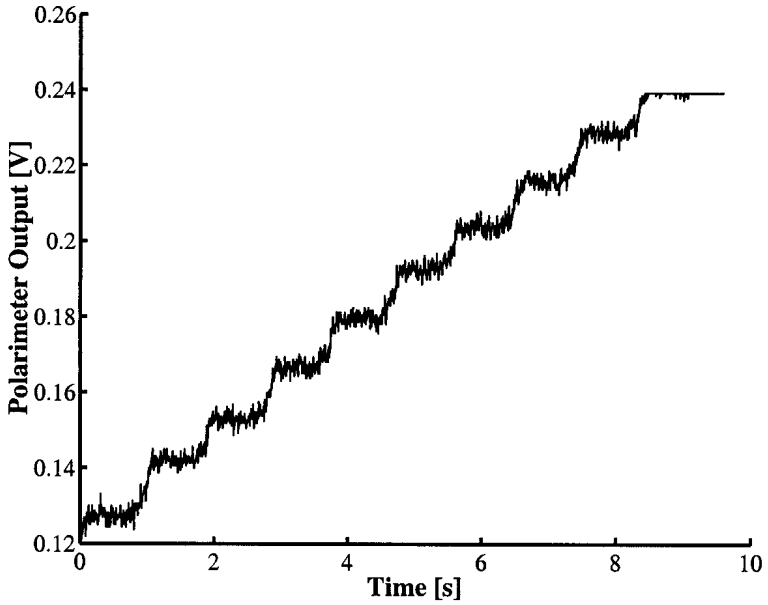

Figure 5.10: Measured polarimeter electronics output for Method 1 with steps of 0.1° Faraday rotation.

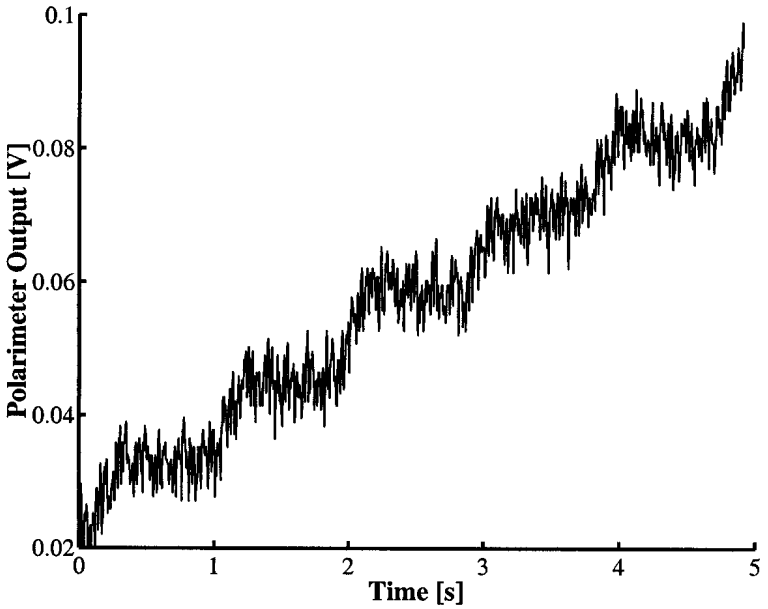

Figure 5.11: Measured polarimeter electronics output for the Method 2 with steps of 0.4° Faraday rotation.

Method 2 was then simulated and a similar polarimeter output acquired. The output is shown in Fig. 5.11 for Faraday rotation steps of 0.4^o. Examination of this plot reveals the resolution of the polarimeter measurement to be approximately 0.3^o which is quite close to the 0.2^o required.

The noise level on the polarimeter output is slightly larger for Method 2 than it is for Method 1, and is dominated by an additional noise component at a low frequency in the region of $1 - 2$ Hz. It was suspected that this additional noise component had its origins in the optical path where the **A** and **B** beams were superimposed, with the likely source being the turbine driven spindle which rotates the half-wave plate. Turbulence in the exhaust gas from both the bearing and turbine of the spindle is a possible source of phase shifts in the beam paths resulting in slowly varying time-dependent changes in ϕ_o, the phase difference between the **A** and **B** beam paths. This phase has to be set to zero or a multiple of π in advance of each measurement to avoid additional unwanted phase terms (see Section 4.4.3).

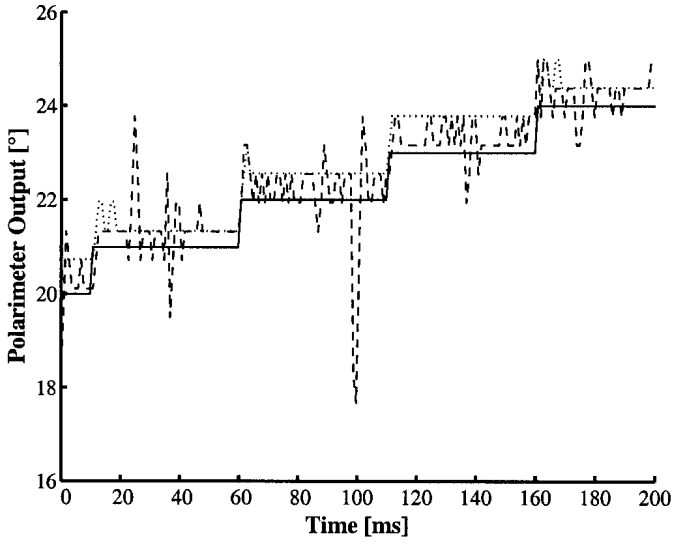

Figure 5.12: Simulated polarimeter electronics outputs for Method 2 with steps of 1^o Faraday rotation (full line), with (dashed line) and without (dotted line) random fluctuations in ϕ_0 for an extreme case with maximum fluctuations of 60^o.

Accordingly, computer simulations were performed to determine the dependence of the polarimeter output on changes in ϕ_0. These simulations are very similar to those described in Section 4.4.3. The results of one such simulation are shown in Fig. 5.12 for Faraday rotation measurements using typical parameters for the extreme case of random fluctuations of ϕ_0 of up to 60^o. The simulated Faraday rotation for the ideal case with $\phi_0 =$

0^o is also plotted in order to indicate the precision of the simulation. It can be seen from Fig. 5.12 that time variations in ϕ_0 are conveyed though the optical system and appear on the polarimeter output. It is difficult to put a precise figure on the maximum allowable variation in ϕ_0 as the noise attributed to it is dependent on many different parameters, including the Faraday angle, the frequency of the variations, the cutoff frequencies of the various electronic filters and the modulation depth of the signals. If, on the other hand, ϕ_0 is time invariant, it can be accounted for in the calibration of the system (see Section 4.4.3). However, as previously mentioned (see Section 4.4.3), ϕ_0 introduces an extra phase term into the measured interferometer data. The error due to this additional term can be kept to within a few percent with a precision in the phase difference of up to 10^o. Experimentally, the noise on the polarimeter output increased significantly by intentionally introducing mechanical vibrations onto the optical components in the **A-B** beam paths. The aforementioned observations provide evidence that the air turbulence is the most likely factor preventing the attainment of the $\pm 0.2^o$ resolution for Method 2. Accordingly, an air-handling plate which pipes all the exhaust gas away from the spindle was installed on the TCV system (see Section 6.2.4).

5.3 Conclusions

The tests described in this chapter confirmed the theoretical conclusions of Chapter 4 where it was seen that Method 2 does indeed overcome the limitations in interferometer operation of Method 1 with a corresponding sacrifice in polarimeter precision. However, the attainment of a polarimeter resolution for Method 2 not significantly removed from the $\pm 0.2^o$ Faraday rotation required was sufficient encouragement to proceed with the implementation of both methods on the full 14 channel diagnostic.

The experiments also provided an opportunity to test the main components which were to be installed on the actual instrument some of which were found to require slight modifications. The bench tests also gave an insight into the accuracy of the alignment required to reduce the polarimeter output noise to an acceptable level.

Chapter 6

Instrument Description

This chapter describes the experimental set-up on TCV from the laser system to the electronics. For clarity the description of the optical set-up has been divided into two sections namely,

- The production of the probing and local oscillator beams in the laser lab and their transfer through two oversized waveguides to the tokamak vessel.
- The optics around the tokamak vessel which form the Mach-Zehnder interferometer.

6.1 The Laser System

The various constraints on the selection of the probing wavelength led to the conclusion that a wavelength of 214.6 μm would be the most appropriate for combined interferometry/polarimetry on TCV (see Chapter 3). This wavelength corresponds to a laser line of optically pumped CH_2F_2.

The duration of a TCV plasma can be up to 2 seconds which is in the order of the thermal constants of typical CO_2 pumped FIR lasers. Consequently, an actively stabilised continuous (cw) laser system, which is in a stable thermal equilibrium throughout the plasma discharge, was used.

The laser line at 214.6 μm in CH_2F_2 was first observed by Danielewics et al.[31] and was assigned to a rotational transition in the molecule by Lachambre et al.[32]. The gas is pumped by a CO_2 laser operating on the 9R34 line and a sketch of the proposed energy level diagram is shown in Fig. 6.1[32]. The strong laser line at 214.6 μm is polarised perpendicular to the CO_2 laser polarisation. The laser can simultaneously emit a weaker line at 287 μm which is polarised parallel to the CO_2 line. Cascade transitions at 230 μm and 248.8 μm are also observed. It was noticed that even if the CO_2 laser emits only a small amount of radiation at the 9R32 line very strong laser lines at 184.6 μm and

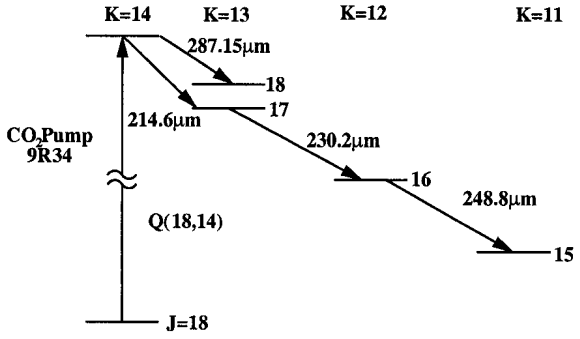

Figure 6.1: The energy level diagram for CH_2F_2 pumped by the 9R34 line of a CO_2 laser.

235.94 μm are excited[33]. Multi-line operation leads to a very unstable output due to line competition and cascade transition effects at 214.6 μm. Consequently, care must be taken to tune the laser correctly so as to avoid the presence of the 9R32 line.

A schematic of the laser system is shown in Fig. 6.2. The pump laser is an PL4 Edinburgh Instruments CO_2 laser which emits about 40 W cw at the 9R34 line. The resonator of the FIR laser is formed by a 1.8 m long Pyrex tube with an inner diameter of 25 mm, a flat gold coated copper mirror on one side and two silicon plates on the other which form a Fabry-Perot output coupler with variable reflectivity. This output coupler helps the selection of the 214.6 μm line from all the aforementioned lines. The inner silicon plate is coated for high reflection of the CO_2 laser beam which is coupled into the FIR laser through a 2.5 mm diameter hole in the copper mirror. The CO_2 laser beam enters the FIR laser through a ZnSe Brewster window and the output window is a 6 mm thick TPX plate. The FIR laser beam is horizontally linearly polarised.

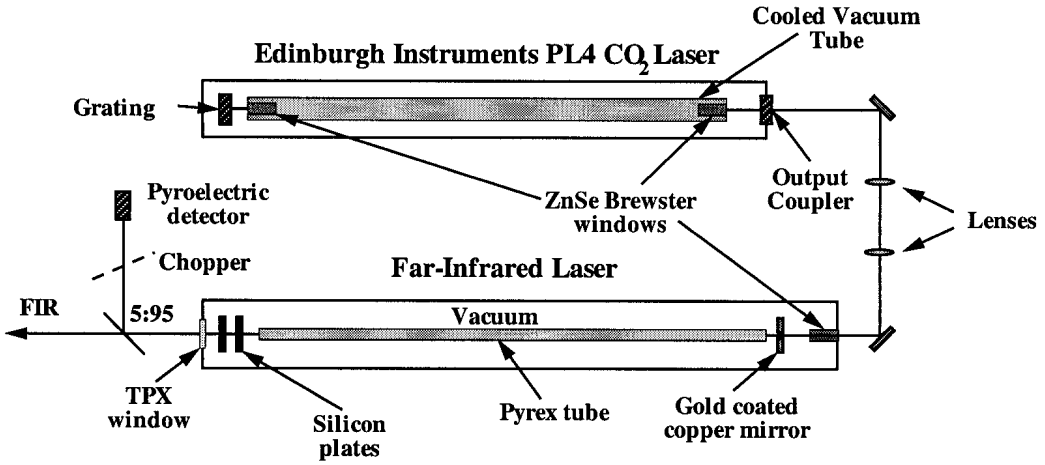

Figure 6.2: Schematic of the laser system.

The FIR output mirror system is mounted on a motorised translation stage and the copper mirror is in a support with motorised alignment screws. Both mirror supports are mounted within the vacuum system and can be adjusted during laser operation. A small fraction of the output FIR beam is split off, chopped and directed onto a pyroelectric detector. The signal from this detector serves as the input signal to an Edinburgh Instruments standard laser stabiliser which is used to tune the CO_2 laser frequency to a position which yields the maximum FIR output from the system. The stabilisation runs continuously resulting in a minor modulation of the FIR output power which can, in general, be neglected. Experience has shown that this stabilisation can be switched off completely once the CO_2 laser has reached a thermal equilibrium which usually takes a couple of hours. Any remaining thermal instabilities are usually in the FIR cavity. The laser beam is nearly Gaussian in shape and had a beam waist radius of about 8 mm close to the output window. The operating FIR pressure is about 0.3 mbar and the output power is of the order of 80 mW.

The laser system has been placed in a separate room outside the TCV security area. Since the absorption of the laser beam by water vapour in the air is significant (0.4 m^{-1} on a typical day with 70% humidity at 20° C) all the waveguides and boxes containing the optics are flushed with dry nitrogen.

6.2 Probe and LO Beam Production

The probing and LO (local oscillator) beams are produced in the laser room and as the space there is limited the optical set-up was designed to be as compact as possible. The optical components are placed on a 1800 × 600 mm optical table mounted on the wall above the laser. The table is enclosed in an air-tight box which is flushed with dry N_2. The box is equipped with dis-mountable plexi-glass windows some of which have been modified to include large gloves to allow access to the optical elements under the slight N_2 pressure. The system, shown in Fig. 6.3, was designed to incorporate both Methods 1 and 2 (see Chapter 4). The incident beam from the FIR laser is split by the beamsplitter at position 2 into the probing and LO beams with the latter being reflected off a rotating grating producing a frequency shift. A large fraction of the other beam is split by the beamsplitter at position 4 forming the **B** beam with the remainder (**A** beam) directed through the half-wave plate in the rotating spindle which rotates its polarisation. The two beams are then recombined on the beamsplitter at position 12. A translator has been placed at position 10b to permit the setting of the phase difference between the **A** and **B** beams to a multiple of π (see Section 4.4). The system can be changed over quite easily

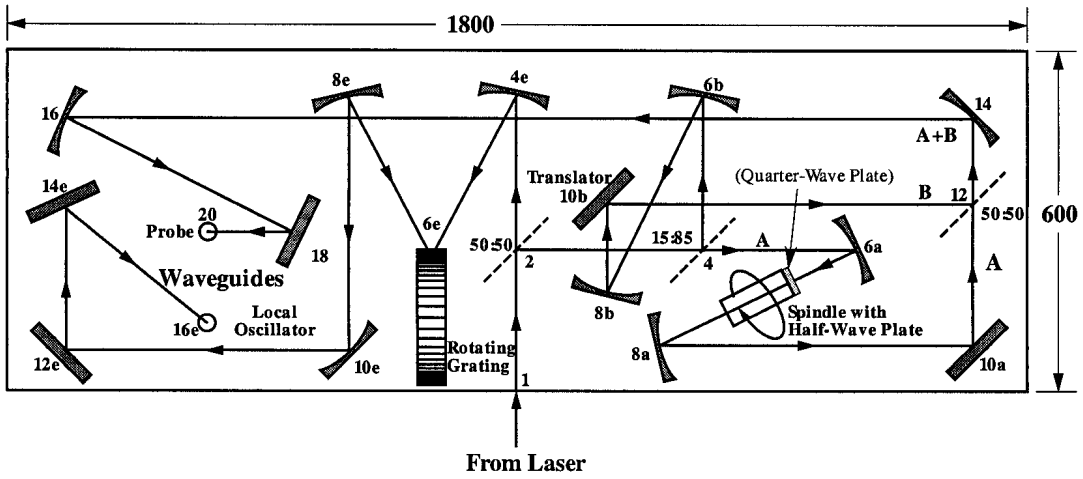

Figure 6.3: The optical arrangement used to produce the probing and local oscillator beams. Elements used for the individual beams are marked with the appendices **a**, **b** and **e** for the **A**, **B** and LO beams respectively. All the distances are in mm.

to Method 1 by removing the beamsplitter at position 4 and turning the quarter wave plate in the entrance of the spindle to introduce some ellipticity into the polarisation of the beam. A series of curved mirrors shape and convey the beams into the waveguides.

6.2.1 ABCD

ABCD is one of the PARAXIA range of Macintosh applications developed at Stanford University for the computation and analysis of laser resonator modes and laser beam propagation problems. The program builds an paraxial optical system from a succession of optical elements. The various parameters such as radii of curvature, angle of incidence, focal length etc. are specified independently for each element. ABCD then propagates a user-defined Gaussian beam through the system and calculates the variation of the Gaussian beam parameters at specified locations[34].

ABCD was used extensively to design the optical set-up. Various parameters including distances between elements and radii of curvature were adjusted until a system was identified which complied with the following requirements,

- correct focusing of the **A** beam through the aperture of the spindle (Section 6.2.4)
- correct focusing the LO beam onto the rotating grating (Section 6.2.3)
- beam waists of approximately 8 mm at the entrances to the waveguides (see Section 6.2.5)

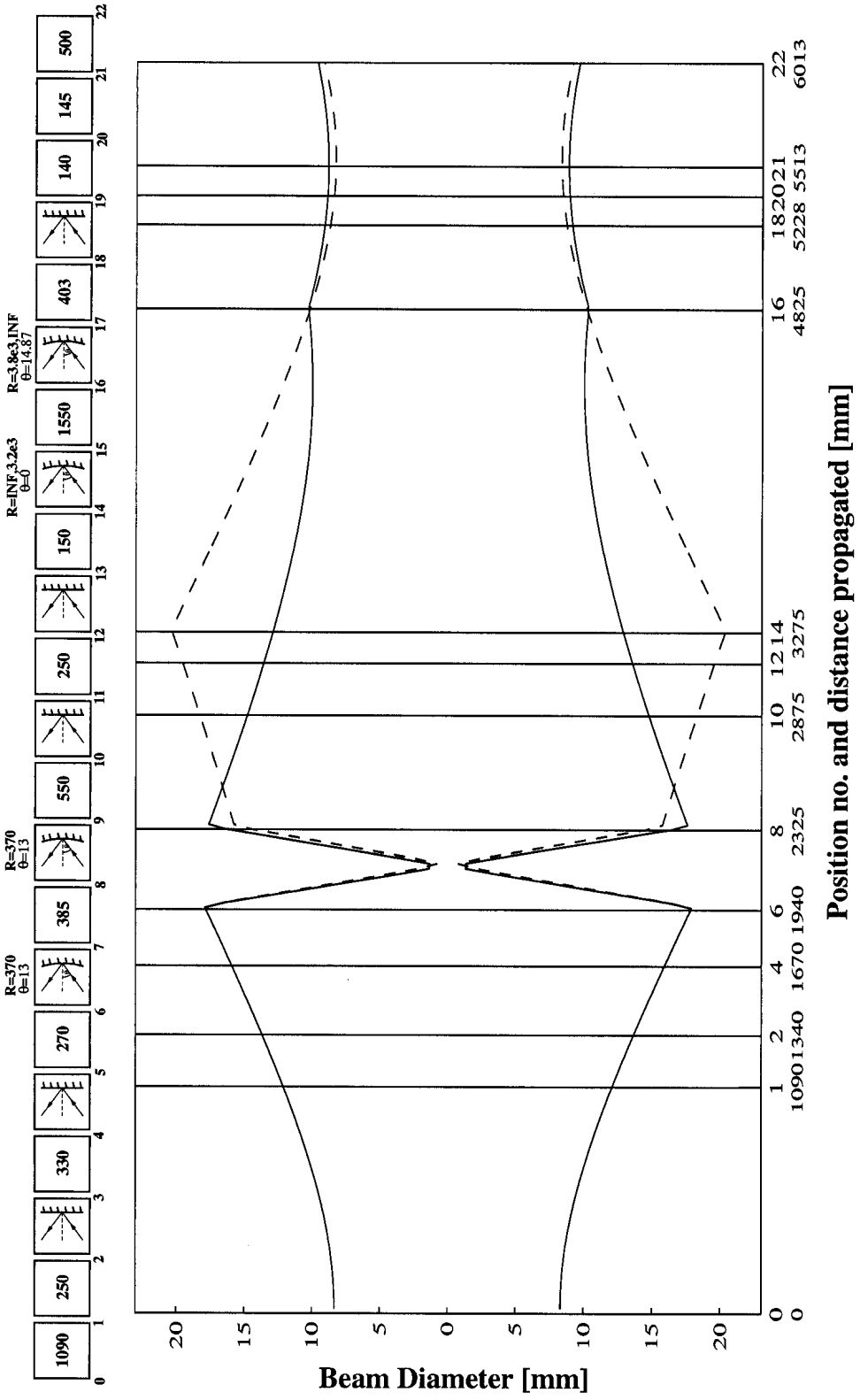

Figure 6.4: The results of the ABCD simulation of the probe beam from the laser output to the waveguide entrance (position 21). The position numbers correspond to those in Fig 6.3. The full and dashed lines represent the two principle planes. All dimensions are in mm unless otherwise stated

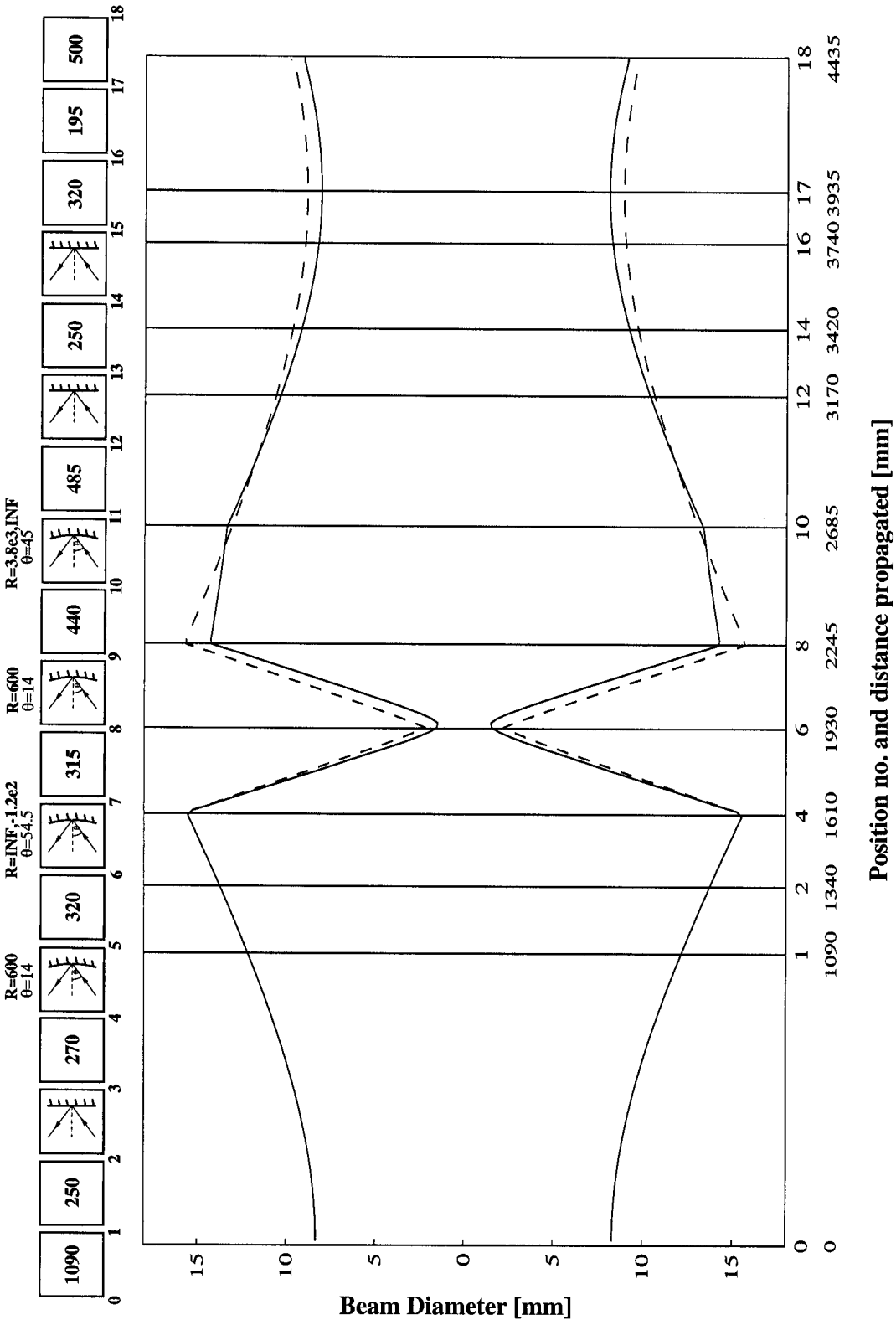

Figure 6.5: The results of the ABCD simulation of the LO beam from the laser output to the waveguide entrance (position 17). The position numbers correspond to those in Fig 6.3. The full and dashed lines represent the two principle planes. All dimensions are in mm unless otherwise stated.

while ensuring that the layout was geometrically feasible. Both spherical and cylindrical mirrors were used to shape the beam. The final design and theoretical beam propagation are shown in Fig. 6.4 for the **A** beam and Fig. 6.5 for the LO. The position numbers of the elements correspond with those on the schematic of the optical arrangement shown in Fig. 6.3. To facilitate the beam matching the **B** beam undergoes the same shaping as as the **A** beam.

6.2.2 Beamsplitters

Beamsplitting devices are required to perform the following functions in the system;

1. The splitting of the incident beam into the probing and LO beams.
2. The splitting the probing beam into its **A** and **B** components.
3. The recombination of the **A** and **B** components to form the complete probing beam.
4. The splitting of the LO and probing beams into their plasma and reference components.
5. The recombination of the probing and LO beams.

To maximise the power on the detectors the devices 1, 3 and 5 above should have splittings ratios of 50:50 with device 3 also being polarisation insensitive. Devices 2 and 4 should have appropriate splitting ratios to produce the desired modulation depth on the signals and adequate power levels on both the plasma and reference detectors.

The original interferometer system on TCV used quartz plates as beamsplitters. Such devices are unsuitable for the interferometer/polarimeter arrangement as they are birefringent and would introduce additional changes into the polarisations of the beams. It was decided, therefore, to replace the quartz plates by metallic meshes.

Metallic Meshes

A schematic diagram of the parameters of a typical inductive mesh are shown in Fig. 6.6. For wavelengths λ, larger than the grid constant g, meshes act as a semi-reflecting plane with very low absorption and with a transmission coefficient varying rapidly with λ. For $\lambda \approx g$ the transmission goes through a maximum while for $\lambda < g$ the optical energy is scattered into several diffraction modes. The metallic mesh has square symmetry and therefore its optical properties are independent of polarisation at normal incidence. However, most of the beamsplitters in the system will have non-zero angles of incidence

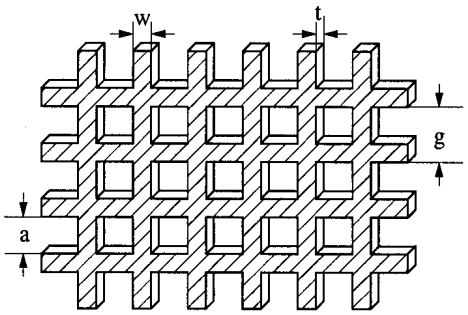

Figure 6.6: Schematic diagram of a metallic mesh.

($\theta \neq 0^o$) and will, therefore, have different transmission coefficients for different polarisations. Polarisation with the E field perpendicular to the plane of incidence (s mode) is labelled as the TE mode (Transverse Electric) or vertical polarisation while polarisation with the E field parallel to the plane of incidence (p mode) is labelled as TM (Transverse Magnetic) mode or horizontal polarisation.

There have been many articles published on both the theory and experiment of free standing metallic meshes at zero incidence[30]. In a summary of the theoretical approaches and their comparison with experimental results, Durschlag and DeTemple[35] concluded that the waveguide array approach of Chen[36] and Lee[37] gave the most accurate results. This theory also has the advantage of the inclusion of polarisation and incidence angle effects. Pickett et al.[38] measured the inductive mesh transmission of the two major polarisations as a function of angle of incidence and found that the data agreed well with Chen's waveguide theory in the thin mesh limit, $w \gg t$. They then used Chen's theory to derive an empirical lumped circuit model which matches the theory and thus the experiment very well. Marcuvitz[39] also developed a equivalent circuit model for the description of the behaviour of a one-dimensional wire grid. The dependence on the angle of incidence has been included providing that the wires are directed perpendicular to the plane of incidence. Consequently, this model can only be used to predict the TE mode transmission. Both models are only applicable when there is no diffraction i.e. $\lambda > g(1 + \sin\theta)$.

The two models were compared with experimental measurements and the results from a 167lpi (lines per inch) mesh, with dimensions as listed in Table 6.1, are shown in Fig. 6.7. The onset of diffraction for this mesh is expected at an angle of incidence of approximately 28^o. Although the experimental and theoretical results do not agree exactly it is seen that the Pickett model predicts well the strong dependence of the TE polarisation on the angle of incidence. The errors involved are quite large, firstly due to basic experimental error

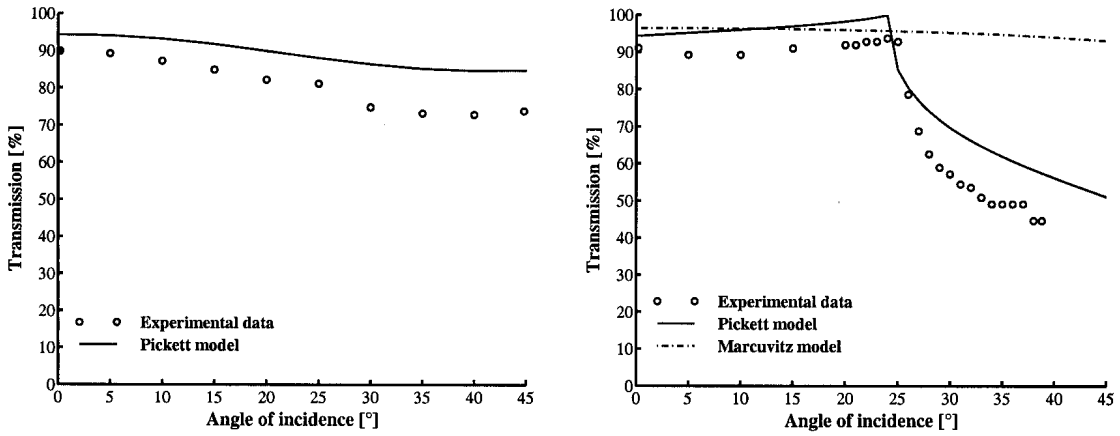

(a) (b)

Figure 6.7: Experimental and predicted transmission of the 167 lpi mesh for (a) TM mode and (b) TE mode operation.

but more importantly due to the error involved in determining the mesh parameters which were measured manually under a microscope. We have no information on the thickness of the mesh and cannot, therefore, conclude whether it is within the thin mesh limit or not. It was nevertheless concluded that the Pickett model would be a useful design tool as it is applicable for both polarisations and variable angles of incidence.

50:50 Beamsplitter

The Pickett lumped circuit model was used to determine which of the commercially available meshes would be the most suitable to provide the 50:50 ratio required for splitting the incident beam into the LO and probing beams. As the incident beam is horizontally linearly polarised this splitting ratio is only required for the TM mode. Simulations

Mesh	lines per inch	g [μm]	w [μm]	a [μm]	t [μm]
Test mesh	167	152.5	10	142.5	-
MN-28	150	169.42	24.64	144.78	5
MN-36	300	84.58	18.54	66.04	5
MN-41	500	50.8	11.68	39.12	5
Asymmetric mesh (hor)	391	65	7	58	-
Asymmetric mesh (ver)	317.5	80	7	73	-

Table 6.1: Specified dimensions of the meshes used in the interferometer/polarimeter system.

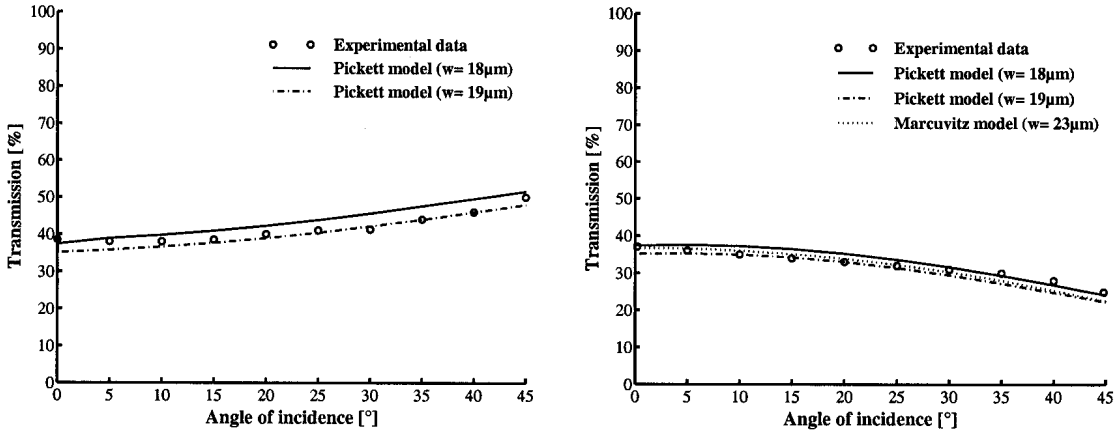

Figure 6.8: Experimental and predicted transmission of the 300 lpi mesh for (a) TM mode and (b) TE mode operation.

predicted that the Buckbee-Mears 300 lpi MN-36 mesh, whose dimensions are listed in Table 6.1, would fulfill the requirements. The experimental and predicted transmission of this mesh as a function of angle of incidence are shown in Fig. 6.8 for both polarisations and indicate quite close agreement. The line width of 18.54 μm had to be increased slightly to 19 μm in the case of the Pickett model and to 23 μm for the Marcuvitz model to fit the data.

A, B Beamsplitter

The splitting ratio for the division of the probing beam into the **A** and **B** beams should produce signals on the detectors which do not become overmodulated over the entire range of expected Faraday rotation angles. The maximum expected phase shift, including the offset, (see Section 3.4) is of the order of 60^0.

The predicted and experimental transmission of a 500 lpi mesh whose dimensions are given in Table 6.1 are shown in Fig. 6.9. The line width of the 500 lpi mesh was increased from 11.68 μm to 13 μm for the Pickett model and 15.75 μm for that of Marcuvitz to fit the data. The actual transmission of the 500 lpi mesh was slightly lower than predicted at approximately 14%. This discrepancy can be explained partially by the fact that the thin mesh approximation is less valid for this mesh than the other meshes (see Table 6.1). The measured transmission corresponds to a transmission to reflection power ratio of 1:6.2, producing a basic signal with a modulation index of 0.4. For this index the signals would

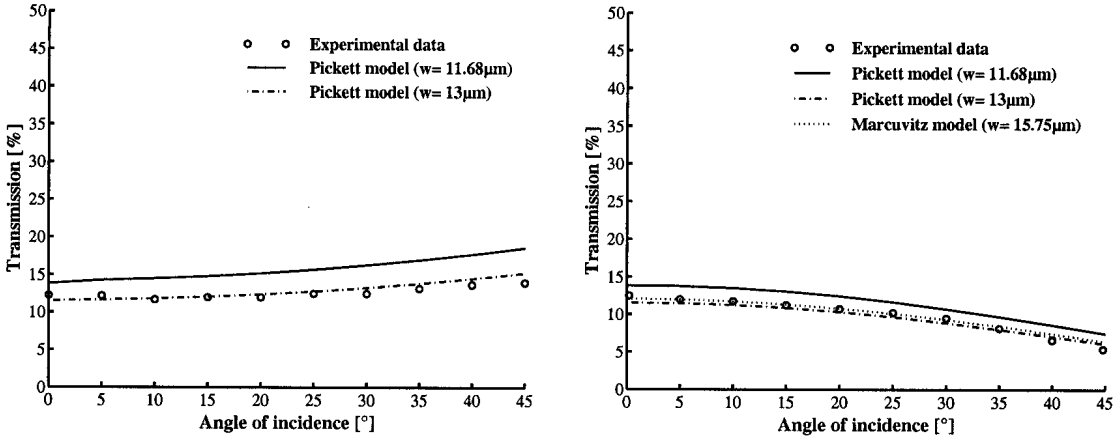

Figure 6.9: Experimental and predicted transmission of the 500 lpi mesh for (a) TM and (b) TE mode operation.

only start to become overmodulated when the phase shift approaches 65^0 (Section 4.4.1) which is well within the range of expected values.

Polarisation insensitive 50:50 beamsplitter

The element which combines the **A** and **B** beams to produce the probing beam should ideally be polarisation insensitive to conserve the rotating polarisation of the **A** beam and should have a 50:50 splitting ratio to maximise the power on the detectors. As mentioned earlier the properties of symmetric meshes are independent of polarisation at zero incidence. However, as can be seen in Fig. 6.8 this polarisation insensitivity is not conserved for non-zero incidence. There is a choice, therefore, between the use of a symmetric mesh at near zero incidence which complicates the geometrical set-up or a custom made non-symmetric mesh at a higher angle of incidence. Dr. Alexander Volkov at the General Physics Institute of the Russian Academy of Sciences was contacted and was able to provide such a mesh designed for a wavelength of $195\,\mu$m and an angle of incidence of 45^o. The dimensions of the mesh are shown in Table 6.1 and the predicted transmission for both polarisations at both the design and operating wavelengths are plotted in Fig. 6.10 as a function of angle of incidence. The measured transmission and reflection of the mesh for $\lambda = 214.6\ \mu$m at 45^o are also shown in Fig. 6.10. While not completely polarisation insensitive this mesh was found to be quite acceptable. These minor distortions of the polarisation of the probing beam due to the slight polarisation sensitivity of the mesh can

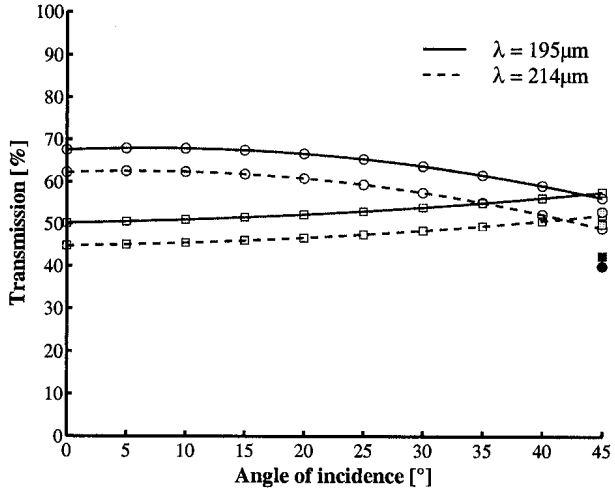

Figure 6.10: Theoretical transmission using the Pickett model of the asymmetric mesh as a function of angle of incidence for both horizontal (circles) and vertical (squares) polarisations for the design wavelength of 195 μm and the operating wavelength of 214.6μm. The experimentally measured values of the transmission (full) and reflection (shaded) for both polarisations are also shown for an angle of incidence of 45°.

be corrected for during calibration of the system (see Sections 4.4.3 and 6.6).

High Transmittance Mesh

A high transmittance mesh is required to split off small portions of both the probe and LO beams to provide the reference signal. The splitting is performed at the exit of the waveguides under the TCV vessel as shown in Fig. 6.17. A 150 lpi Buckbee-Mears MN-28 mesh at near zero incidence where its polarisation insensitivity is almost completely preserved is used in the probing beam path. A similar mesh, set at a higher angle of incidence, is used for the linearly polarised LO. The dimensions of the mesh are listed in Table 6.1 and the measured transmission of approximately 88% at zero incidence compares very well with the Pickett model prediction of 92%.

6.2.3 Rotating Grating

The frequency shift of the LO is obtained by using the Doppler effect generated by a rotating grating[40]. The grating consists of a cylinder with grooves machined parallel to its axis with a blaze angle β as shown in Fig. 6.11. The incident beam is focused so as to reduce its diameter to a few millimeters at the surface of the grating. Since the radius of the cylinder is usually large the curvature of the grating can be neglected and to a good

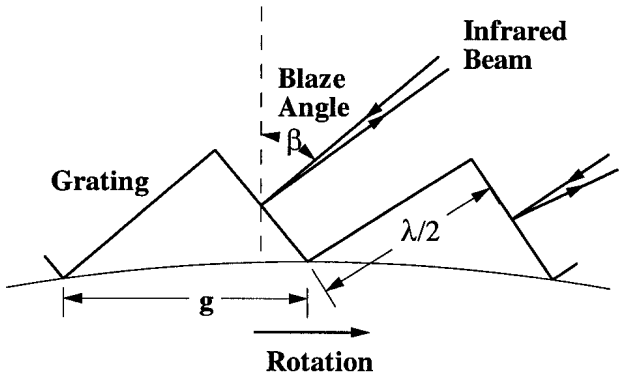

Figure 6.11: The cylindrical rotating blazed grating for Doppler shifting the beam frequency.

approximation the whole beam can be set to the blaze angle. In practice the grating is titled slightly to enable the diffracted beam to be separated from the incident beam. The diffracted beam experiences a Doppler shift equal to[40],

$$\Delta f = 2\frac{2\pi\rho N}{\lambda}\sin\beta \tag{6.1}$$

where λ is the wavelength of the incident radiation, N the angular velocity of the cylinder in revolutions per second and ρ the radius of the cylinder. The total number of grooves G, is given by,

$$G = \frac{2\pi\rho}{g} \tag{6.2}$$

where g, the grating constant, is given by $g = \lambda/(2\sin\beta)$.

The grating used in this experiment was designed for second order operation with wheel and tooth dimensions as shown in Fig. 6.12. The equation for the frequency shift is then given by,

$$\Delta f = \frac{2\pi\rho N}{\lambda}\sin\beta. \tag{6.3}$$

To obtain a frequency shift of 100 kHz the grating must, consequently, rotate at approximately 35 Hz.

The grating support was designed so that both the incident and reflected beams would remain horizontal. The designed height of the optical axis for the entire system is 90 mm as shown in Fig. 6.12. For the ABCD simulations of the optical set-up the beam incident on the grating was assumed to be horizontal and the grating itself was modelled as a simple cylindrical mirror with an angle of incidence of 54.5° in the sagittal plane. The ABCD simulations predict beam waists between $1.55 - 2\,\text{mm}$ on the grating (see position 6 in Fig. 6.5).

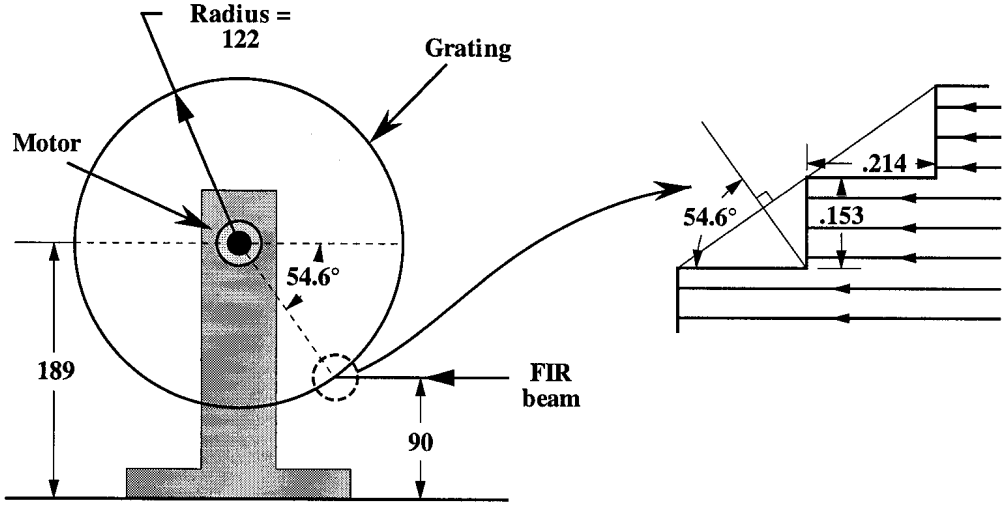

Figure 6.12: Schematic of the rotating grating with detail of the grating teeth. All the dimensions are in mm.

6.2.4 Rotating Spindle

The rotating polarisation required for both methods is produced by passing the FIR beam through a rapidly rotating $\lambda/2$ plate. The polarimeter time resolution is directly linked to the speed at which the plate can be rotated with the only constraint being that this frequency should be well below the frequency shift of the LO to ensure accurate demodulation of the detected signal (see Section 4.5.1). As the frequency shift is set to 100 kHz, rotation speeds of the order of some kHzs would be optimal.

The rotator used is a 16 mm hollow shaft air bearing spindle originally designed for spray painting applications and manufactured by Westwind Air Bearings Ltd.. The spindle is shown schematically in Fig. 6.13. The ABCD simulations predict beam waists of approximately 1 mm at the centre of the spindle (see positions 7-9 in Fig. 6.4). The unit requires 60 psi bearing air pressure and the turbine pressure can then increase the speed up to the design value of 80,000 RPM. The maximum speed depends, however, on the design and balance of the plate support structure fitted to the spindle which in our case was found to be 42,000 RPM at a turbine pressure of 45 psi. The maximum RPM without the air-handling plate was seen to be of the order of 46,500.

The bearing air consumption is 57 litres/min at 60 psi and the design turbine consumption of the basic unit is 118.9 litres/min at 60,000 RPM giving a typical overall consumption of 176 liters/min. As mentioned previously, all the optical components are placed in a box flushed with dry N_2 to avoid the beam being absorbed by the water vapour in air. While tests on the transmission of the FIR beam though the on-site compressed

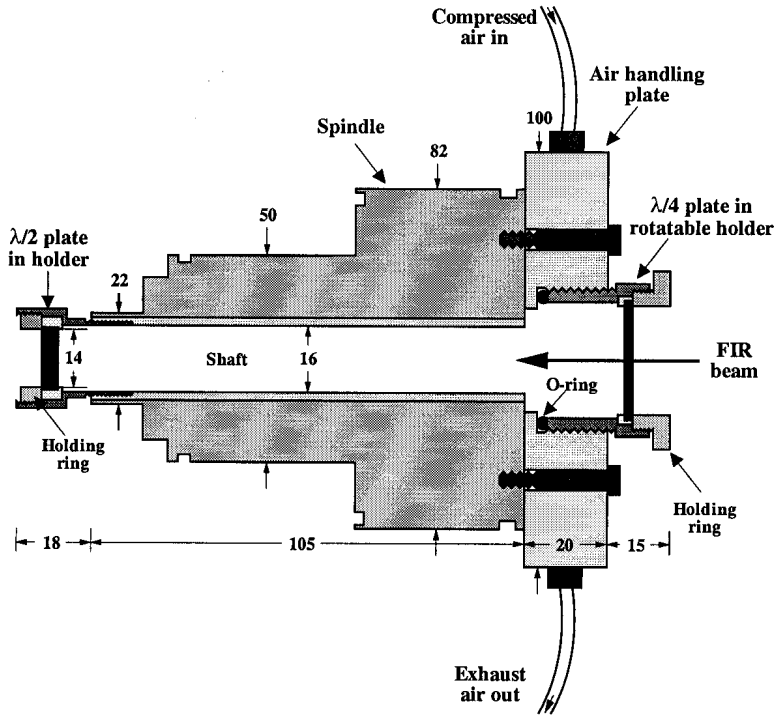

Figure 6.13: A schematic of the rotating spindle, the air-handling plate and the quartz plate support structures with all dimensions in mm.

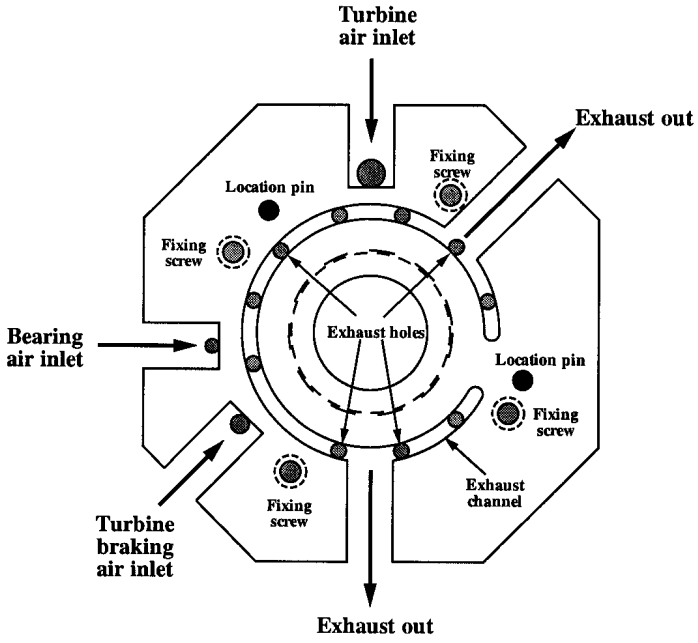

Figure 6.14: Schematic of the cross-section of the air-handling plate with the holes and pins in the spindle shown as full circles.

air showed that the transmission didn't differ considerably from that through N_2 it was nevertheless decided to remove the exhaust gas from the box directly at the exit of the spindle. The volume of the box is approximately 480 litres and such a quantity of air entering it could cause considerable turbulence and induce vibrations in some of the optical elements especially the sensitive metallic mesh beamsplitters. An air-handling plate was therefore designed and its position with respect to the spindle and other elements is shown schematically in Fig. 6.13. A more detailed diagram of the device is shown in Fig. 6.14. The bearing and turbine air are supplied via a filter set and are piped directly into the spindle via large holes in the air-handling plate. The exhaust gas exits the spindle via the 10 holes as shown in Fig. 6.14 and is collected in the exhaust channel of the plate before being piped out of the box. The $\lambda/4$ and $\lambda/2$ quartz plates act as the entrance and exit windows. The turbine braking inlet is not used in this application. Due to the construction of the spindle a minor leakage of the compressed air into the box is unavoidable but acceptable.

Quartz Plates

The $\lambda/2$ plate is a 2.258 mm thick crystalline quartz plate ($\mu_e = 2.1583$, $\mu_o = 2.1107$ at 214.6 μm) with a diameter of 15 mm and anti-reflection coatings on both sides. The measured transmission of 93% compares very well with the theoretical transmission of 96% (with absorption coefficients $\alpha_o = 0.12\ \mathrm{cm}^{-1}$ and $\alpha_e = 0.16\ \mathrm{cm}^{-1}$). The plate sits in a Teflon ring in a brass holder which is in turn fixed to the shaft of the spindle as shown in Fig. 6.13. A PVC ring then screws into the brass holder to hold the plate in place.

The $\lambda/4$ plate, required to introduce some ellipticity into the beam used in Method 1, is also an anti-reflection coated quartz plate which is 1.129 mm thick with a diameter of 25 mm. It is placed in a holder similar to that of the $\lambda/2$ plate which is then screwed into the air-handling plate. A thick soft O-ring allows the plate to be turned through up to 90° without breaking the sealing. The plate can then easily be turned to a position where the beam passes through unaffected, thereby producing the rotating linearly polarised beam required for Method 2. The FIR beam is aligned at a slight angle to the plates to avoid back reflections.

6.2.5 Waveguides

The probe and LO beams are conveyed from the laser lab to the tokamak vessel over a distance of 9 m through oversized waveguides. Amongst the different possible waveguides the most attractive is a hollow circular dielectric waveguide with a large diameter compared

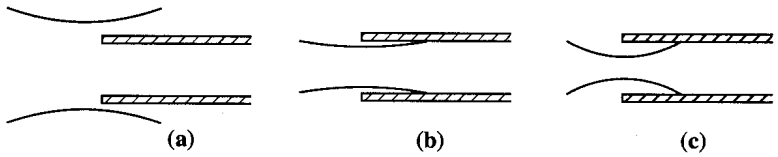

Figure 6.15: The coupling of a beam into a waveguide.

to the wavelength. Its attenuation is small and linear polarisation is well preserved in the guide. It has been shown that there is a beam-waist at the entrance of a hollow oversized circular waveguide with which maximum power is transmitted[41] (Fig. 6.15(b)). A beam with too large a waist as in Fig. 6.15(a) is weakly divergent but part of the beam doesn't enter the guide and the corresponding power is lost. On the other hand for too narrow a waist, as in Fig. 6.15(c), the whole beam power is assumed to enter the guide but with strongly diverging rays resulting in large internal losses due to non-grazing incidence, low values of reflection coefficients and many reflections on the guide walls.

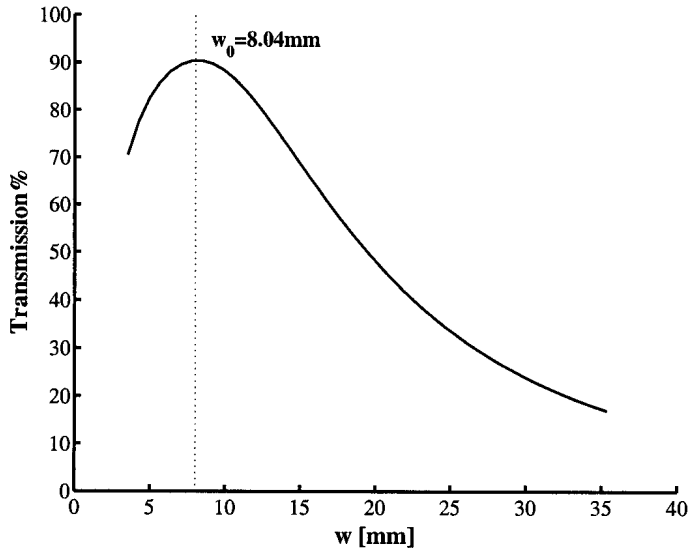

Figure 6.16: Theoretical transmission of a beam of wavelength $\lambda = 214.6\ \mu$m through a circular waveguide of radius $R = 12.5$ mm, length $L = 9$ m and relative dielectric constant $\epsilon_r = 6$ as a function of beam radius with the beam waist located at the entrance of the waveguide.

Belland and Crenn [41] derived a simple formula which gives the optimal beam characteristics for the lowest losses in a waveguide of variable length and internal radius. Using this theory and a waveguide of internal radius $R = 12.5$ mm, length $L = 9$ m and relative dielectric constant $\epsilon_r = 6$ a value of $w_0/R = 0.643$ or $w_0 = 8.04$ mm for maximum transmission was obtained for a wavelength of 214.6 μm, where w_0 is the beam radius at

the 1/e points of the Gaussian field amplitude profile. A plot of the predicted transmission of 214.6 μm through this waveguide versus beam width with the beam-waist at the waveguide entrance is shown in Fig. 6.16.

The design of the optical arrangement required to produce this beam-waist was described in Section 6.2.1. The theoretical beam parameters at both the probing and LO waveguide entrances are listed in Table 6.2. As neither the mirror radii nor the actual distances between the mirrors are exact to the nearest millimetre the transmission obtained initially through the waveguides could be improved upon by making small adjustments to the most critical path lengths, namely the distances between the focusing mirrors of the spindle and rotating grating.

The power of both beams was measured at the entrances to the waveguide with a Thomas Keating submillimetre-wave power meter. Measurements were made both with and without an aperture the size of the waveguides internal area to estimate the percentage of power coupled into the waveguides. The beam power exiting the waveguides was also measured. The coupling of the probe beam into the waveguide was seen to be over 90% with a transmission of approximately 60%. The coupling of the LO was seen to be slightly lower at about 80% with a corresponding transmission of 50%. The better coupling of the probe beam into the waveguide is probably due to incomplete knowledge of the actual shape of the beam reflected off the rotating grating (see Section 6.2.3). The actual transmission through the waveguides is lower than the theoretical (see Fig. 6.16) but still quite acceptable. The waveguides are not continuous straight guides but are comprised of four individual sections coupled by small mirrors all of which contribute to the observed losses. The waveguides and boxes containing the mirrors are all flushed with dry N_2.

	Probe Beam	**LO beam**
Input Ray	R=INF, w=8.3 mm	R=INF,w=8.3 mm
At Waveguide	R=3500 m, w=8.9 mm R=−36 m, w=8.3 m	R=−78 m,w=8.1 mm R=−1300 m, w=8.9 mm
Distance of waist from waveguide entrance	z=-.04 mm z=28.4 mm	z=11.8 mm z=1.0 mm

Table 6.2: ABCD calculated values of beam waist and radius of curvature at the waveguide entrances.

6.3 The Mach-Zehnder Interferometer Optics

6.3.1 Support Structure

In order to minimise vibrations on the experiment a separate support structure for the interferometer/polarimeter and the Thomson scattering experiment has been installed. It is based on two 7 m high concrete pillars on opposite sides of TCV which are fixed to the basement floor. The pillars are connected above the machine by a bridge structure made from a fibreglass composite material, part of which is shown in Fig. 6.17. The boxes containing the optics are made from Fibrelan, a fibreglass material with a honeycomb structure which is both highly stable and relatively light. The boxes are attached to both the pillars and the bridge as shown in Fig. 6.17. All the boxes have dis-mountable covers for access to the optical components and the boxes directly above and below the tokamak have been equipped with large gloves to facilitate the alignment of the optics within the nitrogen atmosphere. No part of the structure touches either the tokamak support structure, the coils or the vacuum vessel.

6.3.2 Beam Expansion Optics

On many interferometers a single FIR beam is split into several separate beams using a series of beamsplitters. These beams are then passed through the tokamak as individual chords. An alternative method had been implemented on several tokamaks[42] where the beam is expanded into a slab-like beam using cylindrical parabolic mirrors. The elongated beam is then directed onto an array of closely spaced detectors. Such an arrangement was installed on TCV.

The TCV vacuum windows have a combined radial length of just over 400 mm as shown in Fig. 6.21 and consequently a beam-waist (defined as half the beam diameter) of approximately 200 mm is required to completely illuminate the accessible portion of the plasma. Beam shaping optics in both the probing and LO paths (see Fig. 6.17) produce beam-waists of approximately 25 mm at the first parabolic mirrors (elements 9l and 8p respectively) and therefore a beam expansion ratio of 1:8 is required. The optical arrangement and ABCD simulation results (see Section 6.2.1) of the designed probing and LO beam trajectories are shown in Figs. 6.18 and 6.19 respectively. The position numbers of the elements in the simulations correspond with those in Fig. 6.17 with the appendices **p** and **l** for the probing and LO paths respectively. Both optical arrangements produce expanded beams with beam waists of approximately 200 mm in the radial direction and 18 mm toroidally. It should be noted that this is a purely theoretical calculation for

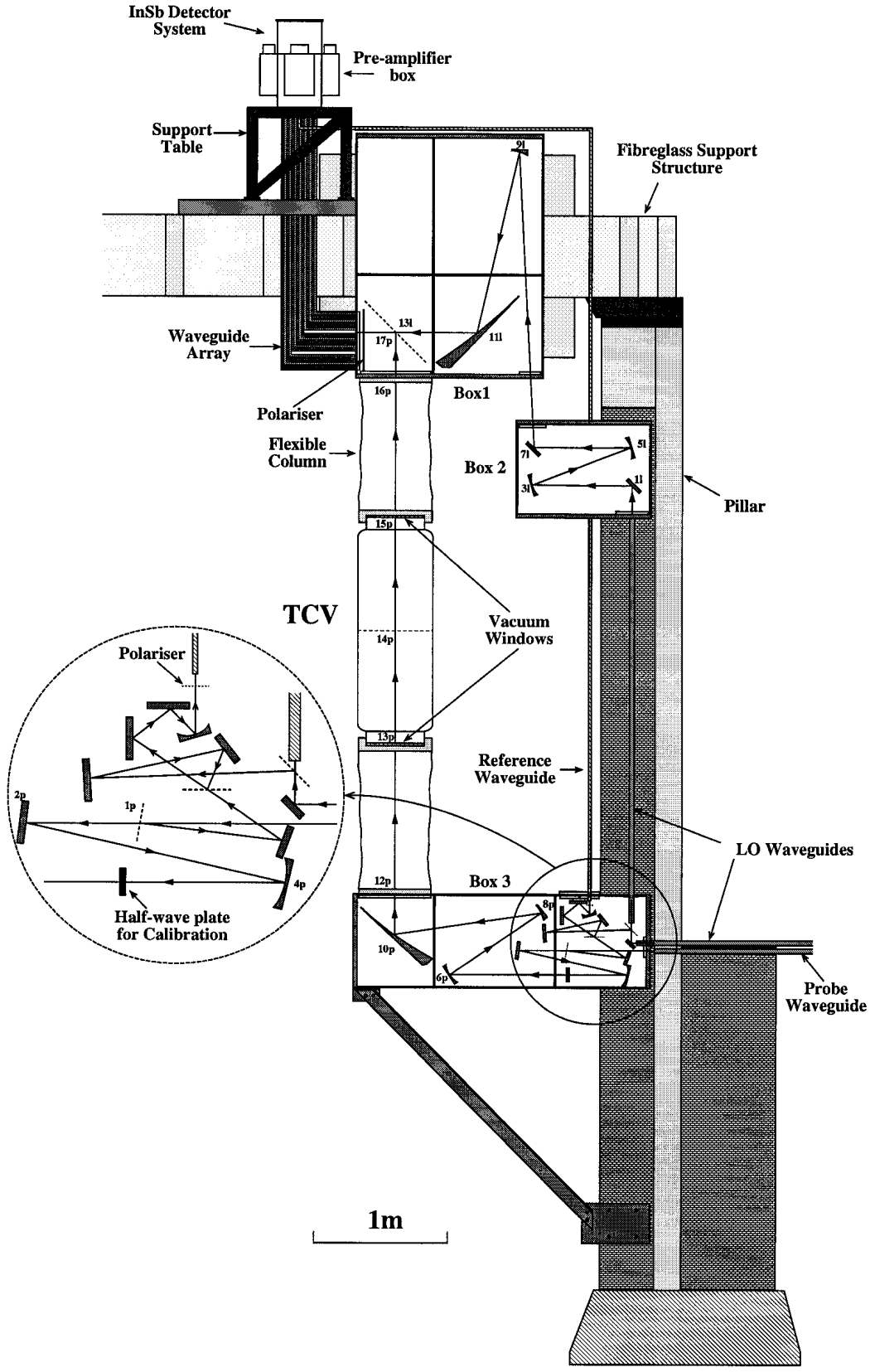

Figure 6.17: An overview of the TCV polarimeter/interferometer.

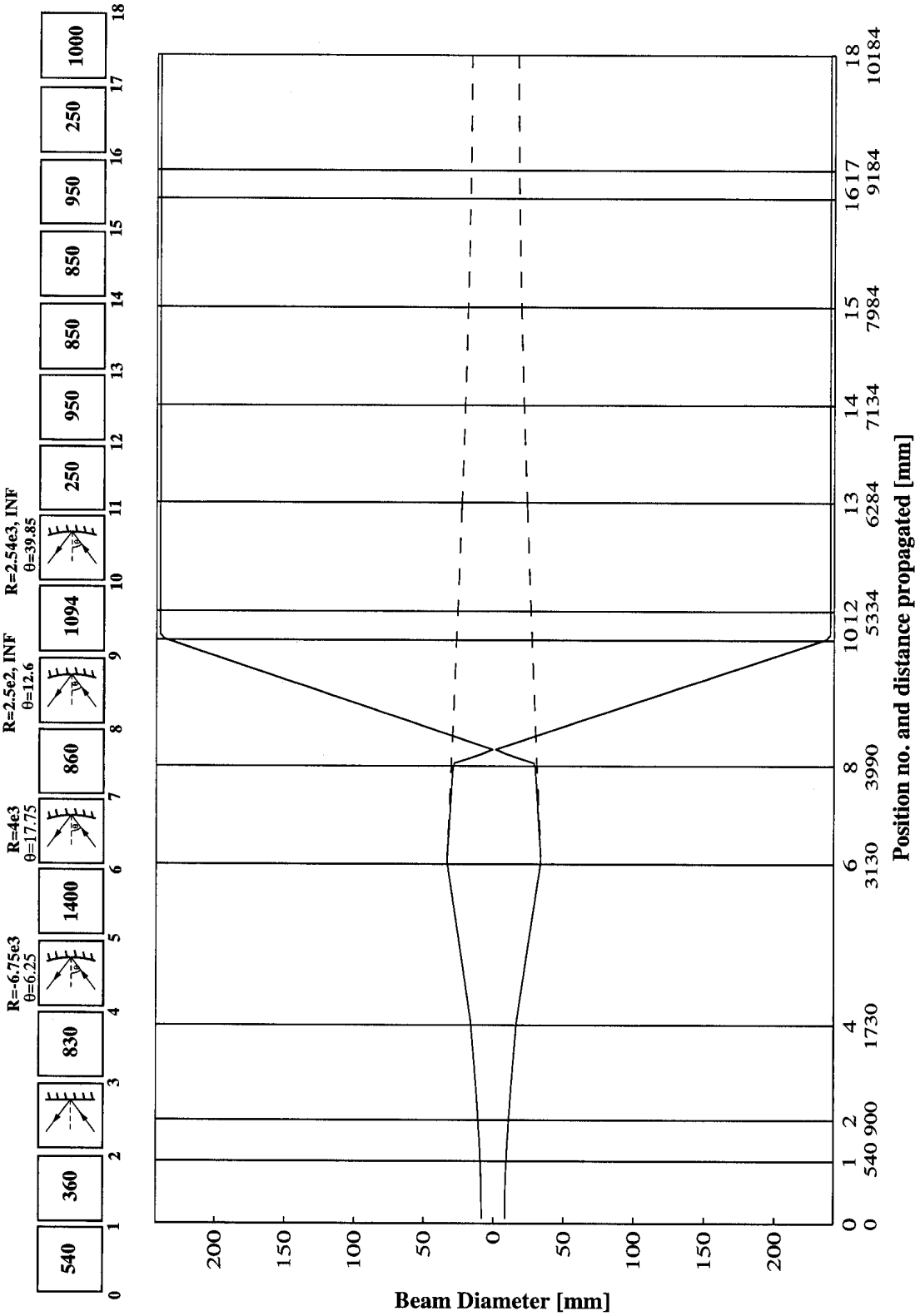

Figure 6.18: The results of the ABCD simulation of the probe beam from the waveguide exit to the main beam re-combiner (position 17). The position numbers correspond to those in Fig 6.17. The full and dashed lines represent the two principle planes. All dimensions are in mm unless otherwise stated.

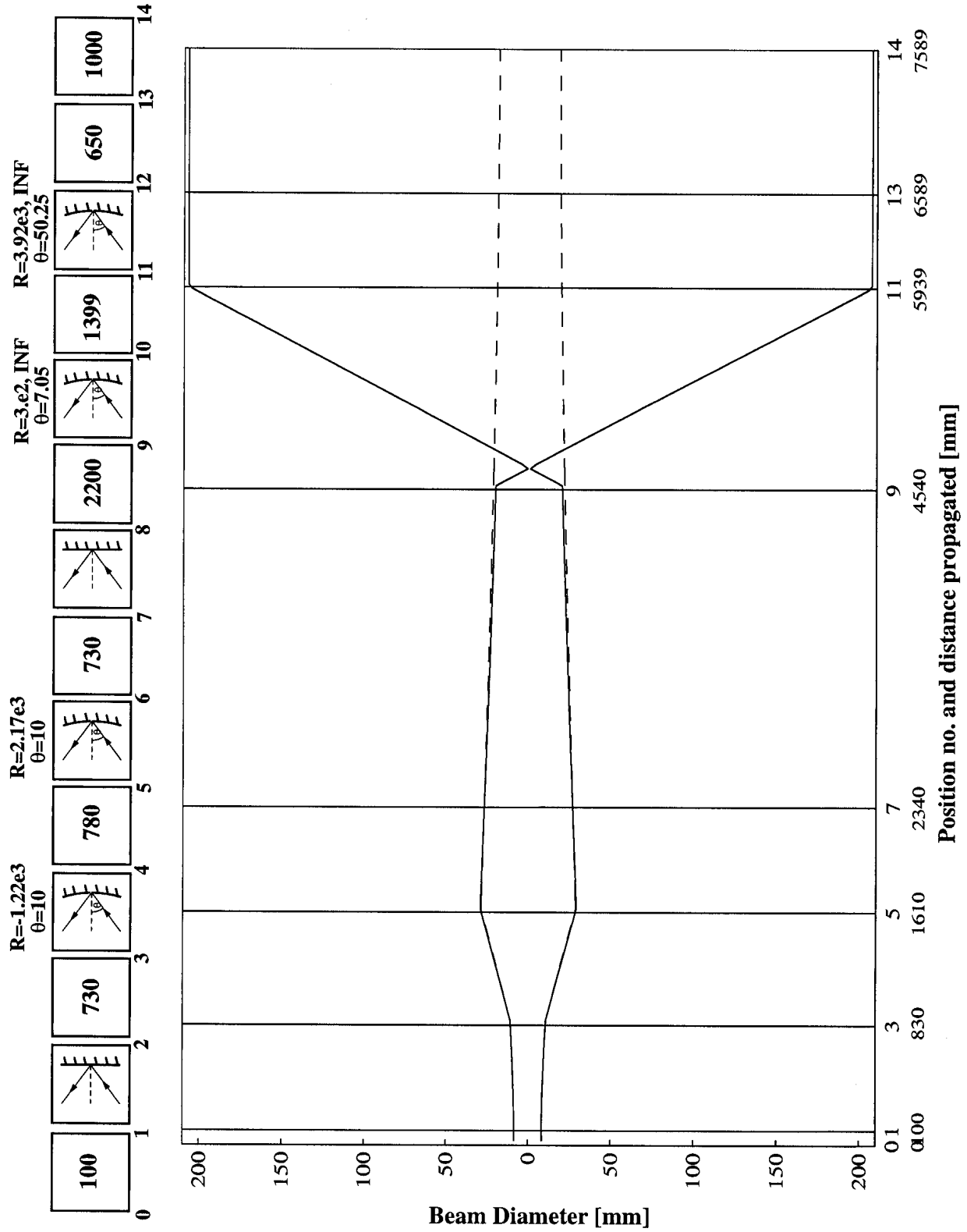

Figure 6.19: The results of the ABCD simulation of the LO beam from the waveguide exit to the main beam recombiner (position 13). The position numbers correspond to those in Fig 6.17. The full and dashed lines represent the two principle planes. All dimensions are in mm unless otherwise stated.

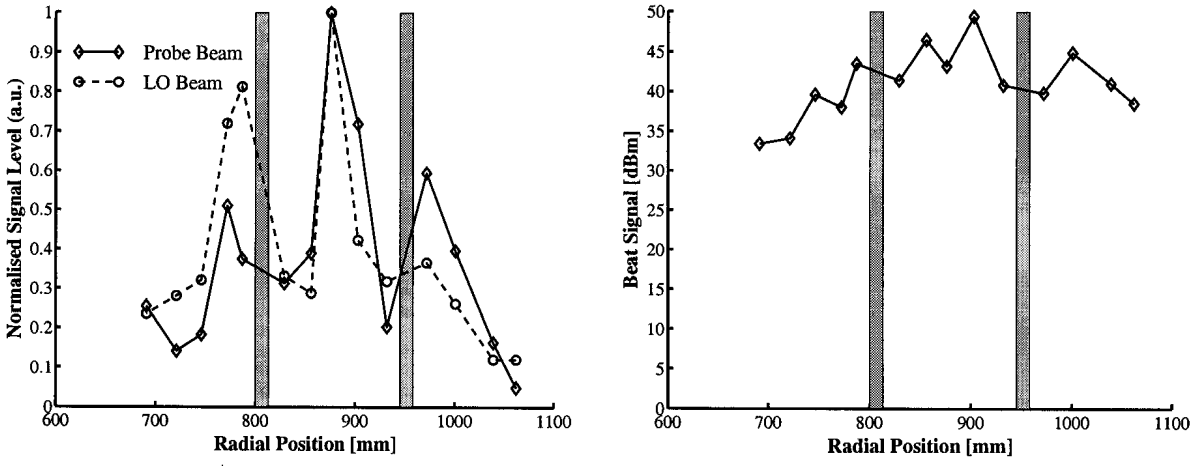

(a) (b)

Figure 6.20: (a) The measured chopped (@ 200 Hz) signal levels of both the probe and LO beams on detectors 1-14 (right to left) divided by the sensitivity of each individual detector element and normalised to 1 and (b) a logarithmic plot of the corresponding 100 kHz probe-LO beat signal levels. The shaded areas indicate the location of the metal spacers between the three TCV window sections (see Section 6.3.4).

which some assumptions and simplifications had to be made. The most important is the assumption of a paraxial condition which is not exactly the case here and the modelling of the parabolic mirrors as cylindrical mirrors. Accordingly, some adjustment to the mirror positions had to be made during the alignment process to ensure that both beams were parallel. In order to check the shape of the beams their individual power levels incident on the detectors were measured by chopping the beam at approximately 200 Hz. A plot is shown in Fig. 6.20(a) of the recorded levels divided by the individual detector's system optical responsivity which ranges from 2.7 kV/Watt on detector 7 (from right) to 9.6 kV/Watt on detector 9. The system optical responsivity is defined as,

$$Resp_{opt} = V_{out}/P_{det} \tag{6.4}$$

where V_{out} is the voltage response of the detector referred to the pre-amplifier input and P_{det} the power incident on the detector. The general shape of the two curves is similar but not Gaussian. The measured signals, however, are those of the outputs of the pre-amplifiers. A possible explanation for the non-Gaussian shape of the curves is that all the pre-amplifiers do not have the same gain at this relatively low frequency, the design frequency being 100 kHz. A logarithmic plot of the corresponding probe-LO beat signal levels at 100 kHz without optical responsivity scaling is presented in Fig. 6.20(b).

6.3.3 Reference Signal

Small portions of the probing and LO beams are split off, as shown in the enlarged section of Fig. 6.17, and are recombined on a 50:50 beamsplitter. The meshes which perform these operations are described in Section 6.2.2. The beams are then focused by a $R = 360$ mm spherical mirror into a small waveguide with an inner diameter of 10 mm. The waveguide conveys the beams, as shown in Fig. 6.17, to the reference detector element (see Fig. 6.24).

6.3.4 Windows

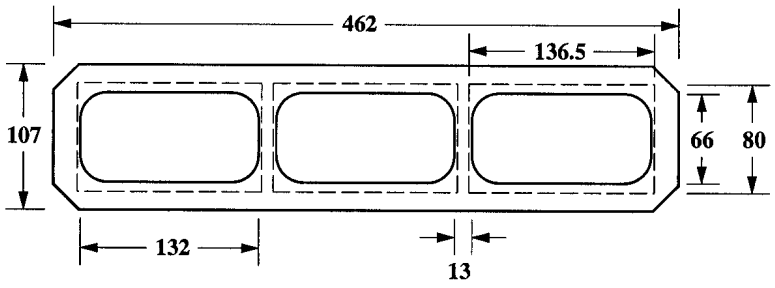

Figure 6.21: The interferometer/polarimeter windows on TCV showing the area covered by the large beamsplitters (dashed lines). All the dimensions are in mm.

The interferometer/polarimeter has access to the plasma in sector 12 of TCV through large windows at the bottom and top of the machine. The windows are divided into three identical section each 132 × 66 mm and divided by metal spacers of 13 mm as shown in Fig. 6.21. There is no access to the plasma at the very inner and outer edges of the vessel as shown in the the diagram of the interferometer/polarimeter chord positions (Fig. 6.22). The windows are mounted in water cooled flanges approximately 10 cm distant from the vacuum vessel. Cooling was foreseen as the entire vacuum vessel of TCV is regularly heated up to at least 300° C during bake-out. The flange was designed in such a way that in the case of a failure in the active cooling, passive radiative cooling of the flange would be sufficient to prevent the windows from breaking. The vacuum sealings are Viton O-rings which do not affect the integrity of the TCV vacuum. A shutter system also prevents the windows from being coated during glow and surface conditioning plasmas.

Crystal quartz was chosen as the window material as it has a high transmission at 214.6 μm and in the visible and is compatible with the vacuum vessel and temperature changes. The windows are 7.422 mm $\pm$ 3 μm thick Z-cut quartz which give an optimum transmission of 86% at 214.6 μm The remaining power is absorbed by the windows.

6.3.5 The Main Beamcombiner

As there is a polariser directly after the recombination device the desired splitting ratio of 50:50 for the beam recombination is only required for one polarisation (see Section 4.4) and consequently the 300 lpi mesh described in Section 6.2.2 can be used.

The beam re-combiner is placed at 45^0 to the TCV windows (see Fig. 6.17) and, therefore, a device of dimensions 600×70 mm approximately would be required to cover the entire open area of the windows (see Section 6.3.4). A mesh of this size was unavailable. These meshes are also very delicate and the damaging of one section would necessitate the replacement of the entire device. Therefore, it was decided to divide the beamsplitter into three equal sections corresponding to the divisions in the window (see Fig. 6.21) and to make the gaps between the sections as small as possible to aid the alignment and to allow for some refraction of the beam (see Section 3.2). Accordingly, 5 mm thick fibreglass frames with borders of 3.5 mm and gaps of 198×80 mm were machined. The effective area of the windows covered by the meshes is shown in Fig. 6.21. As can be seen this area (136.5×80 mm) is only slightly larger than that of the window sections. For general stability of the system, however, the frames could not be made any thinner nor the edges narrower than the values quoted above.

The relatively large meshes were stretched on a custom designed circular stretching frame before being glued onto the fibreglass frames. They are mounted on an adjustable fibreglass support which allows for their alignment.

6.3.6 Polariser

A wire grid polariser supplied by QMC Instr. Ltd. has been placed at the entrance to the waveguide array (see Fig. 6.17). It has been positioned so as to pick out the required polarisation prior to the beams entry into the waveguides (see Chapter 4) in order to avoid the possible mixing of the two polarisations in the waveguides. It has aperture dimensions of 460×60 mm, a line spacing of 25 μm and a line thickness of 10 μm with the wires spun parallel to the short side. A similar, but smaller polariser, has been placed at the entrance to the reference waveguide.

6.3.7 Waveguide Array

The beams are conveyed to the detector array by means of an series of 14 individual waveguides with internal diameters of 10 mm as shown in Fig. 6.17. The vertical positions of the individual guides can be adjusted to alter the radial positions of the chords. The

waveguides have one 90° bend as shown for which there is a small internal adjustable mirror. The waveguides were set for the chord positions listed in Table 6.23 and also shown relative to the TCV vessel in Fig. 6.22.

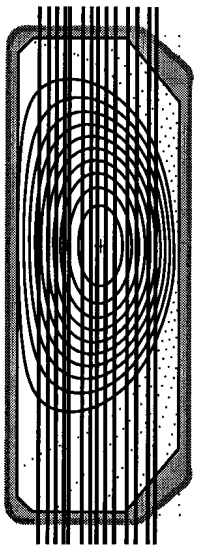

Figure 6.22: The TCV vessel including the tiles and the positions of the interferometer/polarimeter chords.

Chord Number	Major Radius [mm]
1	1062
2	1039
3	1001
4	972
5	932
6	903
7	876
8	856
9	829
10	787
11	772
12	746
13	721
14	691

Figure 6.23: The chord numbers and their corresponding radial positions.

6.4 Detectors

The detection system consists of an array of 15 InSb hot electron bolometers in a single liquid Helium cryostat and was supplied by QMC Instruments Ltd.. An optical high-pass filter has been built into the cryostat to protect against the gyrotron radiation. An attenuation of 90 dB at 120 GHz was specified by the manufacturer. The detectors have an extremely low NEP in the order of 10^{-12} W/Hz$^{-1/2}$ (@214.6 μm). The responsivity is in the order of 100 V/W and the frequency response goes up to 750 kHz.

The detectors are positioned on a support structure which has been placed far enough away from the tokamak, as shown in Fig. 6.17, to avoid the possible influence of stray magnetic fields.

The positions of the detector elements on the detector cold plate are shown in Fig. 6.24. The alignment of the beams onto the InSb detector elements is relatively easy as they are not polarisation sensitive and the radiation is collected by a simple Winston cone.

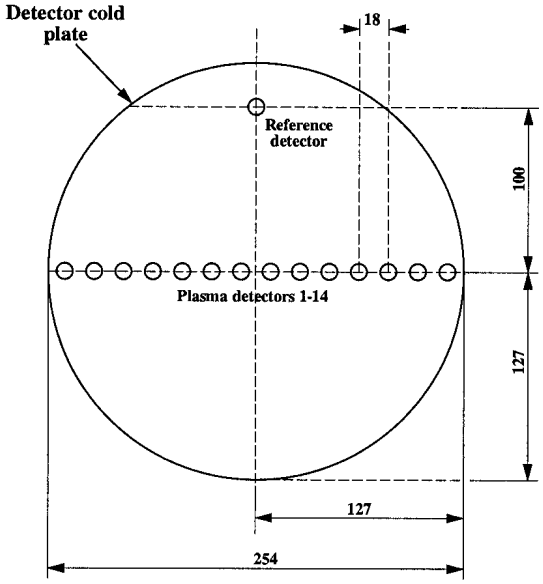

Figure 6.24: A schematic of the detector cold plate showing the detector element positions. All dimensions are in mm.

The detectors are equipped with pre-amplifiers divided between three boxes attached to the cryostat which are controlled remotely via an RS-232 interface. The pre-amplifiers include a low-pass filtering stage with a cut-off at 200 kHz.

Cryogenics

The InSb detector array is cooled to liquid Helium temperatures with the He reservoir requiring refilling once every three weeks. This refill cannot be performed with the detector system in position on top of the tokamak and it must, therefore, be brought down regularly to ground level. To facilitate the correct repositioning of the detector system its base plate and support structure have been equipped with a set of conical pins and holes. All the cabling required for the detector was designed to be easily disconnected.

As the liquid Nitrogen reservoir requires refilling every 2-3 days an automatic refill system was installed. This includes a vacuum line between the main TCV Liquid N_2 line and the detector reservoir and a system of valves and thermocouples which ensure that this line is pre-cooled before the filling of the detector reservoir commences.

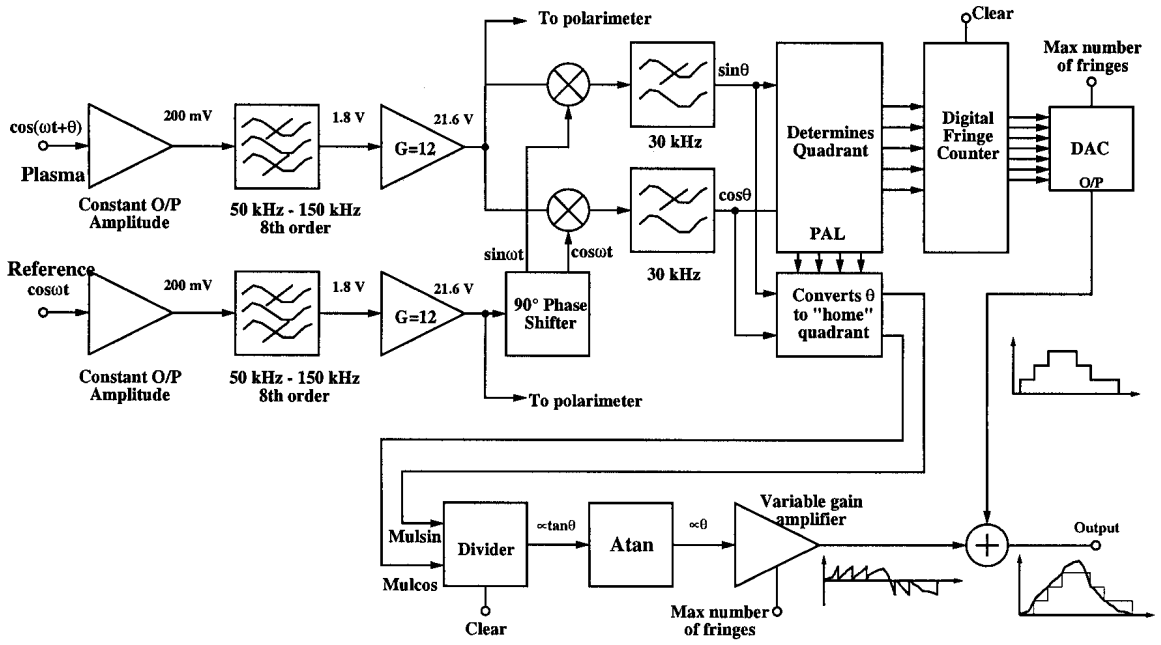

Figure 6.25: A schematic of the interferometer electronics.

6.5 Electronics

6.5.1 Interferometer

The interferometer electronics, shown schematically in Fig. 6.25, can be divided into two distinct sections namely the demodulator which extracts the phase information from the detected signals and the fringe counter which counts the measured fringes. The first stage of the demodulator is a constant output voltage amplifier (COA) which ensures that the signals have an amplitude of approximately 200 mV_{pp} at its output. The next stage is an 8th order band-pass filter with a pass-band between 50 and 150 kHz which filters out the unwanted low frequency terms (see Chapter 4). The filtered signals are then amplified up to approximately 21.6 V_{pp}. These signals also serve as the input to the polarimeter electronics (see Section 6.5.2). The reference signal is then passed though a 90° phase shifting circuit producing both its sine and cosine which are then multiplied individually with the probe signal. The resulting signals are low pass filtered to produce the sine and cosine of θ, the phase difference between the reference and probe signals.

The fringe counter consists of a digital part which counts 1/4 fringes (90°) and an analogue part which fills in the inter-fringe trace. The analogue section consists of a divider which produces a signal proportional to $\tan\theta$ and a circuit which simulates the operation arctan thereby producing an output proportional to θ. The summation of the digital and analogue outputs produces the complete output trace. A PAL (Programmable

Array Logic) controls both the digital counter and converts the angle into the home quadrant for the analogue measurement. In both sections a positive voltage on the *Clear* input sets the output to zero. The *maximum number of fringes* input sets the volts per fringe ratio and the outputs are scaled accordingly.

6.5.2 Polarimeter

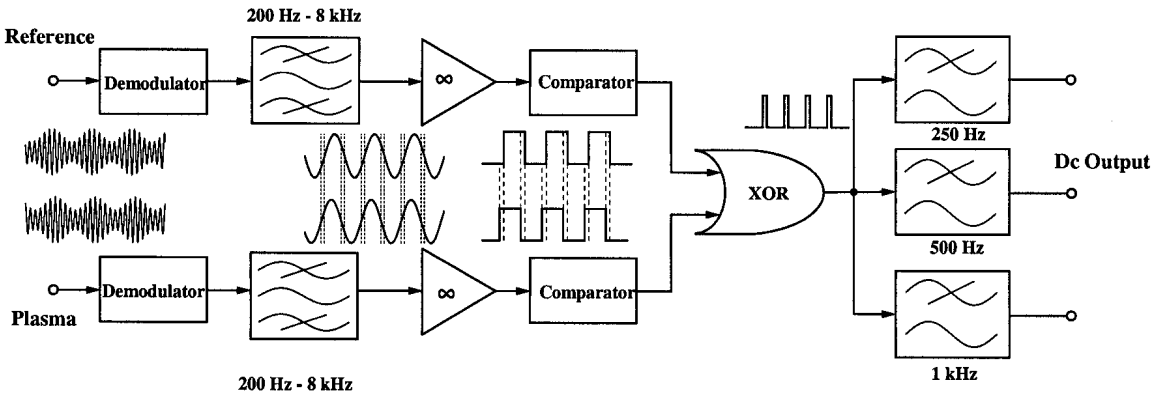

Figure 6.26: A schematic of the polarimeter electronics.

The polarimeter detection electronics, shown schematically in Fig. 6.26, were designed, constructed and tested in UCC. They are based on the preliminary electronic hardware also produced in UCC and used during the bench tests. The inputs are amplitude modulated signals with the design carrier frequency of 100 kHz. The modulation frequency, set by the spindle, is limited to approximately 3 kHz for Method 1 and half that for the Method 2 (see Section 6.2.4). The polarimeter information is contained within the phase shift between the modulation envelopes of the plasma and reference signals.

The inputs are taken from the outputs of the initial filter/amplifier stage of the interferometer electronics (see Section 6.5.1). The signals are electronically demodulated using a standard diode-resistor-capacitor arrangement discussed in Section 4.5.1 and then band-pass filtered (200 Hz - 8 kHz). The phase comparison is performed by passing the demodulated signals through high-gain amplifiers followed by comparators which produce square waves. An XOR gate then produces a train of pulses with widths proportional to the phase difference between the two modulation envelopes. The pulse train is then low-pass filtered producing a dc voltage level proportional to the phase difference.

A final design was adopted in which a single electronics board was assigned to each channel. Each board can, therefore, function as either a reference or measurement channel. The block diagram in Fig. 6.27 shows the various features incorporated into the

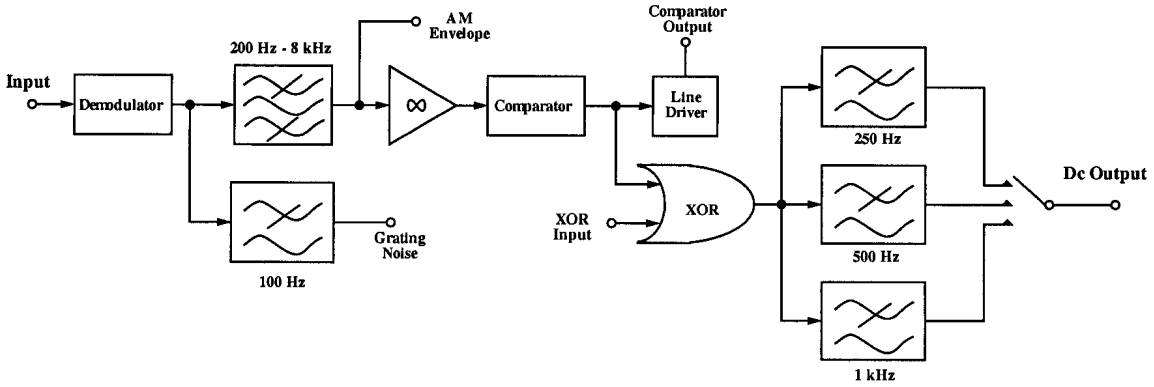

Figure 6.27: A block diagram illustrating the main electronic features incorporated into the design of a single channel polarimeter board.

design of a single channel board. Access to various signals for monitoring purposes was intentionally included in the design. The demodulated signal can, for example, be examined via a connector on the front panel. A further tap-off point is provided to monitor any low frequency fluctuations arising from grating imperfections. A line-driver was also incorporated into each board so that when operating as the reference board it would be capable of driving the XOR gates on all 14 measurement boards.

A separate filter is also included to pick-out the low frequency term used in setting the phase difference ϕ_0 between the **A** and **B** beams to zeros as described in Section 4.4.

An important feature of the electronics is the ability to select the time resolution of the polarimeter measurement. This is performed by the inclusion of three separate final low-pass filters with cut-off frequencies of 250 Hz, 500 Hz and 1 kHz. The filters are shown in both Fig. 6.26 and Fig. 6.27 as having the same inputs whereas in fact they are cascaded with the input of each progressively lower filter being the output of the previous. Connections from the outputs of the filters are fed to a rotary switch mounted on the front panel which is in turn connected to the output connector.

The boards are mounted in a standard 19 inch rack which included a power supply with sufficient capacity to supply all the boards. A front panel distribution junction was also provided to facilitate the connection of the comparator output from the reference board to the 14 separate XOR inputs on the measurement boards.

6.6 Calibration

Theoretically the output of the polarimeter electronics should scale linearly with the Faraday rotation angle. Experimentally, however, this is not necessarily the case and a

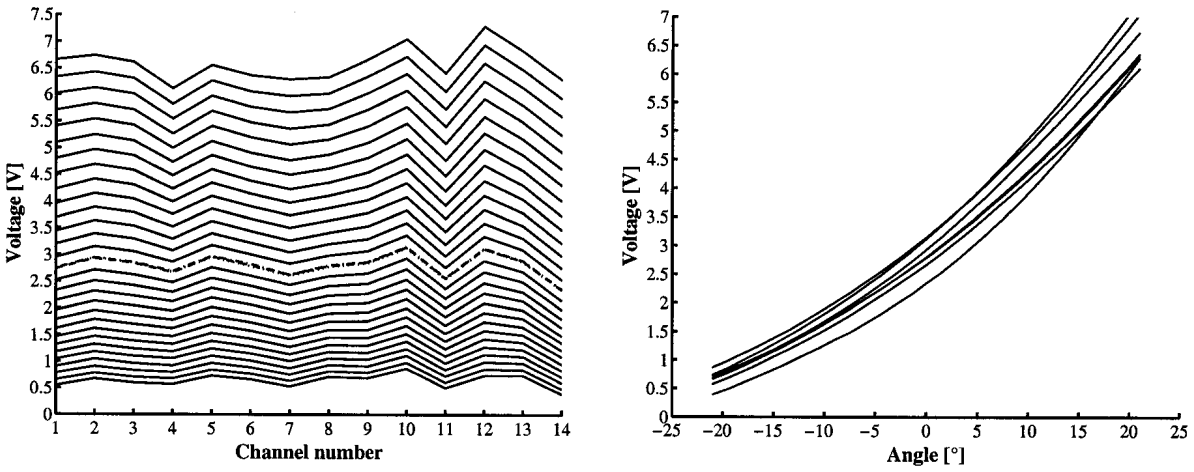

(a) (b)

Figure 6.28: (a) Typical calibration data for the 14 channels stepped though $\pm 21^o$ in steps of 1.5^o and (b) a selection of the corresponding calibration curves as a function of equivalent Faraday rotation angle. Also included in (a) are the signal levels before (dotted) and after (dash-dot) the calibration and at an intermediate stage (dashed). In this example these three lines coincide, indicating a correct calibration sequence.

calibration of the entire system is required. The calibration of the polarimeter is performed by stepping a $\lambda/2$ plate placed in the probing beam path, as shown in Fig. 6.17, though a series of angles and acquiring the output levels of the polarimeter electronics for each channel at each position. The resulting calibration curves are fitted to a polynomial of up to 8 coefficients which is then used to convert the raw data into its corresponding rotation angle. To differentiate between positive and negative rotations an offset greater than the expected maximum rotation is introduced (see Section 3.4).

Prior to commencing the calibration sequence checks are made to ensure that the noise level and the offset are acceptable. The plate then is turned anti-clockwise through the maximum desired angle and stepped successively clockwise with the desired step size until the maximum angle is reached. An acquisition of the signal levels is made after each step. Checks are then made to ensure that the initial, intermediate (when the plate passes though the "zero"position) and final signal levels agree within a certain precision and that the resulting calibration curve for each channel is monotonic. The failure of any of the checks leads to the calibration being aborted. Data from a typical calibration of the 14 channels along with a selection of the corresponding calibration curves are shown in Fig. 6.28.

U100 Controller

The $\lambda/2$ plate is placed in a precision rotary positioning stage mated to a Unidex U100 motion controller. The controller has a resolution of 4000 steps/rev and combined with the motor-to-table ratio of 54:1 produces a system resolution of 0.1 arc min per step. The calibration is, however, usually run with steps sizes no smaller than the equivalent of 0.5^o Faraday rotation (or 0.25^o actual). The system is run under a host mode controlled via an RS-232 interface.

Chapter 7

Experimental Results

This chapter presents the results obtained from interferometer/polarimeter measurements on TCV. The main results of the 14 channel interferometer, upgraded from a 6 channel instrument, are discussed. A method employed to remove perturbations due to vibrations from low density plasmas is briefly presented. A density profile reconstruction method is then presented and the results compared with the LIUQE calculated profiles and the parabolic fits used previously.

The polarimeter results with the instrument operating with both Methods 1 and 2 are presented and the Faraday rotation profiles compared with the predicted values. A method employed to directly determine the central safety factor q_0, from the polarimeter data is presented. This calculation requires the slope of the Faraday rotation profile, the electron density and some geometric parameters and is effectively independent of the reconstruction code LIUQE.

The results of the reconstruction of the plasma equilibrium, both with and without the inclusion of the interferometer/polarimeter data are presented. The temporal evolution of the reconstructed q_0 was seen to differ substantially from the polarimeter determined value. A re-definition of the base functions employed during the run, however, produced a q_0 which were in closer agreement with the polarimeter calculations. LIUQE was then re-run to include the Thomson scattering pressure information and the q_0 was again seen to differ from that predicted by the polarimeter and the x-ray tomography. By introducing an additional constraint on the pressure profile the reconstruction resulted in values which were in better agreement with the measurements. Based on these results a new standard equilibrium reconstruction run for high elongation plasmas is then proposed.

It was seen that the accuracy of the polarimeter data is not yet at the level where its inclusion as input to the reconstruction code results in an obvious improvement in the determination of q_0. Possible modifications to and improvements of the instrument which could lead to an increased precision are discussed briefly.

7.1 Interferometer

The FIR interferometer is the main TCV density diagnostic and also provides the control signal for the density feedback system. The potential interferometer temporal resolution of 100 kHz (see Section 6.3) is presently limited by the acquisition system to 5 kHz. The density feedback input is taken from the output of the central (channel 6) fringe counter. To ensure the attainment of the requested plasma this signal should be free from fringe jumps.

An example of the temporal evolution of the line-integrated density of a typical TCV plasma is shown in Fig. 7.1. This shot (#13987) is a diverted plasma which can be seen to make multiple L to H-mode and H to L-mode transitions, observable as the sharp density rises and drops.

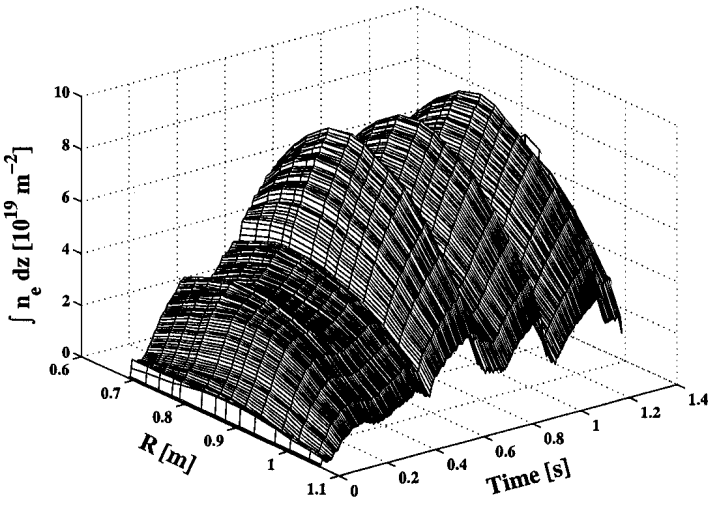

Figure 7.1: The temporal evolution of the line-integrated density of shot #13987 showing three L-mode to H-mode transitions.

The *sin* and *cos* of the interferometer phase which are produced at an intermediate stage of the interferometer fringe count electronics (see Section 6.5.1) are also acquired with the same acquisition frequency as the outputs of the fringe counters and the polarimeter electronics. These signals can be used to reconstruct the interferometer phase in the event of multiple fringe jumps on the interferometer fringe count signals. The interferometer electronics are also equipped with constant voltage output amplifiers which ensure that the signals entering the fringe counters have a constant amplitude (see Section 6.5.1). The time constant of the feedback of this amplifier was designed to be of the order of some seconds so as not to react during a typical TCV shot. Fluctuations of the signal levels on the detectors during a shot can, therefore, be monitored.

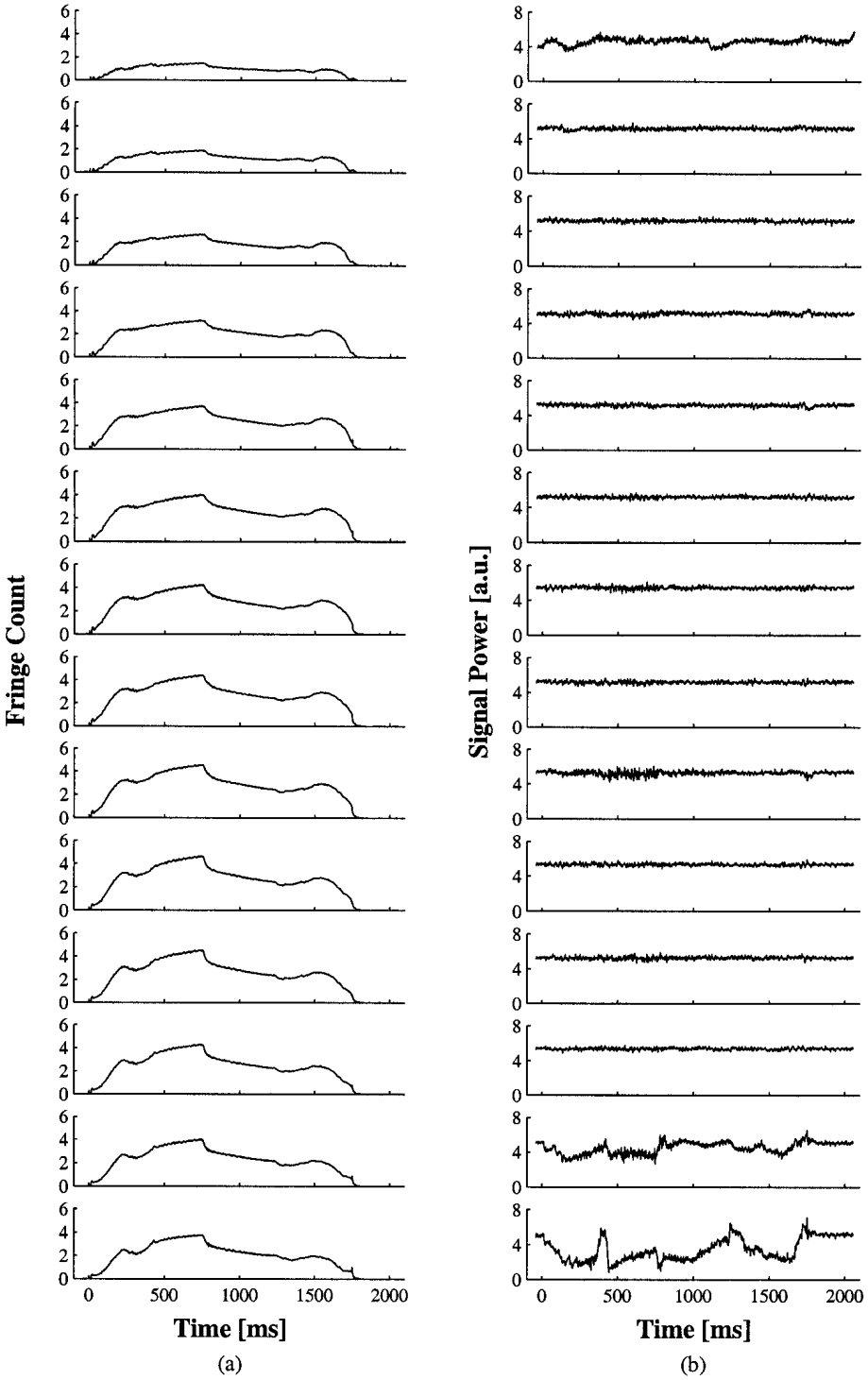

Figure 7.2: The (a) fringe count of a typical standard shot (#15104) and (b) the corresponding signal power levels (channels 1 – 14 top to bottom).

A standard shot is run at the start of daily operation to check the condition of the machine. This shot is a diverted plasma with a maximum central electron density in the order of $n_{e0} = 7 \times 10^{19}\ \mathrm{m}^{-3}$. The interferometer traces from a typical standard shot #15104, are shown in Fig. 7.2 along with the corresponding detector signal levels. The fluctuations in the amplitude of the signals on the edge channels indicates some refraction of the beam at these positions. The channels exhibiting the largest refractive effects are channels 13 and 14 which are probing the inside of the plasma close to the divertor leg as can be seen in the plot of the probing channel positions and the flux contours of the shot at time $t = 1$ s in Fig. 7.3(a). The temporal evolution of the line-integrated density of this shot is shown in Fig. 7.3(b).

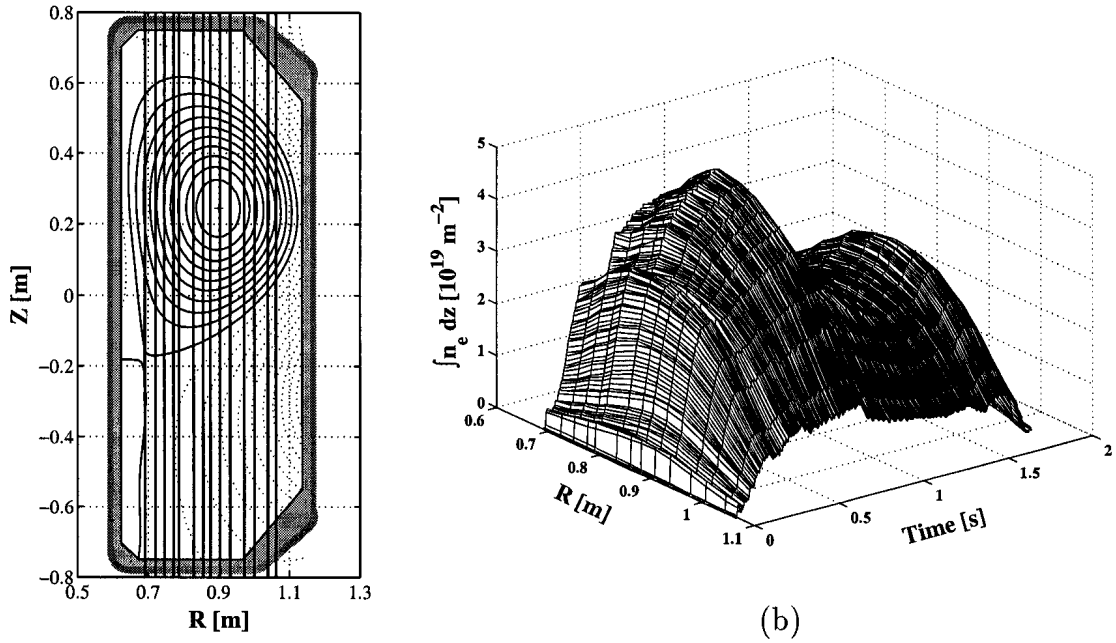

(a) (b)

Figure 7.3: (a) The flux contours of a typical standard shot (#15104) at time $t = 1$ s showing the channel positions $1 - 14$ (right to left) and (b) the temporal evolution of the line-integrated density.

As previously mentioned in Section 3.1, the expected fringe count of typical ECRH target plasmas is relatively low and set the lower limit of the range of acceptable operating wavelengths. The flux contours of a typical ECRH shot #14146, are shown in Fig. 7.4(a) at time $t = 0.7$ s and the temporal evolution of the line-integrated density in Fig. 7.4(b). The maximum line-integrated density is about 1.2 fringes or $1.2 \times 10^{19}\ \mathrm{m}^{-2}$. It can be seen that the changes in line-integrated density are well resolved even for these low density plasmas.

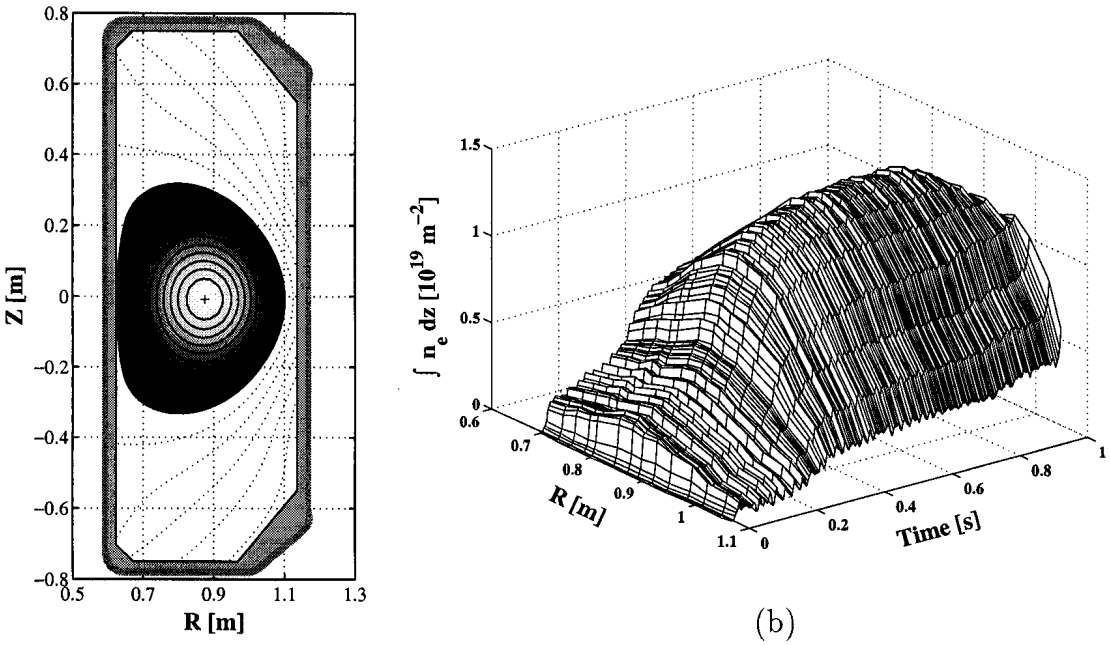

Figure 7.4: (a) The flux contours of a typical ECRH plasma (#14146) at time $t = 0.7$s and (b) the temporal evolution of the line-integrated density.

7.1.1 Vibrations

Vibrations of components in the system which perturbate the signals have been observed during TCV shots. These perturbations could possibly be due to vibrations induced on the optical components around the vessel (see Section 6.3) by magnetic forces. The effect of these vibrations is significant for low density plasmas.

One method which can be employed to remove the effect of the vibrations is to use a compensating interferometer. The traditional approach, discussed in Section 3.3, is to install two interferometers of different wavelengths on the same support structure. The shorter wavelength is chosen to be sensitive mainly to the vibrations while the longer wavelength measures the plasma parameters. The interferometer/polarimeter on TCV has not yet been equipped with such a device. However, the tokamak does have a a second single channel interferometer which operates at a wavelength of 2 mm. An instrument operating at this relatively long wavelength is much less sensitive to vibrations than the FIR interferometer (see Section 3.3). This instrument is also completely de-coupled from the FIR interferometer support structure and probes the plasma at $R = 880$ mm which is reasonably close to channel 7 ($R = 876$ mm) of the FIR interferometer/polarimeter. This diagnostic provides a signal, proportional to that of the FIR channel, which can be used

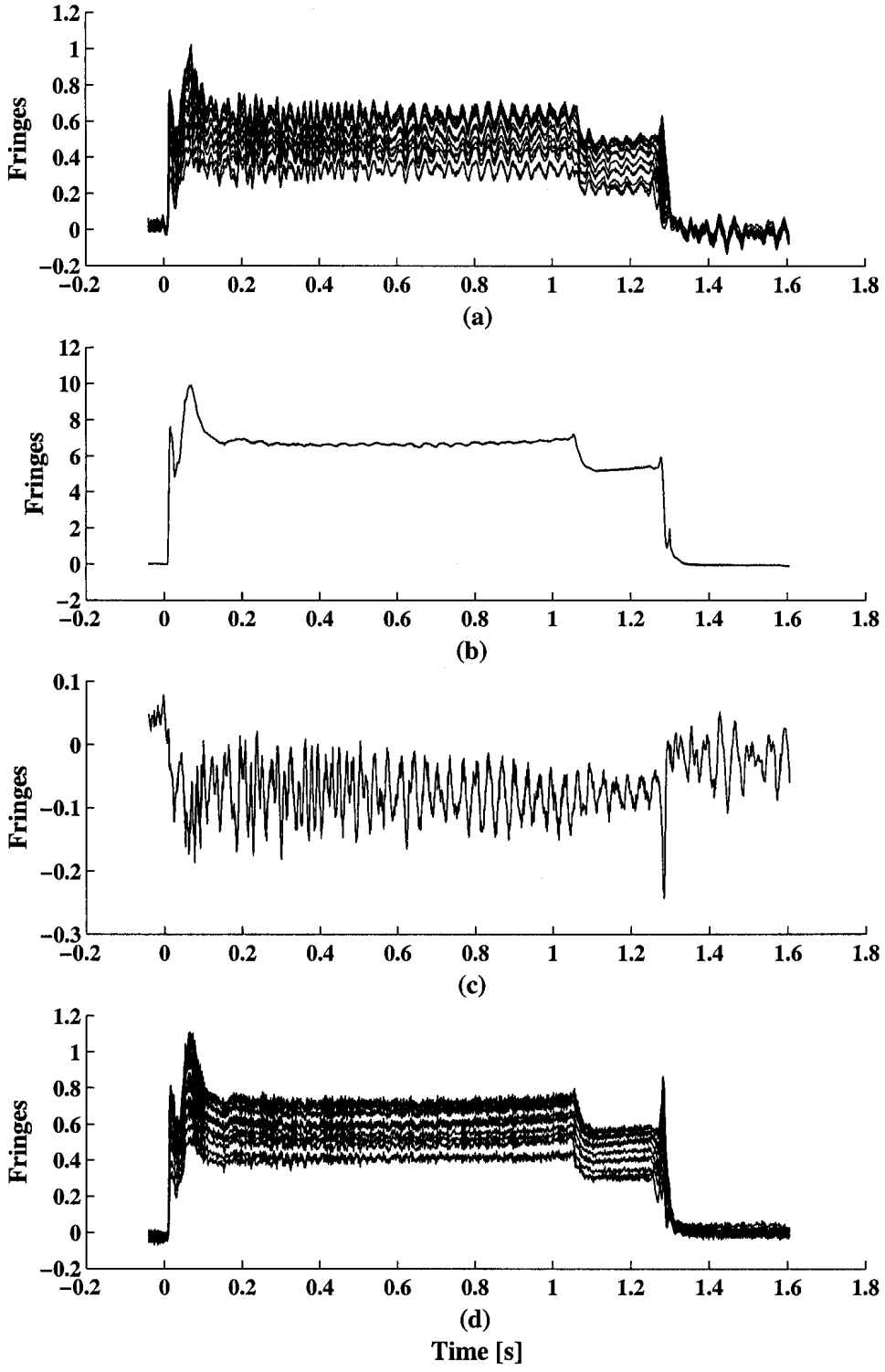

Figure 7.5: (a) The raw FIR fringe counts for shot #14869, (b) the 2mm interferometer fringe count, (c) the scaled 2 mm fringe count subtracted from the FIR fringe count of channel 7 and (d) the corrected FIR fringe counts.

as a reference with which the vibrations on the FIR channel can be determined. These vibrations can then be subtracted from all the FIR channels. The effectiveness of this method is limited as it assumes that the vibrations are equal on all channels.

This method has been used with success on low density plasmas where the effect of the vibrations is relatively high. An example is shown in Fig. 7.5 for shot #14869. The first plot in the figure shows the raw FIR fringe counts with coherent oscillations obvious on all channels. The second plot shows the fringe count of the 2 mm interferometer which does not exhibit these oscillations, thus ruling out plasma effects. The residual trace from FIR channel 7 after the subtraction of the appropriately scaled 2mm trace is shown in the third plot and the compensated FIR traces in the final plot. The corrected interferometer traces show a significant improvement over the raw signals though some vibrational components still remain.

7.1.2 Density Profile Reconstruction

To obtain the local electron density from a small number of measurements it is necessary to assume that the surfaces of constant density are known. It is usually assumed that they coincide with the tokamak flux surfaces, since the parallel particle diffusitivity along the field lines is very high. The density profile reconstruction method employed to reconstruct the TCV density profiles is a base function method where it is assumed that the density can be expressed as a function of the flux coordinate ρ, where,

$$\rho = \sqrt{1-\varphi} = \sqrt{\frac{(\psi_{ax}-\psi)}{(\psi_{ax}-\psi_{lcfs})}}. \tag{7.1}$$

with ψ_{lcfs} and ψ_{ax} the values of the poloidal flux function at the last closed flux surface and magnetic axis, respectively. The flux φ is normalised to 1 at the plasma centre and 0 on the last closed flux surface. The density is then reconstructed from a series of base functions b_i, with weights a_i and can be expressed as,

$$n_e(\rho,t) = \Sigma a_i(t) b_i(\rho). \tag{7.2}$$

The line-integrated density y_j, on a chord j can then be expressed as,

$$\begin{aligned} y_j(t) &= \int n_e(\rho,t)\frac{\mathrm{d}l_j}{\mathrm{d}\rho}\mathrm{d}\rho \\ &= \Sigma a_i(t) B_{ij}(t) \end{aligned} \tag{7.3}$$

with

$$B_{ij}(t) = \int b_i(\rho)\frac{\mathrm{d}l_j}{\mathrm{d}\rho}\mathrm{d}\rho \tag{7.4}$$

where $dl_j/d\rho$ depends on the geometry of the plasma and varies over time. The equation for a series of probing chords can then be written as,

$$\mathbf{Y}(t) - \mathbf{a}(t)\mathbf{B}(t) = 0. \tag{7.5}$$

This equation is then solved for $\mathbf{a}(t)$ using a least squares fit. If the same number of base functions as measurement channels are used the fit will converge to the correct values on the measurement channels but can result in spurious values at other positions. In order to avoid this a second order regularisation is used in which the slope of the profile is forced to be smooth by also minimising the second derivative $\alpha\mathbf{a}(t)\mathbf{B}''(t)$, where the degree of smoothness is set by the regularisation parameter α.

The base functions employed are 14 equally spaced ($\Delta\rho = 0.1$) Gauss functions with equal widths of 0.2. In general the error involved in the least squares fit χ^2, is of the order of the number of channels used. The regularisation parameter α, was varied for a selection of shots and a value of $\alpha = 0.03$ was seen to produce values of χ^2 close to the number of channels for most shots and was therefore chosen as the default value.

Equilibrium Reconstruction Code

The density profiles are also fitted during the runs of the equilibrium reconstruction code LIUQE which include the interferometer and polarimeter data as input (see Sections 3.5 and 7.3). It is again assumed that the density can be expressed in terms of poloidal flux φ, with,

$$n_e = \sum_{n=0}^{N_n} c_n W_n(\varphi) \tag{7.6}$$

where,

$$W_n = \varphi^n. \tag{7.7}$$

The number of base functions is usually set to either $N_n = 3$ or $N_n = 4$. LIUQE was run for a series of high elongation shots with these two values of N_n. The resulting density profiles as a function of normalised flux φ, are plotted in Fig. 7.6(a) for shot #14788 at time $t = 0.6$ s and in Fig. 7.6(b) for shot #15167 at $t = 0.65$. Both plots also show the reconstructed profiles obtained using the base function method described above and from a parabolic fit described in Section 3.2. The plots show that for both shots the LIUQE density profiles follow the base function reconstructed profiles quite well and that there is no significant improved in using $N_n = 4$. The profiles show a slight dip in the centre of the plasma which can possibly be attributed to the limited weight of the central density to the line-integrated measurement. The parabolic fit, shown as a dotted line in both

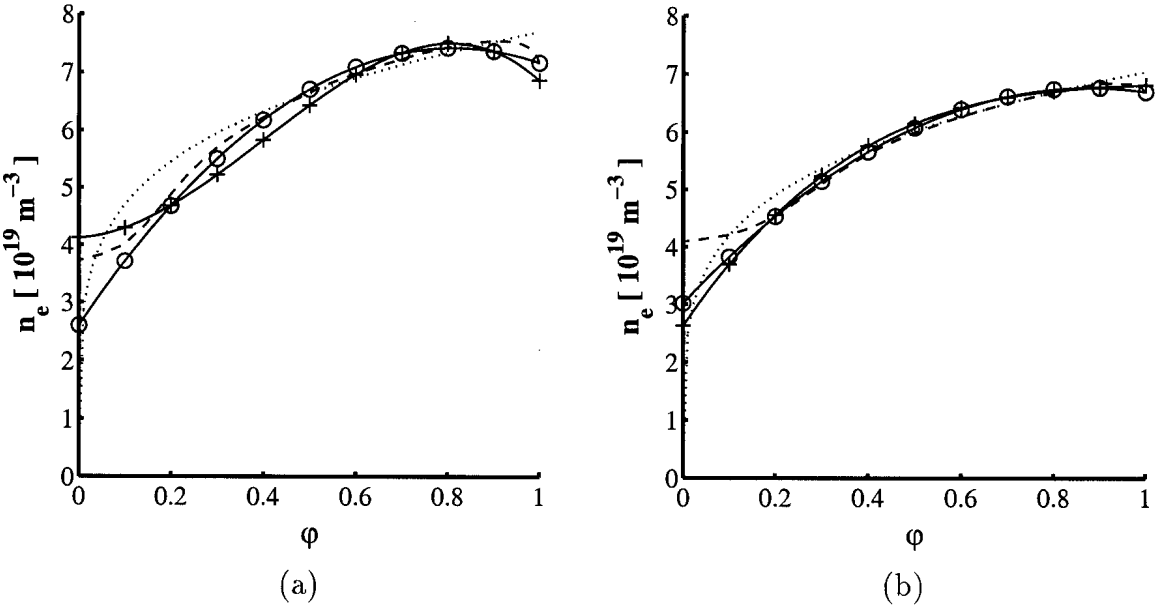

Figure 7.6: The reconstructed density profile obtained using the base function method (dashed line), the parabolic fit (dotted line) and the LIUQE fits with $N_n = 3$ (circles) and $N_n = 4$ (crosses) for shots (a) #14788 at time $t = 0.6$ s and (b) #15167 at $t = 0.65$ s.

plots, also shows a reasonable agreement with the reconstructed profiles which justifies its employment in the calculations of Chapter 3. This fit will continue be used in all further calculations. The effect of the refraction of the beam by the plasma is assumed to be small and has been neglected throughout these calculations (see Section 3.2).

7.2 Polarimeter

The polarimeter was routinely run during the high elongation plasmas of TCV where rotation angles $> 10^o$ are expected (see Section 3.4). A calibration was generally run either just before or just after each shot with steps of 1.5^o (see Section 6.6).

A plot is shown in Fig. 7.7 of the highest Faraday rotation obtained to date and its corresponding line-integrated density. The measurement of 20^o was obtained on shot #14226 at time $t = 0.65$s, smoothed over 20ms. Also included in the plot is the simulated profile calculated using the Jones matrix method described in Sections 2.2.2 and 3.4 with an assumed parabolic density profile (see Section 7.1.2). The simulated values show reasonably good agreement with the measurements, especially on the central channels.

The signal noise was seen to be, in general, higher than the level required to obtain the precision of 0.2^o required (see Section 3.5) being at about the equivalent of 0.5^o using

Method 1. The noise level was also seen to increase dramatically during the plasma shots, examples of which are shown in Fig. 7.8 for shots #14761 and #14886. The noise levels were very dependent on the stability of the laser and a lot of care had to be taken to tune the laser so as to avoid parasitic laser lines (see Section 6.1).

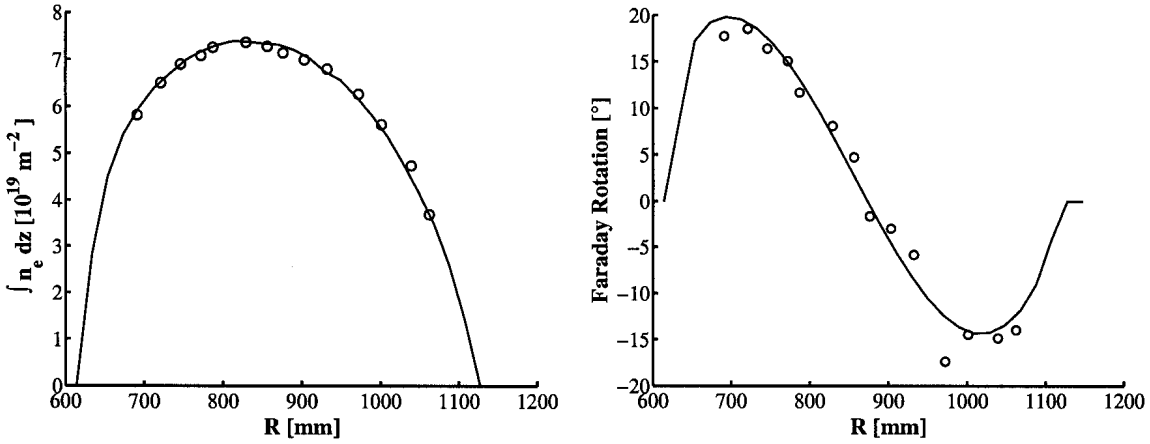

Figure 7.7: The (a) line-integrated density and (b) Faraday rotation profile, smoothed over 20 ms, of shot #14226 at time $t = 0.65$ s and the Jones matrix calculated values (full lines).

Experiments were performed in order to try and determine the source of this additional noise which led to the ruling out of the possibility of stray plasma light. The currents in the transformer coils were also seen to have a minor influence on the bias signal levels of the detectors. This small effect was only obvious during the steep ramping of the current at the start and end of the shot and could, therefore, be ignored. The additional noise on the polarimeter signals during the shot was seen, however, to depend quite strongly on the alignment of the beam though the tokamak. The large parabolic mirror under the TCV vessel which directs the beam through the tokamak (see Fig. 6.17) was seen to move slightly on its toroidal axis over time. The reason for this is unknown as the interferometer/polarimeter support structure is completely decoupled from that of the tokamak (see Section 6.3.1) and should, therefore, be unaffected by vibrations on that structure. The two shots in Fig.7.8 are similar shots produced before and after a a slight re-alignment of this large parabolic mirror. It can be seen that the relative noise on each channel is different for the two shots, in particular that of channel 11.

It was also noticed during the realignment process that there were beat signals on each detector element even when its corresponding window to the tokamak was blocked. The windows are divided into three separate sections as discussed in Section 6.3.4. The

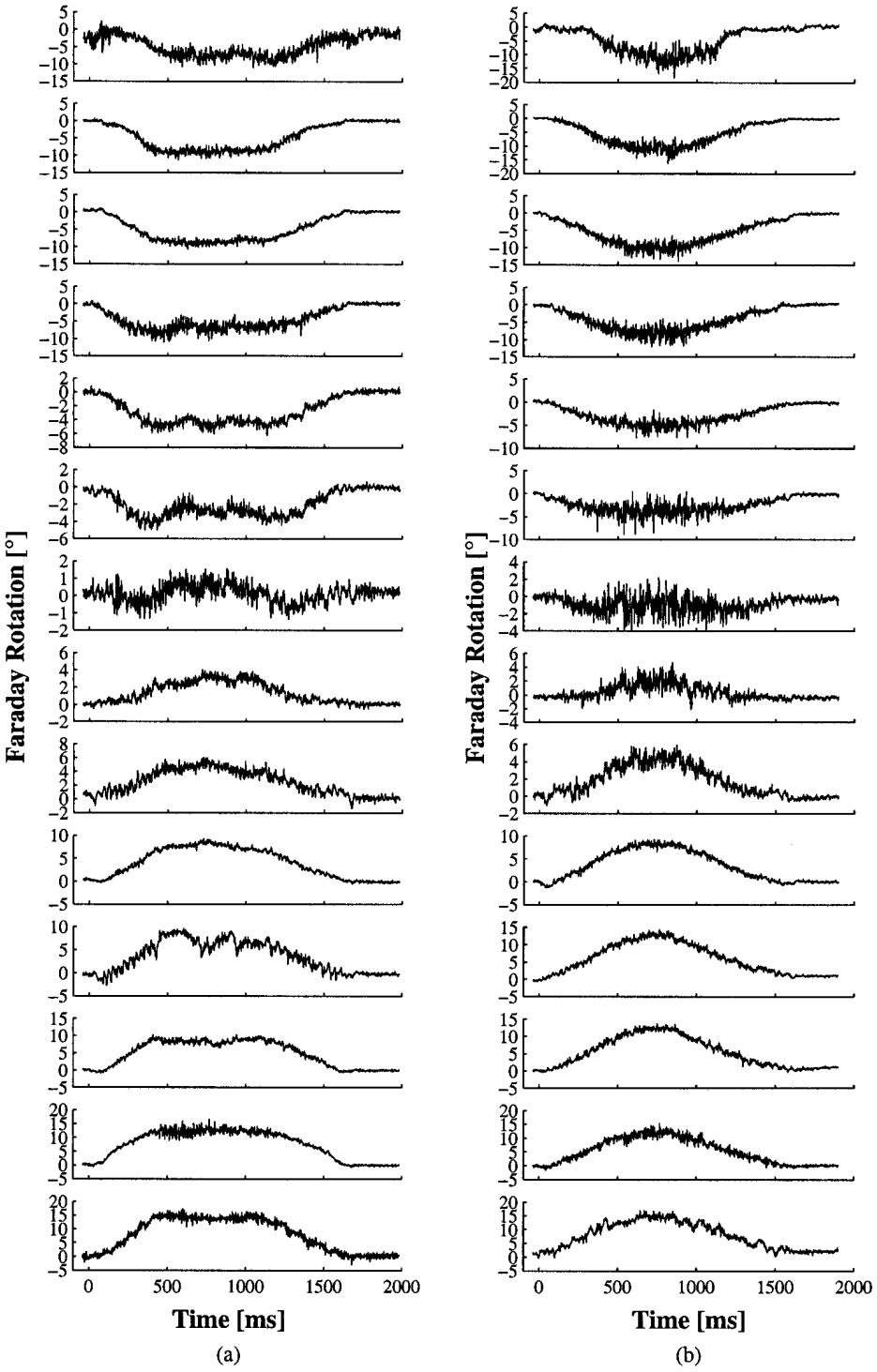

Figure 7.8: The Faraday rotation of channels 1 – 14 (top to bottom) for two similar shots measured (a) before (#14761) and (b) after (#14886) a slight change in the alignment of beam though the tokamak vessel.

amplitude of the signals varied with detector position being, in general, larger on the central channels. It was noticed, during the investigation of the source of these signals, that they disappeared when the edges of the adjacent windows were covered. This led to the conclusion that the source was diffraction of beam by the edges of the windows coupled with possible reflections of the diffracted beam inside the vessel. Accordingly, 14 individual TPX lenses with a focal length of 150 mm were placed in a support just under the main beam-combiner in order to focus only that part of the beam propagating straight through the tokamak onto the detectors. The lenses have dimensions 29×20 mm and are 3 mm thick and the space around them has been blocked by an absorbing material.

Only four high elongation shots were achieved after the installation of the lenses which makes the evaluation of their performance difficult. Of these shots two disrupted (#15166, 15167) and Method 2, which is inherently less precise than Method 1 which was run on all previous shots (see Chapter 4), was in operation during the other two shots (#15140, 15141). The installation of the lenses also coincided with an overall improvement in the alignment of the system. Further shots are, therefore, necessary in order to evaluate the performance of the lenses. The installation of the lenses has led, however, to the system being more susceptible to beam refraction.

The fringe counts and Faraday rotation traces from shot #15167 which disrupted at $t = 0.7$ s are shown in Fig. 7.10. Due to the refractive effects in the plasma near the central column the fringe count of channel 14 was unusable.

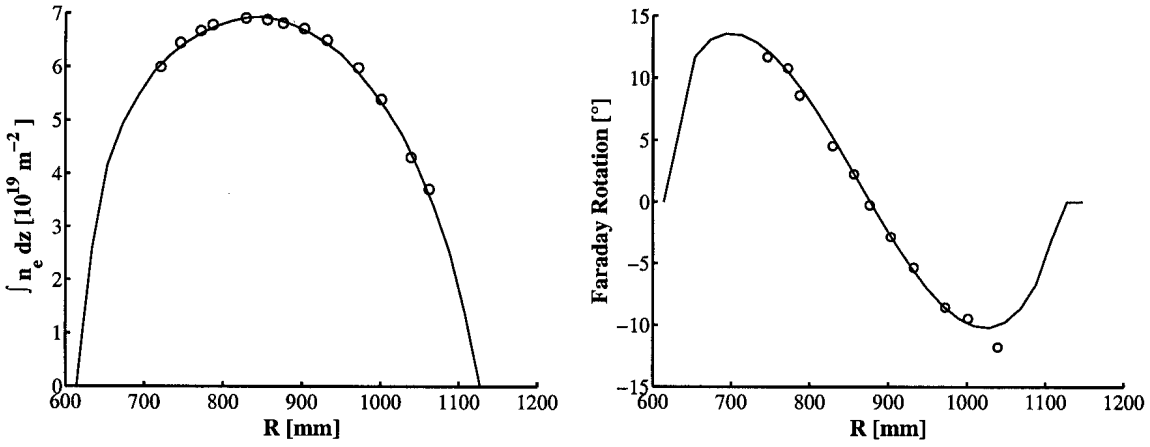

Figure 7.9: The (a) line-integrated density (channels $1-13$) and (b) Faraday rotation profile (channels $2-12$), smoothed over 20 ms, of shot #15167 at time $t = 0.65$ s. Also included are the Jones matrices simulated values (full lines).

The line-integrated density and the measured and simulated Faraday rotation profiles

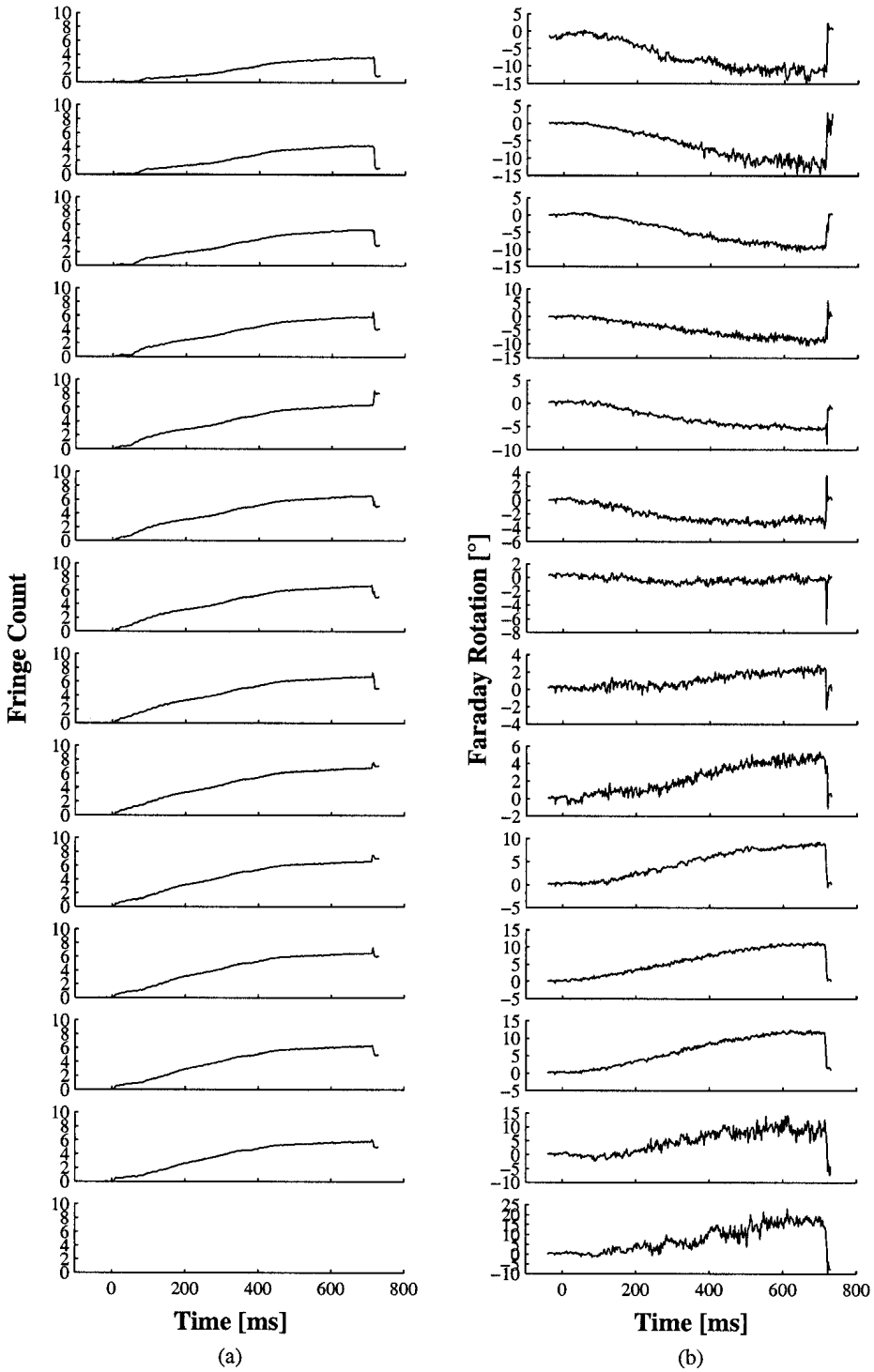

Figure 7.10: The (a) fringe count and (b) Faraday rotation for shot #15167 (channels $1-14$ top to bottom).

for this shot at time $t = 0.65$ s are shown in Fig. 7.9 for polarimeter channels $2 - 12$. The low signal levels coupled with the refraction made the edge channels unusable. The measurements in this case show better agreement with the simulated Faraday rotation than the previous example (see Fig.7.7). Again it is difficult to determine whether this apparent improvement is attributable to the lenses, the improved alignment or a better fit of the simulated data.

7.2.1 Method 1

As the polarimeter output of Method 1 inherently more precise than that of Method 2 (see Chapter 4) it was used initially to evaluate the performance of the instrument. The polarimeter is generally run with a modulation frequency of about 1.5 kHz with a time resolution of 4 ms set by the polarimeter electronics (see Section 6.5.2). The additional term on the interferometer signal due to the cross-talk from the polarimeter, discussed in Section 4.3.2, is, for the moment, simply filtered out in the post-processing of the data which also corrects for fringe jumps. The filter used is a 4th-order Chebychev stop-band filter with a 40 Hz band-width and a 20 dB stop-band attenuation. Zero-phase digital filtering is performed by processing the input data in both the forward and reverse directions. The resulting filtering has precisely zero-phase distortion and double the filter order. An example of typical signals before and after post-processing is shown in Fig. 7.11 for shot #15070.

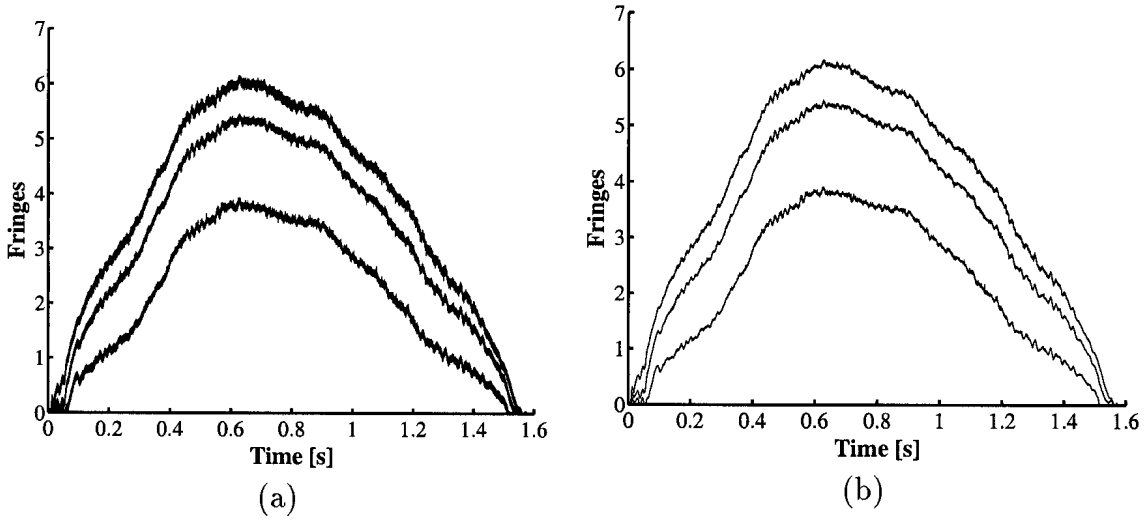

Figure 7.11: The (a) raw and (b) filtered fringe counts of shot #15070 for a selection of the 14 interferometer channels.

The Faraday rotation profile, smoothed over 20 ms, of shot #14886, whose Faraday

rotation traces were plotted in Fig. 7.8(b), is shown in Fig. 7.12 at time $t = 0.75$ s. This is one of the shots which will be used during the analysis of the reconstruction code (see Section 7.3.1). Also included in the plot is the simulated profile calculated using the Jones matrix method described previously with an assumed parabolic density profile. The measurements show good agreement with the predicted values except on the edge channels where the signal levels are relatively low. The errors bars on the data when used as input to the reconstruction code are weighted accordingly.

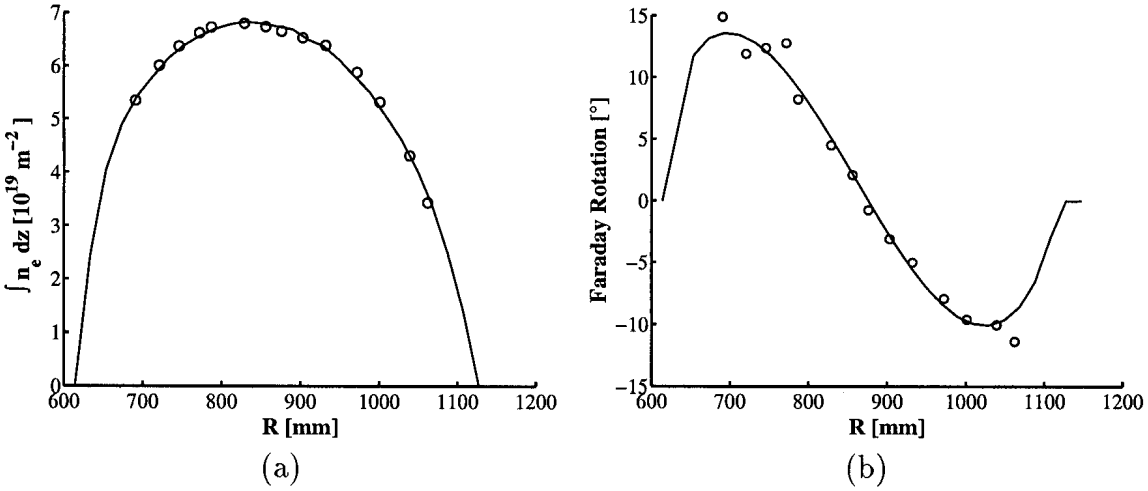

Figure 7.12: The (a) line-integrated density and (b) Faraday rotation profile, smoothed over 20ms, of shot #14886 at time $t = 0.75$s and the Jones matrix calculated values (full lines).

7.2.2 Method 2

The setting of the phase shift between the **A** and **B** beams turned out to be trickier than predicted and it proved difficult to set the phase to exactly zero. As mentioned previously in Section 4.4.3 a non-zero phase shift produces an additional modulation on the interferometer data. It was shown, however, that with a modulation index of $m = 0.4$, a phase difference of up to 10^o would still be acceptable, producing an additional modulation of less than 0.05 fringes (see Section 4.4.3). The phase difference on the central channel (detector number 6 which is used for the density feedback) was set as close to zero as possible. This was performed by maximising the low frequency component of its detected signal by adjusting the position of the translator as described in Section 4.4.

A plot is shown in Fig. 7.13 of the raw fringe counts before the plasma of the central channels of shots #15070 (Method 1) and #15140 (Method 2). It can be seen that the additional term of Method 2 while not zero is smaller than that of Method 1 and is

within the 0.05 fringe precision of the interferometer (see Section 3.3). The additional modulation on the signals is due to the vibrations discussed earlier in Section 7.1.1.

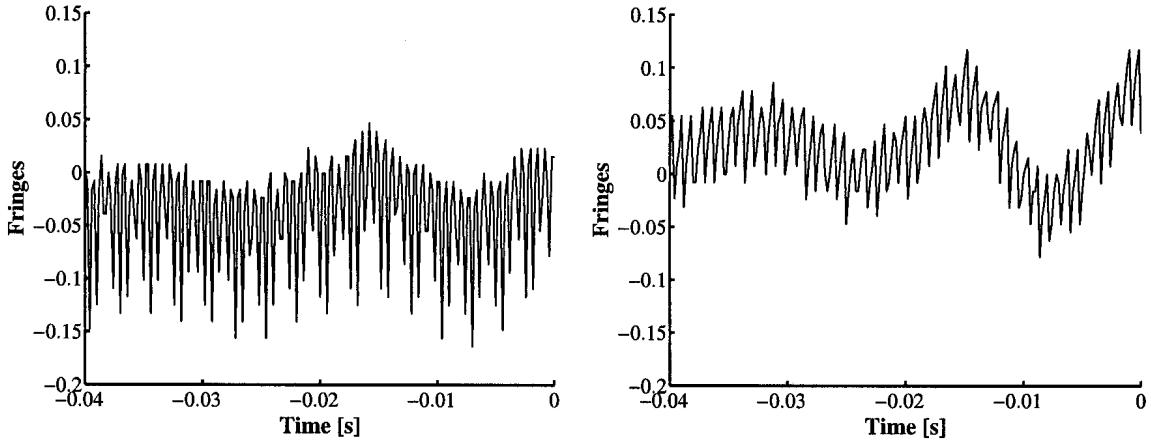

Figure 7.13: The raw fringe counts on the central channel (channel 6) before the plasma for (a) shot #15070 (Method 1) and (b) shot #15140 (Method 2).

A plot is presented in Fig. 7.15 of the raw interferometer and polarimeter traces for a high elongation shot (#15140) using Method 2. The channels adjacent to the central channel were seen to have additional terms similar to that of channel 6 with the amplitude increasing slightly with increasing distance from the centre. The amplitudes of the additional terms on channels 13 and 14 coupled with the power loss due to refraction discussed earlier led to these two channels becoming unusable.

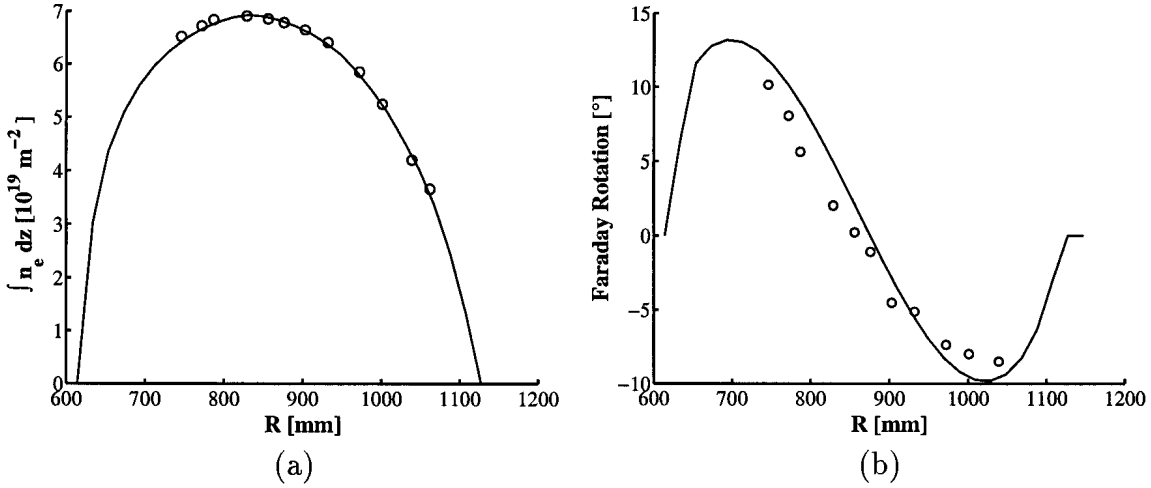

Figure 7.14: The (a) line-integrated density (channels $1-12$) and (b) Faraday rotation profile, smoothed over 20 ms, (channels $2-12$) of shot #15140 at time $t = 0.65$ s. Also included are the Jones matrix calculated values (full lines).

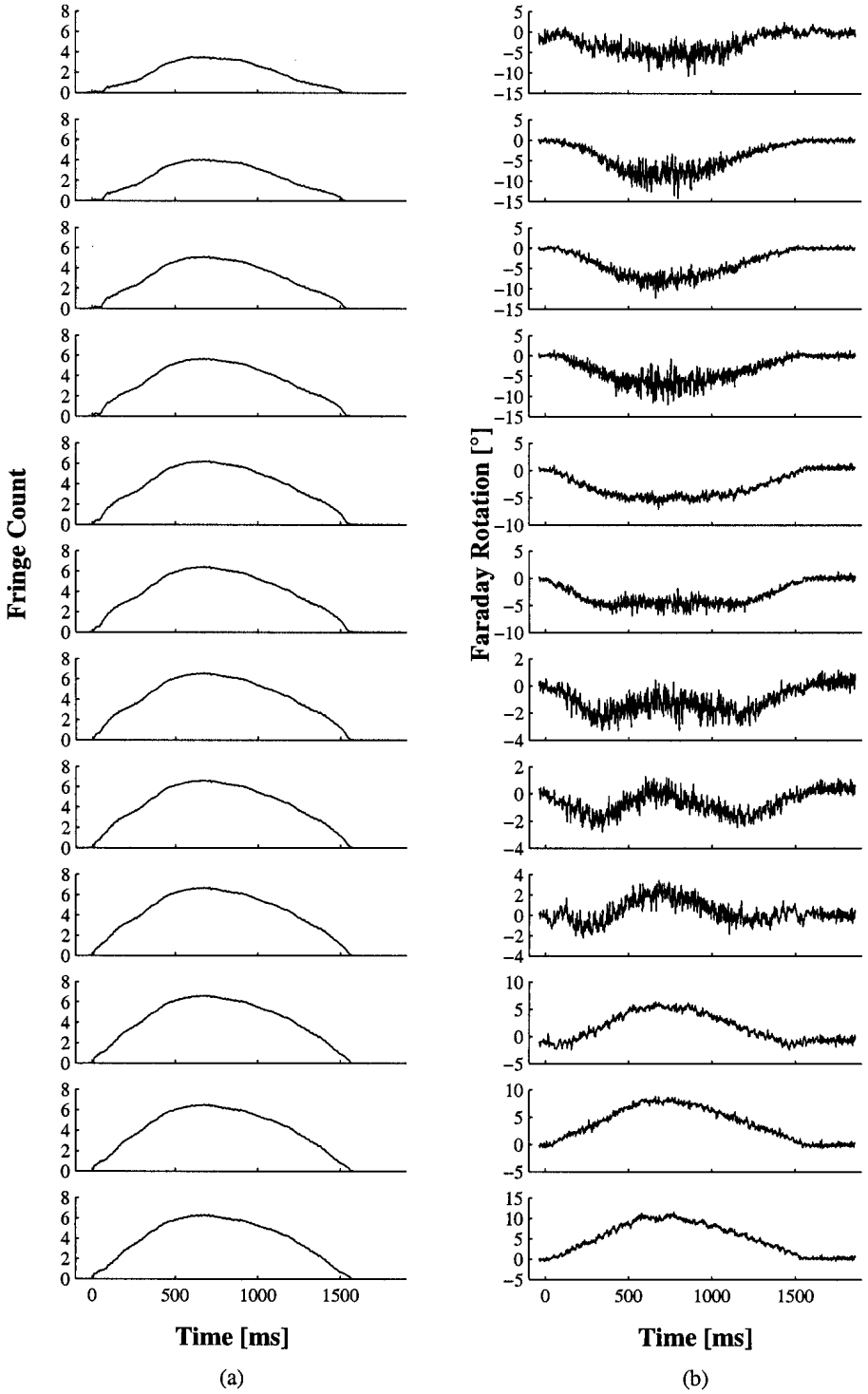

Figure 7.15: The (a) raw fringe count and (b) Faraday rotation from shot #15140 (channels 1 – 12 top to bottom) using Method 2.

The corresponding Faraday rotation profile of this shot at time $t = 0.75\,\mathrm{s}$ is plotted in Fig. 7.14. Due to its low signal level channel 1 was also unusable. The measured values in the case do not agree with the predicated values as well as the previous cases run with Method 1. This is partially due to the fact that Method 2 is inherently less precise than Method 1 (see Chapter 4).

This additional interferometer term could possibly be reduced even further on all channels with the installation of a more elaborate and accessible alignment system. The translator which adjusts the phase between the two beams is in the centre of the optics box (see Section 6.2). This box is under a slight N_2 pressure which makes access to the component difficult.

The advantage of Method 2 compared to Method 1 is the absence or at least the relatively small size of the additional term on the interferometer signal. Its disadvantages, however, are that it measures the Faraday rotation Ψ compared to 2Ψ and that the modulation frequency is lower by a factor of two.

7.2.3 Direct Determination of the Central Safety Factor

The polarimeter data can be used to determine a value of the central safety factor q_0 which is basically independent of the equilibrium reconstruction code. These values can then be used to confirm the LIUQE reconstructed q_0 values.

The safety factor q, specifies the number of complete toroidal circuits a field line must make before completing a single poloidal circuit as described in Section 1.2 and can be expressed as the rate of change of toroidal flux Φ, with poloidal flux per radian ψ,

$$q = \frac{1}{2\pi}\frac{\mathrm{d}\Phi}{\mathrm{d}\psi}. \tag{7.8}$$

Assuming elliptical flux surfaces we can express the poloidal flux function ψ as,

$$\begin{aligned} \psi &= C\left[(R-R_0)^2 + \frac{(Z-Z_0)^2}{\kappa^2}\right] \\ &= C(\rho a)^2 \end{aligned} \tag{7.9}$$

where R_0 and Z_0 are the coordinates at the plasma centre, κ is the vertical elongation and ρ is the normalised minor radius of the flux surface and a the minor radius of the plasma. In the following calculations we assume that the spatial dependence of the poloidal flux is sufficiently well described by the quadratic behaviour in R and Z. Although C is different on each flux surface its derivative with respect to R or ρ will be neglected.

The toroidal flux can be estimated by,

$$\Phi(\rho) = \pi\kappa(\rho a)^2 B_{\phi 0}. \tag{7.10}$$

where $B_{\phi 0}$ is the toroidal magnetic field at the mid-plane ($R = R_0$). Substituting this expression and that for the poloidal flux (Eqn. 7.9) into the definition of the safety factor (Eqn. 7.8) we obtain,

$$q = \frac{1}{2\pi}\frac{\mathrm{d}\Phi}{\mathrm{d}\psi} \approx \frac{1}{2}\frac{\kappa B_{\phi 0}}{C}. \tag{7.11}$$

The radial dependence of C can then be expressed by the safety factor profile,

$$C(\rho) \approx \frac{\kappa B_{\phi 0}}{2q(\rho)}. \tag{7.12}$$

The vertical component B_z of the poloidal field B_p can be determined from the poloidal flux,

$$B_z = \frac{1}{R}\frac{\partial\psi}{\partial R} \approx \frac{1}{R}\frac{\kappa B_{\phi 0}}{2q}2(R - R_0) \tag{7.13}$$

$$= \frac{\kappa B_{\phi 0} x}{(R_0 - x)q} \tag{7.14}$$

where $x = R - R_0$. The basic Faraday rotation equation (Eqn. 2.48) then becomes,

$$\Psi = 2.62 \times 10^{-13}\lambda^2 \int_{Z_1}^{Z_2} n_e B_z \,\mathrm{d}z \tag{7.15}$$

$$\approx c_p \int n_e \frac{B_{\phi 0} x}{(R_0 - x)q}\kappa \,\mathrm{d}z \tag{7.16}$$

$$= c_p B_{\phi 0} \int \frac{n_e}{(R_0 - x)q}\kappa \,\mathrm{d}z \cdot x \tag{7.17}$$

where $\lambda = 214.5\ \mu$m and consequently $c_p = 1.21 \times 10^{-20}$.

Experimental observations have shown that the measured profile of the electron temperature (T_e) in a steady state plasma has a bell-like shape, similar to a Gaussian distribution[43]. The width of this profile seems to depend only on the value of the safety factor at the edge q_a. Because the local plasma resistivity is mainly as function of T_e, the width of the current density profile in equilibrium is likely to also depend on q_a. This self-organising property of the plasma is is commonly referred to as "profile consistency"[44]. A theoretical relationship between the relaxed current and pressure profiles was derived from a variational principle such that the magnetic[45] energy or total energy[46] was minimised leading, for plasmas with circular cross-sections, to current profiles of the form,

$$j = j_0\left[1 + \gamma\rho^2\right]^2 \tag{7.18}$$

where $\gamma = q_a/q_0 - 1$ where q_a is the edge safety factor. The corresponding q profile is known as the natural safety factor profile,

$$q = q_0 \left[1 + \left(\frac{q_a}{q_0} - 1\right)\rho^2\right]. \tag{7.19}$$

We also use the profile form resulting from this model for elongated plasmas although the validity of such an assumption is currently being discussed[47].

It was assumed previously that the derivative of C with respect to ρ in Eqn. 7.9 was very small compared to that of $(\rho a)^2$ and can be neglected. The validity of this assumption for the chosen current profile is governed by,

$$C\frac{\mathrm{d}(\rho a)^2}{\mathrm{d}\rho} \gg (\rho a)^2\frac{\mathrm{d}C}{\mathrm{d}\rho} \tag{7.20}$$

or

$$\frac{1}{q} \gg \frac{\rho}{2}\frac{\mathrm{d}(1/q)}{\mathrm{d}\rho} \tag{7.21}$$

Both sides of the inequality in Eqn. 7.21 are plotted as a function of ρ in Fig. 7.16 for typical values of $q_a = 3$ and $q_0 = 1$. It can be seen that the inequality in Eqn. 7.21 holds and consequently that the derivative of C with respect to ρ can be neglected in these calculations except at the plasma edge ($\rho = 1$).

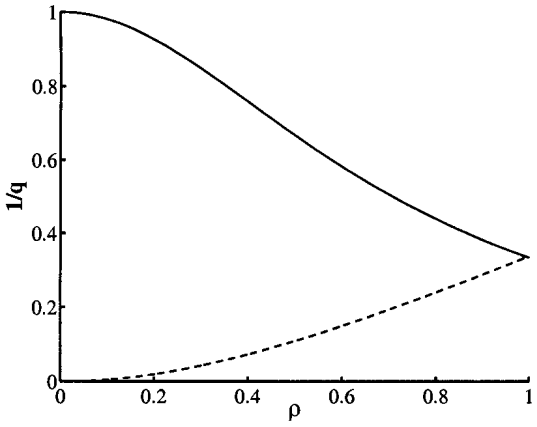

Figure 7.16: A plot of $1/q$ (full line) and $\frac{\rho a}{2}\frac{\mathrm{d}(1/q)}{\mathrm{d}\rho}$ (dashed line) with $q_a = 3$ and $q_0 = 1$.

We also assume a parabolic density profile,

$$n_e = n_{e0}\varphi^{\alpha} \tag{7.22}$$

$$= n_{e0}\left(1 - \rho^2\right)^{\alpha} \tag{7.23}$$

where $\varphi = 1 - \rho^2$ is the flux parameter used in the parabolic density profile fit (see Sections 3.2 and 7.1.2).

We want to investigate the behaviour of Ψ with $x \approx 0$. If $x \approx 0$, $z = \kappa\sqrt{(a\rho)^2 - x^2} \approx a\kappa\rho$ and $(R_0 - x) \approx R_0$ then Eqn. 7.17 for small x can be expressed as,

$$\Psi \approx 2\frac{c_p B_{\phi 0}}{R_0}\int_0^1 \frac{n_{e0}(1-\rho^2)^\alpha}{q_0[1+(q_a/q_0-1)\rho^2]} a\kappa^2 \,\mathrm{d}\rho \cdot x. \tag{7.24}$$

The slope of the Faraday rotation profile at the origin can then be written as,

$$\left.\frac{\mathrm{d}\Psi}{\mathrm{d}x}\right|_{x=0} \approx 2\frac{c_p B_{\phi 0}}{R_0}\int_0^1 \frac{n_{e0}(1-\rho^2)^\alpha}{q_0[1+(q_a/q_0-1)\rho^2]} a\kappa^2 \,\mathrm{d}\rho. \tag{7.25}$$

Now substituting for $\gamma = (q_a/q_0 - 1)$ we get,

$$\left.\frac{\mathrm{d}\Psi}{\mathrm{d}x}\right|_{x=0} \approx 2\frac{c_p B_{\phi 0}}{R_0}\frac{n_{e0}}{q_0} a\kappa^2 \int_0^1 \frac{(1-\rho^2)^\alpha}{1+\gamma\rho^2}\,\mathrm{d}\rho \tag{7.26}$$

$$= 2\frac{c_p B_{\phi 0}}{R_0}\frac{n_{e0}}{q_0} a\kappa^2 h(\rho) \tag{7.27}$$

where $h(\rho)$ is the integral. We can, therefore, roughly approximate q_0 by,

$$q_{0\kappa} \approx 2\frac{c_p B_{\phi 0} n_{e0}}{R_0} a\kappa^2 h(\rho)\left(\frac{\mathrm{d}\Psi}{\mathrm{d}x}\right)^{-1}\Bigg|_{x=0} \tag{7.28}$$

$$= q_{0circl}\kappa^2 \tag{7.29}$$

where q_{0circl} is the value of $q_{0\kappa}$ for a circular plasma ($\kappa = 1$).

This derivation is not completely independent of the plasma reconstruction code, requiring the values of $B_{\phi 0}$, R_0, κ and q_a. These parameters, however are determined from the external measurements and do not vary dramatically with varying reconstruction constraints. A value for q_0 is also required for the calculation of γ in the integral. The integral is not very dependent on the value of q_0 which, for these calculations, is approximated as 0.8. The density fit also requires the reconstructed flux but is relatively independent of minor variations in the flux. The plasma was assumed to consist of concentric ellipses of constant elongation. This is not the case as the plasma elongation decreases towards the centre of the plasma. Weisen et al.[47] fitted the central elongation κ_0 to the elongation at the plasma edge for a range of plasmas and obtained the relationship $\kappa_0 \approx 1 + 0.5(\kappa_{edge} - 1) + 0.2(\kappa_{edge} - 1)^2$. We use this relationship to determine the average elongation $\kappa = (\kappa_0 + \kappa_{edge})/2$, which we then use in the calculations. In practice, at least two measurement channels are required to determine the slope. These channels are some distance away from the magnetic axis so the validity of the $x \approx 0$ assumptions is limited.

This analysis was performed on a range of high elongation shots and the resulting q_{0circl} and $q_{0\kappa}$ for shot #14886 are shown in Fig. 7.17. Also included is a plot of the

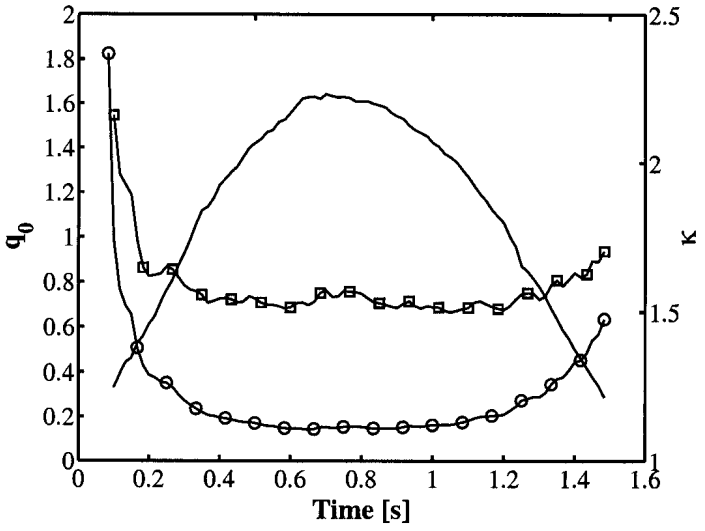

Figure 7.17: The polarimeter derived q_{0circl} (circles) and $q_{0\kappa}$ (squares) for shot #14886. Also included is a plot of the plasma elongation κ.

plasma elongation κ. The $q_{0\kappa} = 1$ crossings agree quite well with the onset and cessation of sawtooth activity, assuming that the presence of sawteeth coincides with the existence of a $q = 1$ surface, as can be seen in the plot in Fig. 7.18 where the calculated q_{0circl} and $q_{0\kappa}$ for shot #14636 are plotted against the soft x-ray trace from channel 10 of the central camera 2. In spite of assumptions made, the polarimeter calculated values of q_0 appear to be quite reasonable.

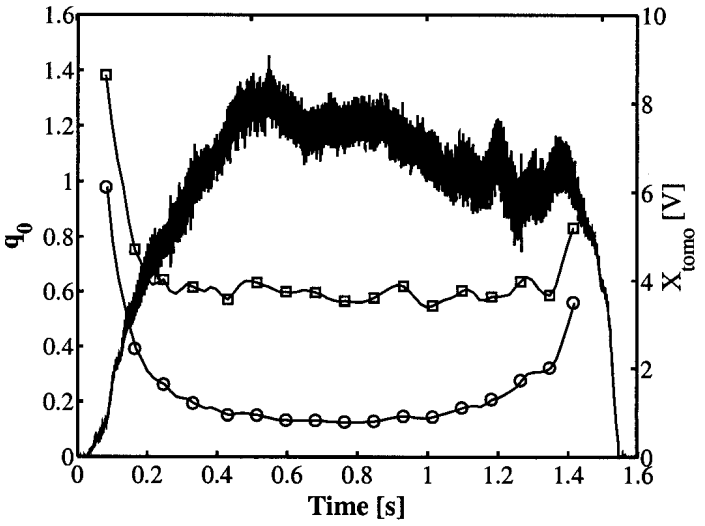

Figure 7.18: The polarimeter derived q_{0circl} (circles) and $q_{0\kappa}$ (squares) for shot #14636. Also included is the soft x-ray trace from channel 10 of the central camera 2.

7.3 LIUQE Reconstructions

As discussed previously in Section 3.5 the reconstruction of tokamak equilibria with arbitrary source functions using magnetic measurements, requires that the toroidal plasma current density be split into two parts. One part is proportional to Rp' and the other to TT'/R where R is the major radius, p the plasma pressure, $T = RB_\phi$ and the prime denotes differentiation with respect to the flux. The relative importance of these terms can, in principle, be determined due to the difference in their R-dependence. The terms p' and TT' and the electron density n_e can be expressed in terms of the normalised flux φ,

$$p' = \sum_{n=0}^{N_p} a_n U_n(\varphi) \tag{7.30}$$

$$TT' = \sum_{n=0}^{N_T} b_n V_n(\varphi) \tag{7.31}$$

$$n_e = \sum_{n=0}^{N_n} c_n W_n(\varphi) \tag{7.32}$$

where φ is normalised to 1 at the plasma centre and 0 on the LCFS, a_n b_n and c_n are constants to be determined and $U_n(\varphi)$, $V_n(\varphi)$ and $W_n(\varphi)$ are arbitrary base functions. As mentioned earlier (see Section 7.1.2) $W_n(\varphi) = \varphi^n$ and N_n is usually set to 3. The base functions V_n, U_n employed during the LIUQE reconstruction of TCV plasmas are,

$$\begin{aligned} U_1, V_1 &= \varphi \\ U_2, V_2 &= 1 - (2\varphi - 1)^2 \\ U_3, V_3 &= (2\varphi - 1) - (2\varphi - 1)^3 \\ U_4, V_4 &= \varphi e^{a\varphi}. \end{aligned} \tag{7.33}$$

The internal LIUQE calculated p' and TT' profiles are only available for the polynomial base functions. Consequently, the exponential base function U_4, V_4 was not used during the course of this work as the resulting profiles could not be evaluated. Plots of base functions U_{1-3}, V_{1-3} are shown in Fig. 7.19.

The equilibrium reconstruction problem being intrinsically non-linear, is solved by an iterative procedure. The method which is employed is as follows[18],

1. A rough approximation to the plasma current distribution is found using one of the fast, magneto-static methods, e.g.[48]

2. The Grad Shafranov equation (Eqn. 1.9) is solved using the measured flux values

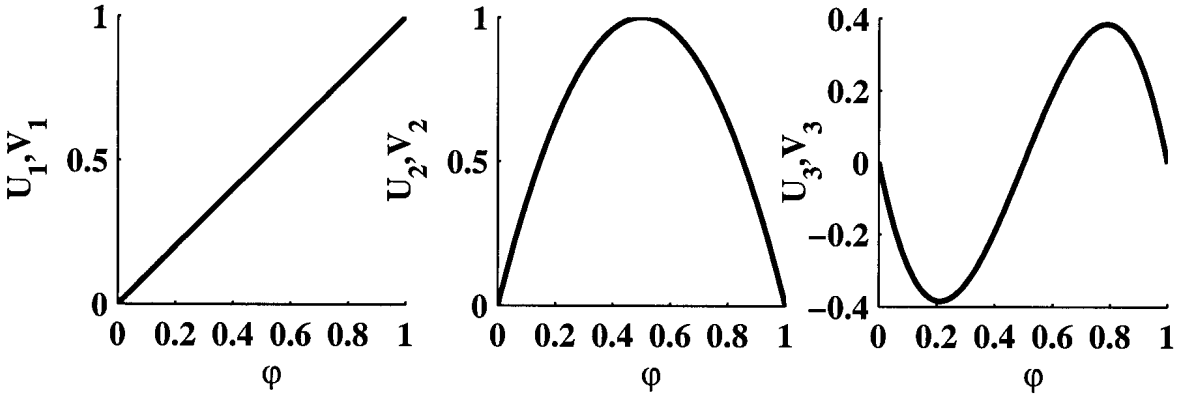

Figure 7.19: The base functions used during the LIUQE reconstructions.

as the boundary condition. The flux surface defining the plasma boundary is then determined by searching for the limiter or X-point with the highest flux value.

3. The profile parameters (a_n, b_n, c_n) are computed so as to obtain the best fit to the measurements, assuming $\psi(R, Z)$ fixed.

4. The toroidal current density $j = Rp' + (R\mu_0)^{-1}TT'$ is computed using Eqns. 7.30 and 7.31.

5. Steps 2, 3, 4 are repeated until a suitable convergence criterion is satisfied.

When the line-integrated density N and the Faraday rotation angle F, are included as inputs to the reconstruction code it is assumed that they are measured along a number of vertical chords,

$$\begin{aligned} N_i &= \int_{L_i} n_e dz \\ F_j &= \int_{L_j} n_e B_z dz. \end{aligned} \tag{7.34}$$

It should be noted that the two sets of chords L_i and L_j may, but do not have to coincide as they do in the case of the TCV interferometer/polarimeter.

The total error between the measurements M, which include the currents in the poloidal field coils, the vessel currents and the magnetic measurements, and the corresponding reconstructed quantities M^* is given by,

$$\chi^2 = \sum_i \left(\frac{M_i - M_i^*}{\Delta M_i} \right)^2 \tag{7.35}$$

where ΔM_i is the typical RMS error associated with the measurement M_i.

The base functions employed during a LIUQE run are chosen by setting the parameters *naas* and *nbbs* for p' and TT' respectively. A list of the possible settings of these parameters and their corresponding base functions are listed in Table 7.1.

naas ,*nbbs*	U, V
1	1
2	1, 2
3	1, 2, 3
4	1, 3
5	1, 4
6	1, 2, 4
7	1, 3, 4
8	2
9	4
10	2, 3

Table 7.1: The possible values of the parameters *naas* and *nbbs* and their corresponding base functions.

The so-called "standard" LIUQE is a reconstruction which uses neither the Faraday rotation nor the Thomson scattering pressure information as inputs and has the parameter settings $naas = 1$ and $nbbs = 2$. This reconstruction is performed automatically after each shot and is stored in the main data tree. Throughout this section all other reconstructions with varying parameters and inputs will be compared to this "standard" reconstruction. This analysis will concentrate on the LIUQE reconstructions of highly elongated plasmas some of which were presented in Section 7.2.

7.3.1 Faraday Rotation

LIUQE runs were performed on a number of high elongation shots, presented in Section 7.2, using the default parameters, $naas = 1$ and $nbbs = 2$ and including the Faraday rotation data as input. Examination of the traces of the reconstructed central safety factor q_0, showed that the values calculated with the inclusion the Faraday rotation information tended to follow the shape of the "standard" as can be seen in the reconstruction results of shots #14636 and #14886 in Fig. 7.20. Plots are shown of the q_0 and the pressure on the magnetic axis p_{axis} and the fitting error χ^2 for the reconstructions with and without the Faraday rotation information. Also included is a plot of the plasma current. It should be noted that the value of χ^2 (given in Eqn. 7.35) is calculated solely from the magnetic measurements, poloidal field currents and the vessel currents and does not include a Faraday rotation error term.

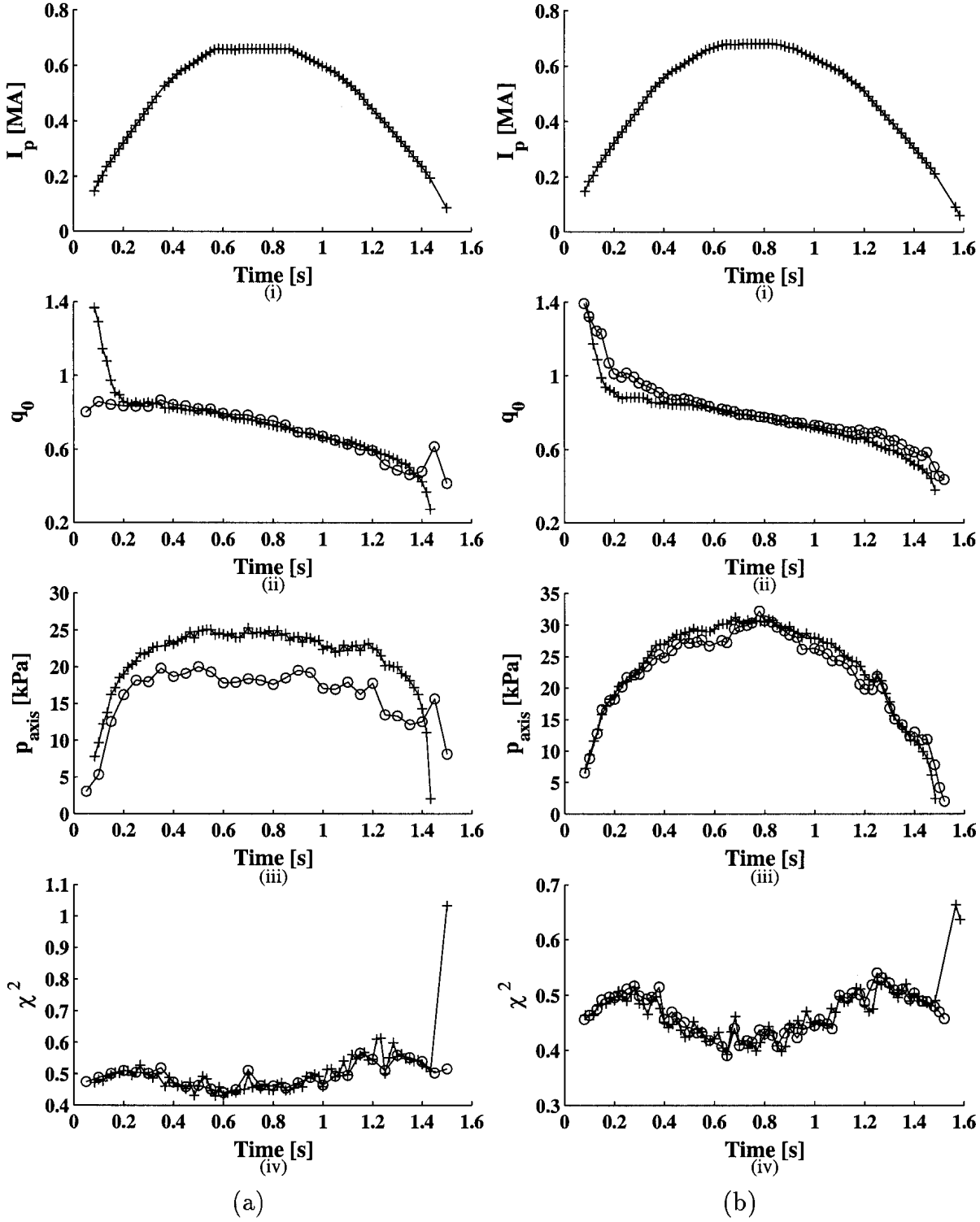

Figure 7.20: The (i) plasma current and the LIUQE reconstruction of (ii) q_0 and (iii) p_{axis} and (iv) the fitting error χ^2 for shots (a) #14636 and (b) #14886 with $naas = 1$, $nbbs = 2$. Both runs include the Faraday rotation data as input. The results of the "standard" LIUQE run are also shown (crosses).

A plot is shown in Fig. 7.21 of the q_0 determined from the polarimeter data (see Section 7.2.3) and the LIUQE reconstructed q_0 from both the "standard" and Faraday rotation runs for shots #14636 and #14886. The polarimeter determined q_0 shows a different temporal evolution to that reconstructed using the "standard" LIUQE. The evo-

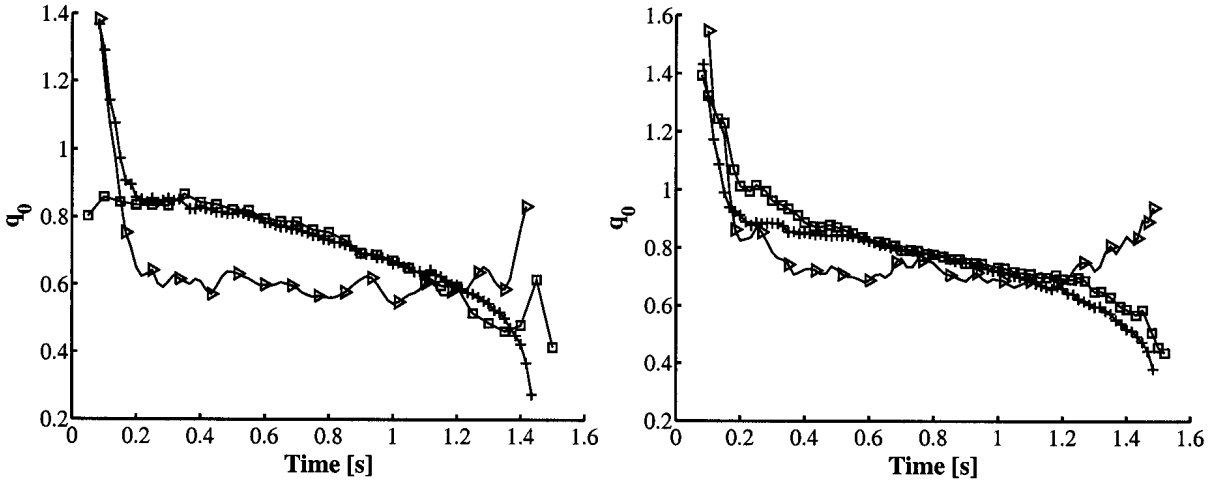

Figure 7.21: The polarimeter determined q_0 (triangles) for (a) shot #14636 and (b) shot #14886 showing the "standard" LIUQE reconstructed q_0 (crosses) and the LIUQE with Faraday rotation ($naas = 1$ and $nbbs = 2$) reconstructed q_0 (squares).

lution of the "standard" q_0 was never fully understood. It is seen to decrease continuously during the shot, even throughout the current flat-top ($0.57 - 0.87$ s for #14636). The return of the q_0 determined from the polarimeter data to values greater than 1 towards the end of the shot is consistent with the cessation of sawtooth activity (see Section 7.2), assuming that the presence of sawteeth coincides with the presence of a $q = 1$ surface.

Figure 7.22: The reconstructed q_0 of shot #14636 from the "standard" (crosses) LIUQE run and with $nbbs = 4$ (circles). Also included is the soft x-ray trace from channel 10 of the central camera 2. The dashed lines indicate the start and end of sawtooth activity and the $q_0 = 1$ line.

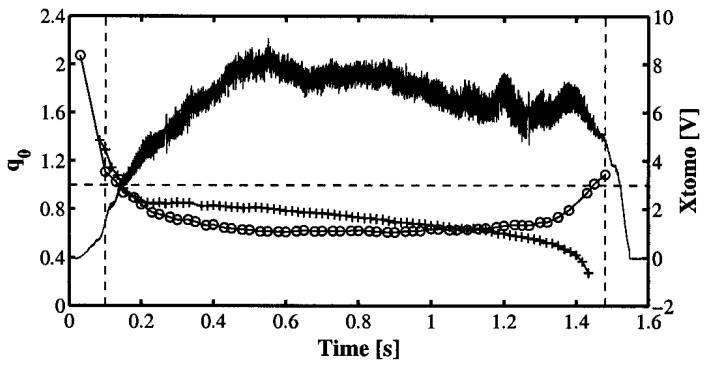

A plot of a typical soft x-ray trace on which sawteeth are visible is presented in Fig. 7.22 for shot #14636. Included in this figure is the trace of the q_0 from the "standard"

reconstruction. The $q_0 = 1$ crossing at the start of the shot coincides quite well with the start of sawtooth activity but towards the end of the shot the sawtooth size decreases while the "standard" q_0 is also still decreasing. The "standard" LIUQE reconstructed q_0 is, therefore, inconsistent with both the polarimeter and soft x-ray data.

In the absence of any other information regarding TT' the range of available base functions (see Table 7.1) were tested to find another combination which provides a better fit to the actual TT' profile. This investigation led to the conclusion that a value of $nbbs = 4$, namely a combination of the linear and cubic base functions, would lead to a shape of the reconstructed q_0 which were more in agreement with the independent predictions. The χ^2 for these reconstruction were comparable with those of the $nbbs = 2$ run.

The q_0 trace from the $nbbs = 4$ reconstruction of shot #14636 is plotted in Fig. 7.22 with the soft x-ray trace and the "standard" reconstructed q_0. Its $q_0 = 1$ crossings show a much better agreement with the presence of sawtooth activity than the corresponding "standard" trace. The q_0 from this reconstruction is also plotted alongside the polarimeter derived value of q_0 in Fig. 7.23(a) and (b) for shots #14636 and #14886, respectively. These LIUQE reconstructed values again show much better agreement with the polarimeter predicted values than the "standard" values also shown on the plots.

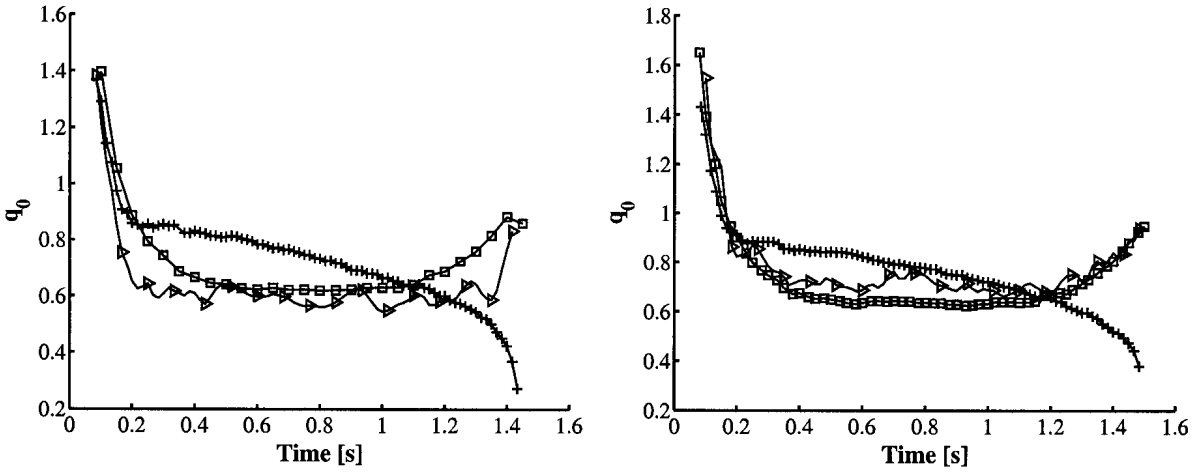

Figure 7.23: The polarimeter determined q_0 (triangles) for (a) shot #14636 and (b) shot #14886 showing the "standard" LIUQE reconstructed q_0 (crosses) and the LIUQE with Faraday rotation ($naas = 1$ and $nbbs = 4$) reconstructed q_0 (squares).

To analyse the effect of the different base function combinations the TT' and p' profiles of the reconstructions at a time point at which they differ considerably were examined.

A plot is presented in Fig. 7.24 of the profiles of shot #14886 at time $t = 1.4s$ for the "standard" LIUQE run and the $nbbs = 4$ runs both with and without Faraday rotation data as input. The TT' profiles of the two $nbbs = 4$ runs are quite similar while that of the "standard" is more peaked at the center. As the absolute value of TT' is, in general, larger than that of p', (the profiles are plotted Fig. 7.24 in arbitrary units) the toroidal current density $j = Rp' + (R\mu_0)^{-1}TT'$, is dominated by the TT' component ($\mu_0 = 4\pi \times 10^{-7}$ Hm^{-1}). The reconstructed current density, as a function of ρ, for the case with $nbbs = 4$ is, therefore, flatter than that of the "standard" reconstruction.

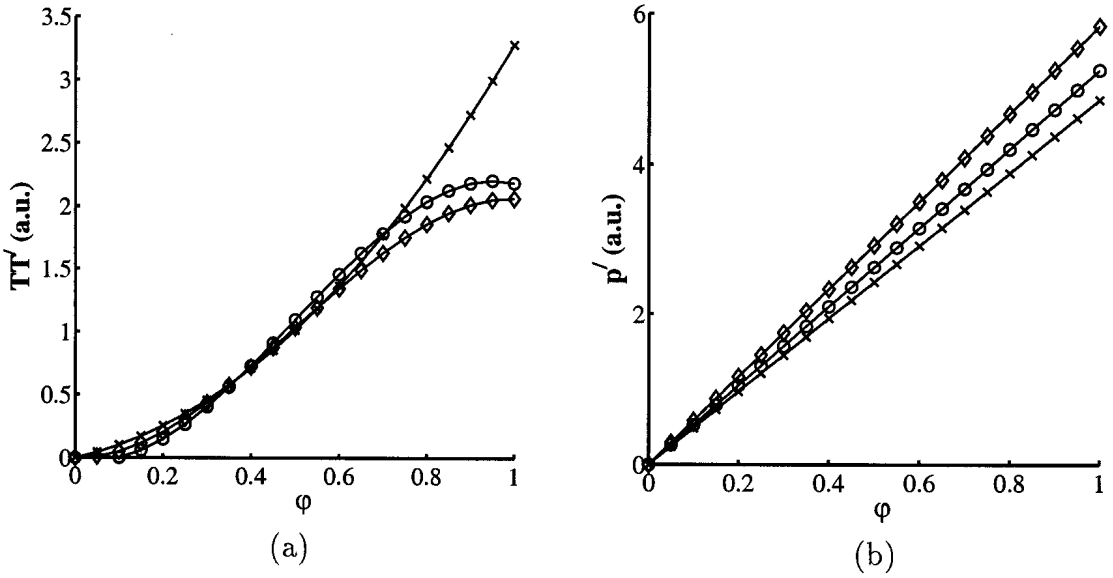

Figure 7.24: The (a) TT' and (b) p' profiles for shot #14886 at time $t = 1.4$ s with $nbbs = 4$ for runs with (diamonds) and without (circles) Faraday rotation information. The profiles from the "standard" LIUQE run with $nbbs = 2$ are also shown (crosses).

It was shown that the inclusion of Faraday rotation and line-integrated density measurements into the reconstruction code would allow for an increase in the number of base functions used[18]. The reconstructions were accordingly run with the settings $naas = 1$ and $nbbs = 3$, thereby including a third base function (V_2) into the TT' profile. The results of these reconstructions were not very promising. They led to values of q_0 which were, in general, larger than 1 throughout the shot which is inconsistent with the presence of sawteeth. The requirement of a precision of 2% of the maximum rotation angle before the Faraday rotation information becomes a useful input to the reconstruction code[18] has not yet been satisfied (see Section 7.2). The present data is not precise enough to allow for the inclusion of a third base function.

A plot is presented in Fig. 7.25(a) of the reconstructed q_0 of shot #15167 resulting from

the various LIUQE runs under investigation. A plot is also presented in Fig. 7.25(b) of the Jones matrix calculated Faraday rotation profiles for this shot using the results of the "standard" run and those of the $nbbs = 4$ run with Faraday rotation at a time $t = 0.65$ s. Whereas the reconstructed q_0 was seen to differ by about 20% the difference between the resulting Jones matrix calculated profiles was seen to be very slight. This analysis is, of course, very dependent on the accuracy of the Jones matrix calculations but provides an indication of the polarimeter precision required to improved the determination of q_0.

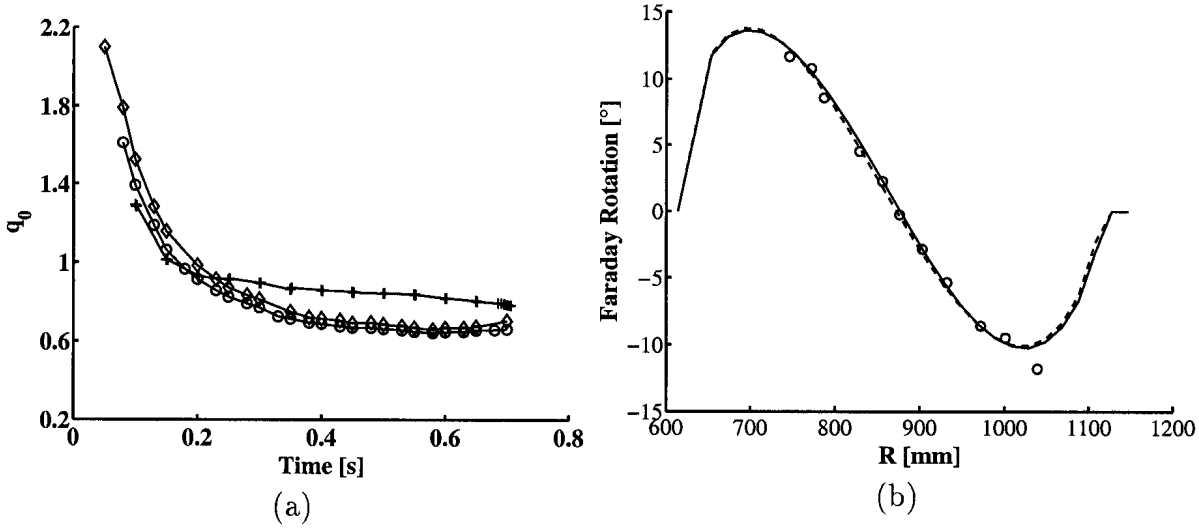

Figure 7.25: The (a) LIUQE reconstructed q_0 from the "standard" run (crosses) and runs with $nbbs = 4$ with (diamonds) and without (circles) Faraday rotation data for shot #15167 and (b) the Jones matrix simulated profile at time $t = 0.65$ for the "standard" (full line) and $nbbs = 4$ run with Faraday rotation (dashed line). Also included are the measured values (circles).

A plot is also shown in Fig. 7.26 of the sawtooth inversion radius (see Section 1.2.2) at time $t = 0.6$ of shot #14636 and the LIUQE calculated q surfaces from both the "standard" LIUQE and the reconstruction with $nbbs = 4$ and Faraday rotation. The q surfaces plotted are $1 - 2.5$ in steps of 0.5. It can be seen that the calculated q surfaces for both reconstructions are very similar in spite of their different values of q_0 and that the $q = 1$ surfaces coincide well with the sawtooth inversion radius.

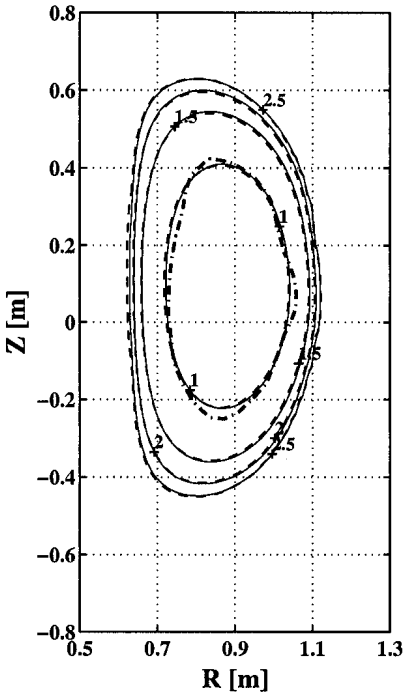

Figure 7.26: The sawtooth inversion radius (dot-dashed line) calculated from the x-ray tomography, alongside the reconstructed q surfaces for shot #14636 at time $t = 0.7$ s from "standard" LIUQE (full line) and a run with $nbbs = 4$ (dashed line).

7.3.2 Thomson Scattering

Having re-defined the standard value of $nbbs$ for the high elongation shots under investigation the reconstructions were re-run to include the Thomson scattering electron pressure data as input. There is a standard reconstruction run with Thomson data where the base functions parameters are set to $naas = 2$, $nbbs = 2$. In the absence of ion pressure information a simple model for the total pressure p_{tot} is used,

$$p_{tot} = 1.4 p_e \tag{7.36}$$

where p_e is the electron pressure. This model is quite basic but is adequate for this analysis. The reconstructions were run setting $naas = 2$ and $nbbs = 4$ and the results from shots #14886 and #15140 are shown in Fig. 7.27. The results of the "standard" reconstruction are also shown. To facilitate the evaluation of the inclusion of the Thomson data the χ^2 in both cases includes a Thomson pressure measurement term. An obvious improvement in χ^2 due to the inclusion of the pressure information can be seen in both shots. However, the reconstructed q_0 in these cases was seen to be higher than that of the standard remaining always above 1 in the case of shot #15140 which is inconsistent with the presence of sawtooth activity.

The TT' and p' profiles of these shots were were examined and the p' profile was seen to be negative at the centre of the plasma ($\varphi = 1$) as can be seen from the plots of the

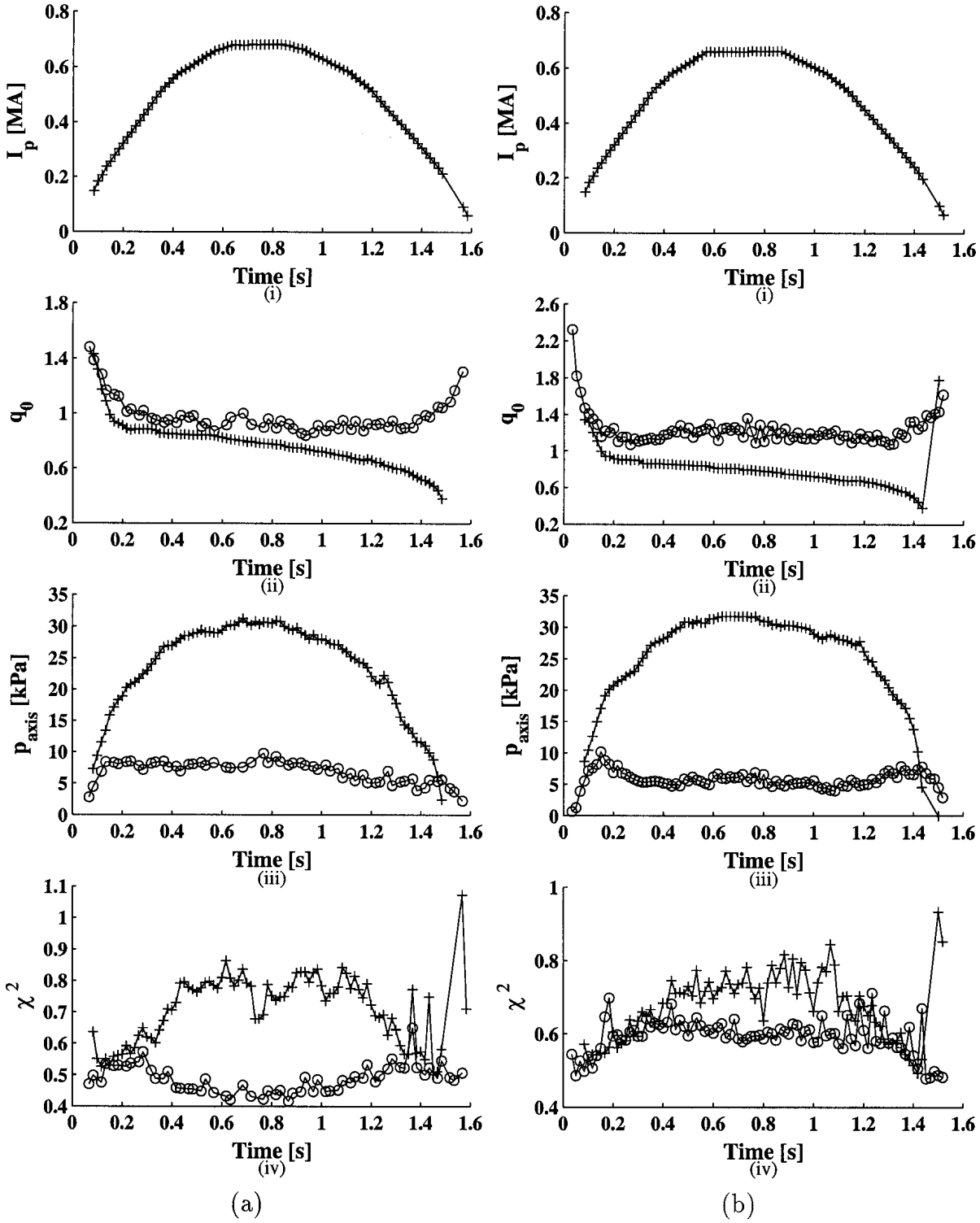

Figure 7.27: The (i) plasma current and the LIUQE reconstruction of (ii) q_0 and (iii) p_{axis} and (iv) the fitting error χ^2 for shots (a) #14886 and (b) #15140 with $naas = 2$, $nbbs = 4$. Both runs include the Faraday rotation and Thomson scattering data as input. The results of the "standard" LIUQE runs are also shown (crosses). The Thomson pressure measurements were included in all cases in the determination of χ^2.

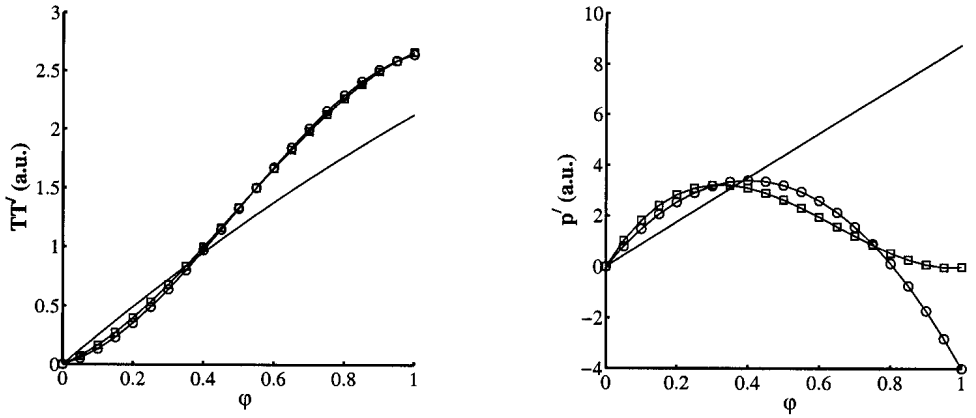

(a) (b)

Figure 7.28: The (a) TT' and (b) p' profiles for shot #14886 at time $t = 0.75$ s with $naas = 2$, $nbbs = 4$ (circles), $naas = 10$, $nbbs = 4$ (squares) and the "standard" run with $naas = 1$, $nbbs = 2$ (full lines).

TT' and p' profiles of shot #14886 in Fig. 7.28. This negative central value of p' implies a hollow pressure profile which can be seen in the plot of the reconstructed pressure profile of this shot in Fig. 7.30(a). The pressure profile calculated from the Thomson measurements is also included in the plot as is the "standard" reconstructed profile. There is no physical evidence, either from the Thomson or other measurements, to suggest that a hollow pressure profile exists. In fact such a profile would require heat transport in a direction opposite to that of the pressure gradient which cannot be explained by purely diffusive transport.

An investigation was made of the available base functions in order to find another combination which might be more applicable in this case. The combination of the quadratic (U_2) and cubic (U_3) base functions, selected with $naas = 10$, was chosen as for this combination p' is always 0 at $\varphi = 1$, forcing a flat density profile in the centre of the plasma. The reconstructions were re-run with this setting of $naas$ and the results from shots #14886 and #15140 are shown in Fig. 7.29. The "standard" reconstruction results are also shown and the Thomson pressure measurements were again included in the determination of χ^2 in all cases. The p_{axis} in both cases was seen to be slightly higher than that of the $naas = 2$ run and the q_0 was seen to be at at lower and more reasonable value. There was again an obvious improvement in χ^2 due to the inclusion of the pressure information. The TT' and p' profiles of this reconstruction at a time $t = 0.65$ s are plotted in Fig. 7.28. The corresponding reconstructed pressure profile is plotted Fig. 7.30(b) with the "standard" reconstructed pressure profile and the Thomson profile measurements. This reconstructed

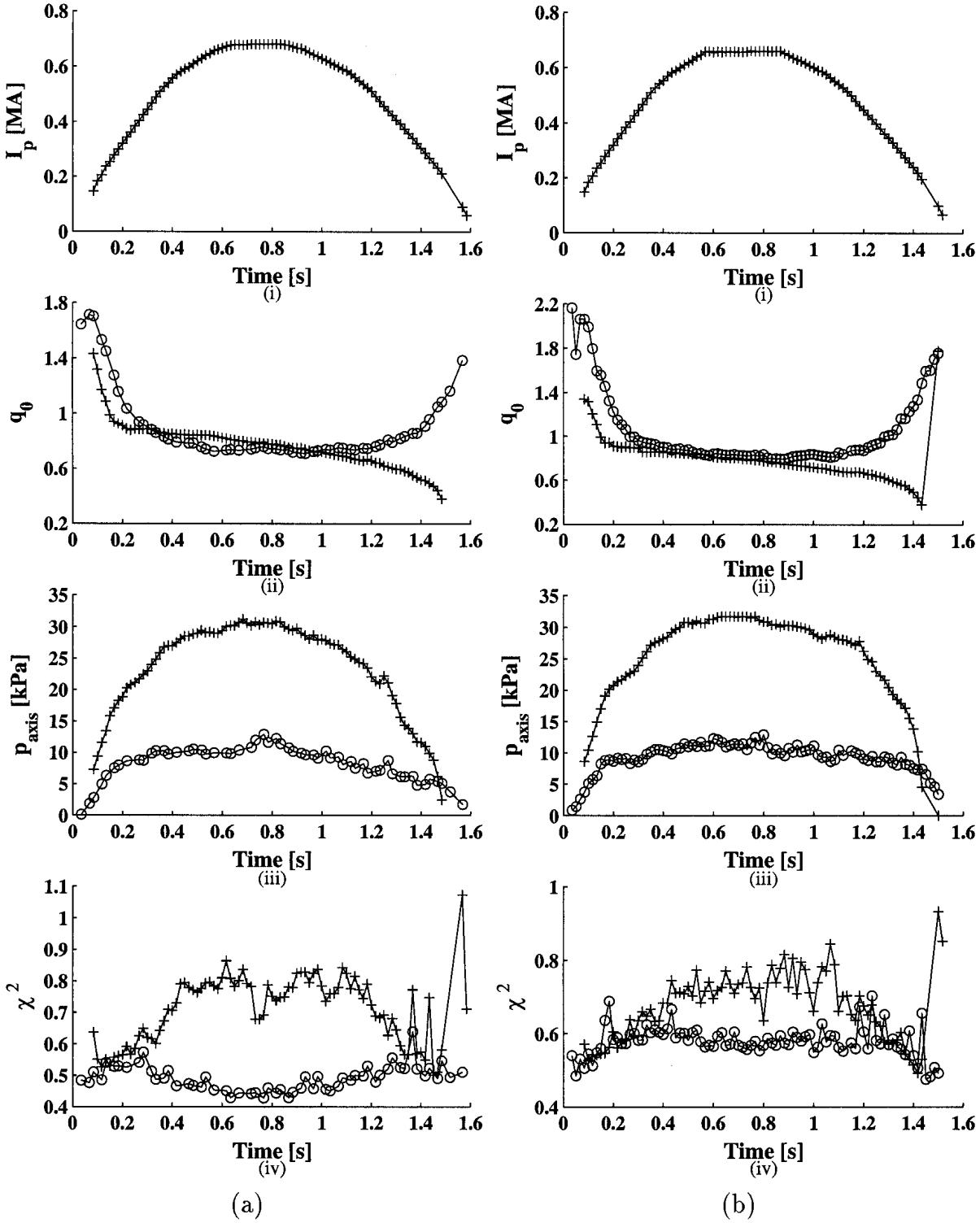

Figure 7.29: The (i) plasma current and the LIUQE reconstruction of (ii) q_0 and (iii) p_{axis} and (iv) the fitting error χ^2 for shots (a) #14886 and (b) #15140 with $naas = 10$, $nbbs = 4$. Both runs include the Faraday rotation and Thomson scattering data as input. The results of the "standard" LIUQE run are also shown (crosses).

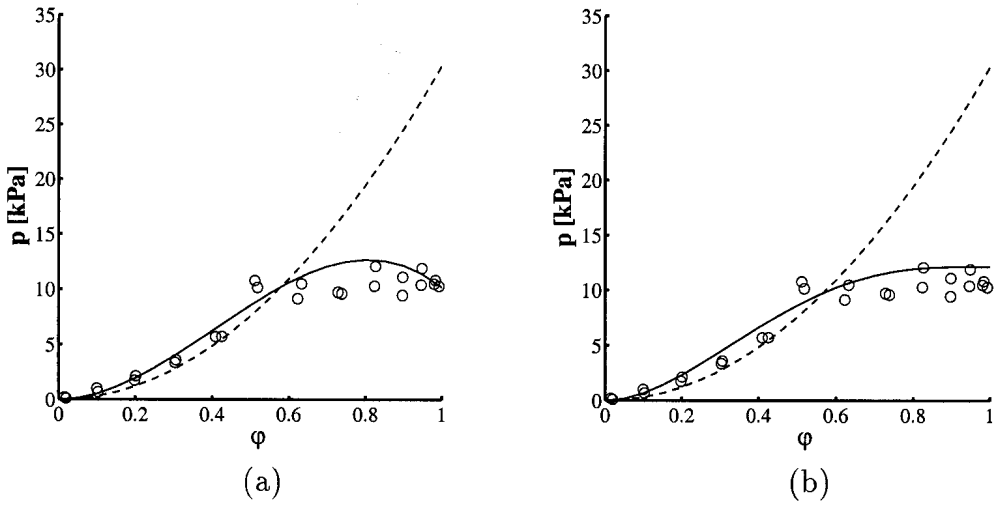

Figure 7.30: The reconstructed pressure profiles for shot #14886 at time $t = 0.75$ s with (a) $naas = 2$ and (b) $naas = 10$. Included are the "standard" profiles (dashed lines) and the Thomson pressure profiles (circles).

profile shows better agreement with the measured values than the previous case.

The selection of the $naas = 10$ and $nbbs = 4$ appears to produce the most reasonable results given the selection of available base functions. Combinations of other types of base function could improved the reconstruction even further.

7.3.3 Standard

It was obvious that the "standard" LIUQE run was not optimised for the high elongation plasmas under investigation here. The choice of $nbbs = 4$ was shown previously in Section 7.3.1 to be a more appropriate choice of base functions for this type of plasma. It was also shown during the investigation of the LIUQE reconstructions with the Thomson scattering pressure data as input that more reasonable results were obtained using a combination of base functions which force the pressure profile, in ρ space, to be flat at the centre of the plasma. In the case of reconstructions run without the inclusion of the Thomson data only a single base function for the evaluation of p' can be used. The base functions which satisfy this criterion are U_2 the quadratic and U_3 the cubic function. Of these only U_2 is available individually with the selection of $naas = 8$ (see Table 7.1).

The basic LIUQE, without Thomson and Faraday rotation data, was accordingly rerun with parameters to $naas = 8$ and $nbbs = 4$. It can be seen from the results of the reconstruction of shot #14886, shown in Fig. 7.31 that the shape of the q_0 trace is similar to the polarimeter predictions (see Section 7.2.3) and that the p_{axis} is lower than

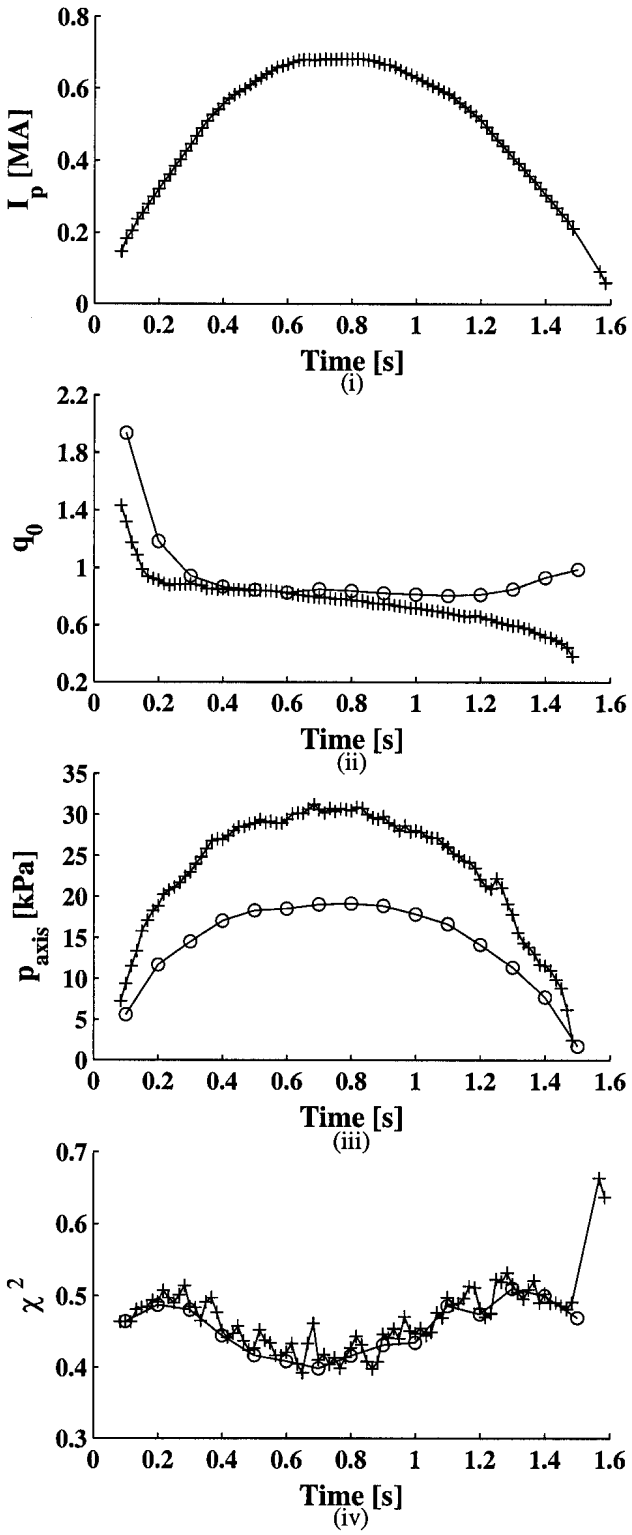

Figure 7.31: The (i) plasma current and the LIUQE reconstruction of (ii) q_0 and (iii) the on-axis pressure p_{axis} and (iv) the fitting error χ^2 for shot #14886 with $naas = 8$, $nbbs = 4$ run without the inclusion the Faraday rotation and Thomson scattering data. The results of the "standard" LIUQE run with $naas = 1$, $nbbs = 2$ are also shown (crosses).

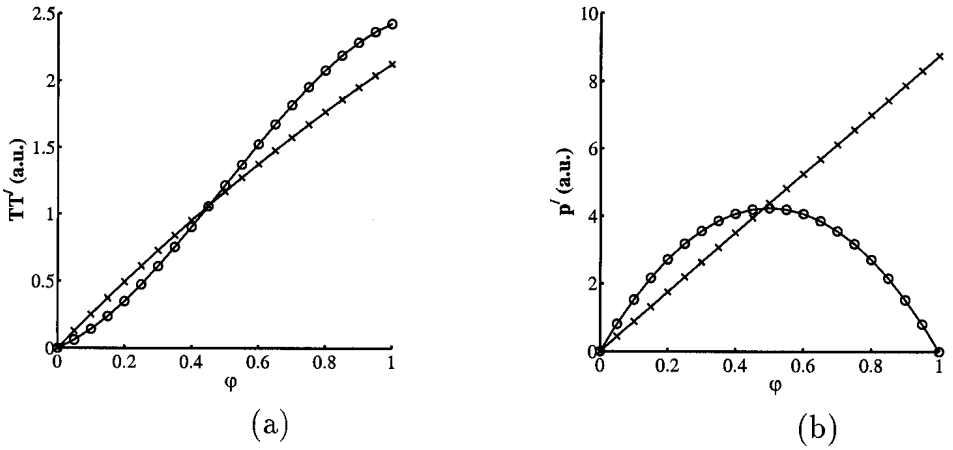

Figure 7.32: The (a) TT' and (b) p' profiles for shot #14886 at time $t = 0.75$ s with $naas = 8$, $nbbs = 4$ (circles) run without the inclusion of Thomson scattering and Faraday rotation data. The profiles from the "standard" LIUQE run are also shown (crosses).

that calculated with "standard" LIUQE. The χ^2, determined without the inclusion of the Thomson measurements, is comparable for both reconstructions. A plot is also produced in Fig. 7.32 of the TT' and p' profiles for both the "standard" and the $naas = 8$, $nbbs = 4$ runs at time $t = 0.75$ s. The plot in Fig. 7.33 shows the reconstructed pressure profiles and the Thomson scattering pressure profiles. It can be seen that the pressure profile with $naas = 4$ is in much better agreement with the measured profiles. It is, therefore, proposed to use these values of $naas$ and $nbbs$ as the new "standard" parameters for the LIUQE reconstruction of high elongation plasmas when Thomson scattering data is not available.

Figure 7.33: The reconstructed pressure profile for shot #14886 at time $t = 0.75$ s with $naas = 8$ $nbbs = 4$ run without the inclusion of Thomson scattering and Faraday rotation data. Also shown are the reconstructed profiles from the "standard" LIUQE run (dashed lines) and the Thomson pressure profile (circles).

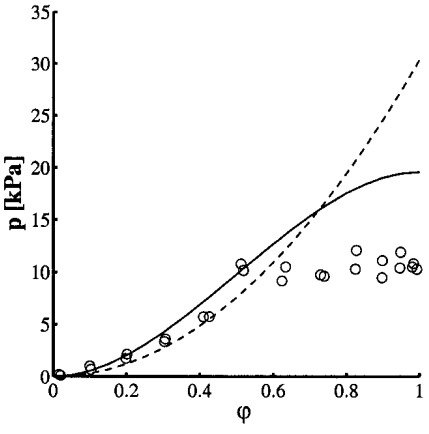

7.4 Modifications/Improvements

To improve the accuracy of the demodulation of the signals (see Section 4.5.1) the carrier frequency of the signals, which corresponds to the frequency shift of the LO could be increased. By using two separate lasers which are slightly detuned in frequency carrier frequencies up to the order of MHz, or higher, could be obtained. The employment of a double-laser system would also avoid the slight modulation on the signals due to the rotating grating (see Section 5.2). The frequency shift on this instrument is, however, limited to 750 kHz, the upper limit of the detectors. The installation of such a system would also require modifications to both the interferometer and polarimeter electronics.

As mentioned in Section 7.2 the noise on the polarimeter signals was very dependent on the alignment of the beam through the tokamak vessel. It was also noticed that there was a contribution on some of the signals from beams diffracted by the edges of the tokamak windows. Lenses have been installed on top of the machine in order to focus only that part of the beam propagating straight through the tokamak onto the detectors. The performance of these devices has still to be evaluated completely. In the long term, however, the solution might be to replace the slab-like beam which traverses the plasma by a series of individual beams, either one for each window section (3) or for each individual chord (14). This would avoid the diffraction effects at the window edges and would result in better control of the alignment of the individual chords through the vessel. This would, of course have to be coupled with a corresponding modification of the LO beam path. The installation of such a modification would be complicated by the beam-splitting arrangement coupled with the corresponding power losses and the restricted access and space available.

7.5 Conclusion

The first measurements of Faraday rotation on TCV have been presented. The results obtained using both of the interferometer/polarimeter methods and their respective limitations have been discussed. The measured Faraday rotation profiles were seen to compare well with the predicted values especially on the central channels where the signal levels are high.

The instrument was seen to suffer from additional noise during the plasma shot which has been investigated but which could not be completely eliminated within the course of this thesis work.

A method employed to directly determine the central safety factor q_0 from the po-

larimeter data which is essentially independent of the reconstruction code was presented. The results of this calculation compared favourably with expected values and the data from the soft x-ray diagnostic.

The results of the reconstruction of the plasma equilibrium, using LIUQE, both with and without the inclusion of the interferometer/polarimeter data was presented. It was seen that the accuracy of the polarimeter data is not yet at the level where its inclusion as input to the reconstruction code results in an obvious improvement in the determination of q_0. However, the polarimeter determined q_0 has been seen to be useful aid in the choice of the base functions and the confirmation of the LIUQE reconstructed values.

Bibliography

[1] J. Wesson, *Tokamaks*, Clarendon Press, Oxford, 1987.

[2] JET Team, Plasma Phys. Control. Fusion **37**, A3 (1995).

[3] F. Hofmann et al., 24th EPS Conference on Plasma Physics and Controlled Fusion, Berchtesgaden, June 1997.

[4] M. Anton et al., Plasma Phys. Control. Fusion **38**, 1849 (1996).

[5] G. E. Forsythe, M. A. Malcolm andd C. B. Moler, *Computer Methods for Mathematical Computations*, Prentice-Hall, Englewood Cliffs, N. J. (1977).

[6] U. Feldmann, J. F. Seely, N. R. Sheeely Jr., J. Appl.Phys. **56 (9)**, 2512 (1984).

[7] D. Wróblewski, L. K. Huang and H. W. Moos, Rev. Sci. Instr. **59 (11)**, 2341 (1988).

[8] D. Wróblewski and L. L. Lao, Rev. Sci. Instr. **63 (10)**, 5140 (1992)

[9] F. DeMarco and S.E. Segre, Plasma Phys. **14**, 245 (1972).

[10] M. Born and E. Wolf, *Principles of Optics*, Pergamon Press, Oxford (1964).

[11] R. C. Jones, J. Opt. Soc. Amer. **31**, 488 (1941).

[12] G. N. Ramachandran and S. Ramaseshan, *Crystal Optics*, Encyclopedia of Physics, Vol.25/1, Springer, Berlin (1961).

[13] M. A. Heald, and C. B. Wharton, *Plasma Diagnostics with Microwaves*, John Wiley & Sons Inc. New York (1965).

[14] H. Soltwisch, Plasma Phys. Control. Fusion **35**, 1777 (1993).

[15] I. H. Hutchinson, *Principles of Plasma Diagnostics*, Cambridge University Press (1987).

[16] J. H. Rommers, Ph.D Thesis, University of Utrecht (1996).

[17] D. Véron, in *Infrared and Millimeter Waves*, edited by K. J. Button (Academic Press, New York, 1979), **2**, 69.

[18] F. Hofmann and G. Tonetti, Nucl. Fusion **28**, 1871 (1988).

[19] Y. Yasutomo, K. Miyata, S. Himeno, T. Enoto and Y. Ozawa, IEEE Trans. on Plasma Sci. **PS-9**, 18 (1981).

[20] S. M. Wolfe, K. J. Button, J. Waldman and D. R. Cohn, Appl. Opt. **15**, 2645 (1976).

[21] D. K. Mansfield, P. A. Krug, M. Vocaturo, L. Guttadora, M. Rockmore and K. Micai Applied Optics **31**, 5030 (1992).

[22] H. Soltwisch, Rev. Sci. Instrum. **57**, 1939 (1986).

[23] G. Dodel and W. Kunz, Infrared Phys. **18**, 773 (1978).

[24] B. W. Rice, Rev. Sci. Instrum. **63**, 5002 (1992).

[25] S. E. Segre, ENEA Report, RT/ERG/FUS/97/18.

[26] D. K. Mansfield and L. C. Johnson, Int. J. Infrared Millimeter Waves **2**, 651 (1981).

[27] W.R. Geck, X. Qin, J. Liao, C. W. Domier and N. C. Luhmann Jr., Rev. Sci. Instrum. **66**, 860 (1995).

[28] J. H. Rommers, S. Barry, R. Behn and C. Nieswand, Plasma Phys. Control Fusion **40**, 2073 (1998).

[29] S. Barry, C. Nieswand, F. Bühlmann, S. Prunty and H. Mansfield, Rev.Sci. Instrum. **67**, 1814 (1996).
S. Barry, C. Nieswand, S. Prunty, H. M. Mansfield and P. O'Leary, Rev.Sci. Instrum. **68**, 2037 (1997).

[30] R. Ulrich, Infrared Phys. **7**, 37 (1967).

[31] E. J. Danielewics, T. A. Galantowics, F. B. Foote, R. D. Reel and D. T. Hodges, Optics Letters **4**, 280 (1979).

[32] J-L. Lachambre, P. Bernard and M. Gagne, IEEE Jour. Quant. Electr. QE-21, 282 (1985).

[33] E. J. Danielewics, Proc. 4th Int. Conf. IR and MMWaves, Miami, 203 (1979).

[34] A. E. Siegman *Lasers*, University Science Books, 1986.

[35] M. S. Durschlag and T. A. DeTemple, Appl. Opt. **20**, 1245 (1981).

[36] C. Chen, IEEE Trans Microwave Theory Tech. **MTT-18**, 627 (1970).

[37] S. W. Lee, IEEE Trans Antennas Propag. **AP-19**, 475 (1971).

[38] H. M. Pickett, J. Farhoomand and A. E. Chiou, Appl. Opt. **23**, 4228 (1984).

[39] N. Marcuvitz, *Waveguide Handbook*, Dover Pub. Inc. New York (1965)

[40] D. Véron, Opt.Comm. **10**, 95 (1974).

[41] P. Belland and J.-P. Crenn, Int. J. Infrared Millimeter Waves **10**, 1279 (1989).

[42] S. K. Kim, D. L. Brower, W.A. Peebles and N. C. Luhmann Jr., Rev. Sci. Instrum. **59**, 1551 (1988).

[43] TRF Group, Proc. 7th European Conf. Contr. Fusion and Plasma Phys., 1-5th Sept. 1975 Lausanne, Vol II 1.

[44] B. Coppi, Comments Plasma Phys. Controlled Fusion **5**, 261 (1980).

[45] D. Biskamp, Comments Plasma Phys. Controlled Fusion **10**, 165 (1986).

[46] B. B. Kadomtsev *Tokamak plasma: a complex physical system*, Institute of Physics publishing, London (1992).

[47] H. Weisen et al. Plasma Phys. Controlled Fusion **40**, 1803 (1998).

[48] F. Hofmann and G. Tonetti, Nucl. Fusion **28**, 519 (1988).